SCUOLA DI DOTTORATO
UNIVERSITÀ DEGLI STUDI DI MILANO-BICOCCA

Department of Physics "G. Occhialini"

Ph. D. program in Physics and Astronomy, XXXVIII cycle
Curriculum of Subnuclear Physics

Measurement of mixing and *CP* violation in $D^0 \to K^0_S \pi^+ \pi^-$ decays with 2024 Data and Performance studies of the RICH detectors in the Upgrade I and Upgrade II of LHCb

Anelli Alessia
Registration number: 906799

Tutor: Prof. Calvi Marta
Supervisor: Prof. Martinelli Maurizio

Coordinator: Prof. D'Alfonso Laura

Academic Year 2024/2025

Abstract

This thesis presents studies of charm mixing and *CP* violation, together with investigations of the performance of the Ring Imaging Cherenkov (RICH) detectors of the LHCb experiment in Run 3 and in the context of the Upgrade II programme.

The first part of this thesis focuses on a measurement of charm mixing and *CP*-violation observables in the decay channel $D^0 \to K^0_S \pi^+ \pi^-$ using Run 3 data collected in 2024 by the LHCb experiment. The analysis employs the bin-flip method, a model-independent approach that avoids reliance on amplitude modelling and reduces systematic effects related to efficiency variations across the Dalitz plane. Although based on a subset of the full Run 3 dataset, the integrated luminosity already exceeds that of Run 2, resulting in sensitivities that are slightly improved.

The stability of the results is investigated as a function of the data-taking blocks, and good overall consistency and robustness of the measurement are observed.

The second part of the thesis evaluates the performance of the upgraded RICH detectors using Run 3 data from 2024. Studies of photon timing and hit distributions validate the detector performance under real data-taking conditions and provide insight into background contributions and their impact on the single photon resolution.

The final part addresses the prospects for particle identification at the high luminosities foreseen for the LHCb Upgrade II. Simulation-based studies of several RICH detector configurations highlight the importance of timing and spatial resolution in maintaining excellent particle identification performance, and provide input to the design choices for the future upgrade of the experiment.

Contents

Introduction

Since the dawn of civilisation, humankind has sought to identify the fundamental building blocks of nature and the laws governing their interactions. This pursuit, initiated by ancient philosophers, has culminated in the formulation of the Standard Model (SM) of particle physics: a theoretical framework capable of describing all known elementary particles and their interactions, with the notable exception of gravity. Over the past century, the SM has withstood a huge number of experimental tests, and the extraordinary discovery of the Higgs boson at the Large Hadron Collider (LHC) in 2012. Despite its remarkable success, the SM accounts for only about 5% of the total energy content of the Universe and leaves several questions unanswered. For instance, it fails to incorporate gravity and general relativity, does not accommodate neutrino oscillations [1, 2] or their non-zero masses [3], and cannot explain the observed dominance of matter over antimatter, known as baryon asymmetry [4].

The search for physics beyond the Standard Model (BSM) follows two main strategies. The first consists of direct searches for new particles or interactions predicted by theoretical models, such as supersymmetry or dark sector extensions. The second relies on precision measurements of known processes, aiming to detect deviations from SM predictions that would indicate the presence of new phenomena. The latter approach, which has historically played a decisive role in shaping our understanding of fundamental physics, is particularly sensitive to virtual effects of particles too massive to be produced directly in current accelerators.

A crucial phenomenon in this context is the violation of the combined charge conjugation (C) and parity (P) symmetries, collectively referred to as CP violation. According to Sakharov's conditions, CP violation (CPV) is a necessary ingredient to generate the baryon asymmetry of the Universe. Within the SM, the sole source of CP violation in the quark sector is a single irreducible complex phase in the Cabibbo–Kobayashi–Maskawa (CKM) matrix [5, 6], which governs the weak interaction of quarks. This paradigm has been extensively tested in the decays of kaons and B mesons [7–15]. However, the CP violation predicted by the SM is insufficient by several orders of magnitude to account for the observed matter–antimatter

imbalance, motivating searches for additional sources of *CP* violation.

Charm hadrons provide a unique environment for such studies. They are the only systems where *CP* violation and flavour-changing neutral currents (FCNC) involving up-type quarks can be probed, offering sensitivity to new interactions that may leave down-type quarks unaffected. In the SM, both *CP* violation and FCNC processes in charm decays are expected to be exceedingly small due to the strong suppression of relevant CKM factors and the effectiveness of the Glashow–Iliopoulos–Maiani (GIM) mechanism [16]. As a result, any significant deviation from these tiny SM expectations could be an indication of new physics.

One particularly intriguing process is the phenomenon of neutral D^0 meson mixing, in which a D^0 oscillates into its antiparticle $\overline{D}^0$ through second-order weak interactions. Such mixing is predicted to occur at a much slower rate than in the kaon or beauty systems, making it experimentally challenging to measure. The study of *CP* violation in the charm sector has seen a renaissance in the past two decades, with milestone contributions from the BaBar [17], Belle [18], and CDF [19] experiments. The LHCb experiment, operating at the LHC since 2010, has advanced the field thanks to the unprecedented production rates of charm hadrons. Notably, it reported the first single-experiment observation of D^0 mixing in 2012 [20] and the first observation of *CP* violation in D^0 decays in 2019 [21].

Despite these remarkable achievements, the full experimental potential of the LHCb detector has yet to be realised, and further studies are essential to address the remaining theoretical challenges. In particular, uncertainties related to low-energy strong-interaction dynamics hinder a definitive assessment of whether the observed *CP* violation is fully compatible with the SM. This situation has sparked renewed theoretical interest in the charm sector. In this context, complementary searches for time-dependent *CP* violation in charm-hadron decays could play a decisive role in disentangling the underlying physics.

In this thesis, a measurement of the mixing and *CP* violation in the three-body decays of $D^0 \to K^0_S\pi^+\pi^-$ through the bin-flip analysis is presented. The bin-flip method is a model-independent approach that is optimised towards the measurement of the mixing parameter x and that avoids the need for an accurate modelling of the efficiency variation across phase space and decay time [22]. In addition to that, during my PhD I also worked in the RICH group, focusing my studies on the performances of the RICH detectors in both Run 3 and Upgrade II. For the Run 3, I used the data collected during 2024, for the Upgrade II I ran simulations.

The thesis is organised into four main parts: an introduction, a second part dedicated to the analysis, and the third and fourth parts focusing on the detector, specifically on Run 3 and on Upgrade II, respectively. Chapter 1 introduces the theoretical formalism to describe mixing and *CP* violation, focusing on the charm sector and including also an overview of the experimental status. Then, in Chapter 2,

the new Run 3 LHCb setup is presented. Then there is the analysis part, covered in Chapters 3–7, which describes the entire analysis workflow: from data selection, through the study of experimental correlations and the investigation of the asymmetry effect, up to the data fitting with the corresponding results and the systematic studies. The third part presents the performances of the rich detectors done with the Run 3 data collected during 2024, so Chapters 8–9 address the evolution of detector occupancies as a function of the applied photon time windows. Chapter 8 focuses on the evolution of the hitmaps under different running conditions, including local runs, global runs, and Monte Carlo simulations, while Chapter 9 presents a study of the background contribution to the single photon resolution and its evolution across detector quadrants.

Then, the fourth part (Chapter 10) focuses on the studies performed for the Upgrade II, used for the Scoping Document [23]. Finally, there is a conclusive part with a summary of all the results obtained.

This thesis has been conducted within the framework of the LHCb collaboration. All studies and results presented, including the associated plots, are based on work carried out during my three years of doctoral research, unless explicitly cited otherwise. References are provided for any material or figures not produced as part of this thesis.

Chapter 1

CP violation in charm decays

This chapter offers a concise overview of CP violation within the framework of the Standard Model of particle physics, emphasising its connection to the mixing phenomena in neutral flavoured mesons. Special attention is given to the charm quark sector, highlighting its distinctive characteristics in comparison to the strange and beauty mesons, where CP violation has been experimentally observed and extensively analysed. The chapter further examines how the CKM matrix framework accounts for quark mixing and CP symmetry violation in weak interactions, and concludes with an overview of both the theoretical foundations and experimental observations of neutral meson mixing and CP violation.

1.1 The Standard Model

The Standard Model (SM) is a quantum field theory that offers a detailed framework for understanding the fundamental particles and their interactions, with the exception of gravity. Its structure is based on the symmetries encoded in the Lagrangian and the way particles transform under these symmetries. The gauge symmetry group governing the SM is expressed as

$$G_{SM} = SU(3)_C \otimes SU(2)_L \otimes U(1)_Y \tag{1.1}$$

where the $SU(3)_C$ factor corresponds to the strong interaction described by Quantum Chromodynamics (QCD) [24–28], with the subscript C indicating colour charge. The electroweak interactions are described by the $SU(2)_L \otimes U(1)_Y$ group [29, 30], following the Glashow-Weinberg-Salam model [31, 32], with L denoting the left-handed nature of weak interactions and Y the hypercharge quantum number.

The fundamental fermions, particles with half-integer spin, are organised according to their representations under G_{SM}:

$$Q^I_{Li}(3,2)_{+1/6}, \quad u^I_{Ri}(3,1)_{+2/3}, \quad d^I_{Ri}(3,1)_{-1/3}, \quad L^I_{Li}(1,2)_{-1/2}, \quad l^I_{Ri}(1,1)_{-1},$$

where the index $i = 1, 2, 3$ labels the fermion families, $L(R)$ specifies left- (right-) handed chirality, and I indicates the interaction basis. In detail, left-handed quarks Q^I_L are colour triplets and weak doublets with hypercharge +1/6; right-handed up-type quarks u^I_R and down-type quarks d^I_R are colour triplets but weak singlets, carrying hypercharges +2/3 and −1/3, respectively. Leptons are colour singlets, with left-handed leptons L^I_L forming weak doublets and right-handed leptons l^I_R being weak singlets. The symmetry group of the SM, given in Equation 1.1, possesses a total of $8 + 3 + 1 = 12$ generators. In the framework of a gauge theory, each generator T corresponds to a vector (spin 1) gauge boson that carries the same quantum numbers as T. When the gauge symmetry remains unbroken, the associated boson is massless. These gauge bosons serve as force carriers for the interactions linked to their respective generators.

In particular, the $SU(3)$ sector gives rise to eight massless gluons, associated with the generators of the colour symmetry. The $SU(2) \times U(1)$ part of the group leads to four gauge bosons: W^+, W^-, Z, and the photon γ. Among these, only the photon is massless, as the symmetry connected to the other three is spontaneously broken. The massive bosons $W^\pm$ and Z have relatively large masses on the scale of particle physics, approximately $m_W \simeq 80.4\,\text{GeV}$ and $m_Z \simeq 91.2\,\text{GeV}$ [33].

Another principle which characterises the SM is the pattern of spontaneous symmetry breaking. The symmetry breaking is due to the system, which has infinite volume and infinite degrees of freedom, being found in one particular vacuum state. This state violates the symmetry in the spectrum of states. In the SM, this spontaneous symmetry breaking is realised by the Higgs mechanism [34–37]. There is a scalar (spin 0) boson with a potential that produces an orbit of degenerate vacuum states. This scalar sector includes a single complex Higgs doublet (Φ^+ and Φ^0) which acquires a vacuum expectation value

$$\langle \Phi \rangle = \frac{1}{\sqrt{2}} \begin{pmatrix} 0 \\ v \end{pmatrix}, \tag{1.2}$$

triggering the spontaneous breaking of the electroweak symmetry. The Higgs doublet Φ can be conveniently parametrised in terms of fluctuations around its vacuum expectation value as

$$\Phi = \exp\left(i \frac{\sigma_i}{2} \theta_i \right) \frac{1}{\sqrt{2}} \begin{pmatrix} 0 \\ v + H \end{pmatrix}, \tag{1.3}$$

where σ_i are the Pauli matrices, θ_i represent three Goldstone bosons, and H corresponds to the physical Higgs boson. This symmetry-breaking pattern reduces the gauge group to

$$G_{SM} \to SU(3)_C \otimes U(1)_{EM}, \tag{1.4}$$

with $U(1)_{EM}$ describing electromagnetism. As a result of this symmetry reduction, the electroweak interaction is split into distinct weak and electromagnetic sectors. Electroweak gauge invariance is effectively lost at low energies, leading to massive $W^{\pm}$ and Z gauge bosons through the Higgs mechanism, while electromagnetic interactions remain governed by an unbroken $U(1)_{EM}$ symmetry and mediated by a massless photon. As a consequence, weak interactions are short-ranged, whereas electromagnetic interactions are long-ranged.

Figure 1.1 provides a schematic representation of the SM particle content.

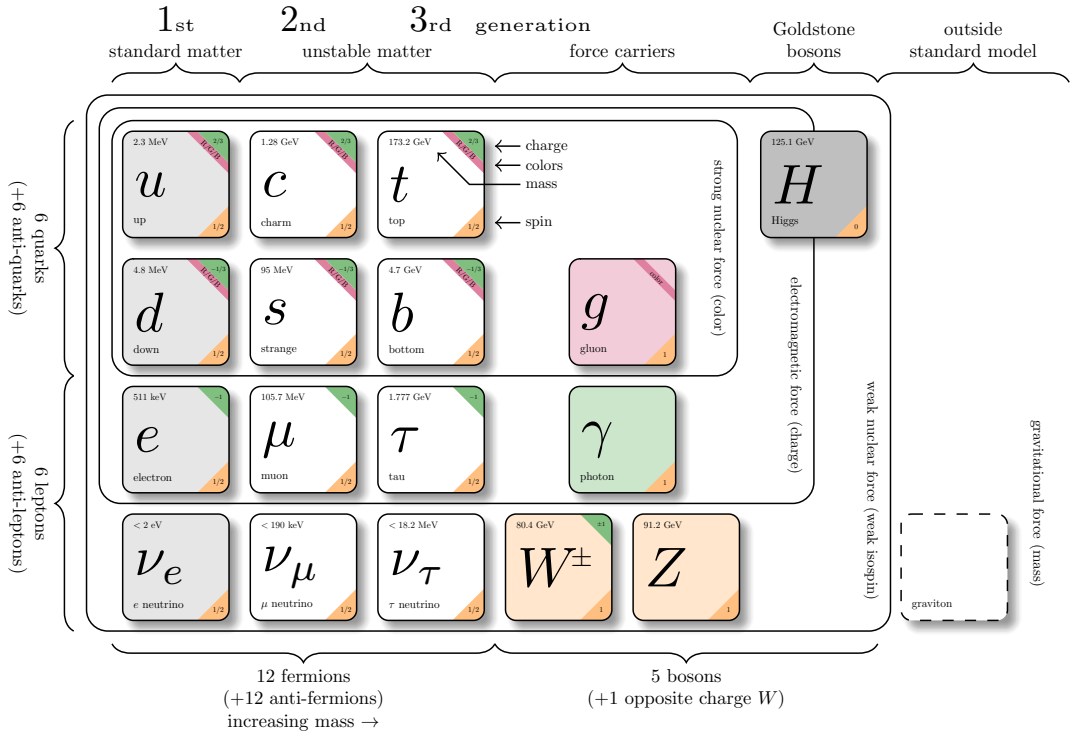

Figure 1.1: The elementary particles of the Standard Model. From [38].

Once the gauge symmetry, particle content, and spontaneous symmetry breaking

are specified, the SM Lagrangian is constructed as the most general renormalizable theory consistent with these properties. It is composed of four main parts:

$$\mathcal{L}_{SM} = \mathcal{L}_{\text{kin}} + \mathcal{L}_{\text{gauge}} + \mathcal{L}_{\text{Higgs}} + \mathcal{L}_{\text{Yukawa}}. \tag{1.5}$$

In detail,

$$\mathcal{L}_{\text{kin}} = \bar{\psi}\gamma^{\mu} i D_{\mu}\psi \tag{1.6}$$

describes the kinetic terms and gauge interactions of fermions, with γ^{μ} being the Dirac matrices and D_{μ} the covariant derivative:

$$D_{\mu} = \partial_{\mu} + i\frac{g}{2}W_{\mu}^{d}\sigma_{d} + i\frac{g'}{2}B_{\mu}Y + i\frac{g_s}{2}G_{\mu}^{a}\lambda_{a}, \tag{1.7}$$

in which Y, σ_d, and λ_a are the generators of $U(1)_Y$, $SU(2)_L$, and $SU(3)_C$, respectively, and g', g, g_s are the corresponding coupling constants.

The gauge boson kinetic terms $\mathcal{L}_{\text{gauge}}$ is

$$\mathcal{L}_{\text{gauge}} = -\frac{1}{4}G_{\mu\nu}^{a}(G^{a})^{\mu\nu} - \frac{1}{4}W_{\mu\nu}^{d}(W^{d})^{\mu\nu} - \frac{1}{4}B_{\mu\nu}B^{\mu\nu}, \tag{1.8}$$

where $G_{\mu\nu}^{a}$, $W_{\mu\nu}^{d}$, and $B_{\mu\nu}$ are the field strength tensors for gluons ($a = 1, ..., 8$), weak gauge bosons (d = 1,...,3), and the hypercharge gauge boson, respectively.

The Higgs sector Lagrangian $\mathcal{L}_{\text{Higgs}}$ includes kinetic and potential terms:

$$\mathcal{L}_{\text{Higgs}} = (\nabla_{\mu}\Phi)^{\dagger}(\nabla^{\mu}\Phi) + \mu^{2}\Phi^{\dagger}\Phi + \lambda(\Phi^{\dagger}\Phi)^{2}, \tag{1.9}$$

where the potential terms μ^2 and λ determine the spontaneous symmetry breaking mechanism.

The Yukawa interactions $\mathcal{L}_{\text{Yukawa}}$ couple fermions to the Higgs field, giving rise to their masses after symmetry breaking:

$$\mathcal{L}_{\text{Yukawa}} = -Y_{ij}^{d}\bar{Q}_{Li}^{I}\Phi D_{Rj}^{I} - Y_{ij}^{u}\bar{Q}_{Li}^{I}\tilde{\Phi}U_{Rj}^{I} - Y_{ij}^{l}\bar{L}_{Li}^{I}\tilde{\Phi}l_{Rj}^{I} + \text{h.c.} \tag{1.10}$$

Despite its impressive successes, the SM does not provide a complete description of nature. It excludes gravity, offers no explanation for dark matter, and leaves open questions such as the origin of fermion masses, which in the SM arise from Yukawa couplings, the number of fermion generations, and the observed asymmetry between matter and antimatter in the universe. These challenges, together with the fact that the SM is an effective theory with a number of free parameters, motivate the search for new physics beyond the SM.

A central aspect in this search is the study of *CP* violation, the breaking of the combined symmetry under charge conjugation C (particle-antiparticle exchange) and parity P (spatial inversion). Investigations into *CP* violation are fruitful in the

domain of heavy flavour physics, involving hadrons containing charm and bottom quarks. The charm quark, in particular, provides a distinctive laboratory for probing potential new physics effects linked to up-type quarks, since the top quark decays before hadronisation and light neutral mesons such as π^0 and η are their antiparticles and thus do not exhibit oscillations.

1.2 *CP* symmetry

A discrete symmetry refers to a transformation that produces a finite, rather than continuous, change in a physical system. Within the SM, three of these specific kinds of transformations can be defined:

- **Charge conjugation** (C): replaces every particle with its corresponding antiparticle, and vice versa.
- **Parity** (P): reverses the spatial coordinates, i.e. $\mathbf{x} \to -\mathbf{x}$.
- **Time reversal** (T): reverses the flow of time, i.e. $\mathbf{t} \to -\mathbf{t}$.

Each of these symmetries and any of their combinations is exactly conserved in both electromagnetic and strong interactions, meaning the physics is unchanged under such transformations. The weak interaction, in contrast, is known to violate all three.

A distinctive feature of the weak interaction is its chirality. Chirality characterises how a particle's spin is oriented relative to its momentum. For a massless left-handed particle, the spin is anti-parallel to the momentum, whereas for a right-handed particle it is parallel. In 1957, Marshak, Sudarshan, Feynman, and Gell-Mann formulated the **V**-A theory [39], which asserts that the weak interaction couples only to left-handed fermions and right-handed anti-fermions. This implies maximal violation of P symmetry.

The non-conservation of parity was experimentally demonstrated before the advent of the electroweak theory. In 1956, Yang and Lee pointed out that the decays of the so-called τ^+ and θ^+ had not been tested for parity conservation, despite their decays leading to final states with opposite parities [40]. They proposed an experiment to verify this. Soon after, Wu carried out a precise study of the beta decay of ^{60}Co, showing that mirror-image processes do not occur with equal probability [41]. This confirmed that the weak interaction violates parity.

In 1964, Cronin and Fitch [7] discovered that the combined C and P symmetry (CP) is also not preserved while studying neutral kaon decays. This was the first observation of CP violation, a phenomenon later measured in the B-meson system

by the BaBar and Belle collaborations [10, 11], and more recently in D^0 mesons by LHCb [21].

The breaking of *CP* symmetry has been proposed as a possible explanation for the predominance of matter over antimatter in the universe. In 1967, Sakharov formulated three criteria that must be met to account for the observed baryon asymmetry [4]:

- Existence of interactions that violate *CP* symmetry.
- Violation of baryon number conservation.
- Departure from thermodynamic equilibrium during some stage of cosmic evolution.

However, the magnitude of *CP* violation predicted by the Standard Model is far too small to explain the observed matter–antimatter imbalance [42]. This strongly motivates the search for new physics beyond the SM.

1.3 *CP* violation in the Standard Model

In the SM, quark flavour is conserved in strong and electromagnetic interactions. However, in weak interactions, a quark can change its flavour through the exchange of a charged $W^{\pm}$ boson, which mediates the weak force and allows such flavour transitions. This process is described by the charged-current interaction Lagrangian:

$$\mathcal{L}_{\text{int}}^{\text{CC}} = \frac{g}{\sqrt{2}} \begin{pmatrix} \bar{u}_L & \bar{c}_L & \bar{t}_L \end{pmatrix} \gamma^{\mu} V_{\text{CKM}} \begin{pmatrix} d_L \\ s_L \\ b_L \end{pmatrix} W_{\mu}^{+} + \text{h.c.} \tag{1.11}$$

Here, the mixing between quark mass eigenstates and weak eigenstates is governed by the Cabibbo-Kobayashi-Maskawa (CKM) matrix, V_{CKM}.

Historically, when only three quarks (u, d, s) were known, Cabibbo proposed in 1963 that the weak eigenstate d' was a superposition of the mass eigenstates d and s, described by a mixing angle θ_c [43]:

$$\begin{pmatrix} d' \\ s' \end{pmatrix} = \begin{pmatrix} \cos\theta_c & \sin\theta_c \\ -\sin\theta_c & \cos\theta_c \end{pmatrix} \begin{pmatrix} d \\ s \end{pmatrix}. \tag{1.12}$$

This led to the 2×2 Cabibbo matrix, which describes the mixing between the first two generations of quarks.

However, this two-generation model predicted rates for flavour-changing neutral current (FCNC) processes for strange quark, such as K^0–$\overline{K}^0$ mixing and $K_L^0 \to \mu^+\mu^-$ decays, that were orders of magnitude larger than what experiments observed.

The solution was provided by the Glashow-Iliopoulos-Maiani (GIM) mechanism [16], which postulated the existence of a fourth quark, charm (c), introducing new decay paths.

In processes like K^0–$\overline{K}^0$ mixing, the amplitude involving the charm quark interferes destructively with that involving the up quark. This interference leads to a strong suppression of FCNC processes, explaining the experimental data. The GIM mechanism's prediction of a heavy charm quark ($m_c \approx 1.5\,\mathrm{GeV}/c^2$) was spectacularly confirmed with the discovery of the J/ψ meson ($c\bar{c}$) in 1974 [44, 45].

Despite its success, the four-quark model could not account for *CP* violation. In 1973, Kobayashi and Maskawa showed that two generations are insufficient to generate a complex phase in the mixing matrix, which is necessary for *CP* violation [5]. They proposed a third generation of quarks, bottom (b) and top (t), expanding the mixing matrix to a 3×3 unitary matrix, now known as the Cabibbo-Kobayashi-Maskawa (CKM) matrix.

For a general $N \times N$ unitary mixing matrix, there are $(N-1)^2$ independent physical parameters: $\frac{1}{2}N(N-1)$ rotation angles and $\frac{1}{2}(N-1)(N-2)$ complex phases.
For $N = 3$, the CKM matrix contains three mixing angles, $(\theta_{12}, \theta_{23}, \theta_{13})$, and one irreducible *CP*-violating phase δ. This phase is the only source of *CP* violation in the quark sector of the Standard Model.

The CKM matrix is written as:

$$V_{\mathrm{CKM}} = \begin{pmatrix} V_{\mathrm{ud}} & V_{\mathrm{us}} & V_{\mathrm{ub}} \\ V_{\mathrm{cd}} & V_{\mathrm{cs}} & V_{\mathrm{cb}} \\ V_{\mathrm{td}} & V_{\mathrm{ts}} & V_{\mathrm{tb}} \end{pmatrix}. \tag{1.13}$$

Global fits to experimental data provide precise values for the magnitudes of its elements [33]:

$$|V_{\mathrm{CKM}}| = \begin{pmatrix} 0.97410 \pm 0.00011 & 0.22650 \pm 0.00048 & 0.00361^{+0.00011}_{-0.00009} \\ 0.22636 \pm 0.00048 & 0.97320 \pm 0.00011 & 0.04053^{+0.00083}_{-0.00061} \\ 0.00854^{+0.00023}_{-0.00016} & 0.03978^{+0.00082}_{-0.00060} & 0.999172^{+0.000024}_{-0.000035} \end{pmatrix}. \tag{1.14}$$

Several parametrisations are used to analyse the CKM matrix. A common approximation highlighting the observed hierarchy $|V_{\mathrm{ud}}| \sim |V_{\mathrm{cs}}| \sim 1 \gg |V_{\mathrm{us}}| \gg |V_{\mathrm{cb}}| \gg |V_{\mathrm{ub}}|$ is the Wolfenstein parametrization [46], expressing the matrix as a power series in the small parameter $\lambda = |V_{\mathrm{us}}| \approx 0.225$:

$$V_{\mathrm{CKM}} = \begin{pmatrix} 1 - \frac{\lambda^2}{2} & \lambda & A\lambda^3(\rho - i\eta) \\ -\lambda & 1 - \frac{\lambda^2}{2} & A\lambda^2 \\ A\lambda^3(1 - \rho - i\eta) & -A\lambda^2 & 1 \end{pmatrix} + \mathcal{O}(\lambda^4). \tag{1.15}$$

The parameters A, ρ, and η are of order unity. The complex phase enters through η, making it clear that CP violation is linked to the smallest elements of the matrix.

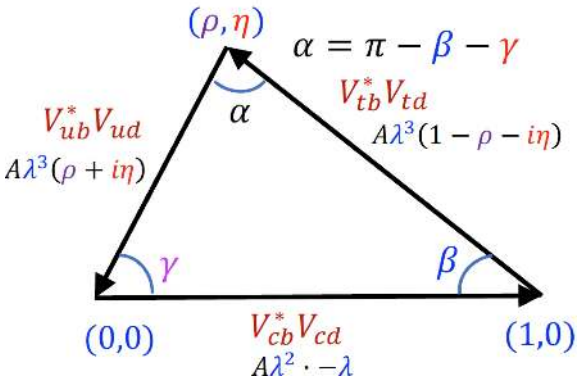

Figure 1.2: Sketch of the unitarity triangle in the $(\bar{\rho}, \bar{\eta})$.

Unitarity of the CKM matrix ($V_{\rm CKM}^{\dagger} V_{\rm CKM} = I$) implies several orthogonality relations. The most studied is:

$$V_{\rm ud} V_{\rm ub}^{*} + V_{\rm cd} V_{\rm cb}^{*} + V_{\rm td} V_{\rm tb}^{*} = 0, \tag{1.16}$$

which describes a triangle in the complex plane known as the *Unitarity Triangle* in Figure 1.2.

The lengths of its sides are $|V_{\rm ud} V_{\rm ub}^{*}|$, $|V_{\rm cd} V_{\rm cb}^{*}|$, and $|V_{\rm td} V_{\rm tb}^{*}|$.
The angles of this triangle are defined as:

$$\alpha \equiv \arg\left(-\frac{V_{\rm td} V_{\rm tb}^{*}}{V_{\rm ud} V_{\rm ub}^{*}}\right),$$
$$\beta \equiv \arg\left(-\frac{V_{\rm cd} V_{\rm cb}^{*}}{V_{\rm td} V_{\rm tb}^{*}}\right),$$
$$\gamma \equiv \arg\left(-\frac{V_{\rm ud} V_{\rm ub}^{*}}{V_{\rm cd} V_{\rm cb}^{*}}\right).$$

A non-zero area of this triangle is a direct measure of *CP* violation. This area is related to the Jarlskog invariant J, a phase-invariant measure of *CP* violation [47] which in the Wolfenstein parametrisation results as $J \approx A^2 \lambda^6 \eta$. A key objective of flavour physics is to precisely measure the sides and angles of the Unitarity Triangle through various weak decays, testing the consistency of the SM and searching for new physics.

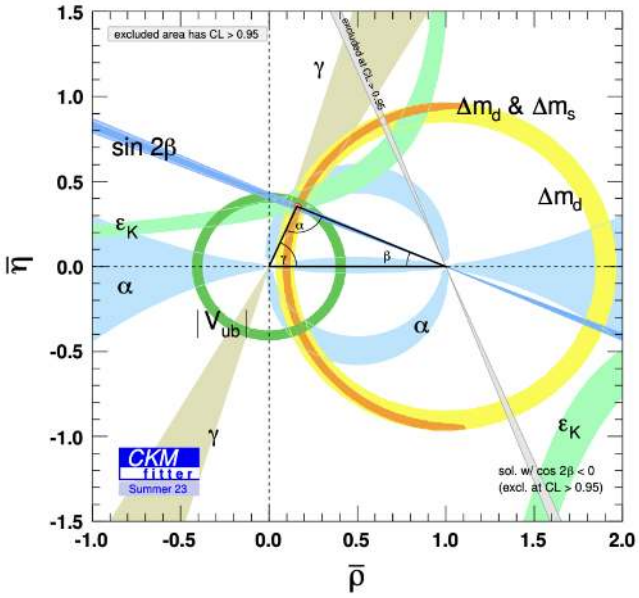

Figure 1.3: Current experimental overview of the global fit incorporating all available measurements connected to unitarity triangle phenomenology.

1.4 Neutral mesons mixing

Within the Standard Model, there exist precisely four neutral mesons, together with their antiparticles, that cannot decay into lighter hadrons through electromagnetic or strong processes. These are the K^0_S (ds), D^0 (cu), B^0 (db), and B^0_s (sb) mesons. Their stability under strong and electromagnetic interactions stems from carrying non-zero flavour quantum numbers. For this reason, they are referred to as *flavoured neutral mesons*. Because weak interactions violate flavour conservation, these flavour eigenstates do not coincide with the eigenstates of the effective Hamiltonian H that controls their time evolution. As a result, these mesons are able to convert into their respective antiparticles before decay, via processes that involve a change of two units in flavour quantum numbers. This quantum phenomenon is known as *mixing*.

To describe the time evolution of a generic neutral meson M^0, one starts from an initial state at $t = 0$ given by a pure linear combination of the two flavour eigenstates:

$$|\psi(0)\rangle = a(0)\,|M^0\rangle + b(0)\,|\overline{M}^0\rangle. \tag{1.17}$$

Its subsequent evolution obeys the Schrödinger equation:

$$i\,\frac{d}{dt}|\psi(t)\rangle = H\,|\psi(t)\rangle, \tag{1.18}$$

where the state vector may be written as

$$|\psi(t)\rangle = a(t)\,|M^0\rangle + b(t)\,|\overline{M}^0\rangle + \sum_k c_k(t)\,|f_k\rangle, \tag{1.19}$$

with $|f_k\rangle$ denoting all the possible decay products.

When the focus lies only on $a(t)$ and $b(t)$, and the time scales under consideration are much longer than those associated with strong interactions, a simplified treatment becomes possible. In this case, the dynamics within the two-dimensional $\{M^0, \overline{M}^0\}$ subspace can be expressed as

$$i\,\frac{d}{dt}\begin{pmatrix} a(t) \\ b(t) \end{pmatrix} = \begin{pmatrix} H_{11} & H_{12} \\ H_{21} & H_{22} \end{pmatrix}\begin{pmatrix} a(t) \\ b(t) \end{pmatrix}. \tag{1.20}$$

The effective Hamiltonian is not Hermitian, reflecting the fact that probability is lost from this subspace due to decays. It is convenient to separate it into Hermitian and anti-Hermitian parts,

$$H = M - \frac{i}{2}\,\Gamma, \tag{1.21}$$

where $M \equiv (H + H^\dagger)/2$ is the mass matrix describing dispersive (off-shell) transitions, while $\Gamma \equiv i(H - H^\dagger)$ is the decay matrix encoding absorptive (on-shell) transitions. *CPT* invariance, a cornerstone of quantum field theory and experimentally respected to high precision, imposes $M_{11} = M_{22} \equiv M$ and $\Gamma_{11} = \Gamma_{22} \equiv \Gamma$, simplifying the problem considerably.

Two parametrisations are commonly used to describe the mixing.

The *phenomenological* approach defines the eigenstates of H as

$$|M_1\rangle = p\,|M^0\rangle + q\,|\overline{M}^0\rangle, \tag{1.22}$$

$$|M_2\rangle = p\,|M^0\rangle - q\,|\overline{M}^0\rangle, \tag{1.23}$$

with $|p|^2 + |q|^2 = 1$ and

$$\left(\frac{q}{p}\right)^2 = \frac{M_{12}^* - \frac{i}{2}\Gamma_{12}^*}{M_{12} - \frac{i}{2}\Gamma_{12}}. \tag{1.24}$$

The corresponding eigenvalues,

$$\omega_{1,2} = M_{1,2} - \frac{i}{2}\Gamma_{1,2}, \tag{1.25}$$

determine the masses $M_{1,2}$ and decay widths $\Gamma_{1,2}$ of the physical states. The mass and width differences are defined as $\Delta M = M_2 - M_1$ and $\Delta\Gamma = \Gamma_2 - \Gamma_1$, and are often expressed in units of the average width:

$$x \equiv \frac{\Delta M}{\Gamma}, \quad y \equiv \frac{\Delta\Gamma}{2\Gamma}. \tag{1.26}$$

The time development of initially pure flavour states, where M^0 ($\overline{M}^0$) is the state at time zero, reads

$$|M^0(t)\rangle = g_+(t)\,|M^0\rangle + \frac{q}{p} g_-(t)\,|\overline{M}^0\rangle, \tag{1.27}$$

$$|\overline{M}^0(t)\rangle = g_+(t)\,|\overline{M}^0\rangle + \frac{p}{q} g_-(t)\,|M^0\rangle, \tag{1.28}$$

with

$$g_\pm(t) \equiv \frac{e^{-i\omega_1 t} \pm e^{-i\omega_2 t}}{2}. \tag{1.29}$$

It is possible to compute the probability of measuring at a time t the same particle that was produced in its flavour eigenstate at the time $t = 0$:

$$|\langle M^0|M^0(t)\rangle|^2 = |\langle \overline{M}^0|\overline{M}^0(t)\rangle|^2 = |g_+(t)|^2, \tag{1.30}$$

and the probability of measuring the particle with opposite flavour quantum numbers is

$$|\langle \overline{M^0}|M^0(t)\rangle|^2 = \left|\frac{q}{p}\right|^2 \cdot |g_-(t)|^2 \propto e^{-\Gamma t}\left|\frac{q}{p}\right|^2 [\cosh(y\Gamma t) - \cos(x\Gamma t)], \tag{1.31}$$

$$|\langle M^0|\overline{M^0}(t)\rangle|^2 = \left|\frac{p}{q}\right|^2 \cdot |g_-(t)|^2 \propto e^{-\Gamma t}\left|\frac{p}{q}\right|^2 [\cosh(y\Gamma t) - \cos(x\Gamma t)], \tag{1.32}$$

with

$$|g_\pm(t)|^2 = \frac{1}{2} e^{-\Gamma t}\left[\cosh(y\Gamma t) \pm \cos(x\Gamma t)\right]. \tag{1.33}$$

This description is subject to a convention choice for the relative signs and phases of p and q, which can be fixed by defining, for example, M_2 as the short-lived state or imposing $y > 0$.

A second, *theoretical* parametrisation [48, 49], avoids convention-dependent definitions and focuses on the magnitudes and relative phase of dispersive and absorptive amplitudes:

$$x_{12} \equiv \frac{2|M_{12}|}{\Gamma}, \quad y_{12} \equiv \frac{|\Gamma_{12}|}{\Gamma}, \quad \phi_{12} \equiv \arg\left(\frac{M_{12}}{\Gamma_{12}}\right). \tag{1.34}$$

Here x_{12} and y_{12} are *CP*-even, while ϕ_{12} is *CP*-odd. In this parametrisation, one can directly solve the Equation 1.20 and the transition amplitudes become:

$$\begin{aligned}
\langle M^0|M^0(t)\rangle &= \langle \overline{M}^0|\overline{M}^0(t)\rangle = e^{-i(M-\frac{i}{2}\Gamma)t}\cos\left[\frac{1}{2}(\Delta M - \frac{i}{2}\Delta\Gamma)t\right], \\
\langle \overline{M}^0|M^0(t)\rangle &= e^{-i(M-\frac{i}{2}\Gamma)t}\frac{\sin\left[\frac{1}{2}(\Delta M - \frac{i}{2}\Delta\Gamma)t\right]}{\frac{1}{2}(\Delta M - \frac{i}{2}\Delta\Gamma)t}\left(e^{-i\frac{\pi}{2}} M_{12}^* - \frac{i}{2}\Gamma_{12}^*\right)t.
\end{aligned} \tag{1.35}$$

The two descriptions can be related through

$$x^2 - y^2 = x_{12}^2 - y_{12}^2, \tag{1.36}$$

$$xy = x_{12} y_{12} \cos\phi_{12}, \tag{1.37}$$

$$\left|\frac{q}{p}\right|^{\pm 2} (x^2 + y^2) = x_{12}^2 + y_{12}^2 \pm 2 x_{12} y_{12} \sin\phi_{12}. \tag{1.38}$$

For all four systems, $|q/p|$ is experimentally close to unity, implying $\sin\phi_{12}$ is small and $x_{12} \approx |x|$, $y_{12} \approx |y|$ up to quadratic corrections.

The phenomenology varies widely among the four meson systems, primarily because the short- and long-distance contributions to M_{12} and Γ_{12} differ in size. Table 1.1 summarises the measured values of x and y.

Table 1.1: Measured mixing parameters $x = \Delta M/\Gamma$ and $y = \Delta\Gamma/(2\Gamma)$ for neutral mesons. The global signs are convention-dependent. The values are taken from [50] for kaons and from [33, 51] for c and b mesons.

System	x	y
K^0–$\overline{K}^0$	-0.946 ± 0.004	0.99650 ± 0.00001
D^0–$\overline{D}^0$	$(0.407 \pm 0.044)\%$	$(0.645^{+0.024}_{-0.023})\%$
B^0–$\overline{B}^0$	0.7697 ± 0.0035	$(0.1 \pm 1.0)\%$
B_s^0–$\overline{B}_s^0$	26.99 ± 0.09	$(-11.9 \pm 0.5)\%$

The cosine term, which is the oscillatory component of neutral meson evolution in the Equation 1.33, depends directly on the parameter x, which measures the mass splitting between the two physical eigenstates. Differences in the exponential decay rates, instead, originate from the hyperbolic term where the parameter y appears. Together, x and y are known as the *mixing parameters*, and they fully characterise the distinctive time-dependent behaviour of neutral meson mixing. Among the K^0, D^0, B^0, B_s^0 systems, the D^0 meson stands out for having markedly different mixing parameters compared to the kaon or B mesons, as can be observed in Figure 1.4.

In the K^0 system, the parameter y is close to unity, which produces two mass eigenstates, K_S^0 and K_L^0, with lifetimes differing by orders of magnitude. Historically, this dramatic difference led to the belief that they were distinct particles. The mass splitting, with $x \approx 1$, also generates sizeable sinusoidal oscillations. This feature enables the selection of nearly pure K_S^0 or K_L^0 samples: close to the production point, K_L^0 decays are rare, whereas far from it, most K_S^0 mesons have already decayed.

For B^0 and B_s^0 mesons, the width difference y is small, but the x parameter takes significant values. The B_s^0 in particular exhibit extremely rapid oscillations, making high spatial resolution essential for their detection, a capability achieved only relatively recently [52].

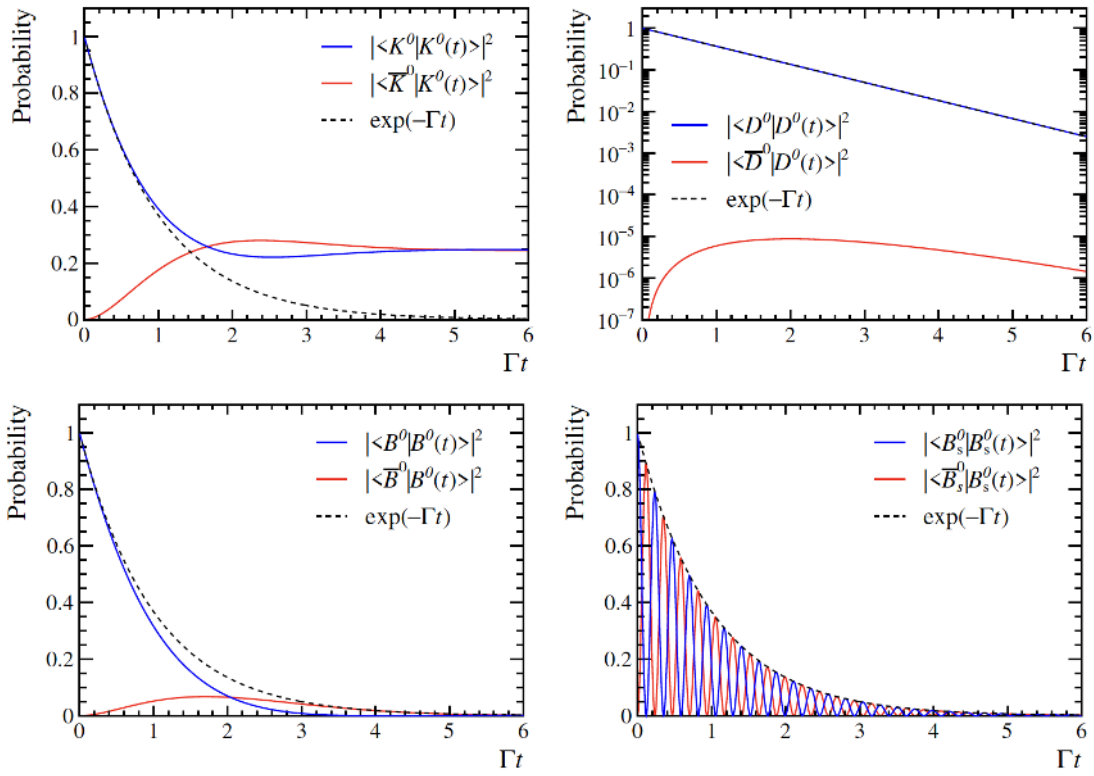

Figure 1.4: Neutral meson oscillations for the K^0 (top left), D^0 (top right), B^0 (bottom left) and B_s^0 (bottom right) decays. The evolution of the probability is depicted as the function of the dimensionless variable t/τ, the decay time unit of the meson. An exponential decay curve not subject to any oscillations is also drawn in a dotted line for comparison. Note for the D^0 meson oscillations, it is a semilog plot to show the very slow oscillations.

The D^0 meson system, by contrast, has both x and y at small values, which demands large datasets to obtain statistically robust measurements. Charm mixing was first detected in 2007 [10, 11], with a high-significance measurement by LHCb following in 2012 [20].

Mixing amplitudes generally arise from two qualitatively different mechanisms: short-distance and long-distance processes. The short-distance contribution originates from box diagrams, as illustrated in the left panel of Figure 1.5 for the D^0 case. These involve only weak interaction vertices, corresponding to a much smaller length scale than strong interactions. In K^0 and B^0 systems, such box diagrams dominate the mixing amplitude. In the D^0 system, however, they are heavily suppressed.

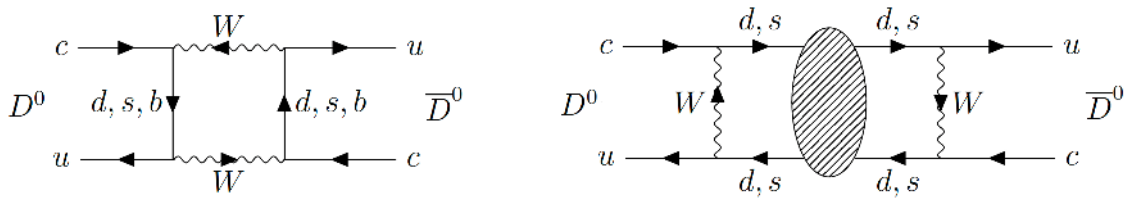

Figure 1.5: Feynman diagrams of (left) short-distance and (right) long-distance contributions to D^0 mixing. In the right diagram, the blob stands for low-energy QCD interactions, possibly involving the exchange of hadrons on the mass shell.

Part of this suppression comes from CKM factors: the loop with a bottom quark is reduced by $|V_{ub}V_{cb}^*|^2/|V_{us}V_{cs}^*|^2 \approx 10^{-5}$. On top of that, the GIM mechanism [16] induces an almost complete cancellation between down- and strange-quark loops, since $V_{cd}^*V_{ud} + V_{cs}^*V_{us} \approx 10^{-5}$. Consequently, predictions for x and y based solely on short-distance effects are of order 10^{-6}, far below the experimental values of about 0.5%. This mismatch reveals the dominant role of long-distance physics in D^0 mixing.

Long-distance contributions are associated with intermediate on-shell states accessible to both a meson and its antiparticle. In the case of the D^0 meson (right panel of Figure 1.5), the process can be visualised as the meson first decaying into a common final state, such as K^+K^- or $\pi^-\pi^+$, after which these decay products re-scatter, forming the meson with the opposite flavour. These effects, unlike the short-distance ones, are not subjected to strong CKM or GIM suppression, and thus they provide the leading contribution to the mixing amplitude in the charm sector.

1.5 Types of *CP* violation

For a final state f that is a *CP* eigenstate, the *CP* transformation acts as $CP|f\rangle = \omega_f|f\rangle$ and $CP|f\rangle = \omega_f^*|f\rangle$, where ω_f is a pure phase factor ($|\omega_f| = 1$). Understanding the origin of the phases appearing in decay amplitudes is crucial, as they give rise to *CP* violation. Two kinds of phases typically occur, known as *weak* and *strong* phases.

Weak phases originate from complex terms in the Lagrangian which enter the *CP*-conjugate amplitude as their complex conjugates. In the SM, such phases appear only in the CKM matrix, part of the electroweak sector, hence the name "weak" phases.

Strong phases, on the other hand, arise from final-state interactions via intermediate on-shell states in the decay process. These rescattering effects occur even when the Lagrangian is real. If hadrons are present in the final state, these phases

are generated by strong interactions and are therefore referred to as strong phases. Strong phases do *not* flip sign under a *CP* transformation.

Experimentally, *CP* violation can be classified into three types:

- *CP* violation in the decay,
- *CP* violation in the mixing,
- *CP* violation in the interference between decay and mixing.

1.5.1 *CP* violation in the decay

The measurable observables depend on squared amplitudes, so the absolute phases are not directly observable, and only their differences can be detected. Direct *CP* violation occurs when the decay amplitude contains at least two contributions with both different weak phases and different strong phases.

Let $A_f = \langle f|H|X\rangle$ be the amplitude for $X \to f$ and $\overline{A}_f = \langle \overline{f}|H|\overline{X}\rangle$ the amplitude for $\overline{X} \to \overline{f}$, where f is a *CP* eigenstate, $\overline{f}$ is the C-conjugated final state and H is the decay Hamiltonian. *CP* violation in decay arises when the likelihood for X to decay into f is not equal to the likelihood for $\overline{X}$ to decay into $\overline{f}$.

If multiple amplitudes contribute to the decay process:

$$A_f = \sum_k |A_k|\, e^{i(\phi_k+\delta_k)}, \qquad \overline{A}_f = \sum_k |A_k|\, e^{i(-\phi_k+\delta_k)}, \tag{1.39}$$

where δ_k are the strong and ϕ_k the weak phases.

The difference between the squared amplitudes is:

$$|A_f|^2 - |\overline{A}_f|^2 = -2\sum_{l,k} |A_l||A_k| \sin(\phi_l - \phi_k)\sin(\delta_l - \delta_k). \tag{1.40}$$

To detect *CP* violation, the condition $|A_f| \neq |\overline{A}_f|$ must be satisfied, implying the presence of at least two interfering amplitudes that carry distinct weak and strong phases. A fundamental quantity used to quantify this effect is the *CP* asymmetry:

$$\mathcal{A}^{CP}(f) = \frac{\Gamma(X \to f) - \Gamma(\overline{X} \to \overline{f})}{\Gamma(X \to f) + \Gamma(\overline{X} \to \overline{f})}, \tag{1.41}$$

with the time-integrated decay widths $\Gamma(X \to f) \propto |A_f|^2$ and $\Gamma(\overline{X} \to \overline{f}) \propto |\overline{A}_f|^2$, yielding

$$\mathcal{A}^{CP}(f) = \frac{|A_f|^2 - |\overline{A}_f|^2}{|A_f|^2 + |\overline{A}_f|^2} = \frac{1 - R_f^2}{1 + R_f^2}, \tag{1.42}$$

where

$$R_f = \left|\frac{\overline{A}_f}{A_f}\right| \neq 1 \tag{1.43}$$

is the condition for *CP* violation in the decay.

1.5.2 *CP* violation in the mixing

CP violation in mixing arises when the time-dependent probability for a neutral meson M^0 to transform into its antiparticle $\overline{M}^0$ differs from the probability for the inverse transition, where $\overline{M}^0$ oscillates back into M^0. For this reason, the dynamics of meson mixing need to be understood. From Equation 1.31, a disparity in oscillation probabilities can arise only if the modulus of the coefficient ratio defining the superposition of $|M^0\rangle$ and $|\overline{M}^0\rangle$ in the mass eigenstates deviates from unity. Since

$$\frac{q}{p} = \sqrt{\frac{M_{12}^* - i\Gamma_{12}^*/2}{M_{12} - i\Gamma_{12}/2}} = \left|\frac{q}{p}\right| e^{i\Phi}. \tag{1.44}$$

CP violation in mixing requires

$$R_m = \left|\frac{q}{p}\right| \neq 1. \tag{1.45}$$

1.5.3 *CP* violation in the interference between decay and mixing

If M^0 and $\overline{M}^0$ both decay to the same final state f, *CP* symmetry can be broken via the interference between the direct decay $M^0 \to f$ and the decay occurring after mixing, $M^0 \to \overline{M}^0 \to f$. Defining

$$\lambda_f = \frac{q\,\overline{A}_f}{p\,A_f}, \qquad \lambda_{\overline{f}} = \frac{q\,\overline{A}_{\overline{f}}}{p\,A_{\overline{f}}} \tag{1.46}$$

CP violation in the interference occurs if

$$\mathcal{I}m(\lambda_f) + \mathcal{I}m(\lambda_{\overline{f}}) \neq 0. \tag{1.47}$$

1.6 The charm sector

Once introduced, the general theoretical framework of *CP* violation and mixing phenomena applicable to all meson systems, we now turn our attention to the specific case of charm. Charmed mesons have masses of about $2\,\mathrm{GeV}/c^2$. The neutral D^0

meson, composed of a charm quark and an up antiquark, has a lifetime of roughly 410 fs. While the decays of strange and beauty hadrons have been extensively studied in the last decades, the dynamics of charm remain only partially explored, due to both experimental and theoretical challenges.

Within the SM, *CP* violation in the charm sector is expected to be extremely small, at the level of $\mathcal{O}(10^{-3})$. This is because all relevant decay amplitudes can, to an excellent approximation, be described using only the physics of the first two quark generations. Indeed, charmed meson decays involve transitions from a charm quark to lighter quarks, meaning that only the first two rows of the CKM matrix are relevant. The corresponding unitarity relation is:

$$V_{\mathrm{cd}}^{*}V_{\mathrm{ud}} + V_{\mathrm{cs}}^{*}V_{\mathrm{us}} + V_{\mathrm{cb}}^{*}V_{\mathrm{ub}} = 0, \tag{1.48}$$

which can be expressed more compactly by defining $\Lambda_q \equiv V_{cq}^{*}V_{uq}$ for $q \in \{d, s, b\}$, yielding:

$$\Lambda_d + \Lambda_s + \Lambda_b = 0. \tag{1.49}$$

From the CKM hierarchy, one expects:

$$\frac{V_{\mathrm{ub}}V_{\mathrm{cb}}^{*}}{V_{\mathrm{us}}V_{\mathrm{cs}}^{*}} \sim 10^{-3}, \tag{1.50}$$

providing a natural SM estimate for *CP* violation in charm.

From the theoretical perspective, precise predictions are difficult. The masses of charmed hadrons, $\mathcal{O}(2\,\mathrm{GeV})$, lie in a region where non-perturbative QCD effects dominate, and many of the approximations successfully applied in the strange and bottom sectors are no longer valid. This results in significant theoretical uncertainties. For instance, current computational power is insufficient to determine all relevant charm properties with lattice QCD at the required precision. Exclusive approaches, which sum over all possible intermediate states, require detailed modelling or direct input from data. Given that D mesons have numerous accessible final states, precise experimental determinations of amplitudes and strong phases are essential to avoid restrictive assumptions that could limit predictive power.

On the experimental side, interest in the charm sector has grown considerably over the last decade, especially following the observation of D^0–$\overline{\mathrm{D}}^0$ mixing by LHCb [20], with supporting evidence from BaBar [53] and Belle [54]. Until recently, experimental sensitivities to mixing and *CP*-violation parameters in charm were still orders of magnitude above most SM and beyond-SM expectations. A milestone was reached in 2019, when *CP* violation was observed for the first time in D^0 decays [21]. However, due to the large theoretical uncertainties within the SM, a precise comparison between theory and measurement is not yet possible [55]. Further measurements in charm are therefore essential to clarify CPV phenomena in the up-type quark

sector, which may probe new dynamics beyond the SM, potentially distinct from those affecting down-type quarks. *CP* violation in charm could thus serve as a sensitive indicator for the presence of non-SM particles entering decay amplitudes in a measurable way.

1.6.1 Experiments

Charm physics has been explored through a wide range of experimental approaches, each operating under different conditions of beam type, centre-of-mass energy, and production mechanism, resulting in a broad range of production cross-sections.

The earliest detailed studies came from fixed-target experiments, such as E691 and FOCUS at Fermilab. In E691, photoproduction processes yielded samples of roughly 10^4 reconstructed charm decays, while about a decade later, the FOCUS experiment reached datasets exceeding 10^6 reconstructed decays, marking a significant advance in statistical precision.

Over the past decades, the field has been dominated by two main classes of facilities: e^+e^- colliders and hadron colliders. In general, e^+e^- machines offer clean experimental conditions, well-defined initial states, low background, nearly hermetic detectors, and high reconstruction efficiency. Hadron colliders, in contrast, operate at much higher energies and achieve charm production cross-sections several orders of magnitude larger, although in a more complex event environment with higher background levels.

Among e^+e^- colliders, there are the D and B factories. The first, operating just above the $D\overline{D}$ production threshold at $\sqrt{s} \approx 3.77\,\text{GeV}$, produce the $\psi(3770)$ resonance, which decays into quantum-correlated $D^0\overline{D}^0$ or D^+D^- pairs with a cross-section of about 8 nb. Since the resonance is produced nearly at rest, decay-time measurements are not feasible in this configuration. Examples include MARK III, CLEO, and BESIII, the latter operating since 2011 with $\sqrt{s}$ between 3.8 and 4.6 GeV.

The second operate at $\sqrt{s} \approx 10.6\,\text{GeV}$, corresponding to the $\Upsilon(4S)$ resonance, which decays predominantly to $B\overline{B}$ pairs. Charm mesons are produced both from B decays and from continuum $e^+e^- \to c\bar{c}$ processes. The cross-section for producing at least one D^0 at this energy is about 1.45 nb, smaller than the corresponding one at the $\psi(3770)$, but compensated by higher instantaneous luminosities. Asymmetric beam energies at BaBar and Belle improve decay-time resolution, enabling time-dependent analyses. Over their operational lifetimes, BaBar, Belle and Belle II collected integrated luminosities of about $500\,\text{fb}^{-1}$, $1000\,\text{fb}^{-1}$ and $620\,\text{fb}^{-1}$ respectively, compared with $0.8\,\text{fb}^{-1}$ for CLEO and $20\,\text{fb}^{-1}$ for BESIII.

Then, in the hadron colliders, the charm production rates in hadronic collisions are vastly larger than in e^+e^- interactions. At the Tevatron (p^+p^- at $\sqrt{s} = 2\,\text{TeV}$), the CDF experiment collected $10\,\text{fb}^{-1}$ and measured a D^0 cross-section of about

13 µb [56]. At the LHC, LHCb has collected datasets of 1.1 fb^{-1}, 2.1 fb^{-1}, and 5.9 fb^{-1} at centre-of-mass energies of $\sqrt{s} = 7, 8$, and 13 TeV, respectively, corresponding to D^0 production cross-sections of 1.4 mb, 1.6 mb, and 2.7 mb. For comparison, the inclusive $c\bar{c}$ cross-section at $\sqrt{s} = 13$ TeV in the LHCb acceptance is measured as

$$\sigma(\text{pp} \to \text{c}\bar{\text{c}}X) = (2940 \pm 3 \pm 180 \pm 160)\,\mu\text{b}$$

for $0 < p_T < 8\,\text{GeV}/c$ and $2 < \eta < 4.5$ [57], roughly six orders of magnitude above B-factory values. LHCb 's vast dataset, currently of the order of one billion reconstructed D^0 decays, has enabled groundbreaking results, including the first observation of *CP* violation in charm decays in 2019. Currently, during Run 3, LHCb has significantly increased its collected luminosity, benefiting from the newly implemented fully software-based trigger system, a major upgrade whose details will be discussed in the following chapter.

1.7 Observables of *CP* violation in charm decays

In this section, the various experimental approaches that exploit different decay modes are outlined, given that each technique presents distinct experimental challenges and theoretical benefits.

1.7.1 Asymmetries

When *CP* symmetry is broken, the phenomenological and theoretical descriptions diverge, requiring observables to be expressed in terms of both parameterisation schemes. The study of *CP* violation employs various decay modes and experimental techniques, each offering distinct sensitivity levels to different effects. It is necessary to define the decay rates of D^0 and $\overline{\text{D}}^0$ into the final state f within the phenomenological framework:

$$\begin{aligned}\Gamma(\text{D}^0 \to f, t) \simeq \mathcal{N}_f\, e^{-\Gamma t}|A_f|^2\Big\{1 + \Big[y\,\mathcal{R}e(\lambda_f) - x\,\mathcal{I}m(\lambda_f)\Big]\Gamma t \\ + \frac{1}{4}\Big[y^2(1+|\lambda_f|^2) - x^2(1-|\lambda_f|^2)\Big](\Gamma t)^2\Big\},\end{aligned} \tag{1.51}$$

$$\begin{aligned}\Gamma(\overline{\text{D}}^0 \to f, t) \simeq \mathcal{N}_f\, e^{-\Gamma t}|\overline{A}_f|^2\Bigg\{1 + \left[y\,\mathcal{R}e\left(\frac{1}{\lambda_f}\right) - x\,\mathcal{I}m\left(\frac{1}{\lambda_{\overline{f}}}\right)\right]\Gamma t \\ + \frac{1}{4}\left[y^2\left(1 + \left|\frac{1}{\lambda_f}\right|^2\right) - x^2\left(1 - \left|\frac{1}{\lambda_{\overline{f}}}\right|^2\right)\right](\Gamma t)^2\Bigg\}.\end{aligned} \tag{1.52}$$

and with the theoretical approach, considering the time evolution of the decay process:

$$\Gamma(\mathrm{D}^0 \to f, t) \simeq \mathcal{N}_f\, e^{-\Gamma t} |A_f|^2 \Bigg\{ 1 - \mathcal{R}e\left(\frac{y_{12}}{\lambda_f^\Gamma} + i\, \frac{x_{12}}{\lambda_f^M} \right) \Gamma t + \frac{1}{4} \left[y_{12}^2 \left(1 + \frac{1}{|\lambda_f^\Gamma|^2} \right) + x^2 \left(-1 + \frac{1}{|\lambda_f^M|^2} \right) + 2 y_{12} x_{12}\, \mathcal{I}m\left(\frac{1}{\lambda_f^\Gamma \lambda_f^{M*}} \right) \right] (\Gamma t)^2 \Bigg\}, \tag{1.53}$$

$$\Gamma(\overline{\mathrm{D}}^0 \to f, t) \simeq \mathcal{N}_f\, e^{-\Gamma t} |A_f|^2 \Bigg\{ 1 - \mathcal{R}e\Big(y_{12} \lambda_f^\Gamma + i\, x_{12} \lambda_f^M \Big) \Gamma t + \frac{1}{4} \left[y_{12}^2 \left(1 + |\lambda_f^\Gamma|^2 \right) + x^2 \left(-1 + |\lambda_f^M|^2 \right) + 2 y_{12} x_{12}\, \mathcal{I}m\Big(\lambda_f^\Gamma \lambda_f^{M*} \Big) \right] (\Gamma t)^2 \Bigg\}. \tag{1.54}$$

Then, the absorptive and dispersive amplitude ratios are respectively defined as:

$$\lambda_f^\Gamma \equiv \frac{\Gamma_{12}}{|\Gamma_{12}|} \frac{A_f}{\overline{A}_f}, \quad \lambda_f^M \equiv \frac{\mathcal{M}_{12}}{|\mathcal{M}_{12}|} \frac{A_f}{\overline{A}_f}. \tag{1.55}$$

1.7.1.1 $\mathrm{D}^0 \to \mathrm{h}^+\mathrm{h}^-$ CS decays

The study of *CP* violation in charm decays to two-body final states such as $\mathrm{K}^+\mathrm{K}^-$ and $\pi^+\pi^-$ represents a crucial experimental probe. These *CP* eigenstate modes enable the measurement of time-dependent asymmetries between D^0 and $\overline{\mathrm{D}}^0$ decay rates:

$$\mathcal{A}^{CP}(\mathrm{h}^+\mathrm{h}^-; t) = \frac{\Gamma(\mathrm{D}^0(t) \to \mathrm{h}^+\mathrm{h}^-) - \Gamma(\overline{\mathrm{D}}^0(t) \to \mathrm{h}^+\mathrm{h}^-)}{\Gamma(\mathrm{D}^0(t) \to \mathrm{h}^+\mathrm{h}^-) + \Gamma(\overline{\mathrm{D}}^0(t) \to \mathrm{h}^+\mathrm{h}^-)} \simeq a^d_{\mathrm{h}^+\mathrm{h}^-} + \Delta Y_{\mathrm{h}^+\mathrm{h}^-} \Gamma t. \tag{1.56}$$

The time-independent component $a^d_{h^+h^-}$ quantifies direct *CP* violation in the decay amplitude:

$$a^d_{\mathrm{K}^+\mathrm{K}^-} \equiv \frac{|A_{\mathrm{K}^+\mathrm{K}^-}|^2 - |\overline{A}_{\mathrm{K}^+\mathrm{K}^-}|^2}{|A_{\mathrm{K}^+\mathrm{K}^-}|^2 + |\overline{A}_{\mathrm{K}^+\mathrm{K}^-}|^2}, \quad a^d_{\pi^+\pi^-} \equiv \frac{|A_{\pi^+\pi^-}|^2 - |\overline{A}_{\pi^+\pi^-}|^2}{|A_{\pi^+\pi^-}|^2 + |\overline{A}_{\pi^+\pi^-}|^2}. \tag{1.57}$$

The difference between individual asymmetries offers exceptional experimental advantages:

$$\Delta\mathcal{A}^{CP} = a^d_{\mathrm{K}^+\mathrm{K}^-} - a^d_{\pi^+\pi^-}. \tag{1.58}$$

This observable provides robust cancellation of both production and detection systematic effects. Assuming U-spin symmetry, the direct *CP* asymmetries for the $\mathrm{K}^+\mathrm{K}^-$

and $\pi^+\pi^-$ final states are expected to have equal magnitudes but opposite signs, although theoretical uncertainties remain due to potential U-spin breaking effects. The most recent results for this variables are taken from [58–60]:

$$\begin{aligned} a^d_{\mathrm{K^+K^-}} &= (7.7 \pm 5.7) \times 10^{-4}, \\ a^d_{\pi^+\pi^-} &= (23.2 \pm 6.1) \times 10^{-4}, \\ \Delta\mathcal{A}^{CP} &= (-15.4 \pm 2.9) \times 10^{-4}, \\ \Delta Y &= (-2.7 \pm 1.3(\mathrm{stat.}) \pm 0.3(\mathrm{syst.})) \times 10^{-4}. \end{aligned}$$

1.7.1.2 $\mathrm{D}^0 \to \mathrm{K}^+\pi^-$ DCS decays

The $\mathrm{D}^0 \to \mathrm{K}^+\pi^-$ decay channel provides a comprehensive probe for all manifestations of *CP* violation: direct decay asymmetries, mixing-induced effects, and interference phenomena. The branching fraction ratios between Double Cabibbo Suppressed (DCS) and Cabibbo Favoured (CF) modes are presented:

$$R^+_D \equiv \left|\frac{A_{\mathrm{K^+\pi^-}}}{A_{\mathrm{K^-\pi^+}}}\right|^2, \quad R^-_D \equiv \left|\frac{\overline{A}_{\mathrm{K^+\pi^-}}}{\overline{A}_{\mathrm{K^-\pi^+}}}\right|^2, \quad R_D \equiv \frac{R^+_D + R^-_D}{2}, \tag{1.59}$$

along with the direct *CP* asymmetries for both decay modes:

$$a^d_{WS} \equiv \frac{|A_{\mathrm{K^+\pi^-}}|^2 - |\overline{A}_{\mathrm{K^-\pi^+}}|^2}{|A_{\mathrm{K^+\pi^-}}|^2 + |\overline{A}_{\mathrm{K^-\pi^+}}|^2}, \quad a^d_{RS} \equiv \frac{|A_{\mathrm{K^-\pi^+}}|^2 - |\overline{A}_{\mathrm{K^+\pi^-}}|^2}{|A_{\mathrm{K^-\pi^+}}|^2 + |\overline{A}_{\mathrm{K^+\pi^-}}|^2}. \tag{1.60}$$

The observable *CP* asymmetry in the ratio of DCS to CF transitions becomes:

$$A_D \equiv \frac{R^+_D - R^-_D}{R^+_D + R^-_D} \simeq a^d_{WS} - a^d_{RS}, \tag{1.61}$$

where

$$R^\pm_D = R_D(1 \pm a^d_{WS})(1 \mp a^d_{RS})\frac{1}{1 - 2a^d_{WS}a^d_{SR}} \simeq R_D[1 \pm (a^d_{WS} - a^d_{RS})]. \tag{1.62}$$

Within the phenomenological framework, the decay ratios can be expressed, including the CPV in the final state $\mathrm{K}^\pm\pi^\mp$:

$$\lambda_{\mathrm{K^-\pi^+}} \equiv \frac{q}{p}\frac{\overline{A}_{\mathrm{K^-\pi^+}}}{A_{\mathrm{K^-\pi^+}}} \equiv \sqrt{R^-_D\frac{1 - a^d_{RS}}{1 + a^d_{RS}}}\left|\frac{q}{p}\right| e^{i(\phi^\lambda_{\mathrm{K\pi}} - \delta_{\mathrm{K\pi}})}, \tag{1.63}$$

$$\lambda_{\mathrm{K^+\pi^-}} \equiv \frac{q}{p}\frac{\overline{A}_{\mathrm{K^+\pi^-}}}{A_{\mathrm{K^+\pi^-}}} \equiv \sqrt{\frac{1}{R^+_D}\frac{1 - a^d_{RS}}{1 + a^d_{RS}}}\left|\frac{q}{p}\right| e^{i(\phi^\lambda_{\mathrm{K\pi}} + \delta_{\mathrm{K\pi}})}, \tag{1.64}$$

$\phi_{\lambda K\pi}$ the *CP* violating weak phase.

The theoretical parametrisation employs separate mixing ratios for absorptive and dispersive processes:

$$\lambda^{\Gamma}_{K^-\pi^+} \equiv \frac{\Gamma_{12}}{|\Gamma_{12}|}\frac{\overline{A}_{K^-\pi^+}}{A_{K^-\pi^+}} \equiv -\sqrt{R_D^- \frac{1-a^d_{RS}}{1+a^d_{RS}}}\, e^{i(\phi^{\Gamma}_{K\pi}+\delta_{K\pi})} \tag{1.65}$$

$$\lambda^{\Gamma}_{K^+\pi^-} \equiv \frac{\Gamma_{12}}{|\Gamma_{12}|}\frac{\overline{A}_{K^+\pi^-}}{A_{K^+\pi^-}} \equiv -\sqrt{\frac{1}{R_D^+} \frac{1-a^d_{RS}}{1+a^d_{RS}}}\, e^{i(\phi^{\Gamma}_{KK\pi}-\delta_{K\pi})} \tag{1.66}$$

$$\lambda^{M}_{K^-\pi^+} \equiv \frac{M_{12}}{|M_{12}|}\frac{\overline{A}_{K^-\pi^+}}{A_{K^-\pi^+}} \equiv -\sqrt{R_D^- \frac{1-a^d_{RS}}{1+a^d_{RS}}}\, e^{i(\phi^{M}_{kaon\pi}+\delta_{K\pi})} \tag{1.67}$$

$$\lambda^{M}_{K^+\pi^-} \equiv \frac{M_{12}}{|M_{12}|}\frac{\overline{A}_{K^+\pi^-}}{A_{K^+\pi^-}} \equiv -\sqrt{\frac{1}{R_D^+} \frac{1-a^d_{RS}}{1+a^d_{RS}}}\, e^{i(\phi^{M}_{K\pi}-\delta_{K\pi})} \tag{1.68}$$

incorporating distinct *CP*-violating phases $\phi^M_{K\pi}$ and $\phi^{\Gamma}_{K\pi}$ related by $\phi^M_{K\pi} - \phi^{\Gamma}_{K\pi} = \phi_{12}$.

To observe the mixing and CPV variables, it is commonly used the Wrong Sign (WS) to Right Sign (RS) decay ratio that can be constructed employing two complementary approaches. The first requires that both WS and RS have the same initial D^0 flavour:

$$R^+(t) \equiv \frac{\Gamma(D^0 \to K^+\pi^-, t)}{\Gamma(D^0 \to K^-\pi^+, t)}, \quad R^-(t) \equiv \frac{\Gamma(\overline{D}^0 \to K^-\pi^+, t)}{\Gamma(\overline{D}^0 \to K^+\pi^-, t)}. \tag{1.69}$$

This approach is the one used in [61].
The other approach requires both WS and RS to decay into the same final state:

$$R'^+(t) \equiv \frac{\Gamma(D^0 \to K^+\pi^-, t)}{\Gamma(\overline{D}^0 \to K^+\pi^-, t)}, \quad R'^-(t) \equiv \frac{\Gamma(\overline{D}^0 \to K^-\pi^+, t)}{\Gamma(D^0 \to K^-\pi^+, t)}. \tag{1.70}$$

The alternative observable offers experimental advantages by reducing systematic uncertainties related to instrumental asymmetries, particularly when the direct *CP* asymmetry in CF decays is negligible, and it is the approach used in [62].

Experimentally,

$$R(t)^{\pm} \simeq R_D^{\pm} + \sqrt{R_D^{\pm}} y'^{\pm} \Gamma t + \frac{x'^{2\pm} + y'^{2\pm}}{4} (\Gamma t)^2, \tag{1.71}$$

with

$$x'^{\pm} = \left|\frac{q}{p}\right|^{\pm} \left(x' \cos\phi^{\lambda}_{K\pi} \pm y' \sin\phi^{\lambda}_{K\pi}\right), \qquad y'^{\pm} = \left|\frac{q}{p}\right|^{\pm} \left(y' \cos\phi^{\lambda}_{K\pi} \mp x' \sin\phi^{\lambda}_{K\pi}\right). \tag{1.72}$$

CP violation in the decay is given by discrepancies between R_D^+ and R_D^-, while *CP* violation in mixing and interference can be seen in differences in (x'^{2+}, y'^{+}) and (x'^{2-}, y'^{-}). The *CP* violation parameters $\left|\frac{q}{p}\right|$ and $\phi^{\lambda}_{\mathrm{K}\pi}$ can be extracted from the quantities $x'^{\pm}$ and $y'^{\pm}$. In literature [63], another approach is also present:

$$y^f_{CP} = y_{12}\cos\phi^M_f \simeq y_{12}, \qquad x^f_{CP} = x_{12}\cos\phi^\Gamma_f \simeq x_{12}, \tag{1.73}$$

$$\Delta y^f = x_{12}\sin\phi^M_f, \qquad \Delta x^f = -y_{12}\sin\phi^\Gamma_f. \tag{1.74}$$

Here, y_{CP} and x_{CP} are defined including explicit corrections for possible *CP*-violating effects. These corrections enter at quadratic order in the CPV phases $\phi^M_{\mathrm{K}\pi}$ and $\phi^\Gamma_{\mathrm{K}\pi}$; therefore, their dependence on *CP*-violation parameters is negligible and so is any dependence on the final state.

The most recent results for the prompt (D^0 tagged from $\mathrm{D}^{*+}\to\mathrm{D}^0\pi^+{}_s$ with the sign of the soft pion) decays are from [62]:

$$R_D = (342.7 \pm 1.9)\times 10^{-5}, \quad A_D = ((-6.6 \pm 5.7)\times 10^{-3},$$

and for the double-tagged (D^0 tagged from $\mathrm{D}^{*+}\to\mathrm{D}^0\pi^+{}_s$ with D^{*+} from $\mathrm{B}\to\mathrm{D}^{*+}\mu^- X$ using the soft pion and the muon) decays from [61]:

$$R_D = (347.0 \pm 5.1)\times 10^{-5}, \quad A_D = (0.9 \pm 1.5)\times 10^{-2}.$$

In both cases, the results come from a combination of Run 1 and Run 2 data from the LHCb experiment.

1.7.1.3 Three-body $\mathrm{D}^0\to\mathrm{K}^0_\mathrm{S}\mathrm{h}^+\mathrm{h}^-$ decays

Three-body decays involving a neutral kaon and two charged hadrons provide enhanced sensitivity to *CP*-violating parameters Δx and Δy through Dalitz plot analysis. The experimental method is based on examining time-dependent ratios of decay rates between opposing regions of the phase space:

$$\begin{aligned} R^{\pm}_b(t) &= \frac{\Gamma_{-b}(\mathrm{D}^0\to\mathrm{K}^0_\mathrm{S}\mathrm{h}^+\mathrm{h}^-,t)}{\Gamma_b(\mathrm{D}^0\to\mathrm{K}^0_\mathrm{S}\mathrm{h}^+\mathrm{h}^-,t)}\left[\frac{\Gamma_{-b}(\overline{\mathrm{D}}^0\to\mathrm{K}^0_\mathrm{S}\mathrm{h}^+\mathrm{h}^-,t)}{\Gamma_b(\overline{\mathrm{D}}^0\to\mathrm{K}^0_\mathrm{S}\mathrm{h}^+\mathrm{h}^-,t)}\right] \\ &\simeq r_b + \sqrt{r_b}[(1-r_b)(y_{CP}\pm\Delta y_f)\cos\delta_{\mathrm{K}^0_\mathrm{S}\mathrm{h}^+\mathrm{h}^-} - (1+r_b)(x_{CP}\pm\Delta x_f)\sin\delta_{\mathrm{K}^0_\mathrm{S}\mathrm{h}^+\mathrm{h}^-}]\Gamma t. \end{aligned} \tag{1.75}$$

This approach offers particular advantages for probing Δx since the strong phase differences $\delta_{\mathrm{K}^0_\mathrm{S}\mathrm{h}^+\mathrm{h}^-}$ can approach $\pm\pi/2$ across different Dalitz plot regions, maximising the coefficient of the Δx term in the linear time dependence.

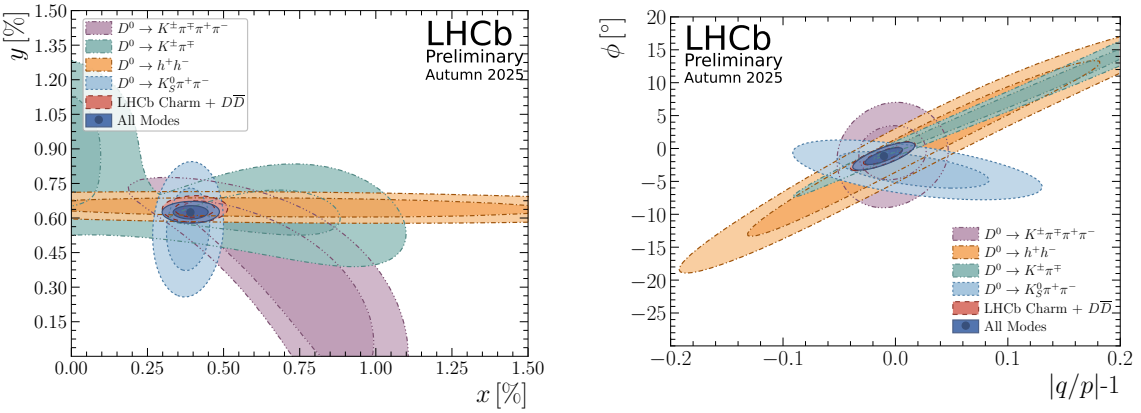

Figure 1.6: Profile-likelihood contours for the charm decay and mixing parameters, illustrating the contribution of different decay modes to the overall sensitivity. The contours represent the 68.3% and 95.4% confidence levels. In the right-hand plot, the red contours from the fit using only charm inputs are obscured beneath the blue contours, which also include beauty inputs; the addition of beauty data does not significantly enhance the precision. From [64].

The most recent LHCb analysis, utilising the complete Run 2 dataset, combining results from prompt [65] and semileptonic decays [63], has measured these *CP*-violating parameters in the $K^0_S\pi^+\pi^+$ final state [63]:

$$\Delta x = (-0.29 \pm 0.18(\text{stat.}) \pm 0.01(\text{syst.})) \times 10^{-3},$$
$$\Delta y = (0.31 \pm 0.35(\text{stat.}) \pm 0.13(\text{syst.})) \times 10^{-3}.$$

These measurements show no significant deviation from *CP* conservation in charm meson mixing or interference phenomena, providing important constraints on potential new physics contributions to the charm sector. The combination of the results can be observed in Figure 1.7.

1.7.2 Mixing

The following discussion presents the various observables that exhibit sensitivity to these mixing parameters while invoking the assumption of *CP* conservation. Indeed, when *CP* symmetry is preserved, the phenomenological description becomes identical to the theoretical framework, as the relations $x_{12} = x$ and $y_{12} = y$ hold true, with all *CP*-violating phases vanishing.

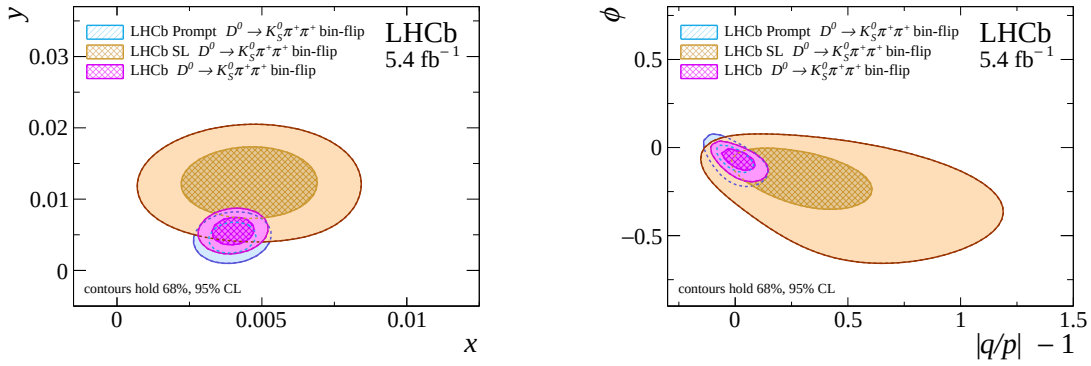

Figure 1.7: Two-dimensional 68% and 95% confidence-level contours on (left) (x, y) and (right) $(|q/p| - 1, \phi)$. Results from Run 2 $D^{*+} \to D^0(\to K^0_S\pi^+\pi^-)\pi^+$ [65], $\overline{B} \to D^0(\to K^0_S\pi^+\pi^-)\mu^-\overline{\nu}_\mu X$, and their combination are shown.

1.7.2.1 $D^0 \to h^+h^-$ CS decays

An approach to studying D^0–$\overline{D}^0$ oscillations involves the measurement of the y^f_{cp} parameter. By implementing the approximation $e^{-x} \simeq 1 - x$, for $|x| \ll 1$, in Equation 1.51, the decay probability becomes:

$$\Gamma(D^0 \to f, t) \simeq \mathcal{N}_f |A_f|^2 e^{-\Gamma t}\{1 + [y\mathcal{R}e(\lambda_f) - x\mathcal{I}m(\lambda_f)]\Gamma t \simeq \mathcal{N}_f |A_f|^2 e^{-\hat{\Gamma}(D^0 \to f)t}, \quad (1.76)$$

where $\hat{\Gamma}(D^0 \to f) \equiv \Gamma \cdot [1 + (y\mathcal{R}e(\lambda_f) - x\mathcal{I}m(\lambda_f))$ is the effective decay width for neutral D mesons decaying to final state f.

The experimental determination of y^f_{CP} relies on measuring this effective lifetime parameter:

$$y^f_{cp} \equiv \hat{\Gamma}(D^0 \to f) - \Gamma = y\mathcal{R}e(\lambda_f) - x\mathcal{I}m(\lambda_f). \quad (1.77)$$

Since in this case $f = \bar{f} = h^+h^- = K^+K^-, \pi^+\pi^-$, assuming *CP* symmetry $\lambda_{K^+K^-}$ and $\lambda_{\pi^+\pi^-}$ equal to −1. Consequently, y^{KK}_{CP} and $y^{\pi\pi}_{CP}$ become equal and can be combined into a single parameter, y_{CP}, which gives direct access to the mixing coefficient: $y_{CP} = y$. To present the most recent result, in which the variable $y_{cp} - y^{K\pi}_{CP}$ is computed, it is important to introduce the $y^{K\pi}_{CP}$.

$$y^{K\pi}_{CP} \approx \sqrt{R_D}\left(x_{12}\cos\phi^M_2 \sin\delta_{K\pi} + y_{12}\cos\phi^\Gamma_2\cos\delta_{K\pi}\right). \quad (1.78)$$

Defined that, the experimentally measured observable is the ratio:

$$\frac{\hat{\Gamma}(D^0 \to f) + \hat{\Gamma}(\overline{D}^0 \to f)}{\hat{\Gamma}(D^0 \to K^-\pi^+) + \hat{\Gamma}(\overline{D}^0 \to K^+\pi^-)} - 1 \approx y^f_{CP} - y^{K\pi}_{CP}. \quad (1.79)$$

The global average, dominated by the LHCb measurement [66] with Run 2 data is:

$$y_{CP} - y_{CP}^{K\pi} = (6.96 \pm 0.26(\text{stat.}) \pm 0.13(\text{syst.})) \times 10^{-3}.$$

1.7.2.2 $D^0 \to K^+\pi^-$ DCS decays

The discovery of D^0–$\overline{D}^0$ oscillations was historically achieved by examining the decay-time dependence of the ratio between DCS decays, $D^0 \to K^+\pi^-$, and CF decays, $D^0 \to K^-\pi^+$. Using D^*-tagging, one can classify decay chains as *wrong-sign* (WS): $D^{*+} \to D^0(\to K^+\pi^-)\pi^+$ and $D^{*-} \to \overline{D}^0(\to K^-\pi^+)\pi^-$, or *right-sign* (RS): $D^{*+} \to D^0(\to K^-\pi^+)\pi^+$ and $D^{*-} \to \overline{D}^0(\to K^+\pi^-)\pi^-$. This terminology reflects whether the soft pion charge matches the kaon charge in the subsequent D decay.

The transition of WS $D^0 \to K^+\pi^-$ proceeds via two interfering mechanisms: direct DCS amplitude with CKM suppression $|V_{cd}V_{us}^*| \simeq \lambda^2 \sim 5\%$, and mixing-assisted CF decay through $D^0 \to \overline{D}^0 \to K^+\pi^-$. Under *CP* conservation, the amplitudes are parametrised using conventional notation where $f \equiv K^-\pi^+$ and $\overline{f} \equiv K^+\pi^-$. The time-evolved WS decay probability is expressed as:

$$\begin{aligned}\Gamma(D^0 \to \overline{f}, t) &= \mathcal{N}_f \left| g_+(t) A_{\overline{f}} + g_-(t) \overline{A}_{\overline{f}} \right|^2 \\ &= \tfrac{\mathcal{N}_f}{2} e^{-\Gamma t} \Big[(1 + |\lambda_{\overline{f}}|^2) \cosh(y\Gamma t) + (1 - |\lambda_{\overline{f}}|^2) \cos(x\Gamma t) \\ &\quad + 2\,\mathrm{Re}(\lambda_{\overline{f}}) \sinh(y\Gamma t) - 2\,\mathrm{Im}(\lambda_{\overline{f}}) \sin(x\Gamma t) \Big]. \end{aligned} \tag{1.80}$$

This could be simplified for small mixing parameters ($x\Gamma t, y\Gamma t \ll 1$):

$$\begin{aligned}\Gamma(D^0 \to \overline{f}, t) \simeq \mathcal{N}_f e^{-\Gamma t} |A_{\overline{f}}|^2 \Big\{ 1 + \big[y\,\mathrm{Re}(\lambda_{\overline{f}}) - x\,\mathrm{Im}(\lambda_{\overline{f}}) \big] \Gamma t \\ + \frac{1}{4} \Big\{ \big[y^2 (1 + |\lambda_{\overline{f}}|^2) - x^2 (1 - |\lambda_{\overline{f}}|^2) \big] (\Gamma t)^2 \Big\}. \end{aligned} \tag{1.81}$$

Assuming *CP* symmetry and $\delta_{K\pi} = \delta_{K\pi}^D - \pi = -\Delta_{K^-\pi^+}$:

$$\lambda_{K^-\pi^+} = \frac{q}{p} \frac{\overline{A}_{K^-\pi^+}}{A_{K^-\pi^+}} = \sqrt{R_D}\, e^{-i\delta_{K\pi}}, \quad \lambda_{K^+\pi^-} = \frac{q}{p} \frac{\overline{A}_{K^+\pi^-}}{A_{K^+\pi^-}} = \sqrt{\tfrac{1}{R_D}}\, e^{i\delta_{K\pi}}, \quad R_D = \left| \frac{A_{K^+\pi^-}}{A_{K^-\pi^+}} \right|^2. \tag{1.82}$$

Then the rotated parameters can be defined as:

$$x' = x \cos\delta_{K\pi} + y \sin\delta_{K\pi} \tag{1.83}$$

$$y' = y \cos\delta_{K\pi} - x \sin\delta_{K\pi} \tag{1.84}$$

The transition of RS $D^0 \to K^-\pi^+$ proceeds via two interfering mechanisms: the CF process $D^0 \to K^-\pi^+$, which is about 300 times larger than its DCS WS counterpart, and DCS $D^0 \to \overline{D}^0 \to K^-\pi^+$.

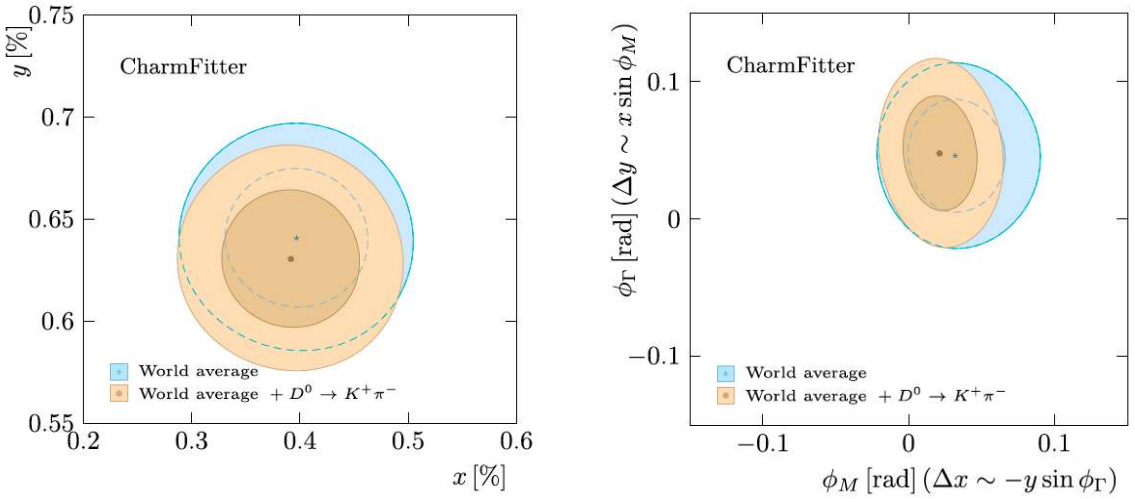

Figure 1.8: Two-dimensional 68% and 95% confidence-level contours on (left) (x, y) and (right) (ϕ_Γ, ϕ_M). Results from [67].

The experimentally accessible observable is constructed as the WS-to-RS ratio, which eliminates numerous systematic uncertainties:

$$R(t) = \frac{\Gamma(\mathrm{D}^0 \to \mathrm{K}^+\pi^-, t)}{\Gamma(\mathrm{D}^0 \to \mathrm{K}^-\pi^+, t)} \simeq R_D + \sqrt{R_D}\; y'\; \Gamma t + \tfrac{1}{4}(x'^2 + y'^2)(\Gamma t)^2. \tag{1.85}$$

The most recent results are from [62], for prompt, and [61], for semileptonic decays, where the mixing variables are defined as $c_{\mathrm{K}\pi}$ and $c'_{\mathrm{K}\pi}$ and for Run 1 and Run 2 data results (Figure 1.8):

$$\begin{aligned} c_{\mathrm{K}\pi} &\approx y_{12} \cos\phi_f^\Gamma \cos\Delta_f + x_{12} \cos\phi_f^M \sin\Delta_f \\ &\approx \begin{cases} (5.28 \pm 0.33) \times 10^{-3} & \text{[prompt]} \\ (5.5 \pm 1.5) \times 10^{-3} & \text{[semileptonic]} \end{cases} \end{aligned}$$

$$\begin{aligned} c'_{\mathrm{K}\pi} &\approx \frac{y_{12}^2 + x_{12}^2}{4} \\ &\approx \begin{cases} (0.012 \pm 0.0035) \times 10^{-3} & \text{[prompt]} \\ (0.012 \pm 0.024) \times 10^{-3} & \text{[semileptonic]} \end{cases} \end{aligned}$$

with $\phi_f^{\Gamma,M}$ are the weak absorptive and dispersive phases from [56] and $\Delta_f \approx -10^\circ \pm 3^\circ$ from [68].

1.7.2.3 Three-body $D^0 \to K^0_S h^+ h^-$ decays

Three-body decays such as $D^0 \to K^0_S \pi^+ \pi^-$ and $D^0 \to K^0_S K^+ K^-$ offer unique sensitivity to mixing parameters, particularly x, through combined analysis of temporal evolution and resonant structure across the Dalitz phase space. The kinematic plane is defined by invariant masses:

$$m^2_{\pm} \equiv \begin{cases} m^2(K^0_S h^{\pm}) & \text{for } D^0 \to K^0_S h^+ h^- \\ m^2(K^0_S h^{\mp}) & \text{for } \overline{D}{}^0 \to K^0_S h^+ h^- \end{cases} \tag{1.86}$$

and is partitioned into two sets of n symmetric bins, distributed around the principal diagonal, with indices $b = -n, ..., -1, 1, ...n$ where positive values correspond to the $m^2(K^0_S h^+) > m^2(K^0_S h^-)$ region.

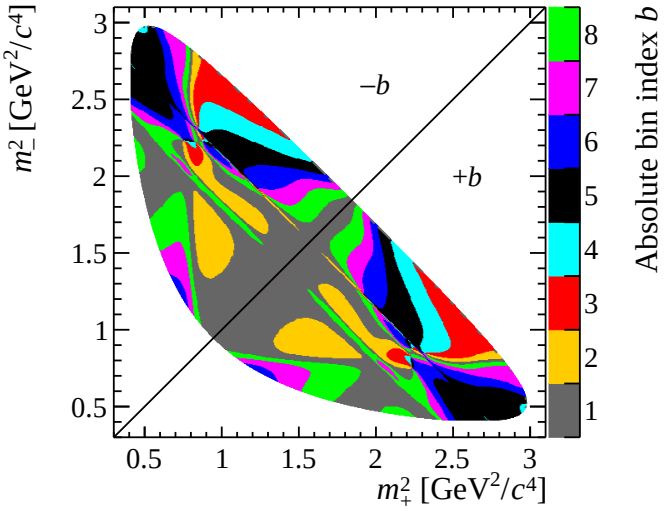

Figure 1.9: Iso-δ binning scheme for the $D^0 \to K^0_S \pi^+ \pi^-$ Dalitz plot, following the BaBar 2008 resonance model [69, 70]. The partition maintains symmetry about the bisector, with positive indices in the lower kinematic region. Colour coding represents the absolute bin index magnitude. Plot from [65].

Integration of the general decay rate expression over individual kinematic regions

yields:

$$\begin{aligned}\Gamma_b(\mathrm{D}^0 \to f, t) &= \int_b \Gamma(\mathrm{D}^0 \to f, t) \\ &= \mathcal{N}_b |A_b|^2 e^{-\Gamma t}\{1 + [y\mathcal{R}e(\lambda_b) - x\mathcal{I}m(\lambda_b)]\Gamma t \\ &\quad + \frac{1}{4}[y^2(1+|\lambda_b|^2) - x^2(1-|\lambda_b|^2)](\Gamma t)^2\}\end{aligned} \tag{1.87}$$

where the average value of each quantity in the Dalitz bin b is denoted by subscript b. The parameter $\lambda_b = r_b, e^{-i\delta^b_{\mathrm{K}^0_{\mathrm{S}}\mathrm{hh}}}$ represents the bin-averaged value of the λ_f factor within bin b, where $\delta^b_{\mathrm{K}^0_{\mathrm{S}}\mathrm{hh}}$ is the effective strong phase averaged over the bin. The quantities $\cos_b \delta_{\mathrm{K}^0_{\mathrm{S}}\mathrm{hh}}$ and $\sin_b \delta_{\mathrm{K}^0_{\mathrm{S}}\mathrm{hh}}$ correspond to the respective trigonometric averages over the same bin and

$$r_b \equiv \frac{\int_{-b} dm^2_+ dm^2_- |A_f(dm^2_+, dm^2_-)|^2}{\int_b dm^2_+ dm^2_- |A_f(dm^2_+, dm^2_-)|^2}. \tag{1.88}$$

From the opposite-bin decay rate ratios, the experimental observable could be constructed:

$$R_b(t) = \frac{\Gamma_{-b}(\mathrm{D}^0 \to \mathrm{K}^0_{\mathrm{S}}\mathrm{h}^+\mathrm{h}^-, t)}{\Gamma_b(\mathrm{D}^0 \to \mathrm{K}^0_{\mathrm{S}}\mathrm{h}^+\mathrm{h}^-, t)} \simeq \frac{r_b + \sqrt{r_b}\; c_{-b}\; \Gamma t + c'_{-b}(\Gamma t)^2}{1 + \sqrt{r_b}\; c_b\; \Gamma t + c'_b(\Gamma t)^2} \tag{1.89}$$

The expansion coefficients are defined as:

$$c_{\pm b} = y \cos_b \delta_{\mathrm{K}^0_{\mathrm{S}}\mathrm{hh}} \pm x \sin_b \delta_{\mathrm{K}^0_{\mathrm{S}}\mathrm{hh}}, \tag{1.90}$$

$$c'_{\pm b} = \frac{1}{4}(y^2 \mp x^2) + \frac{1}{4} r_b (y^2 \pm x^2). \tag{1.91}$$

Since r_b spans the range $\mathcal{O}(0.1 - 1)$, quadratic contributions become negligible, enabling the simplified expression:

$$R_b(t) \simeq r_b + \sqrt{r_b}\; [(1 - r_b) y \cos_b \delta_{\mathrm{K}^0_{\mathrm{S}}\mathrm{hh}} - (1 + r_b) x \sin_b \delta_{\mathrm{K}^0_{\mathrm{S}}\mathrm{hh}}]\Gamma t \tag{1.92}$$

Simultaneous fitting of multiple bin ratios, combined with external strong-phase constraints from amplitude models, provides access to both mixing parameters. The methodology requires an external strong-phase determination through amplitude modelling. The most recent result from LHCb [65] which with a complete Run 2 data from $\mathrm{D}^0 \to \mathrm{K}^0_{\mathrm{S}}\pi^+\pi^-$ decays reports:

$$\begin{aligned} x_{CP} &= (3.97 \pm 0.46(\text{stat.}) \pm 0.29(\text{syst.})) \times 10^{-3} \\ y_{CP} &= (4.59 \pm 1.20(\text{stat.}) \pm 0.85(\text{syst.})) \times 10^{-3} \end{aligned}$$

This measurement represents the first statistically significant observation (exceeding 7σ) of $\Delta m \neq 0$ values in the charm system, but a more detailed discussion of the most

recent measurements is provided in Section 1.8.1. This last measurement reported in this overview of the main results on *CP* violation and mixing is particularly important because the analysis included in this thesis work is on the measurement of mixing and *CP* violation in the $D^0 \to K^0_S \pi^+ \pi^-$ with Run 3 data, collected with the new Upgrade I LHCb detector.

1.8 The $D^0 \to K^0_S h^+ h^-$ decay channel

The purpose of this section is to provide a detailed description of the key decay channel of this analysis, $D^0 \to K^0_S \pi^+ \pi^-$, and of the model-independent *bin-flip* method employed to extract the charm-mixing and *CP*-violation parameters.

Physics features of $D^0 \to K^0_S h^+ h^-$. The self-conjugate three-body modes $D^0 \to K^0_S h^+ h^-$ ($h = \pi, K$) receive sizeable Cabibbo-favoured (CF) and doubly-Cabibbo-suppressed (DCS) contributions that interfere across the Dalitz plane. In addition, intermediate states with definite *CP* eigenvalue (e.g. $K^0_S \rho$, $K^0_S f_0$, ...) populate extended regions, enhancing sensitivity to oscillation parameters when the phase space is partitioned appropriately. Standard-Model weak phases in the decay amplitudes are negligible at $\mathcal{O}(\lambda^4)$, so direct CPV in the amplitude can be neglected, and weak phases can be taken common across the Dalitz plot for the purpose of this analysis. In this limit, the sensitivity is driven by mixing and by the strong-phase variation over phase space, encapsulated in externally measured hadronic inputs.

Dalitz kinematics and amplitudes. The phase space is parametrised with the flavour-dependent Dalitz coordinates $m^2_\pm$ defined in Equation 1.86.

The decay amplitudes for mesons produced as D^0 and $\overline{D}^0$, respectively, and decaying to the final state $f \equiv K^0_S \pi^+ \pi^-$ at the generic point (m^2_+, m^2_-) of the Dalitz plane are denoted by $A_f(m^2_+, m^2_-)$ and $\bar{A}_f(m^2_+, m^2_-)$.

If *CP* symmetry is conserved in the decay, the relation $A_f(m^2_+, m^2_-) = \bar{A}_f(m^2_+, m^2_-)$ holds. The decay rates of D^0 mesons tagged in the flavour eigenstates D^0 and $\overline{D}^0$ at time $t = 0$ evolve in time as:

$$\left|T_f(m^2_+, m^2_-; t)\right|^2 = \left|\mathcal{A}_f(m^2_+, m^2_-)\, g_+(t) + \frac{q}{p}\, \overline{\mathcal{A}}_f(m^2_-, m^2_+)\, g_-(t)\right|^2, \tag{1.93}$$

$$\left|\overline{T}_f(m^2_+, m^2_-; t)\right|^2 = \left|\overline{\mathcal{A}}_f(m^2_+, m^2_-)\, g_+(t) + \frac{p}{q}\, \mathcal{A}_f(m^2_-, m^2_+)\, g_-(t)\right|^2, \tag{1.94}$$

where t is in units of the D^0 lifetime, $g_\pm(t) = \theta(t)\, e^{-imt - t/2}\{\cosh, \sinh\}(zt/2)$, and

$$z = -(y + ix)\,, \qquad x = \frac{\Delta m}{\Gamma}, \quad y = \frac{\Delta \Gamma}{2\Gamma}.$$

Here $m = (m_1 + m_2)/2$ is the average neutral-D mass, $\theta(t)$ is the Heaviside function, and t is the decay time in units of D^0 lifetime $\tau = 1/\Gamma$.

Bin definitions and hadronic inputs. The Dalitz plane is divided into two symmetric sets of n bins about the bisector $m_+^2 = m_-^2$. Positive indices $b = 1, \ldots, n$ label the lower half-plane ($m_+^2 > m_-^2$), dominated by CF $D^0 \to K^*(892)\pi^+$; the negative indices $-b$ label the mirrored bins.
Defined the bin-integrated quantities

$$F_b = \int_b dm_+^2 dm_-^2 \left|\mathcal{A}_f(m_+^2, m_-^2)\right|^2, \qquad \overline{F}_b = \int_b dm_+^2 dm_-^2 \left|\overline{\mathcal{A}}_f(m_+^2, m_-^2)\right|^2, \tag{1.95}$$

$$X_b = \frac{1}{\sqrt{F_b F_{-b}}} \int_b dm_+^2 dm_-^2 \, \mathcal{A}_f^*(m_+^2, m_-^2)\, \overline{\mathcal{A}}_f(m_-^2, m_+^2), \qquad X_{-b} = X_b^*, \ |X_b| \le 1, \tag{1.96}$$

where F_b and $\overline{F}_b$ are event yields in the Dalitz bin b at $t = 0$ and X_b is the hadronic parameter of the interference term, which is related to the strong-interaction phase difference, $\Delta\delta$, and to the weak-interaction phase difference, φ, between $A_f(m_+^2, m_-^2)$ and $\overline{A}_f(m_+^2, m_-^2)$ averaged over bin b. So the expressions for the event yield integrated over each Dalitz-plot bin b are:

$$\begin{aligned} N_b(t) &= \int_b dm_+^2 dm_-^2 \left|T_f(m_+^2, m_-^2; t)\right|^2 \\ &= F_b \left|g_+(t)\right|^2 + \left|\frac{q}{p}\right|^2 \overline{F}_{-b} \left|g_-(t)\right|^2 + 2\sqrt{\overline{F}_{-b} F_b}\, \Re\left[\frac{q}{p} X_b\, g_+^*(t) g_-(t)\right], \end{aligned} \tag{1.97}$$

$$\begin{aligned} \overline{N}_b(t) &= \int_b dm_+^2 dm_-^2 \left|\overline{T}_f(m_+^2, m_-^2; t)\right|^2 \\ &= \overline{F}_b \left|g_+(t)\right|^2 + \left|\frac{p}{q}\right|^2 F_{-b} \left|g_-(t)\right|^2 + 2\sqrt{\overline{F}_{-b}\, \overline{F}_b}\, \Re\left[\frac{p}{q} \overline{X}_b\, g_+^*(t) g_-(t)\right]. \end{aligned} \tag{1.98}$$

In the limit of *CP*-symmetric decay amplitudes $\mathcal{A}_f = \overline{\mathcal{A}}_f$, $F_b = \overline{F}_b$, $\varphi = 0$ and $X_b = \overline{X}_b$. The coefficient $X_b \equiv c_b - i s_b$ with:

$$c_b = \frac{1}{\sqrt{F_b F_{-b}}} \int_b dm_+^2 dm_-^2 \left|\mathcal{A}_f(m_+^2, m_-^2)\right| \left|\mathcal{A}_f(m_-^2, m_+^2)\right| \cos\Delta\delta(m_+^2, m_-^2), \tag{1.99}$$

$$s_b = \frac{1}{\sqrt{F_b F_{-b}}} \int_b dm_+^2 dm_-^2 \left|\mathcal{A}_f(m_+^2, m_-^2)\right| \left|\mathcal{A}_f(m_-^2, m_+^2)\right| \sin\Delta\delta(m_+^2, m_-^2), \tag{1.100}$$

where $\Delta\delta(m_+^2, m_-^2) = \delta(m_+^2, m_-^2) - \delta(m_-^2, m_+^2)$ is the strong-phase difference with $\delta(m_+^2, m_-^2)$ denoting the phase of the amplitude $A_f(m_+^2, m_-^2)$ at point (m_+^2, m_-^2). These hadronic parameters (c_b, s_b) are constrained using independent external measurements, and this allows access to the mixing parameters.

Small-mixing expansion and time-bin integration. For $|z|\,t \ll 1$, one may expand

$$|g_+(t)|^2 \simeq e^{-t}\Big(1 + \tfrac{1}{4}\,t^2 \mathcal{R}e(z^2)\Big)\,, \qquad |g_-(t)|^2 \simeq \tfrac{1}{4}\,e^{-t} t^2 |z|^2, \qquad g_+^*(t) g_-(t) \simeq \tfrac{1}{2}\,e^{-t}\,t\,z. \tag{1.101}$$

Since terms of $O(z^3)$ or higher can be neglected, integrating over a decay-time bin j with averages $\langle t\rangle_j$ and $\langle t^2\rangle_j$ taken over the exponential distribution in decay-time bin j:

$$\int_j dt\,|g_+(t)|^2 \simeq n_j\Big(1 + \tfrac{1}{4}\langle t^2\rangle_j \mathcal{R}e(z^2)\Big), \tag{1.102}$$

$$\int_j dt\,|g_-(t)|^2 \simeq n_j\,\tfrac{1}{4}\langle t^2\rangle_j |z|^2, \tag{1.103}$$

$$\int_j dt\,g_+^*(t) g_-(t) \simeq n_j\,\tfrac{1}{2}\langle t\rangle_j\,z. \tag{1.104}$$

where normalization constant n_j cancels in ratios. If the probability $\varepsilon(t)$ to select and reconstruct the decays is non-uniform as a function of decay time within bin j, the average is performed over the observed decay-time distribution of mesons that did not undergo oscillation, $\varepsilon(t)e^{-t}$. Since in the bin-flip method, the observables are constructed as ratios of decay yields in symmetric Dalitz bins and decay-time intervals, the decay-time-dependent efficiency $\varepsilon(t)$ enters both the numerator and the denominator similarly and largely cancels out. Therefore, the dependence of the results on $\varepsilon(t)$ is minimal, and residual effects arise only from higher-order corrections or possible asymmetries in the efficiency within a given decay-time bin.

Ratios in terms of (x, y) and (c_b, s_b). With the approximation defined, in the limit of *CP*-conserving decay amplitudes, one obtains:

$$\begin{aligned} N_{b,j} &= \int_j dt\,N_b(t) \\ &\approx F_b\big[1 + \tfrac{1}{4}\langle t^2\rangle_j\,\mathcal{R}e(z^2)\big] + \tfrac{1}{4}\langle t^2\rangle_j\,|z|^2\,\left|\tfrac{q}{p}\right|^2 F_{-b} + \langle t\rangle_j\sqrt{F_{-b}F_b}\,\mathcal{R}e\Big(\tfrac{q}{p}\,X_b\,z\Big)\,, \end{aligned} \tag{1.105}$$

$$\begin{aligned} \overline{N}_{b,j} &= \int_j dt\,\overline{N}_b(t) \\ &\approx F_b\big[1 + \tfrac{1}{4}\langle t^2\rangle_j\,\mathcal{R}e(z^2)\big] + \tfrac{1}{4}\langle t^2\rangle_j\,|z|^2\,\left|\tfrac{p}{q}\right|^2 F_{-b} + \langle t\rangle_j\sqrt{F_{-b}F_b}\,\mathcal{R}e\Big(\tfrac{p}{q}\,X_b\,z\Big)\,. \end{aligned} \tag{1.106}$$

Defining $r_b \equiv F_{-b}/F_b$, it is interesting to compute the ratios between the decay yield in Dalitz bin $-b$ and Dalitz bin b for mesons originally produced as D^0 or $\overline{D}^0$, for

each decay-time bin j:

$$R_{bj} \simeq \frac{N_{-bj}}{N_{bj}} \simeq \frac{r_b\Big[1 + \frac{1}{4}\langle t^2\rangle_j \mathcal{R}e(z^2)\Big] + \frac{1}{4}\langle t^2\rangle_j |z|^2\,|q/p|^2 + \sqrt{r_b}\langle t\rangle_j\,\mathcal{R}e\Big[X_b^*(q/p)\,z\Big]}{1 + \frac{1}{4}\langle t^2\rangle_j \mathcal{R}e(z^2) + \frac{1}{4}\langle t^2\rangle_j |z|^2\,r_b|q/p|^2 + \sqrt{r_b}\langle t\rangle_j\,\mathcal{R}e\Big[X_b(q/p)\,z\Big]}, \quad (1.107)$$

$$\overline{R}_{bj} \simeq \frac{\overline{N}_{-bj}}{\overline{N}_{bj}} \simeq \frac{r_b\Big[1 + \frac{1}{4}\langle t^2\rangle_j \mathcal{R}e(z^2)\Big] + \frac{1}{4}\langle t^2\rangle_j |z|^2\,|p/q|^2 + \sqrt{r_b}\langle t\rangle_j\,\mathcal{R}e\Big[X_b^*(p/q)\,z\Big]}{1 + \frac{1}{4}\langle t^2\rangle_j\,\mathcal{R}e(z^2) + \frac{1}{4}\langle t^2\rangle_j |z|^2\,r_b|p/q|^2 + \sqrt{r_b}\langle t\rangle_j\,\mathcal{R}e\Big[X_b(p/q)\,z\Big]}. \quad (1.108)$$

These are the core observables of the bin-flip fit: a joint fit of the R_{bj} and $\overline{R}_{bj}$ ratio is performed to determine the oscillation and *CP* violation parameters in charm mixing, by constraining the coefficients X_b from external measurements.

Additive CPV parametrization $(z_{\rm CP}, \Delta z)$. To avoid instabilities of the fit when $|z| \approx 0$, it is advantageous to reparametrize the CPV effects *additively* via

$$z_{\rm CP} \pm \Delta z \;\equiv\; (q/p)^{\pm 1}\, z. \quad (1.109)$$

In this language,

$$z^2 = (z_{\rm CP} + \Delta z)(z_{\rm CP} - \Delta z) = z_{\rm CP}^2 - \Delta z^2, \qquad \left(\frac{q}{p}\right)^2 = \frac{z_{\rm CP} + \Delta z}{z_{\rm CP} - \Delta z},$$

and Equations (1.107)–(1.108) become

$$R_{bj} \simeq \frac{r_b\Big[1 + \frac{1}{4}\langle t^2\rangle_j \mathcal{R}e(z_{\rm CP}^2 - \Delta z^2)\Big] + \frac{1}{4}\langle t^2\rangle_j \left|z_{\rm CP} + \Delta z\right|^2 + \sqrt{r_b}\langle t\rangle_j\,\mathcal{R}e\Big[X_b^*\left(z_{\rm CP} + \Delta z\right)\Big]}{1 + \frac{1}{4}\langle t^2\rangle_j \mathcal{R}e(z_{\rm CP}^2 - \Delta z^2) + r_b\frac{1}{4}\langle t^2\rangle_j \left|z_{\rm CP} + \Delta z\right|^2 + \sqrt{r_b}\langle t\rangle_j\,\mathcal{R}e\Big[X_b\left(z_{\rm CP} + \Delta z\right)\Big]}, \quad (1.110)$$

$$\overline{R}_{bj} \simeq \frac{r_b\Big[1 + \frac{1}{4}\langle t^2\rangle_j \mathcal{R}e(z_{\rm CP}^2 - \Delta z^2)\Big] + \frac{1}{4}\langle t^2\rangle_j \left|z_{\rm CP} - \Delta z\right|^2 + \sqrt{r_b}\langle t\rangle_j\,\mathcal{R}e\Big[X_b^*\left(z_{\rm CP} - \Delta z\right)\Big]}{1 + \frac{1}{4}\langle t^2\rangle_j \mathcal{R}e(z_{\rm CP}^2 - \Delta z^2) + r_b\frac{1}{4}\langle t^2\rangle_j \left|z_{\rm CP} - \Delta z\right|^2 + \sqrt{r_b}\langle t\rangle_j\,\mathcal{R}e\Big[X_b\left(z_{\rm CP} - \Delta z\right)\Big]}. \quad (1.111)$$

Connection to $(x_{\rm CP}, y_{\rm CP}, \Delta x, \Delta y)$ and to $(x, y, |q/p|, \phi)$. Adopting the conventional phase $\phi \equiv \arg(q/p)$, which assumes the absence of any final-state-dependent weak interaction phase between decay amplitudes (consistent with the limit of *CP*-symmetric decay amplitudes), the usual mixing parameters are:

$$x_{\rm CP} = -\mathcal{I}m(z_{\rm CP}), \qquad y_{\rm CP} = -\mathcal{R}e(z_{\rm CP}), \qquad \Delta x = -\mathcal{I}m(\Delta z), \qquad \Delta y = -\mathcal{R}e(\Delta z). \quad (1.112)$$

These relate to the usual parameters $(x, y, |q/p|, \phi)$ as

$$x_{\rm CP} = \tfrac{1}{2}[x\cos\phi(|q/p| + |p/q|) + y\sin\phi(|q/p| - |p/q|)]\,, \tag{1.113}$$
$$\Delta x = \tfrac{1}{2}[x\cos\phi(|q/p| - |p/q|) + y\sin\phi(|q/p| + |p/q|)]\,, \tag{1.114}$$
$$y_{\rm CP} = \tfrac{1}{2}[y\cos\phi(|q/p| + |p/q|) - x\sin\phi(|q/p| - |p/q|)]\,, \tag{1.115}$$
$$\Delta y = \tfrac{1}{2}[y\cos\phi(|q/p| - |p/q|) - x\sin\phi(|q/p| + |p/q|)]\,. \tag{1.116}$$

In the *CP*-symmetry limit ($|q/p| = 1$ in mixing, $\phi = 0$ in the interference), one recovers $x_{\rm CP} = x$, $y_{\rm CP} = y$, and $\Delta x = \Delta y = 0$.

Binning choice and strong-phase inputs (c_b, s_b). For this analysis, the Dalitz plane is partitioned in "iso-$\Delta\delta$" (Figure 1.9) bins such that $\Delta\delta$ is approximately constant in each bin:

$$\frac{2\pi\,(b-\frac{3}{2})}{n} \;<\; \Delta\delta(m_+^2, m_-^2) \;<\; \frac{2\pi\,(b-\frac{1}{2})}{n}, \qquad b = 1, \ldots, n.$$

This reduces sensitivity to local efficiency variations. Although alternative binning schemes have been developed [71], this analysis uses the same binning approach as Run 2 to ensure consistency and enable direct comparison with previous results. The (c_b, s_b) and their correlations are taken from threshold measurements (CLEO [69] using the BaBar-2008 model [70] to define the bins).

Accounting for non-uniform efficiencies across the Dalitz plot. If the selection efficiency $\epsilon(m_+^2, m_-^2)$ is not uniform, the effective quantities entering the fit are

$$\widetilde{F}_b = \int_b dm_+^2 dm_-^2 \;\epsilon(m_+^2, m_-^2)\,|\mathcal{A}_f(m_+^2, m_-^2)|^2, \tag{1.117}$$
$$\widetilde{c}_b = \frac{\int_b dm_+^2 dm_-^2 \;\epsilon(m_+^2, m_-^2)\,|\mathcal{A}_f(m_+^2, m_-^2)|\,|\mathcal{A}_f(m_-^2, m_+^2)|\cos\Delta\delta(m_+^2, m_-^2)}{\sqrt{\widetilde{F}_b \widetilde{F}_{-b}}}, \tag{1.118}$$
$$\widetilde{s}_b = \frac{\int_b dm_+^2 dm_-^2 \;\epsilon(m_+^2, m_-^2)\,|\mathcal{A}_f(m_+^2, m_-^2)|\,|\mathcal{A}_f(m_-^2, m_+^2)|\sin\Delta\delta(m_+^2, m_-^2)}{\sqrt{\widetilde{F}_b \widetilde{F}_{-b}}}. \tag{1.119}$$

Efficiency patterns that are symmetric under $m_+^2 \leftrightarrow m_-^2$ induce reduced biases on $(\widetilde{c}_b, \widetilde{s}_b)$, and the iso-$\Delta\delta$ binning further mitigates residual effects. In what follows, tildes are omitted with the understanding that external inputs and possible corrections can absorb small biases.

Remarks specific to $D^0 \to K^0_S \pi^+ \pi^-$. Because several bins are dominated by *CP*-eigenstate amplitudes while others are CF–DCS interference–dominated, the slopes of R_{bj} versus $\langle t \rangle_j$ (Figure 1.10) show characteristic bin-to-bin patterns: bins with $r_b \approx 1$ and large s_b (small c_b) carry most of the x sensitivity, while bins with large c_b and small r_b, s_b carry most of the y sensitivity. This complementarity is at the heart of the bin-flip gain on the x combinations.

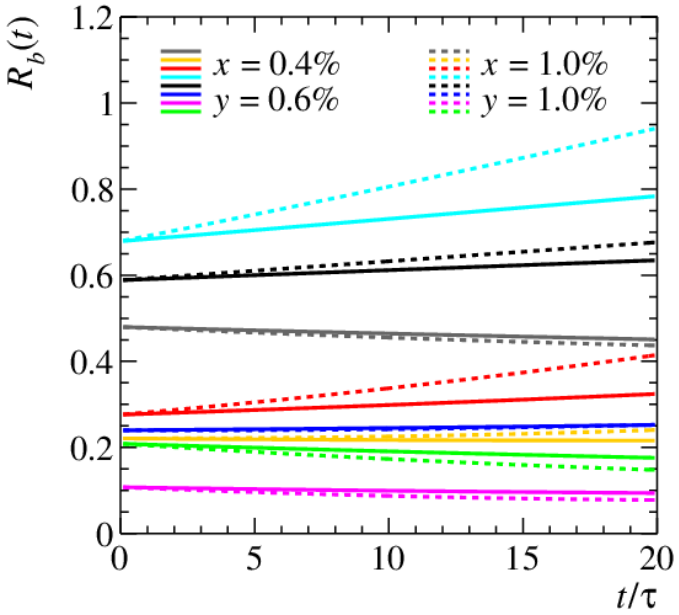

Figure 1.10: Bin-flip ratio in each Dalitz-plot bin as a function of decay time, in the limit of *CP* symmetry and for two sets of mixing parameters. Ratios are computed from Equation 1.110. Colours identify the various Dalitz-plot bins following Figure 1.9 [22].

In summary, the bin-flip analysis of $D^0 \to K^0_S \pi^+ \pi^-$ is a *model-independent* route to measure $(x_{CP}, y_{CP}, \Delta x, \Delta y)$ (and thus $x, y, |q/p|, \phi$) by exploiting mirrored-bin yield ratios as functions of decay time, with external (c_b, s_b) inputs.

1.8.1 Status of the Art

The most recent results in the study of *CP* violation and mixing in the $D^0 \to K^0_S \pi^+ \pi^-$ decay channel are summarised below. These measurements represent the current state of the art in charm physics and provide the most stringent constraints on the fundamental parameters governing neutral D meson oscillations.

The most recent and important results come from two major experimental efforts. The LHCb collaboration achieved a milestone in 2021 with the first observation of a non-zero mass difference in the neutral D meson system [65], while the most recent measurement was performed by the combined Belle and Belle II collaborations in 2024 [72].

The LHCb analysis used a dataset corresponding to an integrated luminosity of 5.4 fb^{-1} of proton-proton collisions collected from 2016 to 2018, analysing 30.6 million $D^0 \to K^0_S \pi^+ \pi^-$ signal decays through the bin-flip method. This model-independent approach partitions the Dalitz plot into eight symmetric bins and measures yield ratios as a function of decay time, achieving unprecedented statistical precision through careful systematic control. The results were (Figure 1.11):

$$\begin{aligned} x_{CP} &= (3.97 \pm 0.46(\text{stat}) \pm 0.29(\text{syst})) \times 10^{-3}, \\ y_{CP} &= (4.59 \pm 1.20(\text{stat}) \pm 0.85(\text{syst})) \times 10^{-3}, \\ \Delta x &= (-0.27 \pm 0.18(\text{stat}) \pm 0.01(\text{syst})) \times 10^{-3}, \\ \Delta y &= (0.20 \pm 0.36(\text{stat}) \pm 0.13(\text{syst})) \times 10^{-3}, \end{aligned}$$

establishing the first observation of D^0–$\overline{D}^0$ mixing with a significance exceeding seven standard deviations.

The most recent measurement comes from the Belle and Belle II collaborations, utilising a combined dataset of 951 fb^{-1} from Belle and 408 fb^{-1} from Belle II, corresponding to approximately 2.05×10^6 reconstructed neutral D mesons in the same decay channel. Using a similar model-independent Dalitz plot binning approach with external hadronic parameter constraints, they obtained under the assumption of *CP* symmetry (Figure 1.12):

$$\begin{aligned} x &= (4.0 \pm 1.7(\text{stat}) \pm 0.4(\text{syst})) \times 10^{-3}, \\ y &= (2.9 \pm 1.4(\text{stat}) \pm 0.3(\text{syst})) \times 10^{-3}, \end{aligned}$$

with negligible correlation between the parameters.

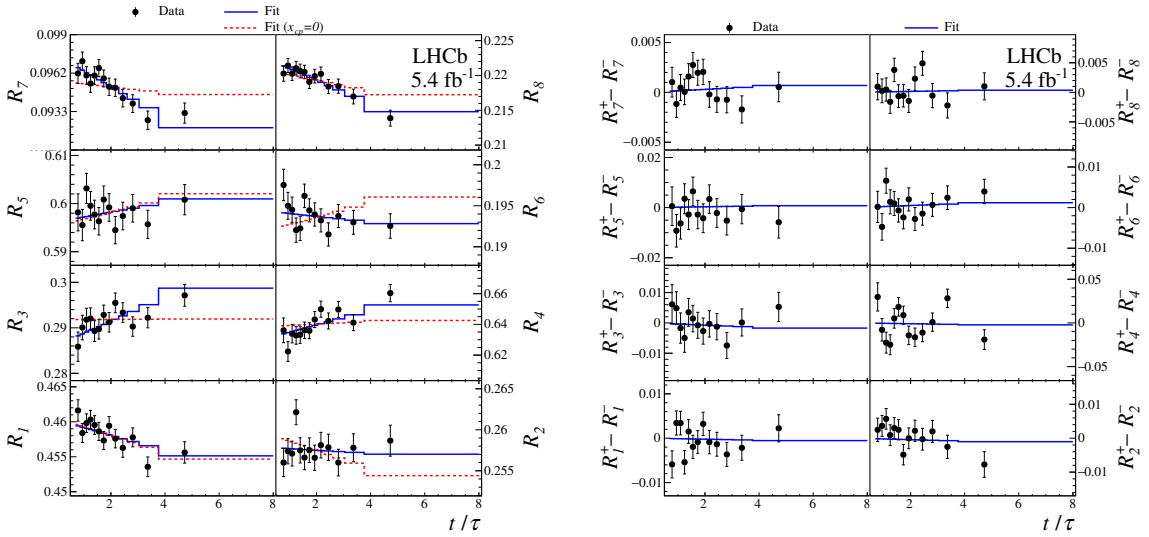

Figure 1.11: (Left) *CP*-averaged yield ratios and (right) differences of D^0 and $\overline{D}^0$ yield ratios as a function of t/τ, shown for each Dalitz- plot bin with fit projections overlaid. Results from [65].

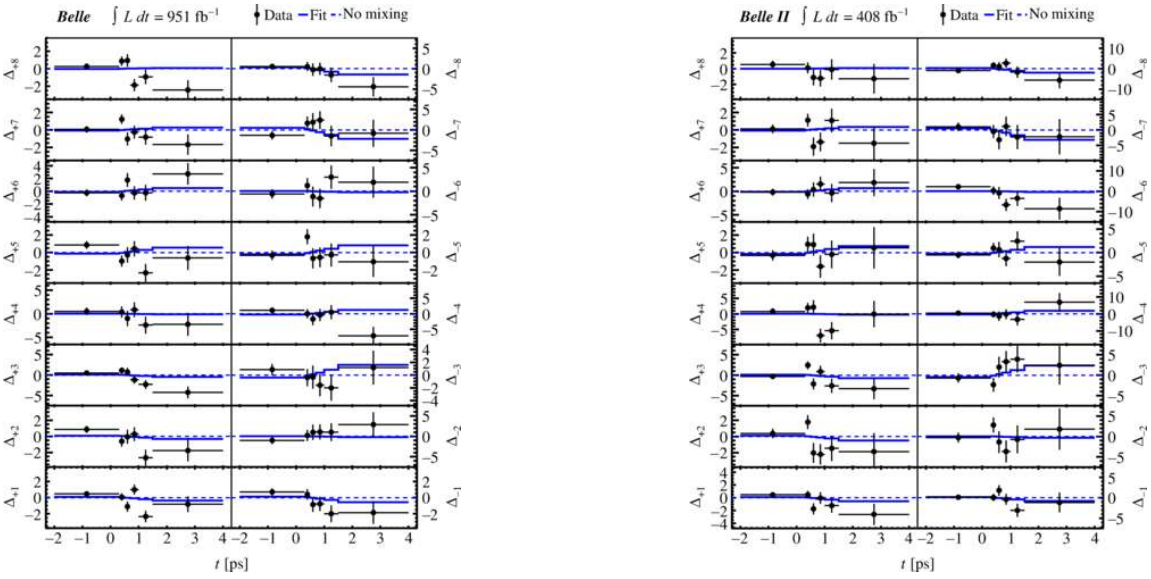

Figure 1.12: Decay-time distributions of the percent relative difference between (left) Belle and (right) Belle II data and the no-mixing model. The quantity $\Delta b = 100 \times \frac{\text{data - no-mixing fit}}{\text{no-mixing fit}}$ is computed in each Dalitz-plot bin b, with fit projections overlaid. Results from [72].

These results are consistent with previous determinations and provide complementary constraints from the clean e^+e^- collision environment.

For completeness, it is worth recalling that time-dependent amplitude analyses based on explicit Dalitz-plot models have also been performed in the past by the BaBar [73] and Belle [74] collaborations. In this model-dependent approach, the decay amplitude is parametrised as a coherent sum of intermediate resonant contributions, allowing a direct extraction of the mixing parameters without relying on external measurements of strong-phase differences. This constitutes a conceptual advantage, as the precision is not limited by the uncertainties on the hadronic strong phases, which could become a dominant source of uncertainty with larger future datasets.

However, the reliability of the extracted parameters depends critically on the accuracy of the amplitude model and on the control of associated systematic uncertainties, which are inherently difficult to quantify. In particular, in a hadronic-collision environment such as that of LHCb, a time-dependent amplitude fit requires an extremely precise knowledge of the reconstruction efficiency across the full Dalitz plane. Such detector effects are challenging to model with sufficient accuracy and can introduce non-trivial biases.

For these reasons, the model-independent binning strategy is not merely an alternative approach, but a robust and experimentally safer solution. By relying on external strong-phase inputs and yield ratios in symmetric Dalitz bins, it avoids explicit dependence on an amplitude model, significantly reducing model-related systematic uncertainties while maintaining competitive sensitivity.

Chapter 2

The LHCb experiment

This chapter introduces the LHCb detector as operated in Run 3. It outlines the tracking and particle-identification subsystems, the dipole magnet and the standard track types, and it summarises the data acquisition and software trigger, with notes on real-time alignment, calibration, and offline processing.

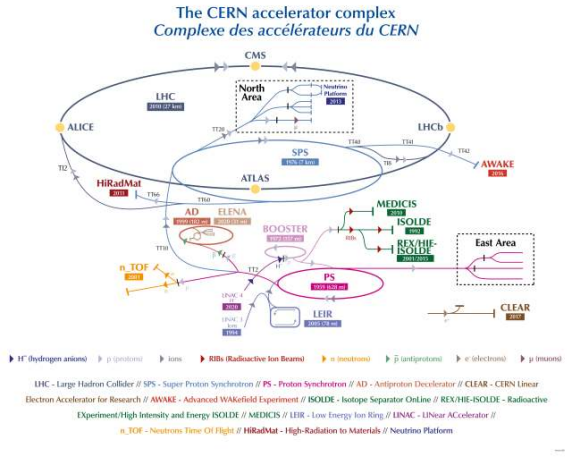

Figure 2.1: The CERN accelerator complex [75]

2.1 The Large Hadron Collider

The Large Hadron Collider (LHC) [76] is a 26.7km superconducting synchrotron (Figure 2.1) installed in a 100 m deep tunnel straddling the French–Swiss border near Geneva. Two counter-rotating beams circulate in separate vacuum pipes and are brought to collision at four interaction points (Figure 2.2) hosting ATLAS (A

Toroidal LHC Apparatus) [77], CMS (Compact Muon Solenoid) [78], ALICE (A Large Ion Collider Experiment) [79], and LHCb (Large Hadron Collider beauty) [80]. The LHC alternates between periods of active data collection and maintenance. The data-taking phases, known as Runs, are followed by Long Shutdowns, during which the accelerator undergoes upgrades and routine maintenance. The LHC's operational schedule is planned well in advance and published by CERN. Currently, the accelerator is in Run 3, which began in 2022 and is expected to continue until 2026. After this, Long Shutdown 3 (LS3) will take place, lasting approximately three years, during which the LHC will be upgraded to become the High-Luminosity LHC (HL-LHC).

Proton–proton centre-of-mass energies evolved from 7 – 8 TeV (Run 1) to 13 TeV (Run 2) and 13.6 TeV in Run 3; heavy-ion running is also performed [81].

Proton beams are generated and accelerated through the injector chain (LINAC4 → Proton Synchrotron Booster → Proton Synchrotron → Super Proton Synchrotron) before injection into the LHC ring. Machine operation alternates between periods of stable beams, when experiments take data, and refills.

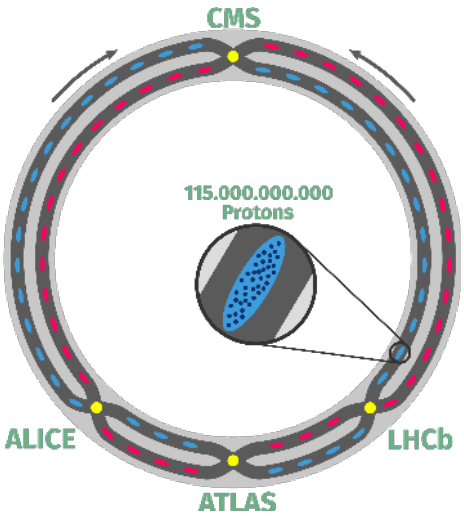

Figure 2.2: Sketch of the two beam pipes (dark grey) in which proton bunches (red and blue dots) are circulated in opposite directions. The 4 locations where the beam pipes cross, and proton bunches are collided (yellow dots) [82].

2.2 The LHCb detector in Run 3

The LHCb experiment [83] (Figure 2.3), located at interaction point 8 of the LHC, is the smallest of the four main LHC experiments and is designed as a single-arm for-

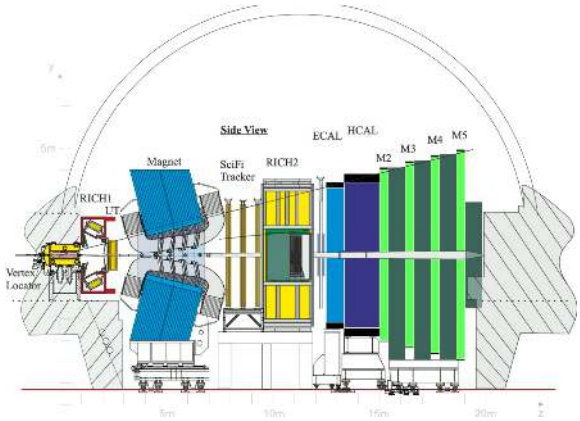

Figure 2.3: Side view of the LHCb Upgrade I detector [83].

ward spectrometer rather than a general-purpose 4π detector. Its geometry exploits the fact that the production of $b\bar{b}$ quark pairs at the LHC is concentrated at small polar angles due to gluon fusion processes, which typically boost the centre-of-mass energy of the pair in the direction of the higher momentum proton. Consequently, the detector acceptance covers particles produced between 10 mrad and 300 mrad in the bending $(x - z)$ plane, and between 10 mrad and 250 mrad in the non-bending $(y - z)$ plane.

While this asymmetric design implies a loss of about 50% of the solid-angle acceptance compared to symmetric detectors, it provides an optimised coverage for the reconstruction of b- and c-hadron decays, whose decay products are typically produced with high momentum at small polar angles. The coordinate system used at LHCb is right-handed, with the origin at the nominal interaction point inside the Vertex Locator (VELO): the z-axis runs along the beam pipe into the detector (downstream), the y-axis points vertically upwards towards the surface, and the x-axis points outward from the accelerator ring. The LHCb detector consists of several sub-detectors, which can be broadly divided into tracking systems and particle identification systems, each employing different technologies to ensure precise reconstruction and identification of the particles produced in proton-proton collisions.

2.2.1 Tracking System

The LHCb tracking system is designed to reconstruct the trajectories of charged particles and to determine their momentum from the bending caused by the dipole magnet. It is composed of three complementary sub-detectors: the VErtex LOcator (VELO), the Upstream Tracker (UT), and the Scintillating Fibre (SciFi) tracker. The VELO, located closest to the interaction point, provides precise measurements

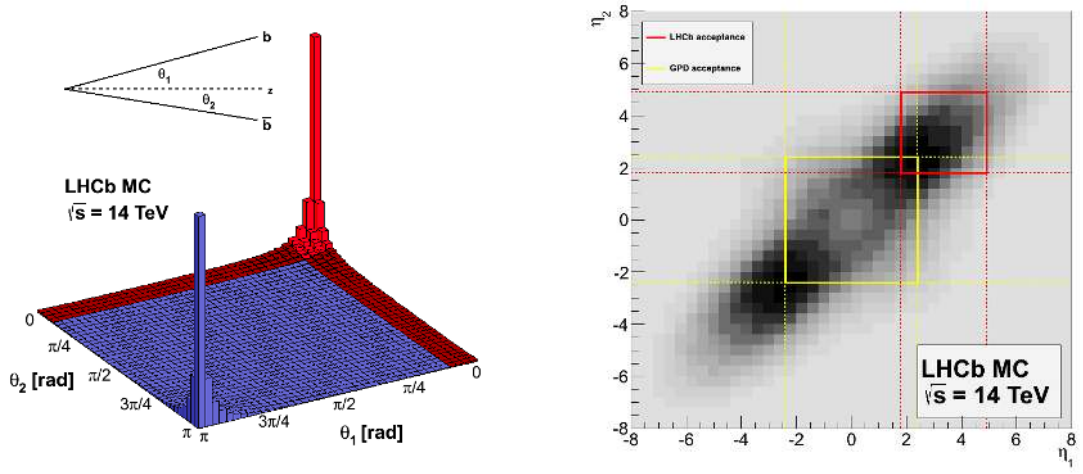

Figure 2.4: (Left) Distributions of $b\bar{b}$ production angles at the LHCb experiment obtained via Monte Carlo simulation. (Right) $b\bar{b}$ production angles in terms of pseudorapidity for the LHCb (red) and general-purpose detectors (yellow). From [84].

of particle vertices, enabling accurate reconstruction of primary and secondary decay vertices. The UT is placed immediately upstream of the magnet and extends the tracking capabilities, providing additional points to improve the resolution of the momentum measurement. Finally, the SciFi tracker, positioned downstream of the magnet, consists of scintillating fibres that allow high-resolution tracking over a large area. Since the tracking detectors are positioned outside the magnetic field region, charged particles are reconstructed as straight line segments both upstream (VELO and UT) and downstream (SciFi). The particle momentum is then determined by measuring the change in slope between the upstream and downstream tracks, combined with the known value of the magnetic field. An overview of the different track types used in LHCb reconstruction is shown in Figure 2.5.

2.2.1.1 The Vertex Locator (VELO)

The VELO [85] is a silicon vertex detector placed close to the LHC interaction point. Its primary function is to determine the position of primary vertices with very high precision, thereby enabling the reconstruction of secondary vertices from particle decays. The detector is composed of two movable halves arranged symmetrically around the beam axis, each shielded by a sequence of thin aluminium radio-frequency (RF) foils, as illustrated in Figure 2.6. During stable beam conditions, the two halves are positioned only 4.9–5.6 mm from the proton beams, allowing optimal

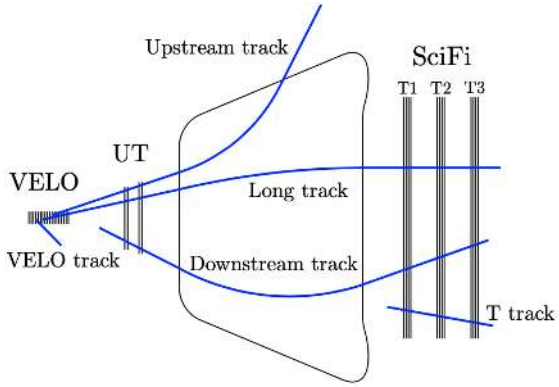

Figure 2.5: Different track types in the LHCb reconstruction. VELO and SciFi hits are required to reconstruct long tracks.

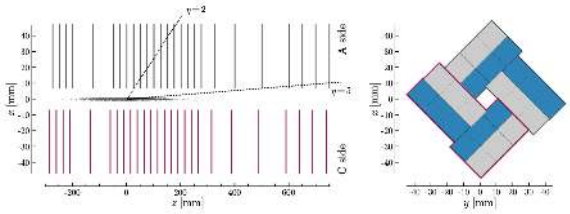

Figure 2.6: (Left) Schematic view of the 52 VELO 's modules along the z axis. (Right) Two modules with the nominal layout of the sensors around the z axis in the closed configuration are shown with half of the ASICs facing upstream (grey) and the other half facing downstream (blue).

resolution. To protect the sensitive sensors during injection or ramp-up phases, the halves can be retracted horizontally by about 3 cm, creating an "open" configuration. When closed, a small overlap between the two halves ensures precise alignment. Owing to its location directly around the interaction point, the VELO serves as the reference system for the alignment of all other LHCb sub-detectors. Its excellent spatial resolution makes it capable of reconstructing vertices even in high pile-up environments, thereby playing a crucial role in track separation and association.

During the LHC year-end technical stop in January 2023, an incident occurred in which one of the RF foils was damaged during an emergency test. As a consequence, for the 2023 data-taking period, the VELO could not be fully closed for safety reasons. This restriction forced the detector to operate in a half-open configuration, significantly reducing the acceptance for particles produced at high pseudo-rapidity and thus limiting the quality of the recorded dataset. The issue was subsequently resolved, allowing the VELO to operate normally for the 2024 data-taking period.

2.2.1.2 The Upstream Tracker (UT)

Located downstream of the VELO, right after the RICH1, and directly upstream of the LHCb dipole magnet, the Upstream Tracker (UT) [86] is the second element of the tracking system. It is composed of four layers of high-granularity silicon micro-strip detectors (Figure 2.7), designed to refine the momentum measurement of charged particles and to bridge the tracking information between the VELO and the SciFi tracker. The sensors are arranged in an x–u–v–x configuration: the first and last layers measure the x coordinate of traversing particles, while the two central layers are tilted by $\pm 5^\circ$ with respect to the vertical axis, providing information on the y coordinate. This stereo geometry enables three-dimensional hit reconstruction.

The micro-strip sensors vary in length and pitch depending on their radial distance from the beam line, in order to accommodate the decreasing particle flux. Resolutions of about $27\,\mu\text{m}$ are achieved in the central regions, while the outer sensors provide resolutions of approximately $55\,\mu\text{m}$. By measuring the deflection of tracks in the bending (x–z) plane, the UT significantly improves the precision of momentum estimation and enhances the overall track reconstruction when combined with the VELO and SciFi information.

An additional function of the UT is the reconstruction of so-called *upstream tracks*, corresponding to low-momentum particles that are deflected out of the spectrometer acceptance by the magnetic field before reaching the SciFi tracker. This ensures that also soft particles, which would otherwise be lost, can be reconstructed.

The installation of the UT experienced delays during the LHCb Upgrade I programme. The detector was finally completed during the year-end technical shutdown of 2023 and entered operation in April 2024. Consequently, data collected before this period were recorded without UT information, while datasets taken afterwards benefit from the enhanced tracking performance it provides.

2.2.1.3 The dipole magnet

A warm dipole magnet with integrated bending power $\int B\,dl \simeq 4$ Tm provides the momentum kick mainly in the horizontal (x–z) plane, with the magnetic field oriented along y. The bending angle α relates to the momentum p through

$$p \simeq \frac{0.3}{\alpha} \int B\,dl, \tag{2.1}$$

with p in GeV/c, $\int B\,dl$ in Tm, and α in rad. The radius of curvature is defined as $R = l/\alpha$. The polarity is regularly reversed (*MagUp*/*MagDown*) to minimise detector-induced charge asymmetries.

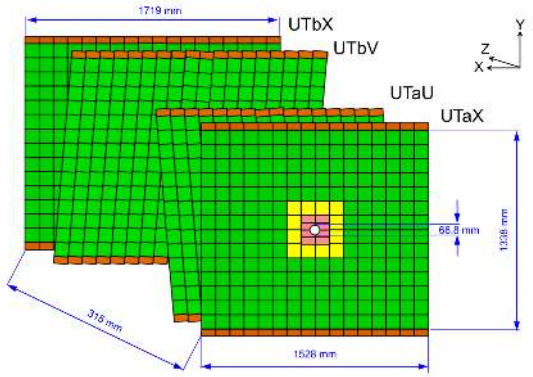

Figure 2.7: Sketch of the four UT silicon planes. Pink sensors in the centre have a pitch of 93.5 µm at a length of roughly 5 cm, yellow sensors have the same pitch, but twice the length. Green sensors have a pitch of 187.5 µm and are also twice as long as the sensors in the centre.

2.2.1.4 The Scintillating Fibre Tracker (SciFi)

The Scintillating Fibre tracker (SciFi) [86] is positioned directly downstream of the LHCb dipole magnet and represents the final element of the tracking system. Its role is to measure the trajectories of charged particles after they have been bent by the magnetic field, thereby enabling precise momentum determination when combined with the upstream measurements from the VELO and UT. By extrapolating SciFi tracks back towards the VELO, complete track reconstruction is possible for most particles that reach the SciFi before being absorbed or deflected out of the spectrometer acceptance.

The detector is organised into three tracking stations, labelled T1, T2, and T3, each consisting of four layers of scintillating fibre mats. The layers follow an x–u–v–x geometry similar to the UT: the first and last layers provide x measurements, while the two inner layers are tilted by $\pm 5^\circ$ to also extract y coordinate information. Altogether, the SciFi is composed of twelve layers. The final station contains twelve modules per layer, whereas in the first two stations, the number of modules per layer was reduced to eight due to cost constraints, giving a total of 112 modules across the full detector. A schematic view of the SciFi location, placed between the magnet and the RICH detector, is shown in Figure 2.9.

The performance of the SciFi is characterised by a single-hit detection efficiency above 95% and a spatial resolution better than 100 µm in the bending plane. Thanks to its design, the momentum of charged particles can be reconstructed with a relative precision better than 1% for momenta up to 200 GeV/c. This high granularity and resolution make the SciFi an essential component for the LHCb physics

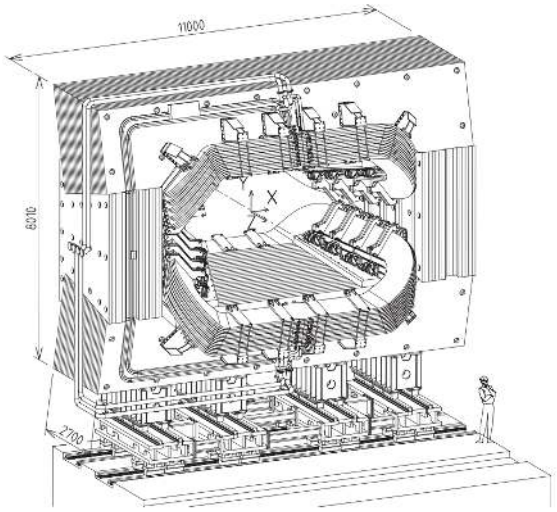

Figure 2.8: The LHCb magnet [87].

programme, especially in analyses requiring accurate momentum determination of charged hadrons.

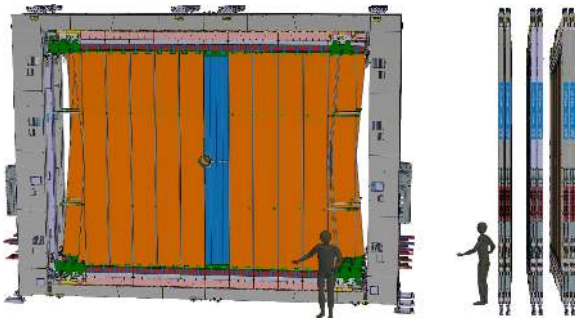

Figure 2.9: Schematic of four SciFi layers making up a station behind each other (left) and the three stations, T1, T2 and T3, behind each other (right), both in comparison to the size of an average human adult.

2.2.1.5 Track reconstruction

Outside the magnet, trajectories are locally straight; the momentum is inferred from the change of slope across the field. The LHCb reconstruction software defines five standard track categories, classified according to the sub-detectors contributing to their reconstruction. The main track types (Figure 2.5) are:

- *VELO tracks*: reconstructed from 3D hits in the VELO, requiring signals in both the r and ϕ sensors. They are not correlated with hits in other tracking stations and are mainly employed for the reconstruction of primary vertices. A simplified Kalman filter is applied, accounting for multiple scattering and tuned noise parameters.
- *Upstream tracks*: built with the VeloUT algorithm, starting from VELO tracks extrapolated linearly to a UT reference plane. Hits within a given tolerance of the predicted trajectory are collected and combined into triplets or quadruplets. A least-squares fit merges the VELO track with these hits; if the fit quality is satisfactory, at most one Upstream track is retained per VELO candidate. These tracks are created by low-momentum particles that are strongly deflected by the magnetic field and cannot reach the T-stations. They are particularly useful in the reconstruction for the RICH1 detector, even though they are not widely used in most physics analyses.
- *Downstream tracks*: reconstructed by extending SciFi seed tracks upstream towards the UT. A parametric model based on the hybrid seeding momentum estimate predicts the expected hit positions in the UT, to which nearby clusters are attached. A Kalman filter removes incompatible measurements and refines the track parameters. Downstream tracks are typically produced by long-lived particles (e.g. K^0_S mesons or Λ baryons) decaying away from the interaction point. Since they do not leave hits in the VELO, the momentum resolution is worse than that of Long tracks, but the longer lever arm still allows a useful determination.
- *T tracks*: reconstructed exclusively from hits in the SciFi layers. These particles often originate from material interactions or decays of very long-lived particles, and are usually not employed in physics analyses.
- *Long tracks*: the most important category for physics analyses, combining information from VELO, UT, and SciFi stations. Their reconstruction relies on two complementary algorithms:
  - The *Forward Tracking algorithm* [88] starts from VELO seeds, extrapolated as straight lines (the magnetic field being negligible in the VELO). Candidate hits in the TT are associated, and a rough momentum estimate is used to predict hit positions in the T-stations, taking into account the bending due to the magnetic field.
  - The *Track Matching algorithm* [89] reconstructs seeds independently in the VELO and T-stations, then extrapolates them to the magnet plane. A

compatibility criterion based on their distance in x and y at the bending plane is used to merge them.

After the initial combination, a Kalman filter [90] refines the track parameters, rejects outliers, and provides covariance estimates. To avoid duplication between the two methods, a *clone killer* [91] algorithm removes multiple reconstructions of the same trajectory. Long tracks achieve the best momentum resolution and are therefore the reference track type in most physics analyses.

Tracks are then extrapolated to the PID systems (muon stations, calorimeters, RICH detectors), where they are assigned global PID likelihoods.

In addition to the standard categories, one may also encounter so-called *ghost tracks*. These are spurious tracks reconstructed from noise, overlapping signals, or accidental scattering, and do not correspond to a real particle. Although not part of the official LHCb classification, the term *ghost track* is widely used in tracking studies. To suppress them, LHCb employs a dedicated neural network classifier, which assigns each reconstructed track a probability of being a ghost (`GhostProb`) [92]. Tracks with a high ghost probability are typically discarded before analysis.

When analysing simulated events, a dedicated tool called `MCTruth` provides the true origin of reconstructed tracks. This allows validation of the reconstruction algorithms and identification of which track categories (primarily Long and Downstream) should be retained for physics analyses.

2.2.2 Particle identification detectors

The classification of detected particles according to their mass, known as Particle Identification (PID), represents a fundamental aspect of flavour physics analyses. The LHCb detector employs a sophisticated three-component system to achieve reliable particle identification: the Ring Imaging Cherenkov (RICH) detectors, calorimetric systems, and muon chambers. The outputs of these subsystems are combined through likelihood-based algorithms that maximise identification performance while reducing background contamination. Calibration studies demonstrate that identification efficiencies typically range from 90 to 100% depending on the particle species under consideration.

In this section, particular emphasis will be placed on the RICH detector system, as it constitutes the primary focus of my research contributions. The detailed concepts presented here will serve as the foundation for the work described in Chapters 8–10, which document my specific contributions to RICH detector studies and applications.

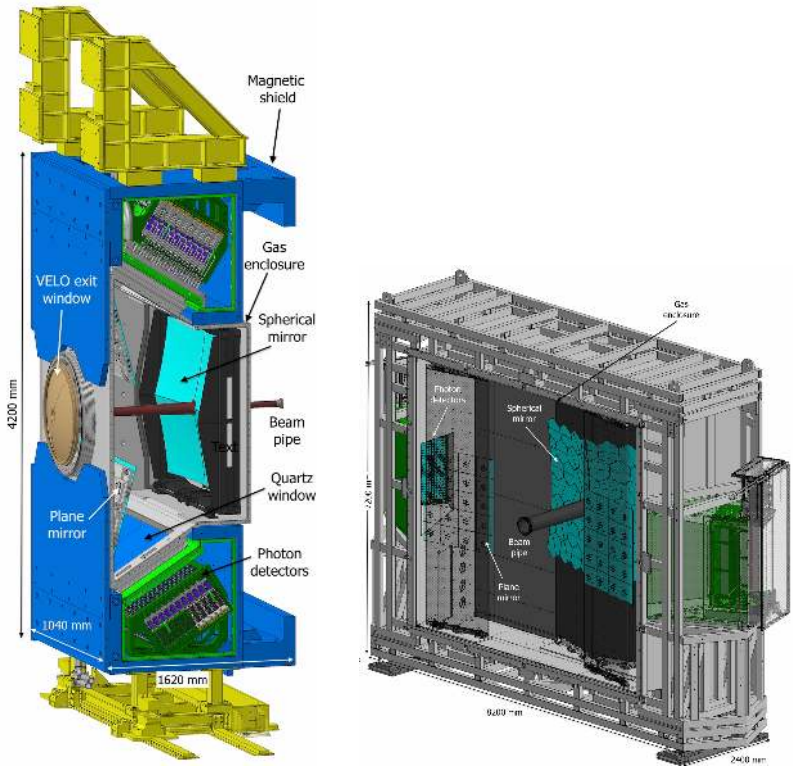

(a) RICH1 (b) RICH2

Figure 2.10: Schematic view of the upgraded (left) RICH1 and (right) RICH2 detectors [83].

2.2.2.1 The Ring Imaging Cherenkov Detectors

The Ring Imaging Cherenkov (RICH) detector system (Figure 2.10) serves as a fundamental component for particle identification [93] within the LHCb framework. These detectors are specifically designed to distinguish charged hadrons (π, K, p) across a momentum spectrum spanning from 2.6 to 100 GeV, while also providing identification capabilities for charged leptons (e, μ), especially in the low-momentum regime. This hadron identification capability proves indispensable for most LHCb physics studies, enabling the separation of final states that would otherwise appear topologically identical. Furthermore, the system substantially suppresses combinatorial backgrounds in hadronic decay modes, where the absence of PID constraints would render the background levels prohibitively high.

The operational foundation of the RICH detectors is based on Cherenkov radiation: when a charged particle moves through a dielectric material with refractive

index n at velocity $\beta > 1/n$, it produces Cherenkov photons emitted at a characteristic angle θ_c, described by

$$\cos(\theta_c) = \frac{1}{\beta n}. \tag{2.2}$$

The particle's mass m can be extracted by combining the momentum p measured by the tracking detectors with the velocity v derived from the Cherenkov angle θ_c. The threshold velocity for Cherenkov photon emission at $\theta_c = 0°$ is expressed as

$$\beta_{th} = \frac{1}{n}, \tag{2.3}$$

whereas the maximum achievable Cherenkov angle corresponds to the limit $\beta \to 1$:

$$(\theta_c)_{max} = \arccos\left(\frac{1}{n}\right). \tag{2.4}$$

Particles reaching this saturation angle provide a means to calibrate the Cherenkov angle resolution. The spectral photon production rate per unit path length is governed by

$$\frac{d^2N_\gamma}{dxd\lambda} = \frac{2\pi z^2\alpha}{\lambda^2}\left(1 - \frac{1}{\beta^2 n^2}\right), \tag{2.5}$$

where z represents the particle charge and α denotes the fine structure constant.

The detector architecture comprises two complementary units, RICH1 and RICH2, each optimised for distinct momentum intervals. RICH1 is positioned before the dipole magnet, following the VELO detector, and utilises C_4F_{10} gas ($n = 1.0014$) as the radiator medium, providing coverage for momenta between 2 and 50 GeV/c. RICH2 is situated after the magnet, preceding the calorimeter system, and employs CF_4 gas ($n = 1.0005$), extending the momentum range from 15 to 100 GeV/c. While the fundamental design philosophy and geometric arrangement have been retained from the previous operational periods (Run 1–2 [94, 95]), significant upgrades were implemented to enable operation at enhanced luminosity levels while preserving the identification performance achieved in earlier runs.

To support the required 40 MHz data acquisition rate, the photon detection systems in both RICH detectors underwent complete reconstruction. The original hybrid photon detectors (HPD) incorporated front-end electronics constrained to 1 MHz operation, which proved inadequate for the upgraded luminosity conditions ($L = 2 \times 10^{33} cm^{-2} s^{-1}$, $\sim 5\times$ Run 2 luminosity). In RICH1, the spherical mirror radius was extended from 2.7 m to 3.7 m, effectively displacing the focal plane further downstream, increasing the Cherenkov ring dimensions, and consequently reducing the peak occupancy levels [96]. Additionally, the photodetectors were relocated deeper within the magnetic shielding structure to minimise background interference (Figure 2.11).

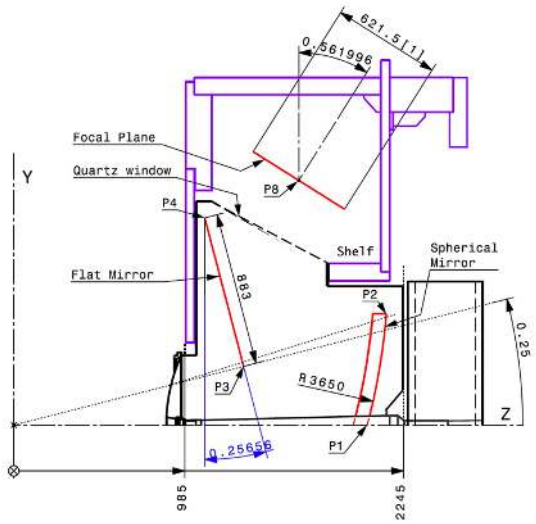

Figure 2.11: The optical geometries the upgraded RICH1. From [83].

The HPDs were substituted with multi-anode photomultiplier tubes (MaPMTs) integrated with redesigned front-end electronics. These MaPMTs incorporate an 8×8 anode configuration. For RICH1 and the central regions of RICH2, 1-inch MaPMTs featuring $2.88 \times 2.88\,\mathrm{mm}^2$ pixel dimensions were deployed in areas experiencing high occupancy rates. The peripheral regions of RICH2 utilise 2-inch devices with $6 \times 6\,\mathrm{mm}^2$ pixels, effectively reducing both the total number of detector units and readout channels while maintaining optimal performance characteristics (Figure 2.12).

The front-end electronics incorporate CLARO (Figure 2.13) application-specific integrated circuits (ASICs), each containing 8 channels with analogue signal conditioning and binary discrimination capabilities optimised for single-photon detection. The system provides signal amplification, digitisation, and channel-by-channel threshold adjustment [100], with data transmission handled through FPGA technology synchronised to the LHC clock system and forwarded to the high-level trigger via GigaBit Transceivers (GBTs) [101].

The detector planes utilise a hierarchical modular architecture built from multi-anode photomultiplier tubes (MaPMTs) as the fundamental detection units. These 64-pixel scintillation detectors are available in two configurations: R-type (1×1 inch^2) and H-type (2×2 inch^2) (Figure 2.14). The photodetector and CLARO chip assemblies are organised into elementary cells (ECs), where EC-R configurations combine four R-type MaPMTs in a 2×2 arrangement with associated front-end boards, while EC-H configurations utilise single H-type MaPMTs as elementary units. Each EC-R unit interfaces with four MaPMTs (totalling 256 pixels), incorporates resistive

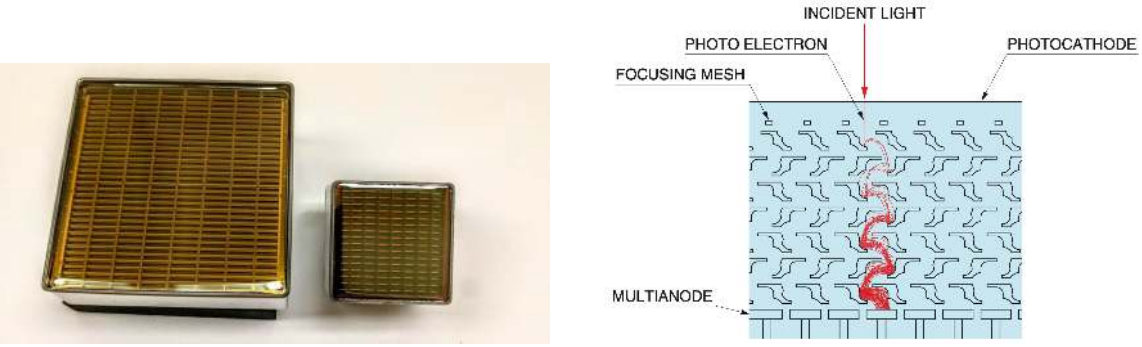

Figure 2.12: (Left) The MaPMTs selected for the upgraded RICH detectors with the 2-inch model (on the left) and the 1-inch model (on the right). (Right) Scheme of the internal structure of the MaPMT. From [83, 97].

voltage dividers for dynode biasing, and includes magnetic shielding that achieves a 20-fold reduction in stray magnetic fields.

Four elementary cells arranged in a 4×1 configuration constitute a Photo Detector Module (PDM), which connects to the LHCb data acquisition system through a Photo Detector Module Digital Board (PDMDB) (Figure 2.15). The PDMDB handles signal digitisation, integration with the Experiment Control System, and provides FPGA-based timing control and data formatting functions.

The front-end electronics mounted behind the MaPMTs generate digital outputs for trigger processing. Anode signals are routed to Front-End Boards (FEBs) housing the CLARO ASICs, with each CLARO functioning as an 8-channel single-photon counting circuit that produces digital outputs when channel signals exceed programmable thresholds. Four FEBs are installed on each EC-R, while two are mounted on each EC-H. The PDMDB aggregates these digital signals and prepares them for transmission, with its FPGA applying hardware time gating to the CLARO output for noise mitigation. The system architecture employs paired PDMDB-R units to manage four EC-R assemblies, while individual PDMDB-H units control four EC-H assemblies. The complete installation comprises 472 EC-R units in RICH1, with RICH2 containing 192 EC-R units in the central region and 384 EC-H units in the outer areas. The RICH2 detector plane features a vertical segmentation into thirds, with the middle section populated by EC-Rs and the upper and lower sections utilising EC-Hs.

Effective particle identification performance requires minimisation of noise contributions in MaPMT channels. Several noise sources can compromise detection quality: charge sharing and crosstalk phenomena occur when Cherenkov photons deposited in one channel induce spurious hits in neighbouring channels, either through pho-

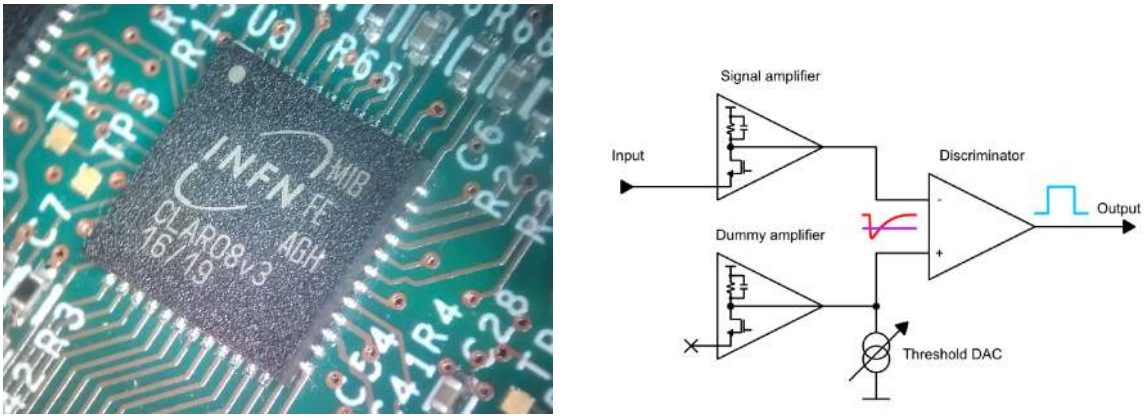

Figure 2.13: ((Left) CLARO ASIC with its packaging. (Right) Block schematic of a CLARO channel. The purpose of the dummy amplifier is to give each channel a differential structure, improving the power supply rejection ratio and allowing DC-coupled input to the discriminator. From [98, 99].

toelectron deviation causing multiplication in adjacent PMTs or through capacitive coupling between PMT anodes. Dark counts arise from thermionic emission at the photocathode, exhibiting exponential temperature dependence.

Temporal Gating for Background Suppression The nature of Cherenkov photon emission combined with the focusing properties of the mirror optical system results in the quasi-simultaneous arrival of photons from particle tracks at the detection plane within the RICH detectors. This temporal characteristic enables the implementation of a timing window at the front-end electronics level, effectively filtering unwanted out-of-time background events while preserving genuine photon signals within a defined temporal interval.

Simulation studies of RICH1 demonstrate that photon hit time distributions exhibit a signal peak with approximately 2 ns width, primarily attributed to the spatial distribution of primary interactions throughout the LHCb acceptance. This natural time spread establishes the minimum required width for the front-end timing gate. However, practical considerations, including CLARO time walk effects, inter-channel timing variations, MaPMT transit time dispersion, and the digital sampling frequency of the front-end electronics, necessitate a timing gate width of 3.125 ns, with the possibility of extension to 6.250 ns when required. This temporal filtering approach proves highly effective not only in rejecting background from beam-related interactions but also in suppressing detector noise sources, including MaPMT crosstalk phenomena and afterpulsing effects. The resulting background reduction

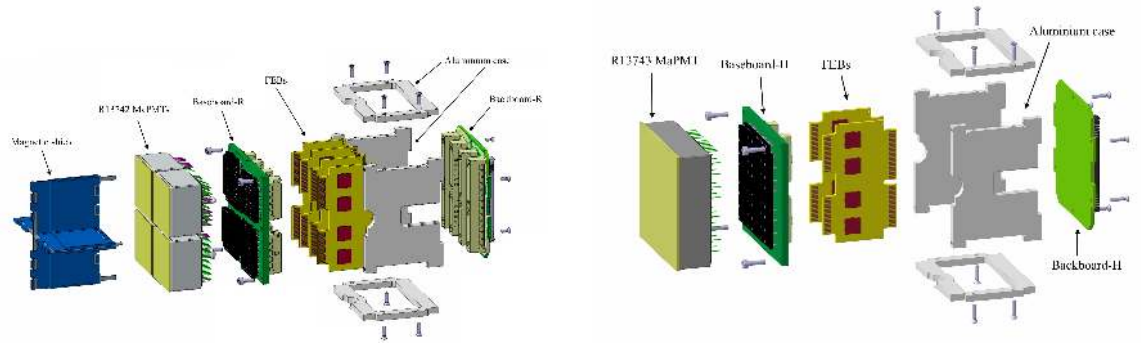

Figure 2.14: Schematic view of the (left) R- and (right) H-type elementary cell. From [83, 97].

substantially improves the performance of particle identification algorithms through enhanced RICH pattern recognition capabilities.

The timing gate generation and temporal alignment procedures are implemented within the FPGA firmware of the Photo Detector Module Digital Board (PDMDB). The time-gating functionality exploits the deserialiser components integrated into each input-output logic block of the FPGA, operating at Gbps transmission rates. The deserialiser captures CLARO output signals using both rising and falling edges of the 160 MHz clock, transferring the sampled data at 320 Mbit/s into an 8-bit shift register configuration. This data byte is compared with signal templates stored in lookup tables, which use memory resources with minimal logic overhead in the FPGA's fabric. If the byte matches one of the programmed patterns, a hit is registered at the next 40 MHz clock edge. The lookup table architecture can be reconfigured for different acquisition scenarios, allowing adjustments to timing gate widths, edge detection modes, and basic spillover checks. The timing gate (Figure 2.16) operates at fixed latency relative to the LHCb clock reference. The FPGA receives both the 40 MHz system clock and 160 MHz sampling clock from the GBT link, with clock phase relationships adjustable across the full 25 ns range in precise increments of 49 ps. This fine adjustment capability allows optimal positioning of the timing gate relative to the signal arrival time characteristics of the RICH detector system.

Particle Identification Methodology in RICH Detectors The identification of short-lived particles relies fundamentally on the characterisation of their longer-lived decay products, with the RICH detectors providing crucial particle identification capabilities for charged hadrons. The particle trajectory and momentum determination utilise measurements from the LHCb VELO, UT, and SciFi tracking systems. By combining this kinematic information with Cherenkov angle measure-

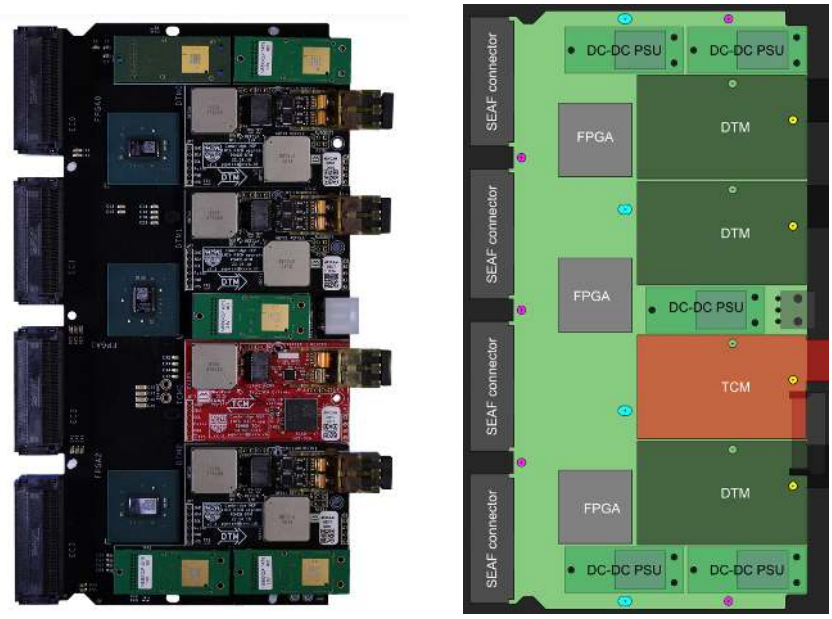

Figure 2.15: (Left) Picture and (right) schematic view of the PDMDB-R board. The PDMDB-H differs by having one less FPGA and DTM compared to the PDMDB-R [83].

ments, particle mass identification becomes possible.

The relationship between the Cherenkov angle and particle properties can be expressed as:

$$\theta_c = \arccos\left(\frac{1}{\eta(\omega)}\sqrt{1+\frac{m^2c^2}{p^2}}\right) \tag{2.6}$$

where m represents the particle mass and p its momentum. Plotting Cherenkov angle versus momentum for various stable particles reveals distinct characteristic curves that enable species discrimination. The Cherenkov angle for electrons approaches $\theta_{\max}$, making accurate measurement challenging; consequently, electron and muon identification rely primarily on the electromagnetic calorimeter (ECAL) and muon detection systems, respectively.

Given the high particle multiplicity typical of LHCb events, maximum likelihood estimation algorithms are employed to determine the Cherenkov angles associated with individual particle tracks. The likelihood function for a given set of mass hypotheses $\mathcal{L}(h)$ is computed as the product over all hit pixels of the Poisson probability

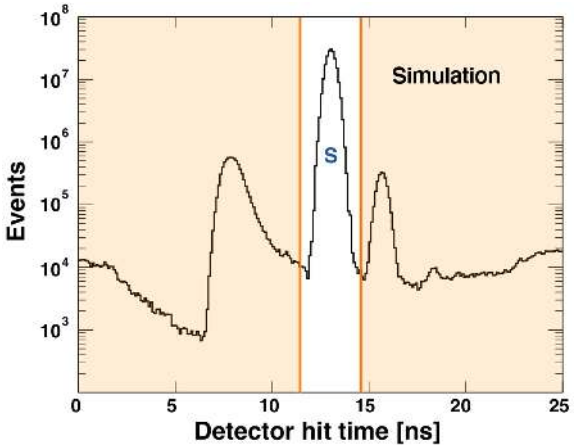

Figure 2.16: RICH1 simulated photon detector hit time distribution showing the signal peak (S) and a possible time gate in the front-end electronics. From [97].

for detecting a hit in pixel i given the expected signal $\nu_i(h)$:

$$\mathcal{L}(h) = \prod_{i=1}^{M_{\text{tot}}} \frac{e^{-\nu_i(h)}\nu_i(h)^{n_i}}{n_i!} \tag{2.7}$$

$$\nu_i(h) = \sum_{j=1}^{N} a_{ij}(h_j) \tag{2.8}$$

where M_{tot} represents the total number of hit pixels, n_i is the observed signal in pixel i, N denotes the total number of tracks, and $a_{ij}(h_j)$ represents the expected number of photoelectrons in pixel i from track j. The delta log-likelihood (DLL) serves as the metric for comparing particle identification performance across different configurations:

$$\text{DLL}_{h\bar{h}} = \log(\mathcal{L}(h)) - \log(\mathcal{L}(\bar{h})) \tag{2.9}$$

2.2.2.2 Electromagnetic and Hadronic Calorimeters

The LHCb calorimeter system is responsible for the identification and energy measurement of electrons, positrons, photons, neutral mesons, and hadrons. It consists of two main sub-detectors: the electromagnetic calorimeter (ECAL) and the hadronic calorimeter (HCAL).

The ECAL plays a crucial role in the reconstruction of photons and neutral mesons such as π^0, which account for roughly one third of heavy-flavour decays at LHCb. Its design provides a balance between high-energy resolution and fast time response,

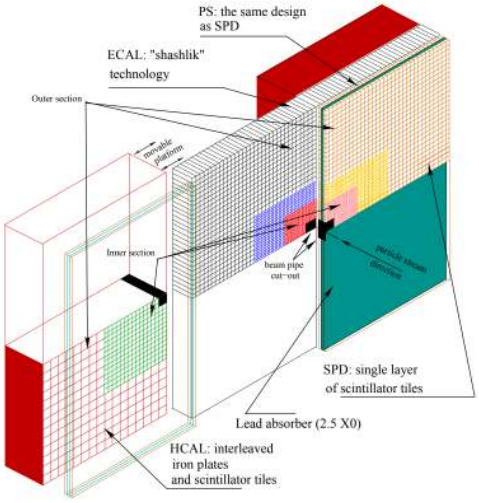

Figure 2.17: The layout of the calorimeter system [102] in the LHCb experiment up to Run 2. The hadronic calorimeter (HCAL) is located at the back, followed by the electromagnetic calorimeter (ECAL) and the preshower (PS) and the scintillating pad detector (SPD) in the front. Both the PS and the SPD were removed for Run 3 of data taking.

enabling precise reconstruction of photon energy and position, as well as the identification of electrons and positrons. The energy resolution of the ECAL is parametrised as:

$$\frac{\sigma_E}{E} = \frac{(9.0 \pm 0.5)\%}{\sqrt{E}} \oplus (0.8 \pm 0.2)\% \oplus \frac{0.003}{E \sin\theta}, \tag{2.10}$$

where E is the particle energy in GeV and θ is the polar angle of the ECAL cell. The first term represents the stochastic component, the second accounts for calibration imperfections and energy leakage, while the last corresponds to the contribution from electronic noise.

The HCAL is optimised for the measurement of hadrons and provides coarser energy resolution, given by:

$$\frac{\sigma_E}{E} = \frac{(67 \pm 5)\%}{\sqrt{E}} \oplus (9 \pm 2)\%. \tag{2.11}$$

Although less precise than the ECAL, it plays an essential role in particle identification (PID), energy measurements of hadrons, and triggering.

Both calorimeters are located downstream of the magnet and tracking stations, perpendicular to the beamline. They are segmented into square cells of different sizes

depending on occupancy and required resolution: the innermost region, closest to the beam pipe, has the highest granularity, while the outer regions use larger cells. The ECAL additionally features an intermediate granularity region. Structurally, both detectors consist of alternating layers of absorber material (lead in ECAL, iron in HCAL) and scintillators. Charged particles crossing the absorbers produce showers, which generate light in the scintillator tiles. This light is collected by wavelength-shifting fibres and read out by photomultiplier tubes (PMTs).

For Run 3, the calorimeter readout electronics were upgraded to allow for a 40 MHz streaming readout, to cope with higher instantaneous luminosities and the fully software-based trigger. The mechanical layout of the ECAL and HCAL remains unchanged: they are divided into two halves (A- and C-sides), which can be moved horizontally for installation and maintenance.

2.2.2.3 The Muon Detection System

A specialised detection system is essential for muon identification, as these particles possess the unique capability to penetrate calorimetric systems and reach the outermost regions of the LHCb detector. Muons, being elementary particles similar to electrons but approximately 200 times more massive, exhibit minimal energy loss characteristics that enable them to traverse the entire LHCb detector assembly due to their reduced electromagnetic and hadronic interaction cross-sections.

The muon detection system for Run 3 operations comprises four stations designated M2 through M5, strategically positioned at the detector's periphery downstream of the calorimeter systems and separated by iron absorber plates. These stations are arranged following a projective geometry with rectangular configurations. The Run 3 configuration represents a modification from the previous Run 1–2 setup, which included an additional station M1 located upstream of the calorimeters.

Each muon station utilises Multi-Wire Proportional Chambers (MWPCs) as the primary detection technology for measuring the positional information of charged particles. The detector employs 1368 MWPCs distributed across the four stations, with each chamber containing four detection layers, termed gaps, comprising anode wires positioned between paired cathode planes. The chambers are filled with ionising gas that generates electrical signals near high-voltage wires when traversed by charged particles, providing efficient and rapid muon detection capabilities while maintaining performance under intense particle flux conditions.

The spatial organisation of each station features four distinct regions (R1, R2, R3, R4) with progressively increasing dimensions as distance from the beam axis increases (Figure 2.18). This regional segmentation ensures uniform distribution of particle flux and channel occupancy across the detector surface. The logical pad segmentation of the cathode planes exhibits asymmetric granularity, with finer segmentation in

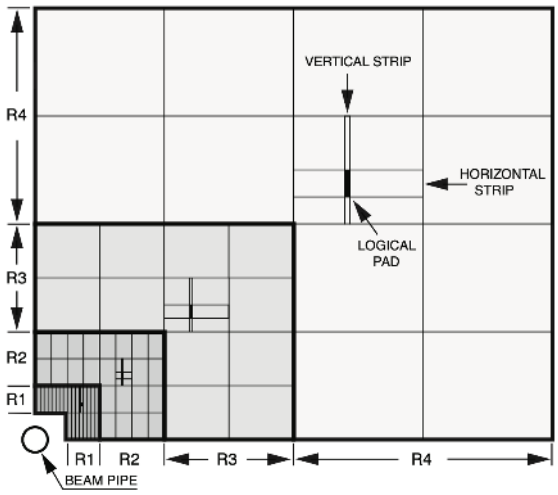

Figure 2.18: Front view of one quadrant of M2 showing the four regions. From [103].

the horizontal direction compared to the vertical direction, reflecting the horizontal bending of muon trajectories in the magnetic field environment. Pad dimensions increase for outer detector regions where multiple Coulomb scattering effects become more pronounced, as charged particles deviate from straight-line trajectories through elastic collisions with atomic nuclei.

The iron absorber plates, functioning as muon filters with 80 cm thickness, are interleaved between stations to suppress low-energy particles and enhance muon selection purity. The minimum momentum requirement for muons to traverse all four stations is approximately 10 GeV/c, establishing the detection threshold for the system.

The front-end electronics incorporate an amplifier-shaper-discriminator stage implemented through dedicated ASICs, coupled with digital processing sections that enable temporal signal alignment and logical combination of individual readout channels into consolidated logical channels. These front-end components, designed for radiation tolerance up to 100kGy, remain unchanged from previous configurations as they meet the requirements for upgraded operational conditions. However, the readout electronics underwent complete restructuring to accommodate the updated LHCb readout architecture, representing the primary upgrade for the muon system. The monitoring and control electronics were similarly redesigned to support the new 40 MHz readout rate and integrate with the experiment's updated data acquisition and control systems.

2.2.3 LHCb Data Processing Framework

The LHCb detector employs a synchronous data acquisition architecture in which all front-end electronics continuously transmit information at each bunch crossing event. The data acquisition infrastructure consists of a distributed farm of 162 event builders (EB) servers, each hosting back-end receiver FPGA boards called TELL40 and graphics processing units (GPUs) responsible for executing the first-level High-Level Trigger (HLT1) algorithms [83, 104].

Each TELL40 board receives data from the various subdetectors and forms Multi-Fragment Packets (MFPs), which are consolidated by the EB servers into Multi-Event Packets (MEPs) containing around 1000 events. The MEPs are then internally transferred to the GPUs for initial event reconstruction and selection. This internal transfer eliminates external network overhead, significantly accelerating processing.

Following initial processing by the EB servers and HLT1 stage, the data stream proceeds to the second-level High-Level Trigger (HLT2) for additional analysis on standard CPU architectures before final archival storage. Detector readout signals are conveyed through optical fibre networks to a centralised computing facility hosting the event builder infrastructure.

The LHCb software framework collects electrical signals from the various subdetectors, reconstructs tracks and vertices, identifies decays, and presorts events. All events not identified as containing decays of interest are permanently discarded to save storage space. Continuous real-time detector alignment and calibration are crucial, as any inefficiency or miscalibration directly impacts the available dataset for physics analyses.

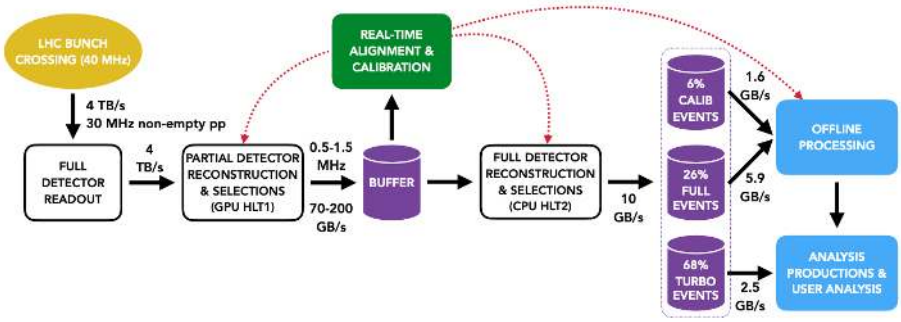

Figure 2.19: LHCb dataflow. From [105].

2.2.3.1 Trigger Architecture

During Run 3 operations, LHCb has deployed a completely software-driven trigger framework designed to handle the enormous data volumes generated by the detector system. This innovative approach utilises a fully synchronised and calibrated real-time software trigger capable of performing offline-quality event reconstruction at the LHC's native bunch crossing rate of 40 MHz.

The motivation for this design stems from LHCb's physics program, which focuses on precision studies of b- and c-hadron decays. These processes have cross-sections of several millibarns at 13.6 TeV, much higher than the nanobarn-level cross-sections of top-quark or Higgs boson production targeted by the ATLAS and CMS experiments. While ATLAS and CMS rely on a coarse hardware-based first-level trigger to select rare events, LHCb requires extremely high statistics, making it essential to operate with a pure software trigger at the full 40 MHz collision rate.

Given that events failing to satisfy any trigger selection criteria are permanently discarded from the data stream, implementing continuous real-time detector alignment and calibration becomes essential. This approach enables immediate identification of trigger-related issues and allows for prompt corrections before significant data loss occurs. Consequently, rapid, accurate, and computationally efficient track reconstruction algorithms are required, with preliminary reconstruction performed during the HLT1 phase and comprehensive reconstruction completed in the HLT2 stage. For this reason, the High-Level Trigger (HLT) consists of two sequential processing stages connected by an intermediate storage buffer.

The first stage, HLT1, performs partial event reconstruction to achieve manageable data throughput rates while maintaining high selection efficiency for physics signatures.

Event reconstruction in HLT1 is implemented through the Allen framework [106], which harnesses about 600 NVIDIA RTX A5000 GPUs. Algorithms written in C++ and CUDA exploit the independence of collision events and the parallel nature of track and vertex reconstruction. So, reconstruction uses information from tracking detectors, ECAL, and muon stations, finding primary and secondary vertices, tracking particles, and identifying muons, while minimum momentum cuts are applied to maintain throughput. Information from the RICH detector is not used at this stage. Each GPU processes multiple events simultaneously, enabled by the relatively small event size of about 100kB, achieving a rate reduction factor between 30 and 60. The HLT1 output rate is around 1 MHz.

Events passing HLT1 are temporarily stored in a disk buffer of roughly 30PB capacity, sufficient for about 80 hours of data at 1 MHz. This buffer not only prevents immediate data loss but also allows real-time detector alignment and calibration procedures to be applied before further processing. The HLT1 sequence is depicted

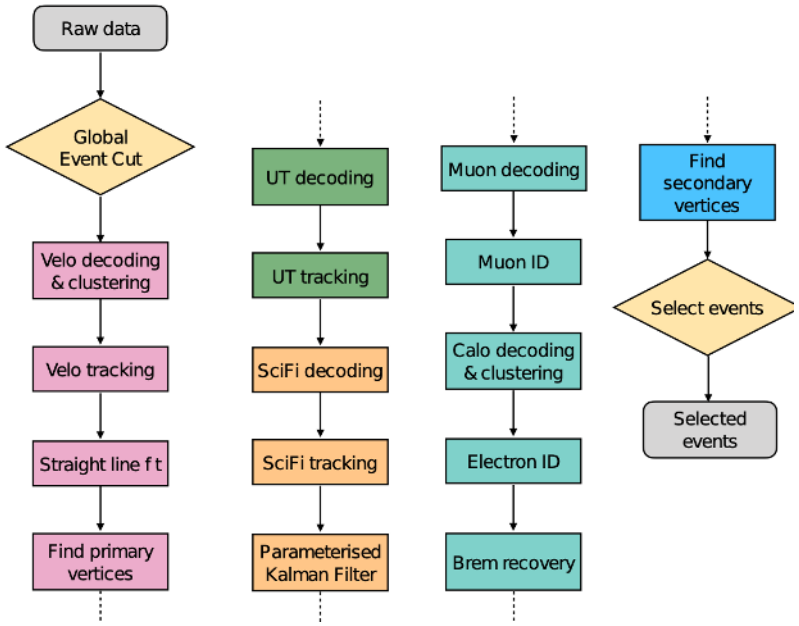

Figure 2.20: Schematic of HLT1 reconstruction flow at LHCb. From [107].

in Figure 2.20.

The second stage, HLT2, operates within the Moore framework [108] on standard CPU-based servers in the Event Filter Farm. Unlike HLT1, it functions asynchronously: event processing begins only after detector calibration and alignment procedures have confirmed satisfactory conditions. Consequently, only a small fraction of buffered data is processed immediately. Once validated, HLT2 processes events at rates matching HLT1 output to avoid buffer overflow. HLT2 performs full event reconstruction, reducing the data stream to about 10 GB/s distributed among (Figure 2.19):

- Full Events: the complete event record is stored;
- Turbo Events: only the decay of interest is preserved to save storage;
- Calib Events: retain full information for calibration and alignment studies.

2.2.3.2 Online Real-Time Alignment Procedures

Within the LHCb context, "real-time" refers to the entire chain from an inelastic collision at bunch crossing to the final recording of data in permanent storage, a

process that may span several days. A critical element of this workflow is the continuous online alignment and calibration of detector subsystems, which ensures optimal efficiency for both HLT1 selection and HLT2 reconstruction.

Alignment at LHCb is divided into time alignment and spatial alignment. Time alignment guarantees that subdetectors correctly register signals within the 25 ns bunch spacing of the LHC. Special runs with single proton bunches, separated by several microseconds, are used for calibration.

Spatial alignment ensures that the geometrical positions of subdetectors are known to high precision. The VELO detector requires frequent alignment updates, since mechanical opening and closing of the VELO halves can shift their positions by nearly a millimetre. Each time the VELO closes, its position is realigned, with quality checks performed by comparing reconstructed primary vertex positions between the two halves. Sequentially, the UT and SciFi tracking systems are aligned relative to the VELO, using track signatures from well-known decays. Alignment parameters, consisting of three translational and three rotational degrees of freedom for each detector element, are optimised iteratively by minimising the track χ^2.

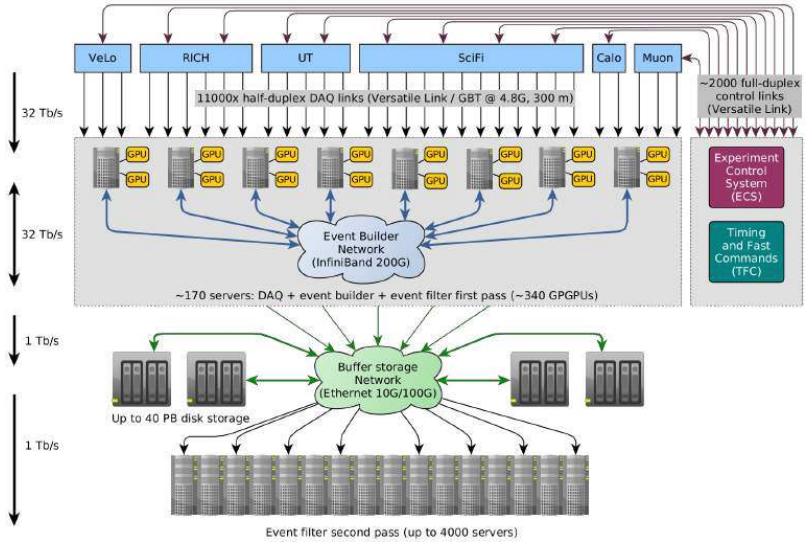

Figure 2.21: LHCb online system. From [83].

Additional subsystems also undergo dedicated calibrations. The RICH mirror alignment, determined by comparing measured and expected Cherenkov angles, is performed once per proton fill and can require several hours, though it may be applied retrospectively since RICH information is not used in HLT1. The muon detector alignment is done infrequently, as most analyses are less sensitive to its precision; nonetheless, misalignment can affect partial muon track reconstruction.

The ECAL is calibrated approximately monthly using the invariant mass of $\pi^0 \to \gamma\gamma$ decays.

The overall alignment sequence follows the order: VELO, UT and SciFi, RICH detectors, and finally the muon system, as illustrated in Figure 2.21. Throughout this process, track reconstruction efficiency plays a dual role: it depends on the quality of alignment but also serves as a sensitive diagnostic tool for evaluating and improving alignment performance.

2.2.3.3 Offline Data Processing

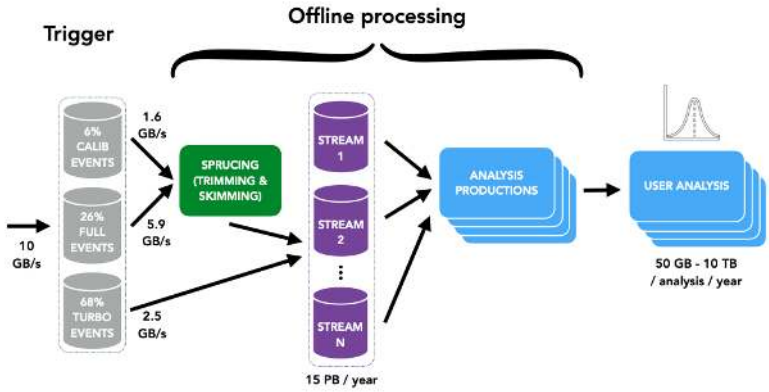

Figure 2.22: LHCb offline data flow. From [83].

The final stage before physics analysis is referred to as "sprucing" [109]. Sprucing applies selective *skimming* (further event selection) and *slimming* (reducing redundant information) to optimise datasets. Events passing HLT2 are divided between the FULL and Turbo streams: the FULL stream constitutes approximately 30% of the total output and retains the full raw data, allowing for reprocessing in yearly re-sprucing campaigns, whereas the Turbo stream comprises the remaining 70% and persists only the information related to particle signal candidates, preventing full reprocessing.

Compared to earlier processing stages, sprucing operates with relaxed timing constraints, allowing for more computationally intensive procedures. This enables detailed analyses of complex particle decays, ensuring that high-level derived quantities are readily available to analysts.

Typical events stored in the FULL stream include those selected by inclusive topological lines, such as two- or three-body decays with specific requirements on vertex quality and particle momenta. Events selected by exclusive lines, targeting precise decay topologies and final-state particles, are typically processed in the Turbo

stream. Both FULL and Turbo data are then organised into optimised physics streams, providing analysts with reduced datasets categorised by physics topics.

The sprucing procedure also processes calibration events to ensure detector monitoring and alignment needs are met. Compared to earlier stages, sprucing operates with relaxed timing constraints, permitting more computationally intensive procedures and ensuring that high-level derived quantities are readily available to analysts.

Following sprucing, the processed data are made available through centralised production systems. The Analysis Productions framework [110] is responsible for generating the final output files, managing monitoring, and archiving the data in an automated and centralised manner. Analysts then typically use the DaVinci software [111] to produce ntuples, which constitute the fundamental data format for physics analyses. The complete workflow from raw detector signals to analysis-ready data is summarised in Figure 2.22.

2.2.4 Dedicated trigger HLT1 line for $D^0 \to K^0_S h^+ h^-$

The introduction of a dedicated HLT1 line for $D^0 \to K^0_S h^+ h^-$ decays addresses one of the main systematic limitations in time-dependent Dalitz plot analyses of charm decays. The enhanced real-time processing capabilities of the LHCb Run 3 trigger architecture enable the selection of such multi-body final states already at the 30 MHz input rate of the first trigger level.

The key motivation for this new selection is the intrinsic limitation of multivariate approaches such as `TrackMVA` and `TwoTrackMVA`, widely used during Run 1 and Run 2. Although highly efficient, these algorithms correlate decay-time acceptance with the momentum distributions of the final-state particles. In $D^0 \to K^0_S h^+ h^-$ decays, this introduces phase-space dependent biases that are strongly correlated with the D^0 lifetime, leading to significant systematic uncertainties in time-dependent measurements, in particular for the determination of the y parameter. The Run 2 analysis with the bin-flip method [65] highlighted the severity of this issue: while the x parameter was measured precisely, the uncertainty on y was dominated by acceptance effects.

To overcome this limitation, the new strategy is based on well-controlled kinematic requirements that can be modelled reliably with fast or ultra-fast simulation. Monte Carlo studies of $D^0 \to K^0_S \pi^+ \pi^-$ decays under Upgrade I conditions were used to identify the most discriminating variables, including momentum, transverse momentum, impact parameters (Equation 2.12) with respect to the primary vertex, pseudo-rapidity of both D^0 and K^0_S, and the D^0 proper decay time.

$$IP = \frac{(\vec{PV} - \vec{V}) \times \vec{n}}{|\vec{n}|} \tag{2.12}$$

where $\vec{PV}$ and $\vec{V}$ are the position vectors of the primary and secondary vertex from which the track originates, respectively, and $\vec{n} = \vec{p}/|\vec{p}|$ denotes the unit momentum vector.

In particular, impact parameter requirements proved to be powerful, as tracks from displaced K^0_S decays allow for strong background rejection without significant loss of signal. Prompt production kinematics, such as the correlation between $p_T(\mathrm{D}^0)$ and the soft pion in $\mathrm{D}^{*+} \to \mathrm{D}^0\pi^+$,

$$p_T(\mathrm{D}^0) \approx 10.7\, p_T(\pi_s) - 650 \text{ MeV}, \tag{2.13}$$

were also taken into account to ensure compatibility with downstream selections.

Algorithmically, the line makes use of the flexible *GenericSVCombiner* framework, which allows the combination of two independent secondary vertices: one from a $\mathrm{K}^0_\mathrm{S} \to \pi^+\pi^-$ candidate and one from a two-hadron pair. This modular approach reuses the existing K^0_S reconstruction while providing a dedicated two-body vertex for the directly produced hadrons. Selection proceeds hierarchically: basic quality requirements on tracks, construction of intermediate two-body vertices with mass and topology constraints, and finally the combination into a D^0 candidate subject to mass window and lifetime requirements. Compared to previous K^0_S-based lines (*TwoTrackKs*), this represents a generalisation rather than a direct extension.

Efficiency studies confirm that the overall efficiency of this kinematic line is lower than that of multivariate approaches by a factor of about 2.1, but the distribution of efficiency across the Dalitz plot and as a function of decay time is markedly more uniform. This behaviour reduces systematic uncertainties in time-dependent analyses. Moreover, a sizeable fraction of events are triggered exclusively by this line, especially at low $p_T(\mathrm{D}^0)$ and short lifetimes, complementing the coverage of other selections. The dependence of efficiency on decay time shows the expected smooth behaviour, even if not perfectly flat, thus representing a significant improvement over MVA-based lines. A visual comparison of the efficiency versus decay time, included in Figure 2.23, illustrates this improvement.

The implementation also incorporates tunable parameters to accommodate bandwidth constraints during data-taking. In particular, the minimum D^0 proper lifetime requirement and the minimum impact parameter of charged hadrons provide adjustable handles that allow the rate to be reduced in a controlled manner, while preserving the central goal of systematic robustness.

Integration with HLT2 was also considered. Low-bias HLT2 selections of D^0 decays were adapted to better match the kinematic-based HLT1 approach, including a relaxation of momentum thresholds for K^0_S and D^0 daughters, and the correction of overly restrictive requirements that would otherwise reduce efficiency. This ensures consistent efficiency behaviour across the full trigger chain.

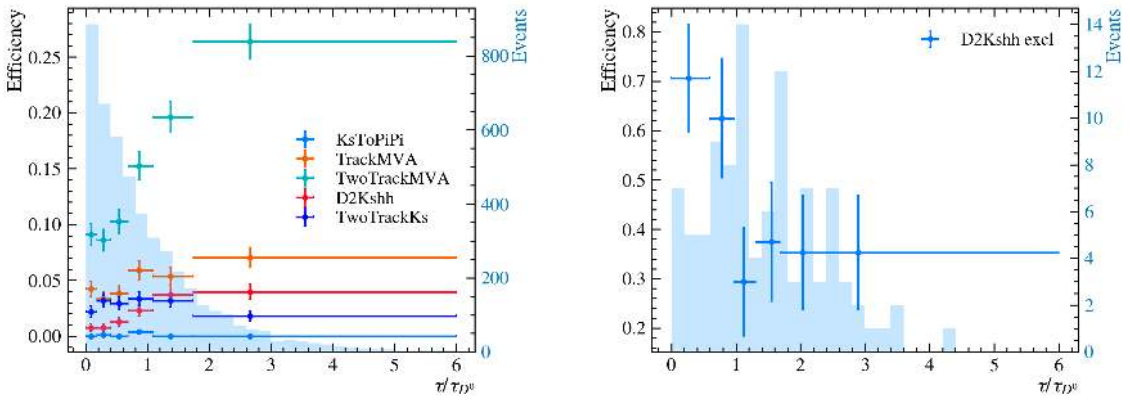

Figure 2.23: (Left) The efficiency distribution for each of the considered trigger lines depending on D^0 lifetime. The shaded area shows the distribution of all the events reconstructible as LL. (Right) The exclusive efficiency distribution for the *D2Kshh* trigger line depending on D^0 lifetime. The shaded area shows the distribution of all the events selected by the *D2Kshh* line. In both plots, the x-axis represents the generated decay time of the D^0 meson for particles that can be reconstructed.

Finally, dedicated rate and throughput studies showed that the exclusive contribution of this line to the overall HLT1 rate is small, and the computational overhead on GPUs is negligible. This validates the feasibility of implementing complex multi-body charm selections already at the first trigger level.

In summary, the dedicated $D^0 \to K^0_S h^+ h^-$ line demonstrates that systematic control can be prioritised over raw efficiency thanks to the flexibility of the Run 3 trigger system. The shift from multivariate to purely kinematic selections constitutes an important methodological advance for precision charm measurements, and sets a precedent for future flavour physics triggers where systematic uncertainties are the limiting factor.

Bin-flip analysis with $\mathrm{D}^0 \to \mathrm{K}^0_\mathrm{S}\pi^+\pi^-$ decays

The decay channel $\mathrm{D}^0 \to \mathrm{K}^0_\mathrm{S}\pi^+\pi^-$ plays a central role in the study of mixing and *CP* violation in the neutral charm meson system. The phenomenon arises because the flavour eigenstates (D^0, $\overline{\mathrm{D}}^0$) do not coincide with the mass eigenstates, leading to time-dependent oscillations between the two. These oscillations are characterised by the dimensionless mixing parameters $x = \Delta m/\Gamma$ and $y = \Delta\Gamma/(2\Gamma)$, where Δm and $\Delta\Gamma$ denote the mass and width differences of the eigenstates, and Γ is the average decay width. Since virtual heavy particles can contribute to the mixing amplitude, measurements of x and y provide a sensitive probe of possible new physics beyond the Standard Model.

The self-conjugate decay $\mathrm{D}^0 \to \mathrm{K}^0_\mathrm{S}\pi^+\pi^-$ offers direct experimental access to the mixing parameters through a combined analysis of the Dalitz-plot and decay-time distributions. Traditional approaches rely on a full amplitude model to describe the Dalitz-plot distribution and to account for efficiency and resolution effects, which introduces systematic uncertainties.

To overcome these limitations, a novel model-independent technique known as the *bin-flip method* was developed a few years ago [22]. In this approach, the Dalitz plot is divided into pairs of regions that are symmetric with respect to the bisector $m^2_+ = m^2_-$. Within each pair, the strong-phase difference is approximately constant. The ratios of decay yields observed in each symmetric bin pair are then measured as functions of the decay time. These time-dependent ratios, known as *bin-flip ratios*, depend only on the mixing parameters and on hadronic parameters (c_b, s_b) that can be obtained from independent measurements, such as those performed by the CLEO or BESIII collaborations.

By fitting these ratios as a function of decay time, one can extract the mixing parameters (x, y) and potential *CP* violation effects without the need for an explicit amplitude model or detailed knowledge of the reconstruction efficiency over the Dalitz plane.

Although the model-dependent amplitude analysis achieves a higher statistical

sensitivity for both parameters, the bin-flip method removes the reliance on an explicit amplitude model, thereby avoiding the associated systematic uncertainties, which become dominant in large data samples.

Within the bin-flip framework, the sensitivity to the parameter x is slightly higher than that to y, mainly due to acceptance corrections.

This channel plays a key role in precision measurements using the large datasets collected by the LHCb and Belle II experiments.

Chapter 3

Candidate selection and reconstruction

In this chapter, the model-independent analysis based on $\mathrm{D}^0 \to \mathrm{K}^0_\mathrm{S}\pi^+\pi^-$ *decays is described. For the physics motivation and the theoretical framework related to charm mixing and CP violation in this decay channel, the reader is referred to Section 1.8. The present chapter instead introduces the data sample used for the analysis, the trigger strategy, and the selection criteria applied to the reconstructed candidates.*

3.1 Data sample

This analysis is based on the dataset collected by the LHCb detector during the Run 3 data-taking period, focusing on 2024, corresponding to an integrated luminosity of approximately $6.77\,\mathrm{fb}^{-1}$. The D^0 mesons used in this analysis are reconstructed from the decays of charged $\mathrm{D}^{*\pm}$ mesons produced directly at the primary vertex (PV) of the pp interaction. The $\mathrm{D}^{*\pm}$ candidates are required to satisfy the decay chain

$$\mathrm{D}^{*+} \to \mathrm{D}^0\pi^+{}_s, \qquad \mathrm{D}^{*-} \to \mathrm{D}^0\pi^-{}_s,$$

where the subscript s denotes the "soft" pion emitted in the $\mathrm{D}^{*\pm}$ decay. Due to the limited phase space available for this transition, the soft pion carries a very low momentum, typically below a few hundred MeV/c. The charge of the soft pion is used to perform the flavour tagging for the neutral D meson at production: a $\pi^+{}_s$ indicates a D^0, while a $\pi^-{}_s$ corresponds to a $\overline{\mathrm{D}}{}^0$ candidate.

The neutral D meson is reconstructed in the self-conjugate three-body final state

$$\mathrm{D}^0 \to \mathrm{K}^0_\mathrm{S}\pi^+\pi^-,$$

which provides direct sensitivity to the mixing and *CP* violation parameters through a time-dependent Dalitz-plot analysis. The K^0_S mesons are reconstructed via their

decay

$$K^0_S \to \pi^+\pi^-,$$

using pairs of oppositely charged tracks that form a detached vertex consistent with the K^0_S invariant mass. Depending on the location of the K^0_S decay, two categories are defined:

- **Long** candidates, where both daughter pions are reconstructed with hits in the VELO, providing excellent mass and vertex resolution;
- **Downstream** candidates, where the K^0_S decays outside the VELO acceptance, reconstructed using information from the tracking stations only.

Both categories are included in the analysis, and dedicated selection criteria are applied to ensure optimal purity and resolution.

3.1.1 Trigger selection

In the LHCb trigger framework, events can satisfy a given trigger line either through objects associated with the signal decay itself or through activity elsewhere in the event. This distinction is encoded in the *Trigger On Signal* (TOS) and *Trigger Independent of Signal* (TIS) categories. An event is classified as TOS if at least one of the objects responsible for firing a trigger line is built from tracks belonging to the signal decay under study, while the TIS category identifies events that are triggered exclusively by other particles in the event, unrelated to the signal decay products. TIS candidates are essential for evaluating trigger efficiencies and for recovering signal decays that do not satisfy the dedicated TOS selections.

As already described in Section 2.2.3, the LHCb Run 3 data-taking strategy introduced a fully software-based trigger system, removing the hardware stage and making the High Level Trigger 1 (HLT1) the first real-time selection layer. In this framework, the reconstruction of the decay $D^0 \to K^0_S\pi^+\pi^-$ exploits several complementary HLT1 trigger lines, which can broadly be classified as either *inclusive* or *exclusive*. Inclusive lines select events based on general signatures, like the presence of displaced, high-quality tracks or vertices, without requiring a fully reconstructed decay topology. Exclusive lines, instead, target well-defined decay topologies and use invariant-mass and vertex-quality constraints to identify specific intermediate or final-state resonances.

The *One Track MVA* and *Two Tracks MVA* lines fall into the inclusive category. The *One Track MVA* line selects events in which at least one pion from the D^0 decay, excluding pions originating from the K^0_S, satisfies the requirements of a multivariate classifier based on variables such as the track transverse momentum (p_T) and the impact-parameter significance (χ^2_{IP}). The *Two Tracks MVA* line instead uses both

directly produced pions, applying the Multivariate Analysis (MVA) criteria built from their combined kinematic and geometric properties, including the transverse momentum of the two-track system and the individual χ^2_{IP} values.

More exclusive options are provided by lines that exploit partial or full reconstruction of the decay topology. The *D2Kshh* line (Section 2.2.4) considers all four final-state tracks and applies requirements on the reconstructed masses of the intermediate resonances (K^0_S and D^0), together with selections on track transverse momenta and impact parameters. This makes it particularly efficient for well-reconstructed, high-quality candidates. Similarly, the *Two Tracks KS* line focuses specifically on the reconstruction of the K^0_S meson using only its two daughter tracks; its selection is based on the invariant mass of the pair, their transverse momentum, and their displacement from the primary vertex.

In addition to these signal-driven (TOS) trigger paths, the analysis also makes extensive use of the TIS category. TIS events are triggered by objects unrelated to the $\text{D}^0 \to \text{K}^0_\text{S}\pi^+\pi^-$ decay, thereby recovering candidates that do not satisfy the dedicated signal lines and enabling an unbiased determination of trigger efficiencies. The combined use of both inclusive and exclusive TOS lines, together with TIS categories, maximises the overall signal yield while maintaining high purity and ensuring robust control of trigger-related systematic effects.

3.1.2 Offline selection

The offline selection is designed to suppress background contributions while retaining a high efficiency for $\text{D}^0 \to \text{K}^0_\text{S}\pi^+\pi^-$ decays. The sample comes from the reprocessing of 2024 data, which includes both long (LL) and downstream (DD) track categories, corresponding to the two K^0_S reconstruction topologies described above. The 2024 dataset was divided into eight blocks according to the different running conditions of the experiment, such as detector alignment, magnetic field polarity (magup or magdown), trigger configuration, and detector calibration settings. For this reason, the analysis was performed separately for each block to account for possible variations in detector performance or reconstruction efficiency across different data-taking periods. The results obtained from the individual blocks were then combined to produce the final measurement, ensuring consistency and robustness of the analysis against changes in experimental conditions. The blocks with their respective fill ranges are reported in Table 3.1.

In addition, events are required to pass at least one of several high-level trigger (HLT1) decision lines. The logical OR of the following trigger selections is applied:

- `D0_Hlt1TrackMVADecision_TOS`,
- `D0_Hlt1TwoTrackMVADecision_TOS`,

Table 3.1: Subdivision of the 2024 dataset into eight blocks according to the corresponding fill ranges. The corresponding integrated luminosity for each block is shown in Figure 3.1.

Block	Fill range
Block 4	[9808, 9910]
Block 3	[9911, 9943]
Block 2	[9945, 9978]
Block 1	[9982, 10056]
Block 5	[10059, 10102]
Block 6	[10104, 10138]
Block 7	[10197, 10213]
Block 8	[10214, 10232]

- `KS0_Hlt1TwoTrackKsDecision_TOS` (*for downstream:* `KS0_Hlt1DownstreamKsToPiPiDecision_TOS`),
- `D0_Hlt1D2KshhDecision_TOS` (*for downstream:* `D0_Hlt1DownstreamD2KshhDecision_TOS`),
- `Dst_Hlt1Global_TIS`.

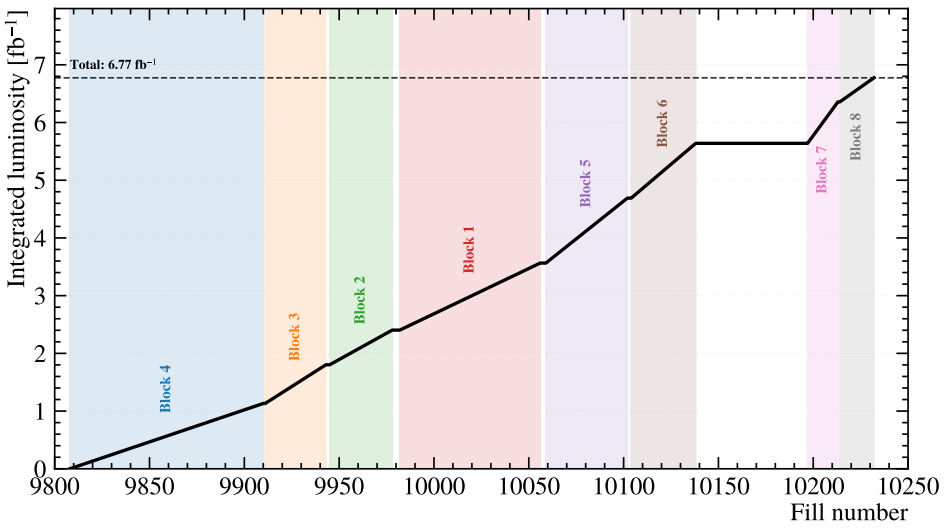

Figure 3.1: Integrated luminosity collected in 2024 divided by blocks.

A set of offline selection requirements is applied to the reconstructed candidates to

improve signal purity and reduce combinatorial and secondary background contamination:

- The reconstructed D^0 invariant mass is required to satisfy

$$m_{\mathrm{D}^0} \in [1840, 1890]\ \mathrm{MeV}/c^2.$$

  For block 4, a further shift on the left of $2.5\,\mathrm{MeV}/c^2$ is added to compensate for preliminary tracker alignment of the detector that will be solved in the upcoming reprocessing of the data (Figure 3.2a).

- The impact parameter significance of the D^0 candidate must fulfil

$$\log(\chi^2_{\mathrm{IP}}(\mathrm{D}^0)) < 2.2,$$

  to suppress secondary charm mesons originating from b-hadron decays (Figure 3.2b).

- The distance of closest approach between the two pions forming the D^0 candidate is required to be

$$\mathrm{DOCA}(\pi^+\pi^-) < 0.1\ \mathrm{mm} \quad \text{(Figures 3.2c–3.5)}.$$

- To ensure proper vertex separation between the $\mathrm{K}^0_{\mathrm{S}}$ and the D^0 candidates and suppress background from $\mathrm{D}^0 \to \pi^+\pi^-\pi^+\pi^-$ decays, the longitudinal vertex displacement is required to be
  - for LL: $z_{\mathrm{Vtx}}(\mathrm{K}^0_{\mathrm{S}}) - z_{\mathrm{Vtx}}(\mathrm{D}^0) > 10\,\mathrm{mm}$,
  - for DD: $z_{\mathrm{Vtx}}(\mathrm{K}^0_{\mathrm{S}}) - z_{\mathrm{Vtx}}(\mathrm{D}^0) > 220\,\mathrm{mm}$.

  This selection has a negligible impact on $\mathrm{K}^0_{\mathrm{S}}$ candidates, while removing almost exclusively combinatorial background.
  In Figures 3.2d-3.5 are shown some plots for LL sample.

  The distributions of the $\mathrm{K}^0_{\mathrm{S}}$ vertex z-position shown in Figure 3.5 could suggest the application of a tighter requirement at larger values of Δz. However, no additional selection is applied on this variable, as such a cut was found not to provide a significant improvement in the overall sensitivity of the measurement. The requirement on the $\mathrm{K}^0_{\mathrm{S}}$ vertex displacement is instead driven by the optimisation of the $\mathrm{K}^0_{\mathrm{S}}$ invariant mass resolution. The chosen selection represents a compromise between background suppression and signal efficiency, ensuring a stable and unbiased reconstruction of the $\mathrm{K}^0_{\mathrm{S}}$ candidate across the full dataset. Further details are discussed in Appendix A.

- Also a cut on the minimum transverse momentum (p_T) threshold is imposed on the D^0 candidate. Since different trigger selections correspond to distinct kinematic regimes, specific p_T requirements are applied depending on the trigger line used to select the event. The applied thresholds are summarized in Table 3.2 and the corresponding distributions are shown in Figures 3.2e and 3.6.

Table 3.2: Minimum $p_T(D^0)$ requirements applied for each trigger line.

Trigger line	Minimum $p_T(D^0)$ [MeV/c]
`TIS`	3750
`D2Kshh`	2500
`KS`	4500
`OneTrack`	4000
`TwoTracks`	2500

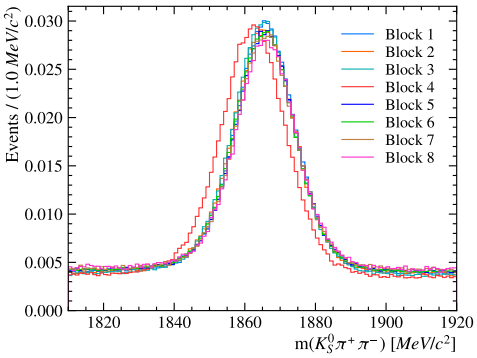

(a) D^0 invariant mass spectra for all blocks. It is evident the shift in Block 4.

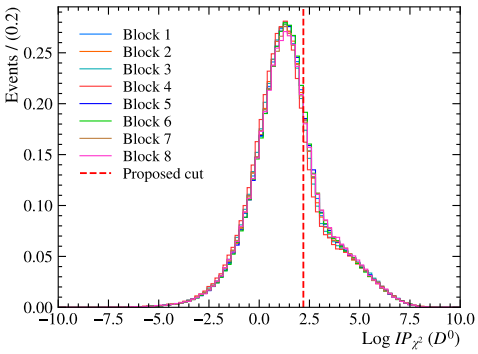

(b) Distribution of the $\log IP_{\chi^2}(D^0)$ for all blocks with the applied cut.

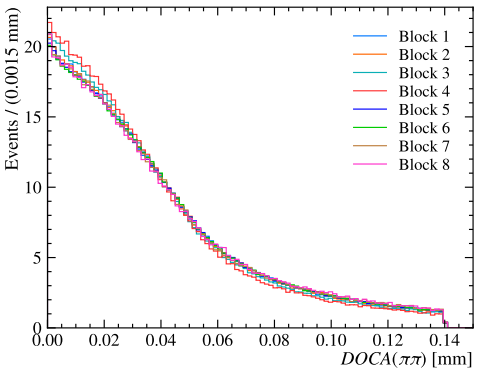

(c) Distribution of the $DOCA(\pi\pi)$.

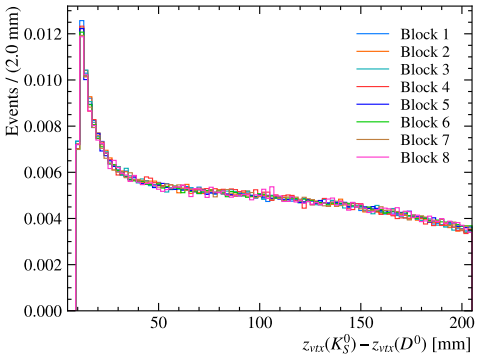

(d) Distribution of K^0_S vertex z-position.

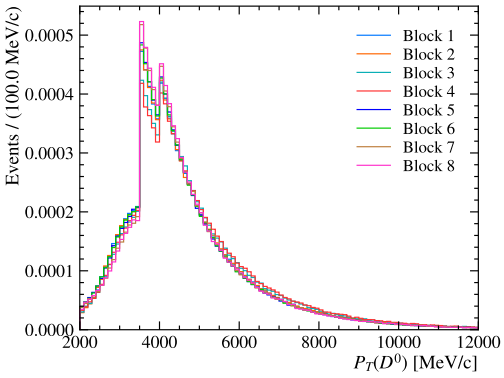

(e) Distribution of $p_T(D^0)$.

Figure 3.2: Overview of key variables distributions across data-taking blocks for the LL tracks.

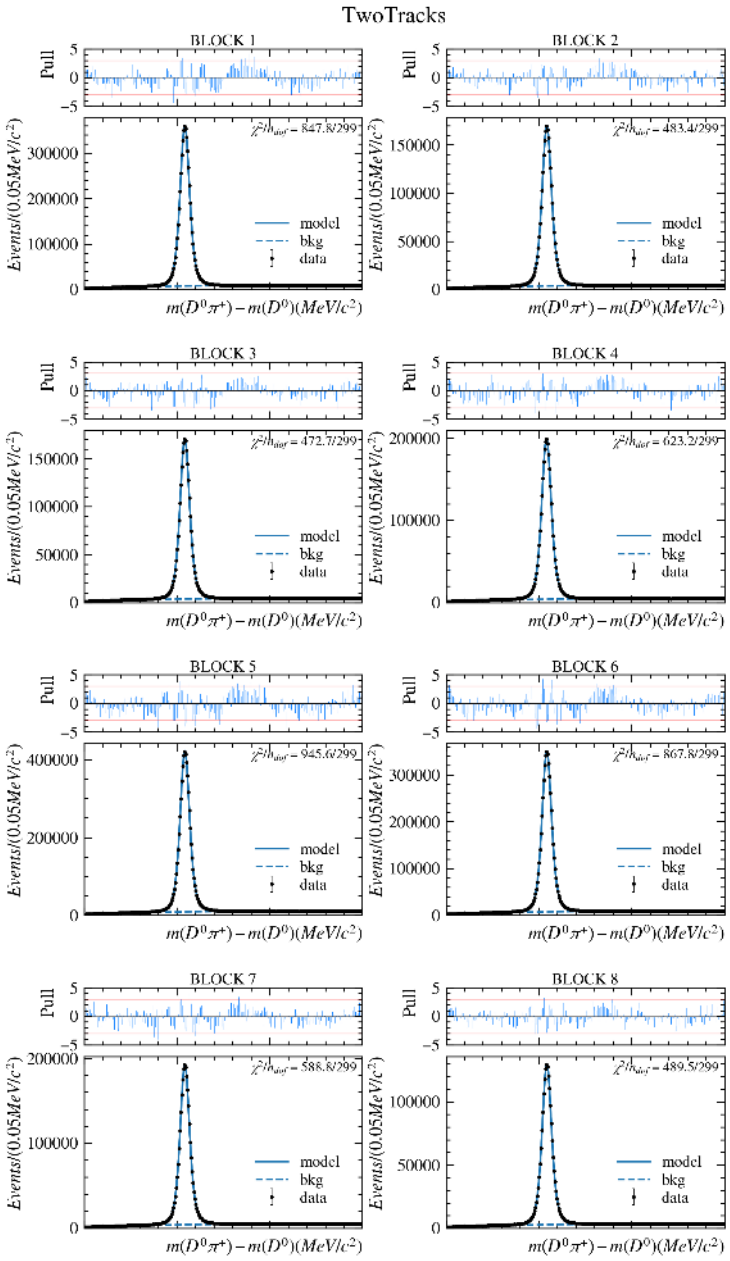

Figure 3.3: Fits of the $\Delta m = m(\mathrm{D^0\pi^+}) - m(\mathrm{D^0})$ distribution for each block for `TwoTracks` LL sample. From these fits, the *sWeights* used to separate signal and background are computed.

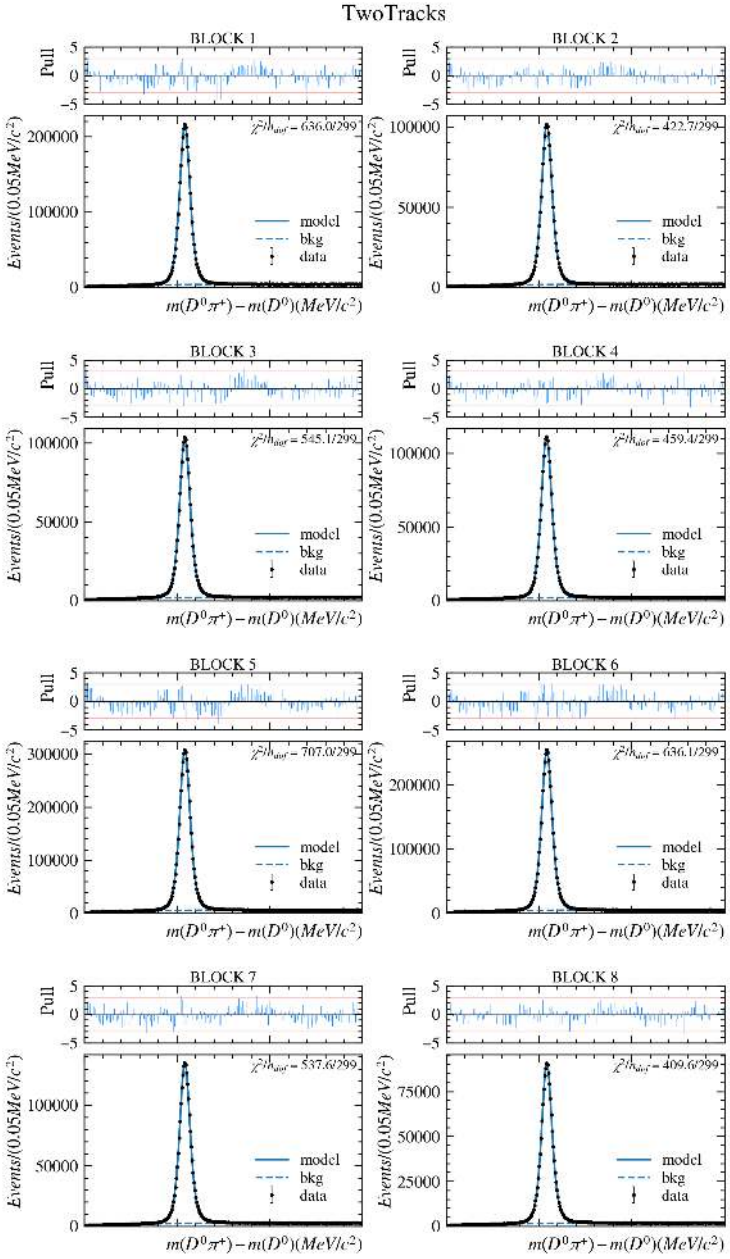

Figure 3.4: Fits of the $\Delta m = m(\mathrm{D^0\pi^+}) - m(\mathrm{D^0})$ distribution for each block for `TwoTracks` DD sample. From these fits, the *sWeights* used to separate signal and background are computed.

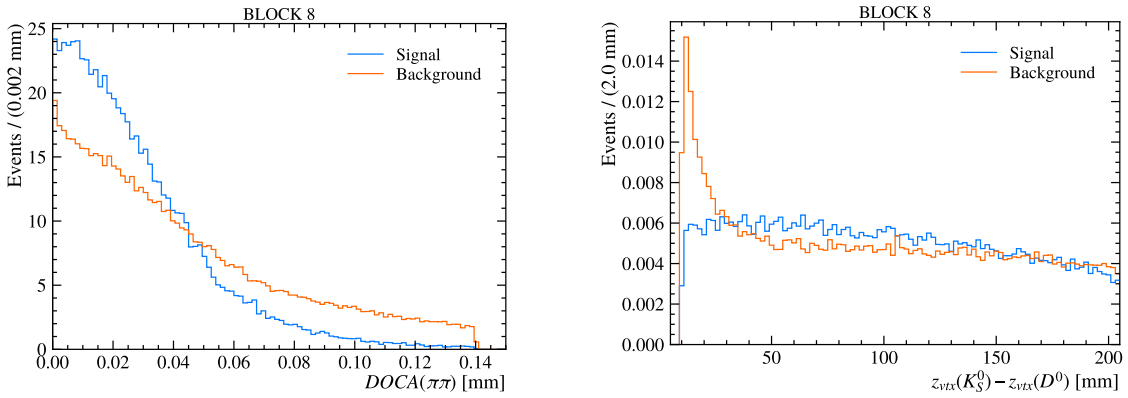

Figure 3.5: Signal and background distributions of the (Left) $DOCA(\pi\pi)$ and (Right) K^0_S vertex z-position for data block 8 for LL tracks. The signal and background are computed using weights obtained from the fits in Figure 3.3.

3.2 $D^{*+} \to D^0(\to K^0_S\pi^+\pi^-)\pi^+$ signal yields

The data are divided into subsamples according to the block category, the `HLT1` trigger, the D^0 flavour at production, the Dalitz-plot bin, and the decay-time bin.

For each subsample, the $D^{*+} \to D^0(\to K^0_S\pi^+\pi^-)\pi^+$ signal yield is determined from unbinned maximum-likelihood fits to the $\Delta m \equiv m(D^{*+}) - m(D^0)$ distribution in the range $\Delta m \in [140, 155]\,\text{MeV}/c^2$. Each candidate is assigned a weight from the efficiency-correction procedure to remove residual correlations between decay-time and Dalitz position.

The Δm spectrum is modelled as the sum of a D^{*+} signal component and a smooth combinatorial background dominated by true D^0 mesons paired with a random soft pion.

The signal probability density function is described by a mixture of a Johnson S_U function and a Gaussian core. The Johnson S_U function is:

$$J_{S_U}(x|\mu,\sigma,\delta,\gamma) = \frac{1}{N_J}\frac{e^{-\frac{1}{2}\left[\gamma+\delta\sinh^{-1}\left(\frac{x-\mu}{\sigma}\right)\right]^2}}{\sqrt{1+\left(\frac{x-\mu}{\sigma}\right)^2}}, \tag{3.1}$$

where μ and σ determine the mode and scale of the distribution, while γ and δ control its asymmetry and tail behaviour.

The full Δm model is then:

$$\begin{aligned} \mathrm{P}(x) = f_{\text{sig}}\left[f_{J_{S_U}}\cdot J_{S_U}(x) + (1-f_{J_{S_U}})\cdot w_1 G_1(x)\right] \\ + (1-f_{\text{sig}})\cdot \mathrm{B}(x;\theta,a,b), \end{aligned} \tag{3.2}$$

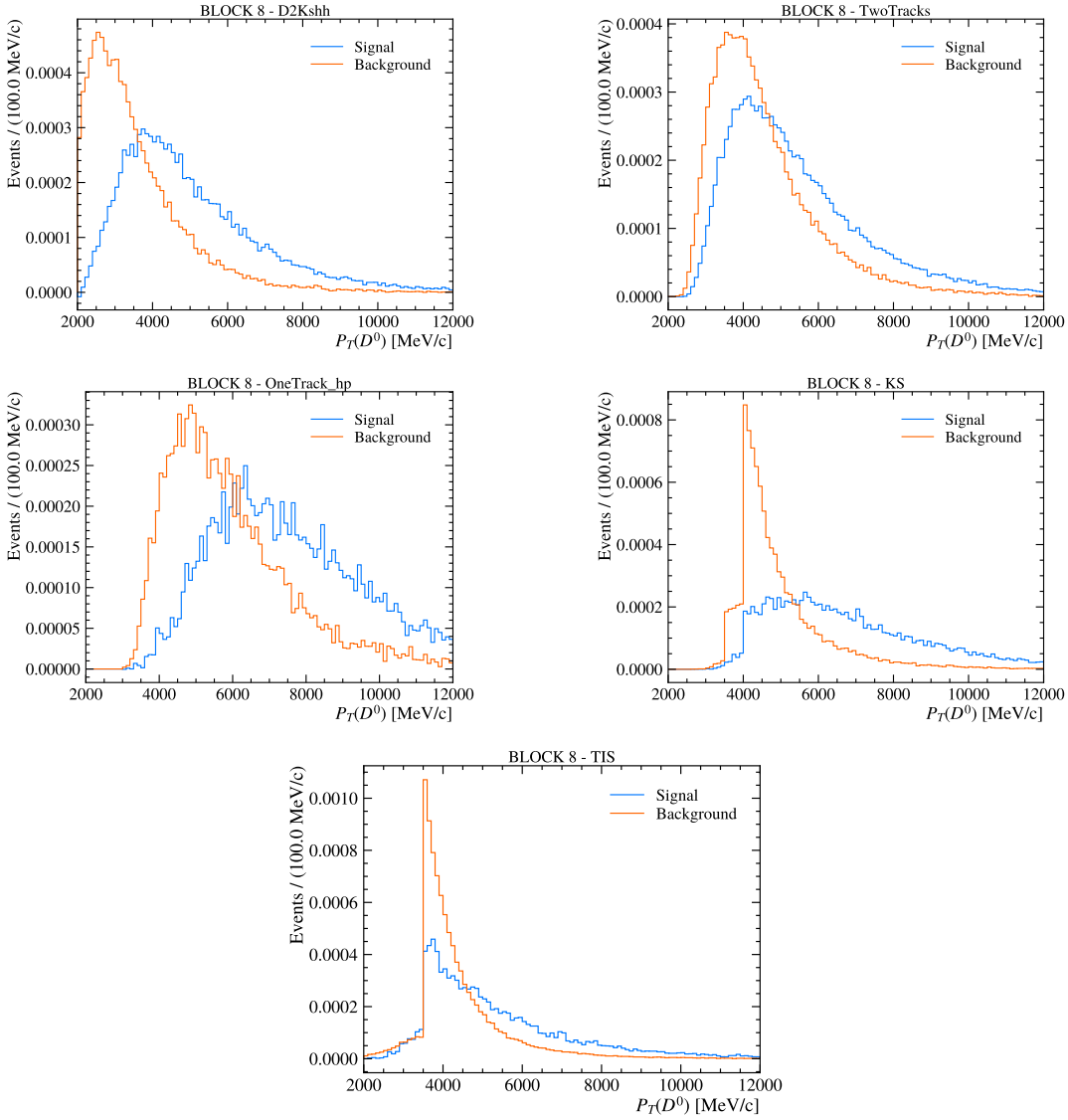

Figure 3.6: Signal and background distributions of the $p_T(\mathrm{D}^0)$ for data block 8 LL, for (top left) `D2Kshh`, (top right) `TwoTracks`, (middle left) `OneTrack`, (middle right) `KS` and (bottom) `TIS`. The signal and background are computed using weights obtained from the fits in Figure 3.3. The observed differences in the $p_T(\mathrm{D}^0)$ distributions among the trigger lines clarifies the distinct p_T selection requirements, as summarised in Table 3.2.

where $G_1(x)$ is a Gaussian with mean μ and width proportional to σ, and f_{sig} and $f_{J_{S_U}}$ denote the signal and JSU fractions, respectively.
The background is parametrised with an empirical threshold function:

$$B(x;\theta,a,b) = \Theta(x - x_{\text{th}})\,(x - x_0)^a\, e^{-b(x-x_0)}, \tag{3.3}$$

where Θ is the step function ensuring the physical kinematic threshold.

The fits are performed independently for HLT1 category, D^0 flavour, and decay-time bin (more details in Section 3.2.1), but simultaneously for the 16 bins of the Dalitz plot.

Representative projections of the fitted Δm distributions are shown in Figure 3.3 for LL and Figure 3.4 for DD, and the extracted signal yields are reported in Tables 3.3–3.4 and showed in Figures 3.7-3.8. For the comparison between Run 2 and Run 3, the `TwoTracks` trigger line is used as a reference. While Run 2 relied only on the `OneTrack` and `TwoTracks` selections, a significant overlap between these categories is observed in Run 3, preventing a meaningful combination of their yields. The `TwoTracks` category, therefore, provides the most consistent benchmark for the comparison.

The signal yields per unit of integrated luminosity obtained in Run 3 ($6.77\,\text{fb}^{-1}$), computed using only the `TwoTracks` sample, amount to $(4.11 \pm 0.02) \times 10^6\,\text{fb}^{-1}$ for the LL sample and $(3.05 \pm 0.01) \times 10^6\,\text{fb}^{-1}$ for the DD sample. For comparison, the corresponding yields recorded in Run 2 ($5.4\,\text{fb}^{-1}$) were $(1.83 \pm 0.01) \times 10^6\,\text{fb}^{-1}$ for LL and $(3.84 \pm 0.02) \times 10^6\,\text{fb}^{-1}$ for DD. An improvement in signal efficiency is observed for LL decays with the Run 3 trigger strategy, while no comparable gain is seen for the DD category. This behaviour is likely driven by a combination of effects, including a reconstruction efficiency for downstream tracks that is not yet fully optimised during the 2024 data-taking period and has been significantly improved for 2025, as well as differences in the geometrical acceptance of the VELO. The latter may result in candidates that were reconstructed as DD in Run 2 being classified as LL in Run 3.

3.2.1 Decay-time binning

The decay time distributions are binned using an adaptive quantile-based strategy to ensure approximately uniform statistical population across bins. The procedure is performed on an *sWeighted* signal sample, where the *sWeights* are computed from preliminary fits to the Δm distribution. The binning is performed within the decay time range $[0.5, 8.0]\,\tau_{D^0}$, where the signal is well-defined, and backgrounds are manageable. For a given number of bins N, the bin edges are determined by the quantiles of the observed decay time distribution: the i-th edge corresponds to the i/N quantile, with $i = 1, \ldots, N-1$. This approach naturally produces narrower bins

Table 3.3: Signal yields for each run block and trigger line for LL tracks. Values and uncertainties in the table are expressed in units of 10^3.

Block	`OneTrack`	`TwoTracks`	`D2Kshh`	`KS`	`TIS`
1	1604 ± 2	4997 ± 4	1795 ± 2	1338 ± 2	1002 ± 2
2	755 ± 1	2369 ± 3	860 ± 1	630 ± 1	470 ± 1
3	599 ± 1	2396 ± 3	986 ± 2	743 ± 1	412 ± 1
4	705 ± 1	2810 ± 3	1228 ± 2	911 ± 2	480 ± 1
5	1835 ± 2	5869 ± 4	2586 ± 3	1645 ± 2	1142 ± 2
6	1528 ± 2	4889 ± 4	2147 ± 2	1377 ± 2	954 ± 2
7	887 ± 1	2663 ± 3	1226 ± 2	803 ± 2	585 ± 2
8	598 ± 1	1802 ± 2	830 ± 2	541 ± 1	399 ± 1
Total	8511 ± 4	27795 ± 9	11658 ± 6	7988 ± 5	5444 ± 5

Table 3.4: Signal yields for each run block and trigger line for DD tracks. Values and uncertainties in the table are expressed in units of 10^3.

Block	`OneTrack`	`TwoTracks`	`D2Kshh`	`KS`	`TIS`
1	1612 ± 3	3269 ± 3	–	–	747 ± 1
2	696 ± 1	1560 ± 2	–	–	354 ± 1
3	589 ± 1	1588 ± 2	–	–	312 ± 1
4	635 ± 1	1715 ± 2	–	–	334 ± 1
5	1969 ± 2	4702 ± 4	–	–	1274 ± 12
6	1629 ± 2	3883 ± 3	–	–	846 ± 2
7	899 ± 1	2046 ± 2	50 ± 1	210 ± 2	483 ± 1
8	605 ± 1	1377 ± 2	35 ± 1	121 ± 1	328 ± 1
Total	8634 ± 5	20140 ± 7	85 ± 1	331 ± 2	4678 ± 12

Figure 3.7: (Top) Signal yields for each run block and trigger line for (left) LL and (right) DD tracks. (Bottom) The corresponding signal yield heatmaps, highlighting the overlap among trigger lines.

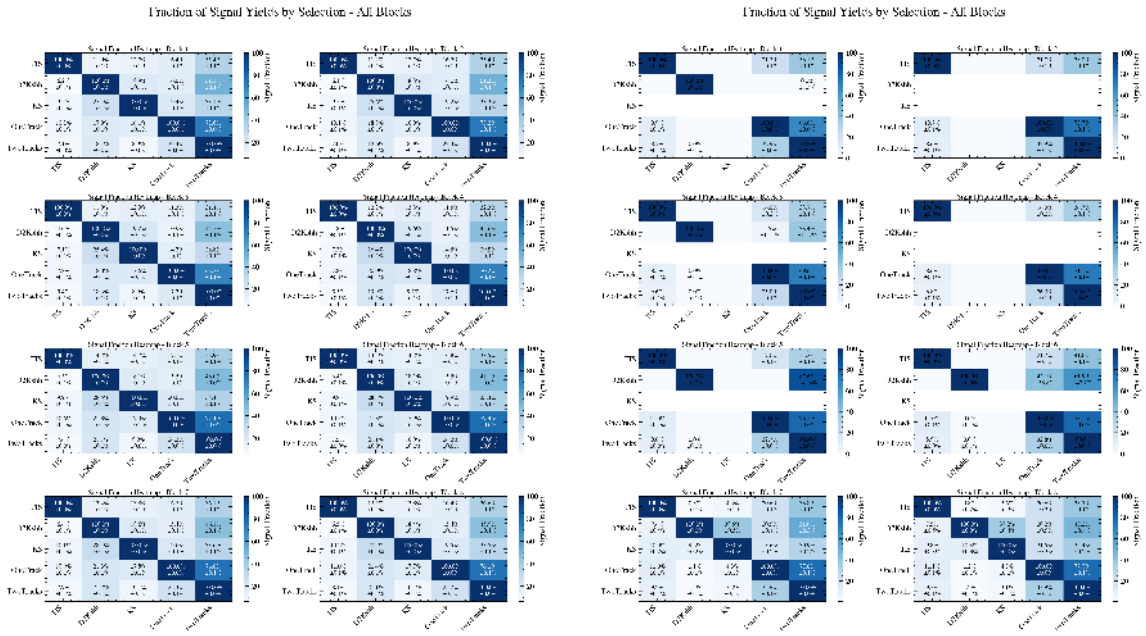

Figure 3.8: Signal yield fraction heatmaps for LL (left) and DD (right) tracks, showing the overlap among trigger lines. Each cell represents the fraction of the selection in a given row that is also selected by the trigger line in the corresponding column.

in regions of high event density and wider bins where statistics are limited, thereby optimising sensitivity across the decay time spectrum.

The number of bins is optimised separately for each trigger line and for LL and DD tracks to account for variations in signal yields and distribution shapes. The configuration is summarised in Table 3.5 and the corresponding bin edges are reported in Table 3.6. Samples with higher statistics (e.g., `TwoTracks` LL) employ up to 20 bins, while those with lower yields use $10 - 15$ bins to maintain sufficient statistical power per bin. The bin edges are computed once from the full dataset and applied consistently throughout the analysis.

Table 3.5: Number of decay time bins for each trigger line and for LL and DD tracks.

Trigger line	LL	DD
`OneTrack`	15	15
`TwoTracks`	20	15
`KS`	15	10
`D2Kshh`	15	10
`TIS`	15	15

Table 3.6: Decay time bin edges for each trigger line and track type (values in units of D^0 lifetime [410 fs]).

Trigger	**LL Bin Edges**	**DD Bin Edges**
`OneTrack`	[0.50, 0.91, 1.10, 1.26, 1.41, 1.55, 1.70, 1.85, 2.01, 2.19, 2.39, 2.63, 2.93, 3.34, 4.00, 8.00]	[0.50, 0.82, 1.00, 1.14, 1.28, 1.41, 1.55, 1.69, 1.84, 2.01, 2.21, 2.44, 2.72, 3.11, 3.74, 8.00]
`TwoTracks`	[0.50, 0.90, 1.04, 1.15, 1.26, 1.35, 1.45, 1.55, 1.65, 1.75, 1.86, 1.98, 2.11, 2.26, 2.42, 2.61, 2.84, 3.13, 3.53, 4.21, 8.00]	[0.50, 0.87, 1.03, 1.17, 1.29, 1.42, 1.55, 1.69, 1.84, 2.01, 2.20, 2.43, 2.72, 3.13, 3.79, 8.00]
`KS`	[0.50, 0.58, 0.66, 0.74, 0.82, 0.92, 1.02, 1.14, 1.26, 1.41, 1.58, 1.79, 2.06, 2.44, 3.07, 8.00]	[0.50, 0.65, 0.78, 0.93, 1.09, 1.27, 1.49, 1.77, 2.16, 2.81, 8.00]
`D2Kshh`	[0.50, 0.68, 0.80, 0.91, 1.03, 1.15, 1.28, 1.42, 1.57, 1.73, 1.93, 2.17, 2.46, 2.88, 3.57, 8.00]	[0.50, 0.73, 0.89, 1.05, 1.22, 1.42, 1.65, 1.95, 2.37, 3.05, 8.00]
`TIS`	[0.50, 0.59, 0.66, 0.74, 0.82, 0.91, 1.01, 1.12, 1.25, 1.40, 1.58, 1.80, 2.09, 2.49, 3.19, 8.00]	[0.50, 0.61, 0.70, 0.79, 0.88, 0.97, 1.08, 1.20, 1.33, 1.49, 1.67, 1.90, 2.20, 2.62, 3.35, 8.00]

3.2.2 Determination of $\langle t \rangle_j$ and $\langle t^2 \rangle_j$

Charm mixing observables depend on the average decay-time and the squared decay-time within each decay-time bin. These quantities,

$$\langle t \rangle_j = \frac{\sum_i w_i t_i}{\sum_i w_i}, \qquad \langle t^2 \rangle_j = \frac{\sum_i w_i t_i^2}{\sum_i w_i}, \tag{3.4}$$

are evaluated separately for each HLT1 category to account for the different decay-time binning.

Uncertainties are propagated from the finite size of the weighted signal sample, assuming candidates are statistically independent:

$$\sigma^2(\langle t \rangle_{bj}) = \frac{\sum\limits_{i\in(b,j)} w_i^2 \left(t_i - \langle t \rangle_{bj}\right)^2}{\left(\sum\limits_{i\in(b,j)} w_i\right)^2}, \tag{3.5}$$

and analogously for $\langle t^2 \rangle_{bj}$.

The weights w_i incorporate both the *sWeights* derived from the Δm fits and the correction factor $1/\tilde{\epsilon}(t_i \,|\, \vec{\Omega}_i)$ which removes residual correlations between decay-time and Dalitz position (Chapter 4). This ensures unbiased estimates of the moments of the decay-time distribution while preserving sensitivity to mixing.

3.2.3 Dalitz distributions and kinematic projections in data blocks

In this subsection, the *sWeighted* event distributions in the Dalitz plot are shown for the different data blocks (Figures 3.9–3.10). These two-dimensional distributions provide a direct visualisation of the phase-space population and allow for a comparison of the kinematic structure across blocks. A difference in the acceptance pattern is observed between different trigger samples: the `D2Kshh` one exhibits a flatter acceptance over the Dalitz plane compared to the `TwoTracks` sample. This improved uniformity enhances the sensitivity to resonant contributions, in particular allowing the reconstruction of candidates originating from K^* resonances, which populate regions corresponding to lower values of $m(\pi\pi)$.

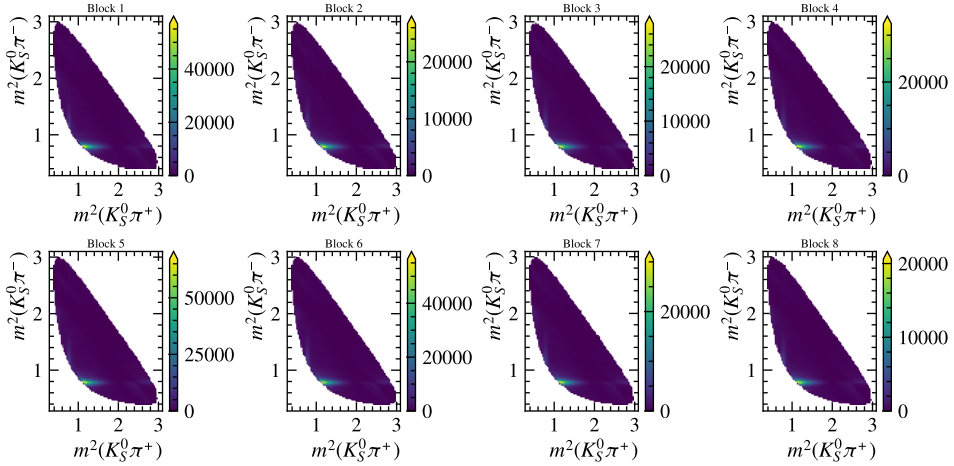

Figure 3.9: Dalitz distributions for `TwoTracks` for each data block. The second K^* lobe is not visible in this trigger category, as the low $\pi^+\pi^-$ invariant-mass region is depleted.

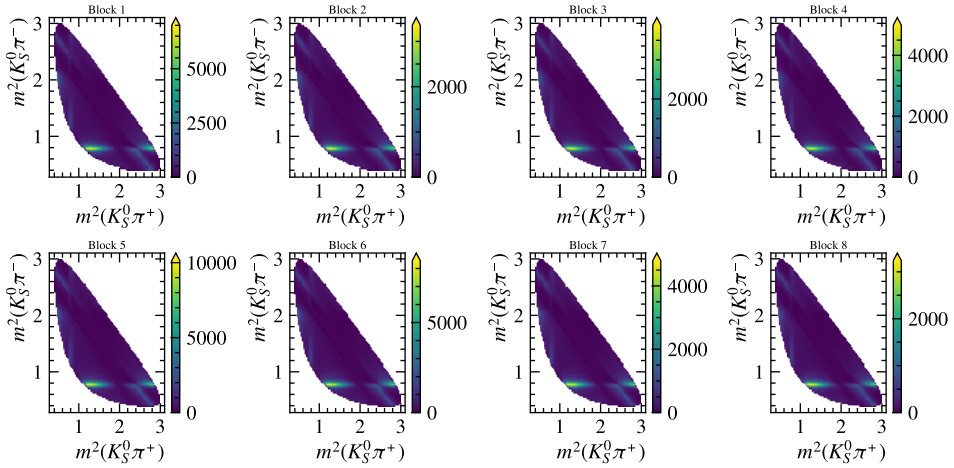

Figure 3.10: Dalitz distributions for `D2Kshh` for each data block. In contrast to the `TwoTracks` selection (Figure 3.9), the second K^* lobe is clearly visible, indicating that the exclusive selection is less restrictive across the Dalitz plane.

In addition, the corresponding projections onto the kinematic variables invariant mass $m^2(K^0_S\pi^+)$, $m^2(K^0_S\pi^-)$, $m^2(\pi^+\pi^-)$ and helicity angles $|\cos\theta_{K^0_S\pi^+}|$, $|\cos\theta_{K^0_S\pi^-}|$, and $|\cos\theta_{\pi^+\pi^-}|$ are presented (Figures 3.11–3.12). These projections are used to assess

the stability of the kinematic shapes and to verify the consistency of the *sWeighted* distributions among the different blocks.

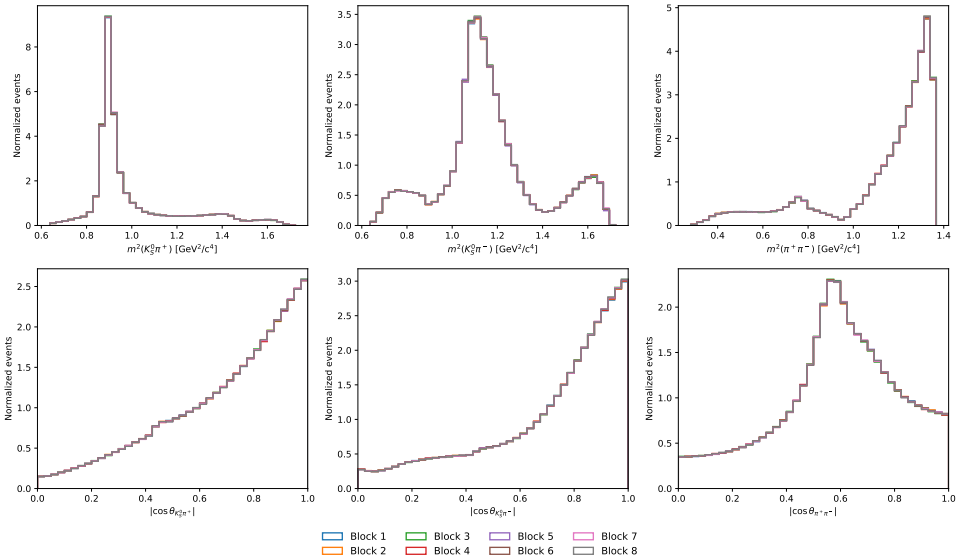

Figure 3.11: Projections of the `TwoTracks` dataset onto the kinematic variables (top) invariant mass [(left) $m^2(K^0_S\pi^+)$, (middle) $m^2(K^0_S\pi^-)$, (right) $m^2(\pi^+\pi^-)$] and (bottom) helicity angles [(left)$|\cos\theta_{K^0_S\pi^+}|$, (middle) $|\cos\theta_{K^0_S\pi^-}|$, and (right) $|\cos\theta_{\pi^+\pi^-}|$.

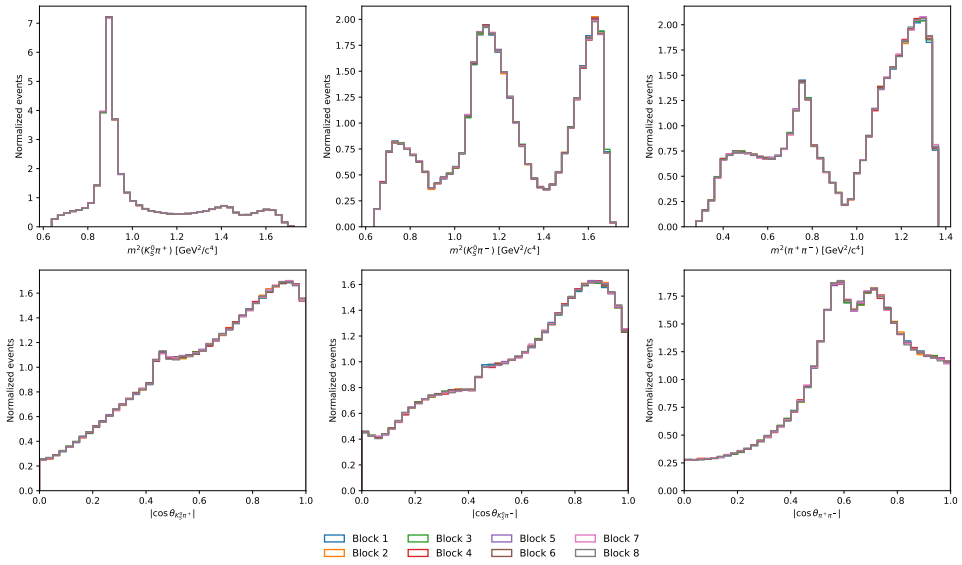

Figure 3.12: Projections of the `D2Kshh` dataset onto the kinematic variables (top) invariant mass [(left) $m^2(\mathrm{K}^0_\mathrm{S}\pi^+)$, (middle) $m^2(\mathrm{K}^0_\mathrm{S}\pi^-)$, (right) $m^2(\pi^+\pi^-)$] and (bottom) helicity angles [(left)$|\cos\theta_{\mathrm{K}^0_\mathrm{S}\pi^+}|$, (middle) $|\cos\theta_{\mathrm{K}^0_\mathrm{S}\pi^-}|$, and (right) $|\cos\theta_{\pi^+\pi^-}|$.

3.3 Bin-flip observables and efficiency assumptions

In the bin-flip analysis, the primary experimental observables are the ratios of signal yields measured in pairs of Dalitz-plot bins that are symmetric with respect to the principal bisector, as a function of the decay-time bin. For a given Dalitz bin b and decay-time bin j, the measured bin-flip ratio is defined as

$$R_{bj} = \frac{N'(\mathrm{D}^0; -b; j)}{N'(\mathrm{D}^0; b; j)}, \tag{3.6}$$

where $N'(\mathrm{D}^0; \pm b; j)$ denotes the observed number of D^0 signal decays in the corresponding Dalitz and decay-time bins. The measured yields are related to the true signal yields through the reconstruction and selection efficiency, such that

$$R_{bj} = \frac{N(\mathrm{D}^0; -b; j)}{N(\mathrm{D}^0; b; j)} \frac{\varepsilon(\mathrm{D}^0; b; j)}{\varepsilon(\mathrm{D}^0; -b; j)}, \tag{3.7}$$

where $N(\mathrm{D}^0; \pm b; j)$ are the efficiency-corrected signal yields and $\varepsilon(\mathrm{D}^0; \pm b; j)$ are the corresponding efficiencies.

In the ideal case, the efficiency factorises into a contribution depending only on

the Dalitz-plot position and a contribution depending only on the decay-time,

$$\varepsilon(\mathrm{D}^0; b; j) = \varepsilon_{\mathrm{DP}}(\mathrm{D}^0; b)\, \varepsilon_t(\mathrm{D}^0; j), \tag{3.8}$$

which leads to

$$\frac{\varepsilon(\mathrm{D}^0; b; j)}{\varepsilon(\mathrm{D}^0; -b; j)} = \frac{\varepsilon_{\mathrm{DP}}(\mathrm{D}^0; b)}{\varepsilon_{\mathrm{DP}}(\mathrm{D}^0; -b)}. \tag{3.9}$$

Since the Dalitz-plot bins are constructed to be symmetric with respect to the bisector, the Dalitz-plot efficiency ratio is expected to be close to unity, and the bin-flip ratios R_{bj} directly probe the underlying decay dynamics and mixing parameters without requiring explicit efficiency corrections.

In practice, however, the efficiency does not perfectly factorise (Figure 3.13), as residual correlations between the decay-time and the Dalitz-plot position can arise from detector acceptance and event selection effects.

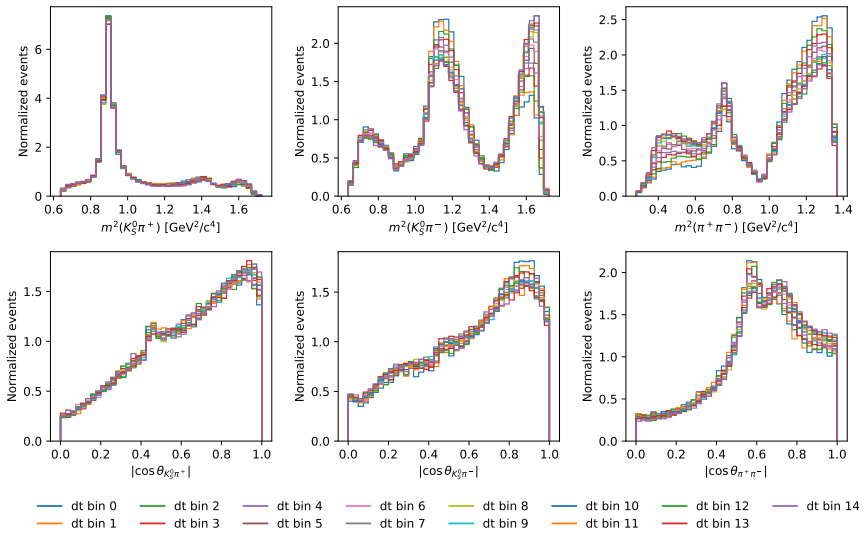

Figure 3.13: Dalitz plot projections in bins of decay time of `D2Kshh` block 8 sample for (top) the squared invariant masses [(left) $m^2_{\mathrm{K}^0_{\mathrm{S}}\pi^+}$, (middle) $m^2_{\mathrm{K}^0_{\mathrm{S}}\pi^-}$, (right) $m^2_{\pi^+\pi^-}$] and (bottom) the cosine of helicity angles [(left) $|cos_{\mathrm{K}^0_{\mathrm{S}}\pi^+}|$, (middle) $|cos_{\mathrm{K}^0_{\mathrm{S}}\pi^-}|$, (right) $|cos_{\pi^+\pi^-}|$].

These correlations introduce deviations of the measured ratios R_{bj} from their ideal behaviour and must be corrected in order to ensure an unbiased determination of

the charm mixing parameters. The strategy adopted to remove such experimentally induced correlations is described in the following chapter.

Chapter 4

Experimentally-Induced Correlations

This chapter describes the data–driven procedure developed to remove experimentally–induced correlations between decay-time and phase–space variables, ensuring an unbiased extraction of the charm mixing parameters.

4.1 Introduction

A precise measurement of charm mixing parameters requires an accurate description of the signal decay-time distribution, independent of the position of the event in the Dalitz plane. However, real data are affected by non-uniform detector efficiency and event selection criteria, which induce correlations between the reconstructed decay-time t and the phase-space coordinates of the $D^0 \to K^0_S \pi^+ \pi^-$ decay. The phase-space variables are denoted as

$$\vec{\Omega} \equiv \left(m^2_{\pi^+\pi^-}, \, |\cos\theta_{\pi^+\pi^-}| \right). \tag{4.1}$$

The bin-flip method has been specifically designed to minimise the impact of reconstruction and selection effects on the determination of the mixing parameters. In particular, non-uniform efficiencies across the Dalitz plane largely cancel when taking ratios of yields between conjugate Dalitz bins, provided that the efficiency varies slowly within each bin and that the binning scheme is constructed such that the strong-interaction phase differences are approximately constant over the bin area. Under these assumptions, the efficiency factors cancel to first order when forming ratios of yields as a function of decay time, which constitute the core observables of the method. For the measurement of *CP*-violation parameters, additional care is required. In this case, the acceptance over the Dalitz plot must be symmetric under the exchange of m_+ and m_-, corresponding to the interchange of the two conjugate

decay configurations. Any residual asymmetry in the acceptance could otherwise introduce instrumental effects that mimic genuine *CP*-violating asymmetries.

Studies of the LHCb Run 2 data [112] confirm that both the decay-time acceptance and the Dalitz-plot acceptance show significant structures due to vertexing requirements, particle identification criteria, and detector geometry. These features are not problematic for the analysis as long as they do not introduce correlations between decay-time and Dalitz plot coordinates.

The only case in which the bin-flip method becomes sensitive to efficiency effects is when the decay-time acceptance varies across the Dalitz plane. In this situation, different phase-space regions are affected by different effective decay-time distortions. This violates the factorisation assumption and can generate artificial asymmetries between *CP*-conjugate bins, directly biasing the extraction of x_{CP} and y_{CP}.

If the full three-dimensional efficiency $\epsilon(t, \vec{\Omega})$ were known, one could correct each candidate with a weight proportional to $1/\epsilon(t, \vec{\Omega})$. Nevertheless, since only the removal of the correlations is required and the bin-flip method can handle efficiency variations that independently affect the decay-time and the phase space distributions, it is sufficient to ensure that the decay-time acceptance becomes uniform across the Dalitz plane. This can be achieved through a relative, conditional efficiency $\tilde{\epsilon}(t\,|\,\vec{\Omega})$.

A data-driven procedure has been developed to estimate this relative efficiency from the signal data themselves, while statistically subtracting backgrounds. The construction of this correction and its integration into the fit strategy are the focus of the following sections.

4.2 Efficiency Determination from Data

The central assumption of the method is that any observed difference in decay-time distributions across different phase-space regions is attributed to experimental effects. By aligning these distributions to the phase-space averaged decay-time distribution, the efficiency-induced correlations can be removed.

First, the signal yields are extracted using the sPlot technique [113]. The data are then binned in $(\vec{\Omega}, t)$ using variable-width bins, finer at low decay-times to capture fast variations in efficiency. For each bin in $m^2_{\pi^+\pi^-}$ (i), $|\cos\theta_{\pi^+\pi^-}|$ (j), and t (k), the relative efficiency is evaluated from the *sWeighted* yields n_{ijk} as

$$\epsilon_{ijk} = \frac{n_{ijk}}{\sum_l n_{ijl}} \Bigg/ \frac{\sum_{l,m} n_{lmk}}{\sum_{l,m,n} n_{lmn}}. \tag{4.2}$$

Here, the numerator gives the decay-time distribution for a given phase-space region (i, j), while the denominator corresponds to the decay-time distribution averaged

over the full Dalitz plane. This yields an estimate of $\tilde{\epsilon}(t|\vec{\Omega})$ defined up to an irrelevant normalisation factor.

Finally, a trilinear interpolation is applied between bin centres to obtain a smooth efficiency map across the three-dimensional space.

This correction reduces the intrinsic mixing sensitivity in the data, a feature that must be accounted for, as discussed in Section 4.3.

4.3 Accounting for Mixing Effects

Since the relative efficiency is measured directly using data, genuine physics effects, especially the variation of the effective decay width across $\vec{\Omega}$ driven by mixing, are partially removed. The wash-out component is proportional to the mixing parameter y and depends on the strong-phase variation of the decay amplitudes over the Dalitz plot. Oscillation effects governed by x remain unaffected due to their symmetric behaviour under phase-space reflection.

These distortions would lead to biases at the level of statistical sensitivity if not corrected. To restore mixing sensitivity, the effect must be explicitly included in the efficiency model.

A correction factor $f_{y,\delta}(t|\vec{\Omega})$ is introduced to account for the effect of charm mixing in the efficiency evaluation. This factor is calculated directly from the amplitude model obtained from the combination of Belle and BaBar [114], in which the decay amplitude over the Dalitz phase space is expressed as

$$A(x) = a(x)\, e^{i\delta(x)}, \tag{4.3}$$

providing both the magnitude $a(x)$ and the strong phase $\delta(x)$ of the decay amplitude at each point x in the phase space.

The time evolution of the amplitudes associated with flavour eigenstates is given by

$$T_f(m_+^2, m_-^2; t) = A_f(m_+^2, m_-^2) g_+(t) + \overline{A}_f(m_-^2, m_+^2) \frac{q}{p} g_-(t), \tag{4.4}$$

$$\overline{T}_f(m_+^2, m_-^2; t) = \overline{A}_f(m_+^2, m_-^2) g_+(t) + A_f(m_-^2, m_+^2) \frac{p}{q} g_-(t), \tag{4.5}$$

where

$$g_\pm(t) = \theta(t) e^{-imt} e^{-t/2} \begin{pmatrix} \cosh \\ \sinh \end{pmatrix} \left(\frac{zt}{2} \right), \tag{4.6}$$

t is the decay time in units of the D^0 lifetime $\tau = 1/\Gamma$, $m = (m_1 + m_2)/2$ is the average mass of neutral D mesons, $\theta(t)$ is the Heaviside function, and $z = -(y + ix)$.

The correction factor is defined as the ratio between the time-dependent decay rate including mixing and the corresponding rate in the absence of mixing, evaluated locally at each phase-space point $\vec{\Omega}$:

$$f_{y,\delta}(t|\vec{\Omega}) = \frac{\Gamma(t|\vec{\Omega}; y \neq 0)}{\Gamma(t|\vec{\Omega}; y = 0)}, \tag{4.7}$$

where $\Gamma(t|\vec{\Omega}; y)$ is the decay rate at time t including the effect of the charm mixing parameter y.

For the self-conjugate final state $K^0_S\pi^+\pi^-$, the time-dependent decay rate is constructed from the sum of the amplitudes evaluated at *CP*-conjugate Dalitz coordinates:

$$\Gamma(t|\vec{\Omega}; y) = |T_f(m^2_+, m^2_-; t)|^2 + |T_f(m^2_-, m^2_+; t)|^2. \tag{4.8}$$

Defining δ_{+-} as the *CP*-conserving phase of the decay amplitude $A_f(m^2_+, m^2_-)$, and expanding the terms in Equation 4.4, the squared amplitude can be expressed as

$$\begin{aligned}
|T_f(m^2_+,&m^2_-; t)|^2 = \\
&\frac{1}{4}e^{-t}\Big[|A_f(m^2_+, m^2_-)|^2(e^{-ty} + e^{ty} + 2\cos(xt)) \\
&+ |\bar{A}_f(m^2_-, m^2_+)|^2 \left|\frac{q}{p}\right|^2 (e^{-ty} + e^{ty} - 2\cos(xt)) \\
&+ 2|\bar{A}_f(m^2_-, m^2_+)||A_f(m^2_+, m^2_-)| \left|\frac{q}{p}\right| \Big(\cos(\delta_{+-} - \delta_{-+} - \phi)(e^{-ty} - e^{ty}) \\
&\qquad - 2\sin(\delta_{+-} - \delta_{-+} - \phi)\sin(xt)\Big)\Big]
\end{aligned} \tag{4.9}$$

Assuming *CP* conservation in mixing ($q/p = 1$ and $\phi = 0$), the sum of the square amplitudes can be written as

$$\begin{aligned}
|T_f(m^2_+, m^2_-; t)|^2 &+ |T_f(m^2_-, m^2_+; t)|^2 = \\
&\frac{1}{2}e^{-t}\Big[(|A_f(m^2_+, m^2_-)|^2 + |A_f(m^2_-, m^2_+)|^2)(e^{-ty} + e^{ty}) \\
&+ 2|A_f(m^2_-, m^2_+)||A_f(m^2_+, m^2_-)|(\cos(\delta_{+-} - \delta_{-+})(e^{-ty} - e^{ty}))\Big] \\
&\approx e^{-t}\Big[(|A_f(m^2_+, m^2_-)|^2 + |A_f(m^2_-, m^2_+)|^2)(1 + (ty)^2) \\
&- 2|A_f(m^2_-, m^2_+)||A_f(m^2_+, m^2_-)|(\cos(\delta_{+-} - \delta_{-+})(ty))\Big]
\end{aligned} \tag{4.10}$$

Here, the effect of mixing enters via the parameter y. A nominal value $y = 0.006$ is used.

Finally, the efficiency is corrected by weighting each candidate with the inverse of the correction factor:

$$\tilde{\epsilon}_{y,\delta}(t|\vec{\Omega}) = \frac{\epsilon(t|\vec{\Omega})}{f_{y,\delta}(t|\vec{\Omega})}, \tag{4.11}$$

yielding a locally corrected estimator of the efficiency that accounts for the dilution of correlations due to charm mixing.
Following the Run 2 procedure, the correction, has been applied to the ratios R_{bj}

$$c_{bj;y,\delta} = \frac{\sum_i^{N_{bj}} \left(\frac{w_i}{\epsilon_{y,\delta}(t_i|\vec{\Omega}_i)} \right) \Big/ \sum_i^{N_{bj}} w_i}{\sum_i^{N_{-bj}} \left(\frac{w_i}{\epsilon_{y,\delta}(t_i|\vec{\Omega}_i)} \right) \Big/ \sum_i^{N_{-bj}} w_i}, \tag{4.12}$$

where w_i are *sWeights*. It is the bin-by-bin correction method.

The effects of corrections on the Dalitz projections are shown in Figure 4.1. The dependence of these correction factors on y is parametrised by a second-order polynomial and accounted for directly in the fit. The strong-phase dependence is also propagated, keeping the measurement model-independent. Systematic uncertainties cover residual biases.

4.4 Phase-space and decay-time efficiency

The efficiency $\epsilon_{y,\delta}(t|\vec{\Omega})$ varies significantly across the phase space and decay time, with the specific behaviour depending on the trigger line and K^0_S reconstruction category. This section presents the efficiency maps obtained for all trigger selections, illustrating the multidimensional structure of the acceptance effects. Figures 4.2–4.5 show two-dimensional projections of the efficiency as a function of decay time and the Dalitz variables, integrated over the third dimension, for all five trigger lines (`TwoTracks`, `D2Kshh`, `OneTrack`, `KS`, and `TIS`) in both LL and DD categories for data-taking block 8. The comparison between trigger selections reveals notable differences in the efficiency structure: as expected, the exclusive `D2Kshh` line exhibits a flatter efficiency behaviour across the phase space, with higher minimum efficiency values, reflecting its more targeted selection criteria compared to the inclusive `TwoTracks` selection.

4.4.1 Adaptive 3D binning strategy

The determination of the efficiency correction requires a binning of the three-dimensional phase space spanned by the Dalitz plot variables ($m^2_{\pi\pi}$, $|\cos\theta_{\pi\pi}|$) and

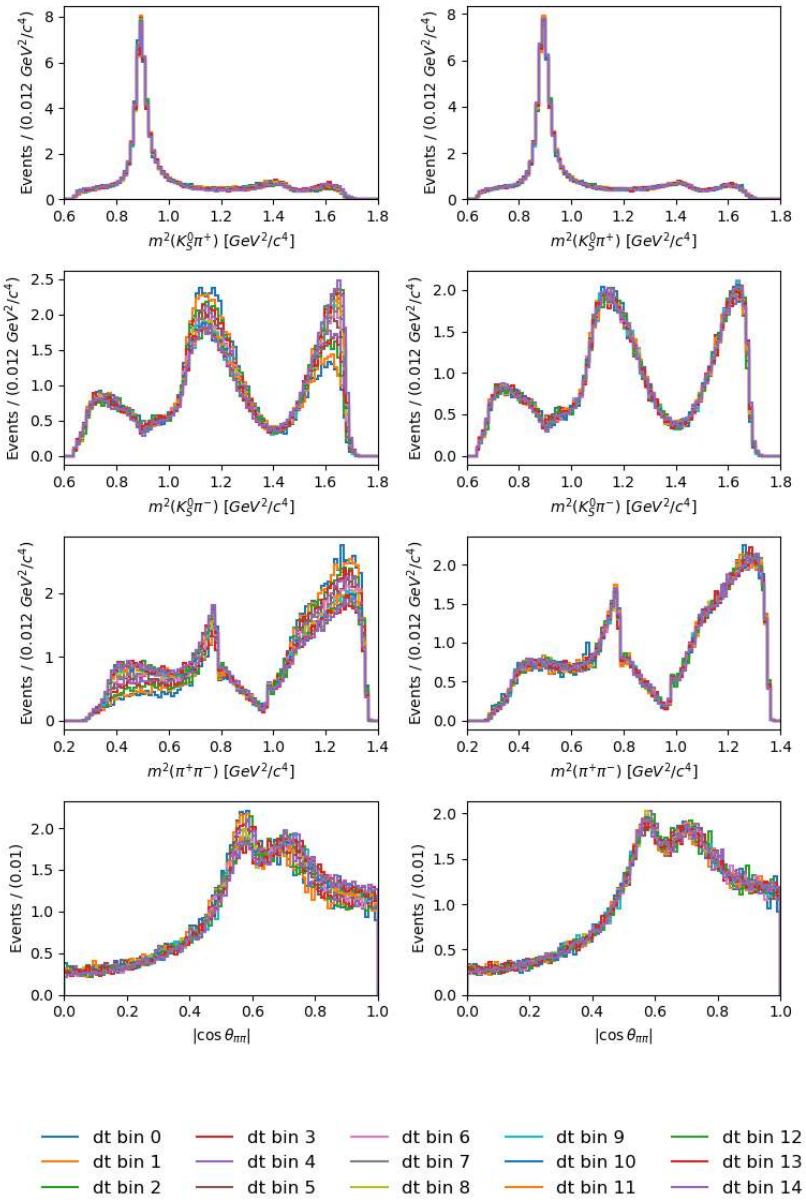

Figure 4.1: Dalitz plot projections in bins of decay time of `D2Kshh` block 8 sample (left) before and (right) after correction for (first row) $m^2_{\mathrm{K^0_S}\pi^+}$, (second row) $m^2_{\mathrm{K^0_S}\pi^-}$, (third row) $m^2_{\pi^+\pi^-}$ and (fourth row) $|cos_{\pi^+\pi^-}|$.

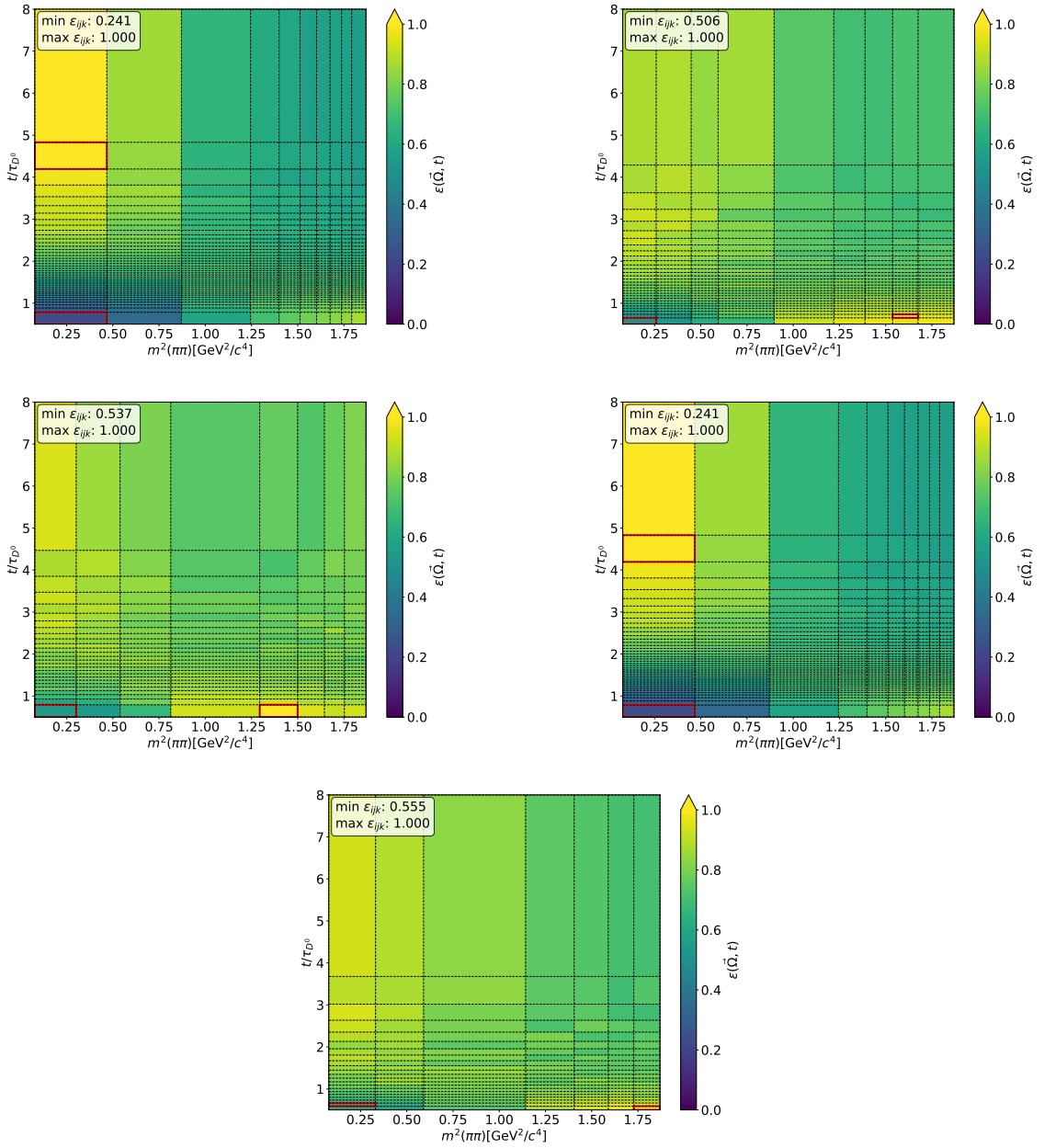

Figure 4.2: 2D projections of the efficiency $\epsilon_{y,\delta}(t|\vec{\Omega})$ as a function of decay time and $m^2_{\pi\pi}$, integrated over $|\cos\theta_{\pi\pi}|$, for all trigger lines in the LL category (block 8): (top left) `TwoTracks`, (top right) `D2Kshh`, (middle left) `OneTrack`, (middle right) `KS` and (bottom) `TIS`. In each panel, the red boxes highlight the cells containing the minimum and maximum values.

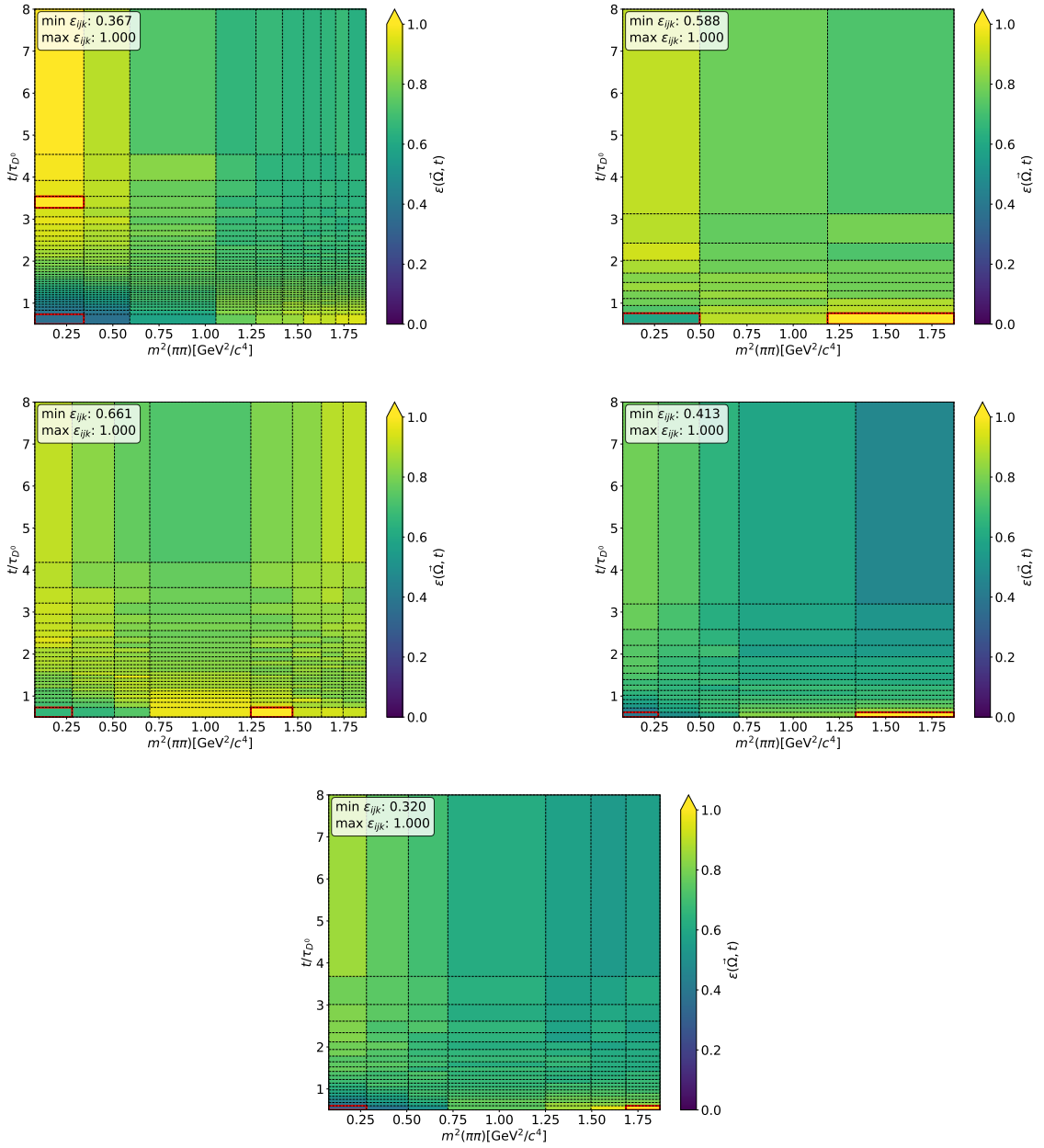

Figure 4.3: 2D projections of the efficiency $\epsilon_{y,\delta}(t|\vec{\Omega})$ as a function of decay time and $m^2_{\pi\pi}$, integrated over $|\cos\theta_{\pi\pi}|$, for all trigger lines in the DD category (block 8): (top left) `TwoTracks`, (top right) `D2Kshh`, (middle left) `OneTrack`, (middle right) `KS` and (bottom) `TIS`. In each panel, the red boxes highlight the cells containing the minimum and maximum values.

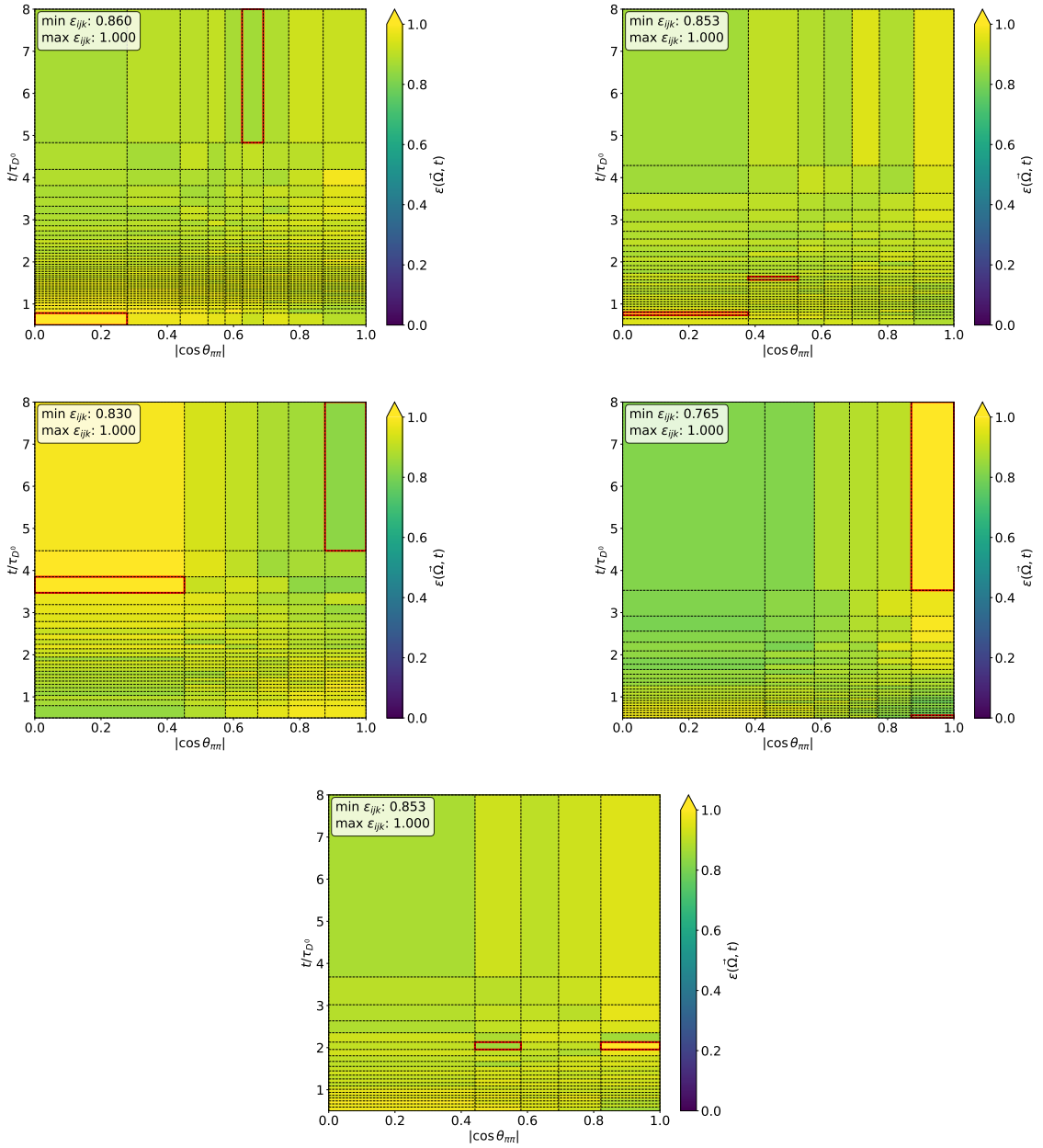

Figure 4.4: 2D projections of the efficiency $\epsilon_{y,\delta}(t|\vec{\Omega})$ as a function of decay time and $|\cos\theta_{\pi\pi}|$, integrated over $m^2_{\pi\pi}$, for all trigger lines in the LL category (block 8): (top left) `TwoTracks`, (top right) `D2Kshh`, (middle left) `OneTrack`, (middle right) `KS` and (bottom) `TIS`. In each panel, the red boxes highlight the cells containing the minimum and maximum values.

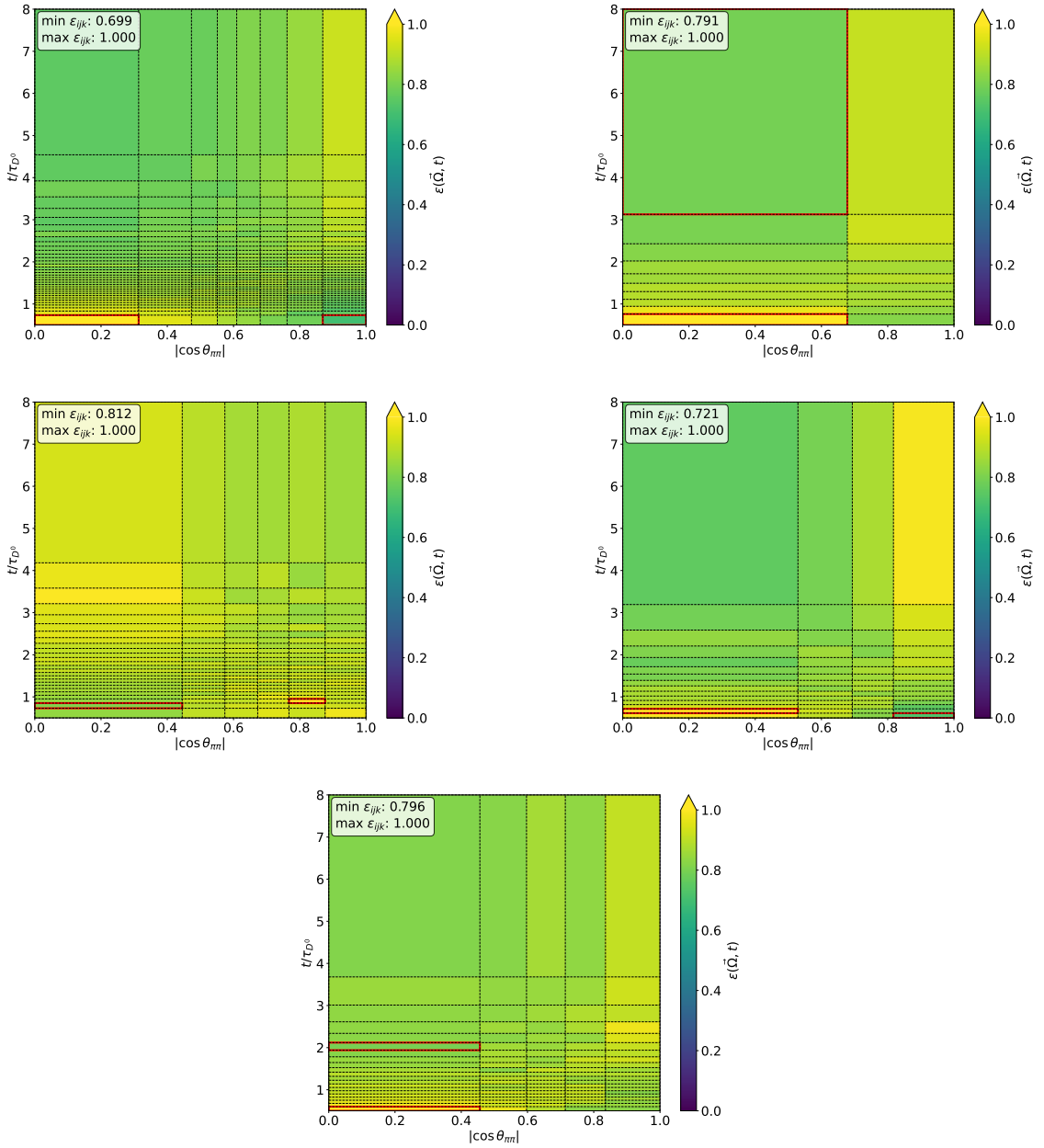

Figure 4.5: 2D projections of the efficiency $\epsilon_{y,\delta}(t|\vec{\Omega})$ as a function of decay time and $|\cos\theta_{\pi\pi}|$, integrated over $m^2_{\pi\pi}$, for all trigger lines in the DD category (block 8): (top left) `TwoTracks`, (top right) `D2Kshh`, (middle left) `OneTrack`, (middle right) `KS` and (bottom) `TIS`. In each panel, the red boxes highlight the cells containing the minimum and maximum values.

the decay time (t/τ). A fixed, uniform binning scheme would be suboptimal: regions of high event density would be over-binned, while regions of low statistics would suffer from large statistical uncertainties. To address this, an adaptive binning strategy is employed, in which the bin boundaries are determined recursively based on the local event density in each dimension.

The binning procedure operates recursively across the three dimensions. First, the $m^2_{\pi\pi}$ axis is divided into bins using the quantile-based method described in Section 3.2.1, ensuring approximately equal signal yield per bin. For each $m^2_{\pi\pi}$ bin, the $|\cos\theta_{\pi\pi}|$ axis is then subdivided adaptively within that specific $m^2_{\pi\pi}$ slice, again targeting uniform population. Finally, within each ($m^2_{\pi\pi}$, $|\cos\theta_{\pi\pi}|$) bin, the decay time axis is binned adaptively. This recursive approach produces a nested binning structure in which the bin edges of each dimension depend on the data distribution within the bins defined by the previous dimensions, naturally adapting to the multidimensional event density.

The total number of 3D bins is determined by a target number of signal events per bin, denoted N_{target}. Given the total signal yield N_{sig} within the specified ranges, the target number of 3D bins is $N^{\text{3D}}_{\text{bins}} = N_{\text{sig}}/N_{\text{target}}$. Two strategies are implemented to distribute this total number of bins across the three dimensions:

- **Equal strategy**: Each dimension receives an equal share of bins, i.e., $N_x = N_y = N_z = \lceil (N^{\text{3D}}_{\text{bins}})^{1/3} \rceil$, where N_x, N_y, and N_z denote the number of bins along $m^2_{\pi\pi}$, $|\cos\theta_{\pi\pi}|$, and t/τ, respectively.
- **Proportional strategy**: The number of bins in each dimension is allocated proportionally to the weighted standard deviation of that variable, reflecting the "spread" of the distribution. Specifically, let σ_x, σ_y, and σ_z denote the weighted standard deviations of $m^2_{\pi\pi}$, $|\cos\theta_{\pi\pi}|$, and t/τ. T he scaling factor k is determined by

$$k = \left(\frac{N^{\text{3D}}_{\text{bins}}}{\sigma_x \cdot \sigma_y \cdot \sigma_z} \right)^{1/3}, \tag{4.13}$$

  and the number of bins in each dimension is given by $N_x = \lceil k \cdot \sigma_x \rceil$, $N_y = \lceil k \cdot \sigma_y \rceil$, and $N_z = \lceil k \cdot \sigma_z \rceil$. This approach allocates more bins to dimensions with larger variance, thereby achieving finer granularity where the data is more spread out.

The proportional strategy is adopted as the default choice, as it provides a more balanced resolution across dimensions with different intrinsic scales. The adaptive 3D binning is applied separately for each trigger line and K^0_S reconstruction category, optimising the bin structure for the specific characteristics of each sample. The target number of events per 3D bin is set to 500, which is enough to ensure sufficient statistics for reliable efficiency determination while maintaining fine granularity to capture the efficiency variations across the phase space and decay time.

4.4.2 Validation with toy Monte Carlo

In this section, the acceptance correction procedure is validated using toy Monte Carlo (MC) simulations. Two independent toy MC samples of approximately one million $D^0 \to K^0_S\pi^+\pi^-$ decays are generated. In both samples, the decay time is generated with the nominal D^0 lifetime, and the underlying decay dynamics are identical.

- The *No ACC* sample is generated uniformly in phase space and without any acceptance effects. It represents the ideal reference case and defines the ground-truth distributions and bin-flip ratios.
- The *With ACC* sample includes realistic acceptance effects that depend on the Dalitz plot position and on the decay time, mimicking the impact of detector geometry, reconstruction, and trigger requirements.

Any difference observed between the two samples can therefore be unambiguously attributed to acceptance effects. The impact of acceptance on the observables is shown in one-dimensional projections of the Dalitz plot variables and the decay time (Figures 4.6).

Impact on bin-flip ratios. The acceptance-induced distortions propagate to the physics observables used in the analysis. This effect is illustrated by comparing the bin-flip ratios R_{bj} obtained from the *No ACC* and *With ACC* samples as a function of decay time (Figure 4.7). Acceptance effects introduce systematic, decay-time-dependent biases whose magnitude and sign vary across bin-flip bins.

Construction of the three-dimensional efficiency map. To correct for acceptance effects, the three-dimensional efficiency map $\epsilon_{ijk} = \epsilon\left(m^2_{\pi\pi}, |\cos\theta_{\pi\pi}|, t/\tau\right)$ is constructed using the *With ACC* sample (Figure 4.8). The phase space is partitioned using an adaptive binning scheme in the Dalitz variables and decay time.

Event-by-event acceptance correction. Each event in the *With ACC* sample is assigned a weight

$$w_i = \frac{1}{\epsilon_{ijk}(t_i, \vec{\Omega}_i)}, \tag{4.14}$$

where $\vec{\Omega}$ denotes the Dalitz plot coordinates of the event. After applying these corrections, the one-dimensional variables from Figure 4.6 were replotted to verify that the distributions of the *With ACC* sample remain unchanged (Figure 4.9).

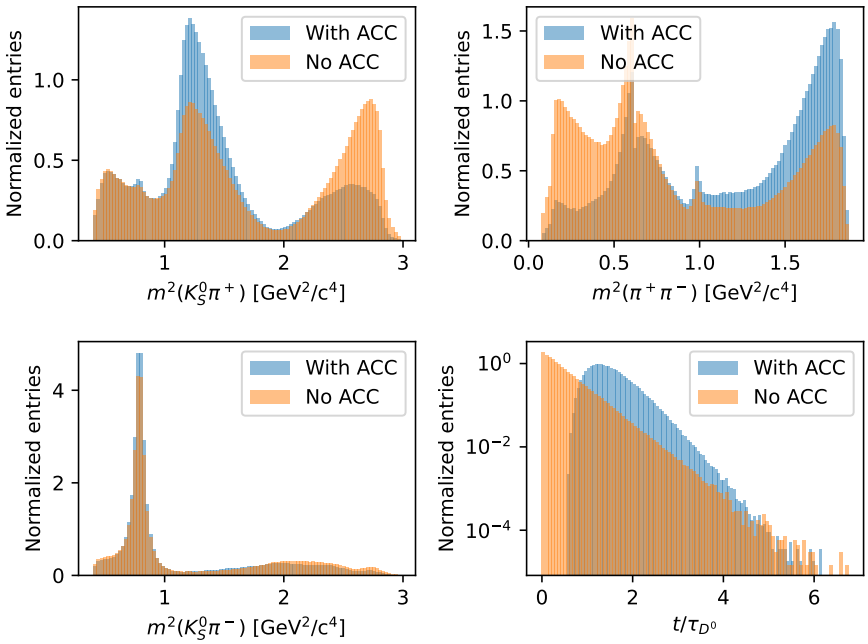

Figure 4.6: 1D projections of the Dalitz plot variables and decay time for the toy samples without acceptance (*No ACC*) and with acceptance (*With ACC*). All distributions are normalised.

Decay-time dependence of the Dalitz distributions. The validity of the correction is further tested by studying Dalitz plot projections in bins of decay time. Before correction, the phase-space distributions exhibit a clear decay-time dependence induced by acceptance effects. After correction, the distributions in different decay-time intervals become mutually consistent (Figure 4.10).

Correction of bin-flip ratios. The acceptance correction is finally applied to the bin-flip ratios, either by computing the ratios directly from weighted yields or by applying bin-by-bin correction factors. Both approaches lead to equivalent results within statistical uncertainties (Figure 4.11).

Fit of the bin-flip ratios. As a further validation step, the corrected bin-flip ratios are used as input to the nominal fitting procedure employed in the analysis. The ratios R_{bj} are fitted as a function of decay time using the same parametrisation adopted for data, with the mixing parameters left free in the fit. Since the toy samples are generated without *CP* violation, the fit is expected to return mixing values

consistent with the generation hypothesis. This step tests not only the acceptance correction itself, but also its interplay with the full fitting framework.

Then, the fitted values of the physics parameters are compared to the nominal generation values (Figure 4.12). After acceptance correction, the fitted parameters are found to be consistent with zero within statistical uncertainties, and no significant bias is observed.

Conclusion. This validation using toy Monte Carlo simulations demonstrates that the acceptance correction procedure based on a 3D efficiency map successfully removes acceptance-induced correlations from both phase-space distributions and decay-time-dependent bin-flip ratios. The corrected observables are in agreement with the reference distributions within statistical uncertainties, validating the method for application to data.

To further test the robustness of the procedure, it was applied to 700 toy experiments with the same acceptance model, and generated using different random seeds, assuming no *CP* violation. For each toy, the distributions of the pulls were studied (Figure 4.13). The results show that the correction procedure does not bias the values of x and y, confirming the reliability of the method. However, it was observed that the uncertainties are underestimated by approximately 23% for x and 28% for y, which could be due to the treatment of the strong phases.

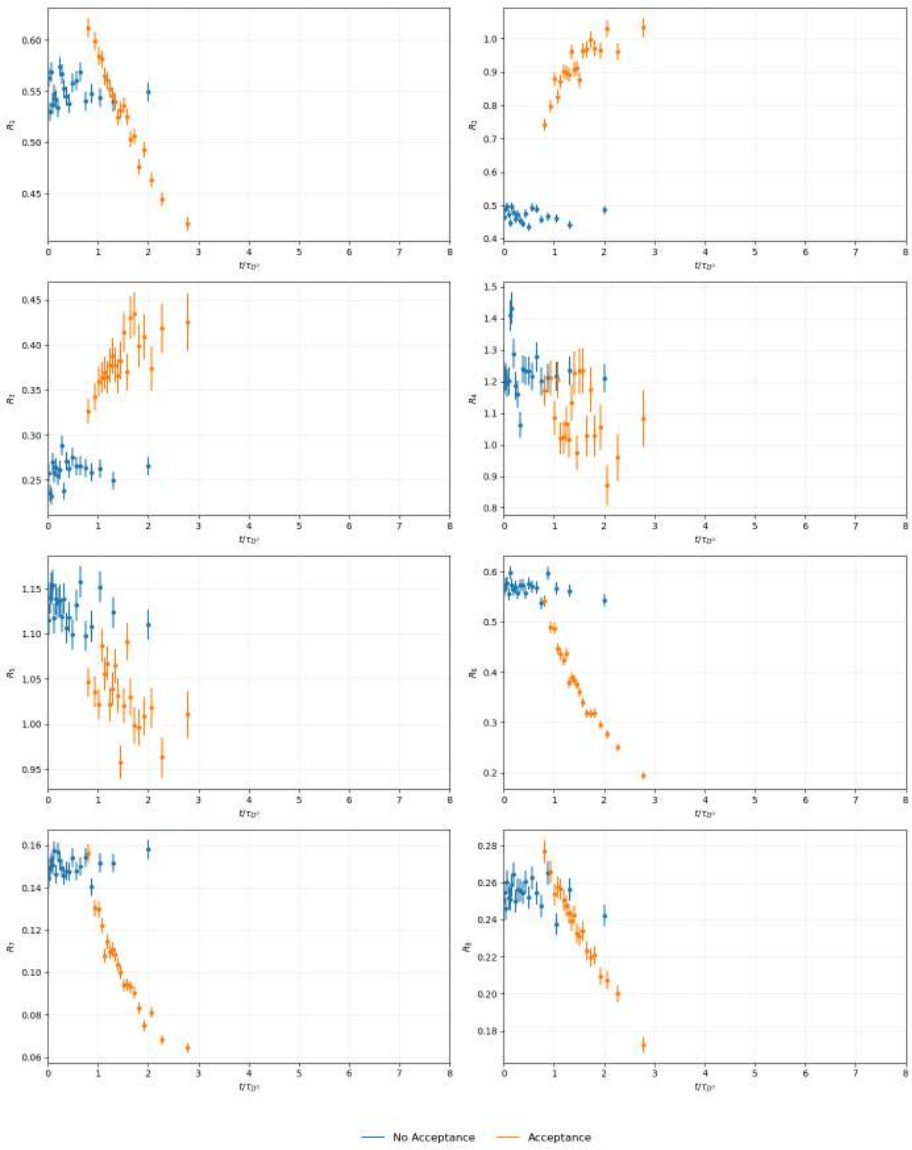

Figure 4.7: Bin-flip ratios R_{bj} as a function of decay time for the toy samples without acceptance and with acceptance, before applying any correction.

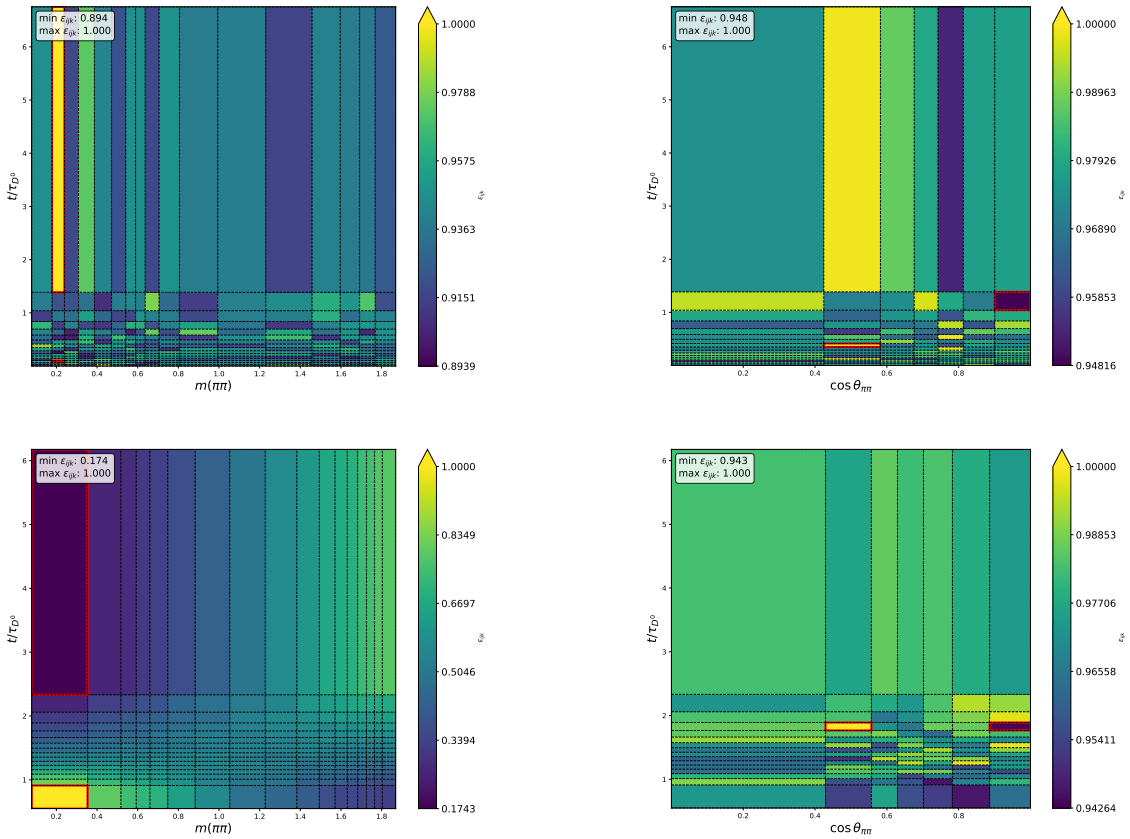

Figure 4.8: 2D projections of the efficiency $\epsilon(t|\vec{\Omega})$ as a function of decay time and (left) $m^2_{\pi\pi}$ integrated over $|\cos\theta_{\pi\pi}|$, (right) $|\cos\theta_{\pi\pi}|$ integrated over $m^2_{\pi\pi}$, for sample (left) without acceptance and (right) with acceptance.

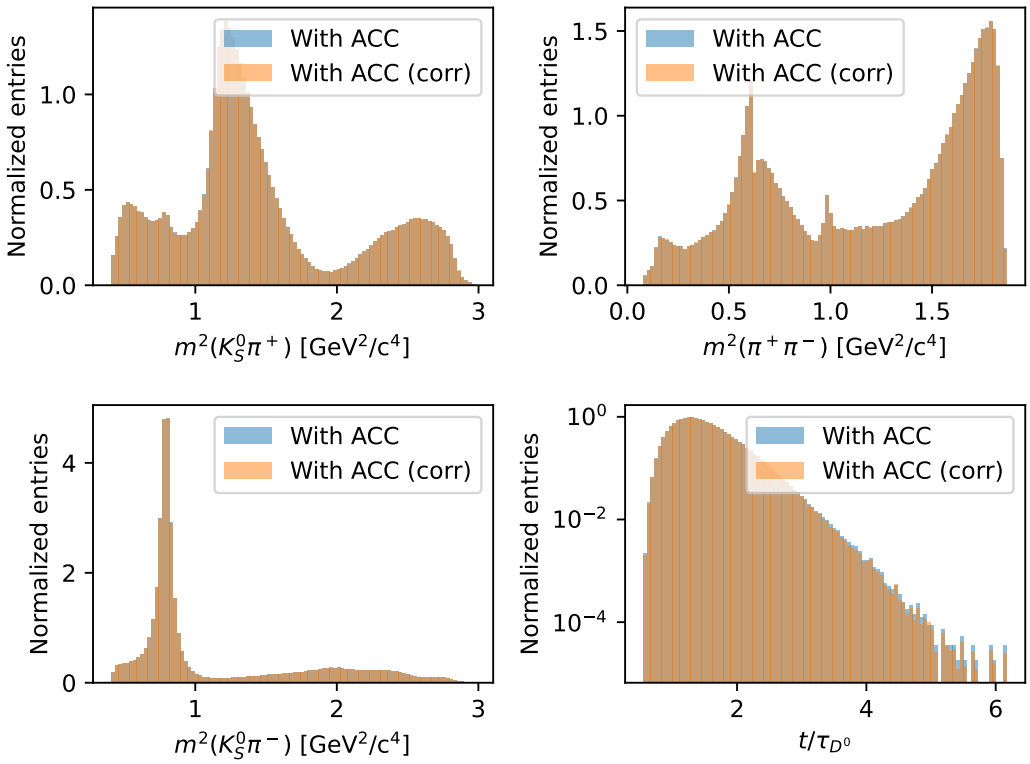

Figure 4.9: 1D projections for the sample with acceptance before and after applying the event-by-event efficiency correction.

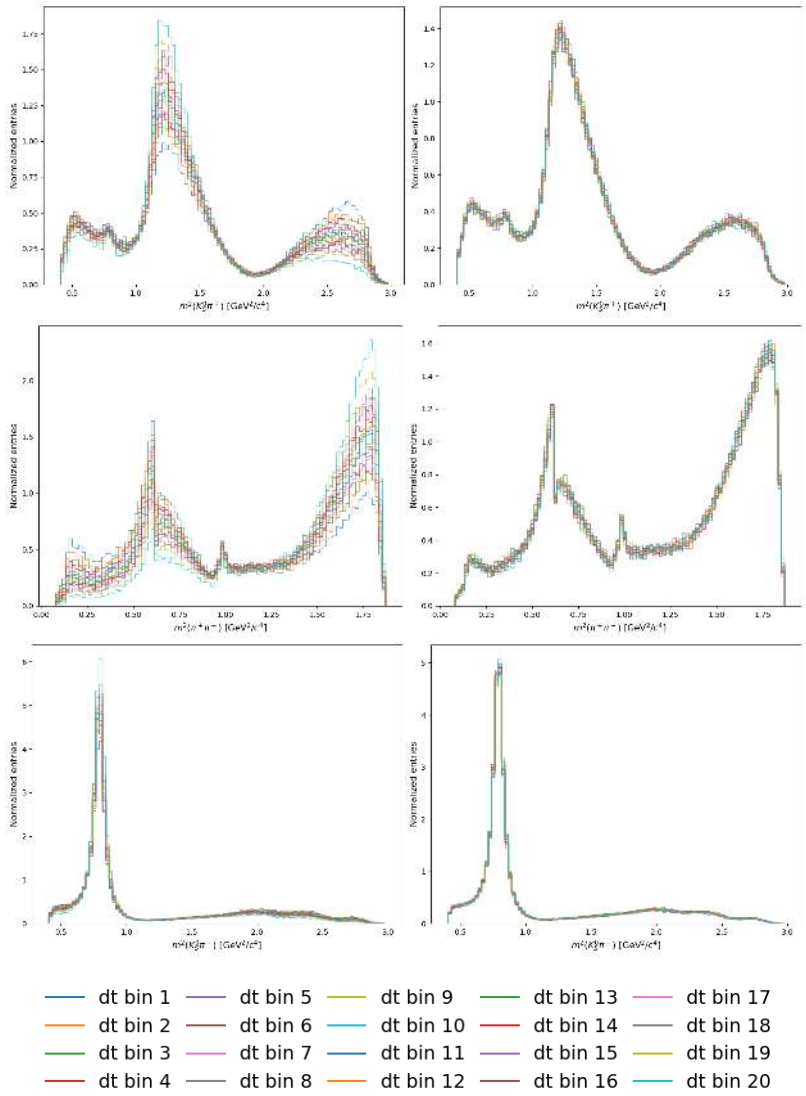

Figure 4.10: Dalitz plot projections in bins of decay time (left) before and (right) after acceptance correction for (top) $m^2_{\mathrm{K}^0_{\mathrm{S}}\pi^+}$, (middle) $m^2_{\pi^+\pi^-}$ and (bottom) $m^2_{\mathrm{K}^0_{\mathrm{S}}\pi^-}$

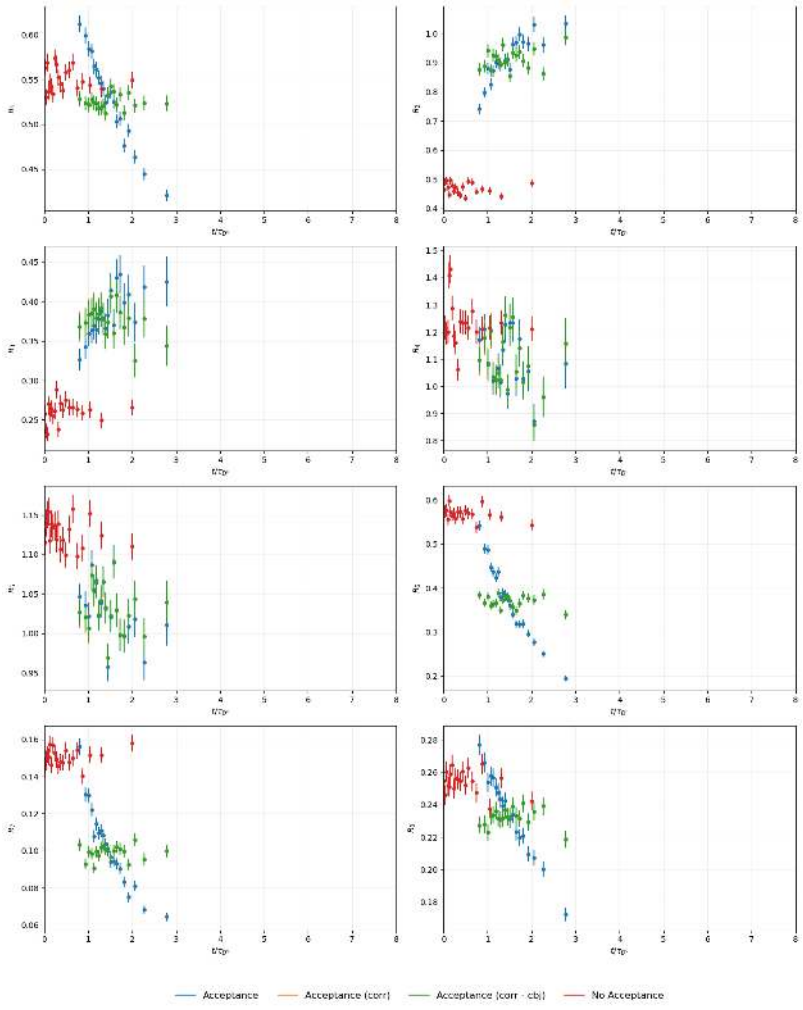

Figure 4.11: Bin-flip ratios as a function of decay time. The *Acceptance (corr)* dataset corresponds to the *Acceptance* one, corrected using efficiency maps before computing the ratio. For the *Acceptance (corr-cbj)* points, the ratio is corrected directly before plotting. The orange and green points overlap perfectly, demonstrating that the two procedures yield the same results. The correction successfully restores the expected linear behaviour.

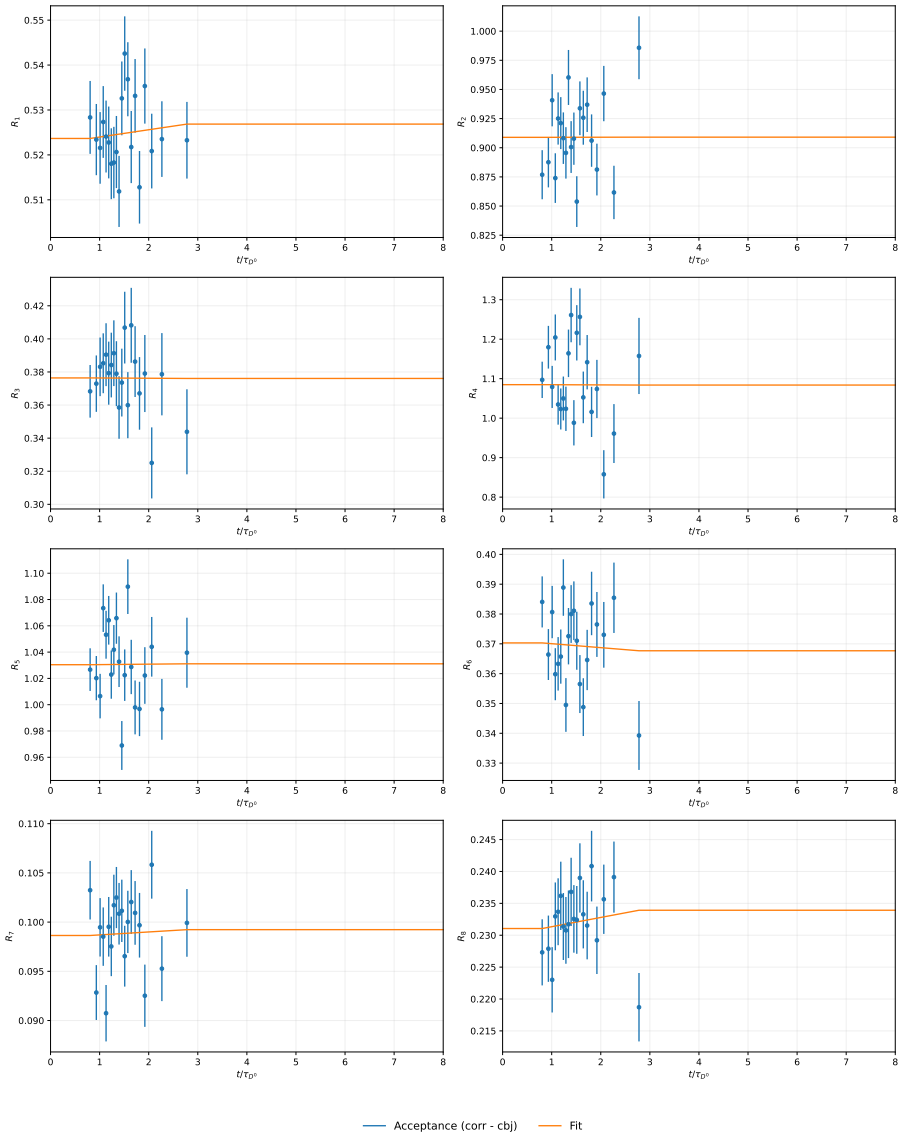

Figure 4.12: Corrected bin-flip ratios as a function of decay time for a toy Monte Carlo sample. Blue points represent the corrected ratios, while the orange lines show the fit projections.

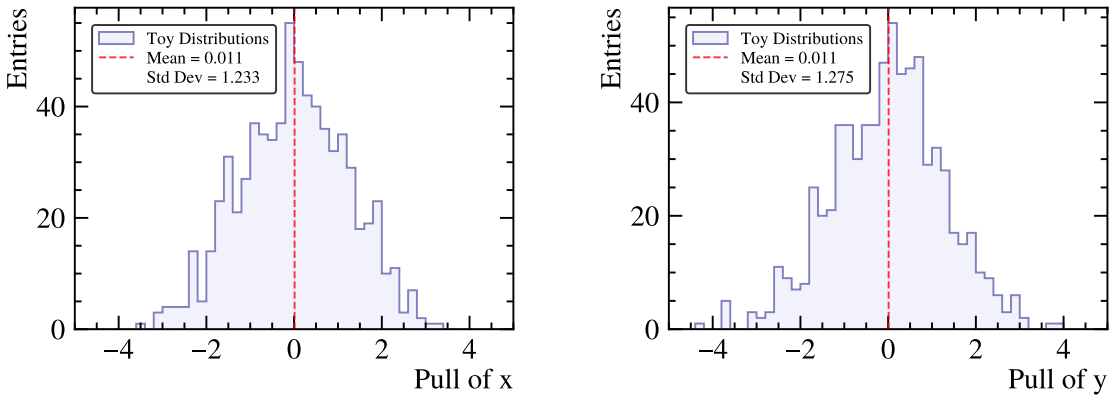

Figure 4.13: Distributions of pulls for 700 toys after applying the acceptance correction procedure: (left) x and (right) y.

Chapter 5

Detection asymmetry effects

Detection asymmetries arising from different reconstruction efficiencies for positively and negatively charged pions can induce efficiency variations across the Dalitz plot that are not symmetric with respect to its bisector. Such effects can mimic CP-violating signatures and introduce biases in the determination of the mixing parameters x and y in time-dependent Dalitz plot analyses. In this chapter, the impact of detection asymmetries is discussed, and the strategy adopted to account for them is outlined. Although no final quantitative result is derived within the scope of this work, this discussion is included as detection asymmetries are relevant for the interpretation of the fit parameters and for the overall understanding of the analysis. Dedicated studies of these effects are currently ongoing.

5.1 Determination of π^+ and π^- detection asymmetry with D_s^+ decays

The dominant source of detection asymmetry in the decay $D^0 \to K^0_S\pi^+\pi^-$ originates from the different reconstruction efficiencies of π^+ and π^- mesons, which depend on their kinematic properties. As the kinematics of the two pions vary across the Dalitz plot, this effect can lead to an efficiency variation that is not symmetric with respect to the Dalitz plot bisector. If not properly accounted for, such an asymmetry can mimic *CP*-violating effects and bias the determination of the mixing parameters.

The combined detection asymmetry of the $\pi^+\pi^-$ pair is determined using Cabibbo-favoured D_s^+ decays. In particular, the decays $D_s^+ \to \pi^+\pi^+\pi^-$ and $D_s^+ \to \phi\pi^+$ are exploited. The raw asymmetries measured in these two modes differ only by the contribution of the $\pi^+\pi^-$ pair, while production asymmetries of the D_s^+ meson and detection asymmetries of the bachelor pion cancel to first order when taking their difference.

Residual effects due to differences in kinematic distributions between the two decay modes are removed by a dedicated weighting procedure. The weighting aligns the momentum and pseudo-rapidity distributions of the pions and the D_s^+ candidates with those of the signal $D^0 \to K^0_S\pi^+\pi^-$ decays. This procedure is performed independently in each Dalitz plot bin to properly account for the strong kinematic dependence of the detection asymmetry. The possible contribution to the detection asymmetry arising from differences in the kinematic distributions of the two kaons from the $\phi \to K^+K^-$ decay [115], induced by interference between the $\phi \to K^+K^-$ and S-wave K^+K^- amplitudes, has not been studied yet and will be considered in the future development of the analysis.

5.2 Detection asymmetry variations vs Dalitz and decay-time

The detection asymmetry is studied as a function of the Dalitz plot position and the decay-time. Instead of the standard Dalitz variables, the asymmetry is parameterised in bins of $(m^2_{\pi^+\pi^-}, |\cos\theta_{\pi^+\pi^-}|)$, which are more directly correlated with the pion kinematics.

The measured asymmetries are found to be small on average, but exhibit clear variations across the phase space. Larger asymmetries are observed near the edges of the Dalitz plot, where the momenta of the two pions differ most strongly. This behaviour is consistent with the underlying dependence of the tracking efficiency on particle momentum.

Since the pion kinematics are correlated with the decay-time, a time-dependent detection asymmetry can arise. The asymmetry is therefore also evaluated in bins of decay-time. While only weak variations are observed when binning in $m^2_{\pi^+\pi^-}$, more pronounced trends are seen as a function of $|\cos\theta_{\pi^+\pi^-}|$ and decay-time. Such effects, if neglected, could induce biases in time-dependent *CP*-violation measurements.

5.3 Input to toys

The measured detection asymmetries are used as input to pseudo-experiments to quantify their impact on the fitted observables. The reconstruction efficiency is modified by an asymmetry term that depends on the Dalitz plot coordinates, the decay-time, and the flavour of the decaying meson.

An efficiency correction factor is constructed such that the asymmetry enters with opposite sign for D^0 and $\overline{D}^0$ decays. The asymmetry maps are obtained in bins of $(m^2_{\pi^+\pi^-}, |\cos\theta_{\pi^+\pi^-}|)$, while the time dependence is modelled by linear functions in

decay-time determined in bins of $|\cos\theta_{\pi^+\pi^-}|$. The resulting parametrisation is applied consistently across the full Dalitz plot, preserving the average asymmetry in each bin.

Variations of the time-dependent slopes are considered in the pseudo-experiments to account for statistical uncertainties and to provide a conservative estimate of the associated systematic effects.

5.4 Correction for bin-flip fit

In the bin-flip formalism, the presence of detection asymmetries leads to an additional multiplicative correction in the ratio of yields between symmetric Dalitz plot bins. The pion reconstruction efficiencies are expressed in terms of an average efficiency and a momentum-dependent asymmetry term.

Neglecting terms of second order in the asymmetry, the ratio of efficiencies between a bin and its mirror bin can be written as a correction factor that depends on the difference between the average asymmetries in the two bins. This correction enters the bin-flip fit as an external constraint.

The required asymmetry parameters are obtained from the calibrated $\mathrm{D}_\mathrm{s}^+ \to \pi^+\pi^+\pi^-$ sample, weighted to the kinematics of the $\mathrm{D}^0 \to \mathrm{K}^0_\mathrm{S}\pi^+\pi^-$ signal. The procedure is repeated for all trigger categories, years, and magnet polarities, and the results are combined using yield-weighted averages. Correlations between bins and trigger categories are explicitly taken into account.

5.4.1 Systematic uncertainty of detection asymmetry

The calibration sample differs slightly from the signal sample due to tighter selection requirements on particle identification and transverse momentum. To account for this mismatch, alternative tag-and-probe methods are employed to estimate single-particle tracking and particle identification asymmetries.

These alternative asymmetry maps are weighted to the signal kinematics and used to evaluate the impact of events not covered by the calibration selection. The resulting contributions are treated as systematic uncertainties and combined in quadrature with the statistical uncertainties of the detection asymmetry correction. The total uncertainties are propagated to the bin-flip fit via the external constraints.

5.5 Uncertainties on x and y due to detection asymmetries

The inclusion of detection asymmetry corrections in the fit leads to a small increase in the overall uncertainty on the mixing parameters. The additional uncertainty induced by the external constraints is expected to be subdominant with respect to

the statistical uncertainty, and dedicated studies to quantify this effect are currently ongoing.

Systematic effects associated with time-dependent detection asymmetries are evaluated using pseudo-experiments. Their impact on the parameter x is negligible, while for y the associated systematic uncertainty amounts to a sizeable fraction of the statistical uncertainty. Overall, detection asymmetries are shown to be well controlled and do not limit the precision of the measurement.

Chapter 6

Results

This chapter presents the results of the bin-flip analysis applied to the data sample under study. The charm mixing and CP-violation parameters are extracted from fits to the acceptance-corrected bin-flip ratios as a function of decay time, following the methodology described in the previous chapters.

6.1 Determination of the mixing and *CP*-violation parameters

The determination of the charm mixing and *CP*-violation parameters is based on a fit to the acceptance-corrected bin-flip ratios as a function of decay time. The bin-flip observables and the underlying efficiency assumptions are discussed in detail in Section 1.8 and Section 3.3. In the following, only the steps required to extract the physics parameters from the corrected ratios are described.

Input observables. The input to the fit consists of the bin-flip ratios R_{bj} measured in bins of Dalitz index b and decay-time index j, separately for D^0 and $\overline{\mathrm{D}}^0$ samples. The ratios are corrected for residual decay-time–Dalitz correlations using the procedure described in Chapter 4, and the corresponding statistical uncertainties are scaled by the same correction factors.

Theoretical model. The time-dependent bin-flip ratios are described by an analytical model derived within the bin-flip formalism. For each Dalitz bin b, the predicted ratio depends on the hadronic parameter r_b, the strong-phase inputs (c_b, s_b), and the complex mixing parameters

$$z = -(y + ix), \qquad \Delta z = -(\Delta y + i\,\Delta x), \tag{6.1}$$

The decay-time dependence is expanded up to second order in t/τ_{D^0}:

$$R_{bj}^{\pm} \approx \frac{r_b + \frac{1}{4} r_b \langle t^2 \rangle_j \,\mathrm{Re}(z_{CP}^2 - \Delta z^2) + \frac{1}{4} \langle t^2 \rangle_j |z_{CP} \pm \Delta z|^2 + \sqrt{r_b} \langle t \rangle_j \,\mathrm{Re}[X_b^*(z_{CP} \pm \Delta z)]}{1 + \frac{1}{4} \langle t^2 \rangle_j \,\mathrm{Re}(z_{CP}^2 - \Delta z^2) + r_b \frac{1}{4} \langle t^2 \rangle_j |z_{CP} \pm \Delta z|^2 + \sqrt{r_b} \langle t \rangle_j \,\mathrm{Re}[X_b(z_{CP} \pm \Delta z)]}, \tag{6.2}$$

already discussed in details in Section 1.8 (Equation 1.110). The flavour of the initial state enters through sign changes in the interference terms, allowing a simultaneous description of D^0 and $\overline{\mathrm{D}}^0$ samples within the same framework.

Construction of the χ^2 function. The determination of the charm mixing and *CP*-violation parameters is performed by minimising a total χ^2 function that accounts both for the measured bin-flip ratios and for external constraints on the strong-phase parameters. The total χ^2 is defined as

$$\chi^2 = \chi^2_{\mathrm{ratios}} + \chi^2_{\mathrm{ext}}, \tag{6.3}$$

where the first term quantifies the agreement between the acceptance-corrected bin-flip ratios and the theoretical model, and the second term imposes Gaussian constraints on the strong-phase parameters c_i and s_i.

The contribution from the bin-flip ratios is

$$\chi^2_{\mathrm{ratios}} = \sum_{\mathrm{flavour}} \sum_{b=1}^{8} \sum_{j} \left(\frac{R_{bj}^{\mathrm{corr}} - R_b^{\mathrm{th}}(t_j)}{\sigma_{bj}^{\mathrm{corr}}} \right)^2, \tag{6.4}$$

where R_{bj}^{corr} and $\sigma_{bj}^{\mathrm{corr}}$ are the acceptance-corrected ratio and its statistical uncertainty in Dalitz bin b and decay-time bin j, and $R_b^{\mathrm{th}}(t_j)$ is the theoretical prediction evaluated at the centre of the decay-time bin. Statistical uncertainties are treated as uncorrelated. The sums run over all decay-time bins, Dalitz bins, and, when applicable, both initial flavours.

External information on the strong-phase parameters is included through a multivariate Gaussian term,

$$\chi^2_{\mathrm{ext}} = \left(\vec{X} - \vec{X}_{\mathrm{ext}}\right)^T V_{\mathrm{ext}}^{-1} \left(\vec{X} - \vec{X}_{\mathrm{ext}}\right), \tag{6.5}$$

where

$$\vec{X} = (c_1, \ldots, c_8, s_1, \ldots, s_8)$$

is the vector of fitted strong-phase parameters, $\vec{X}_{\mathrm{ext}}$ denotes the externally measured central values, and V_{ext} is the full covariance matrix including both statistical and systematic uncertainties. This ensures that the uncertainties and correlations from the external measurement propagate correctly into the determination of the charm mixing and *CP*-violation observables.

The external inputs are taken from the combined results of the BESIII and CLEO measurements [71] and are summarised in Tables 6.1–6.3. Table 6.1 lists the measured values of c_b and s_b for each Dalitz bin, with the first uncertainty statistical and the second systematic. Tables 6.2 and 6.3 provide the statistical and systematic correlation coefficients, respectively. These inputs are used to construct the covariance matrix V_{ext}, which is then inverted and included in the χ^2_{ext} term in the fit.

Table 6.1: Measured values of the strong-phase parameters c_b and s_b for each Dalitz bin b. The first uncertainty is statistical, and the second is systematic.

b	$c_b \pm \sigma_{\text{stat}} \pm \sigma_{\text{syst}}$	$s_b \pm \sigma_{\text{stat}} \pm \sigma_{\text{syst}}$
1	$0.682 \pm 0.017 \pm 0.008$	$-0.007 \pm 0.052 \pm 0.006$
2	$0.602 \pm 0.035 \pm 0.013$	$0.270 \pm 0.120 \pm 0.022$
3	$0.060 \pm 0.034 \pm 0.009$	$0.666 \pm 0.088 \pm 0.015$
4	$-0.553 \pm 0.043 \pm 0.012$	$0.681 \pm 0.123 \pm 0.023$
5	$-0.955 \pm 0.017 \pm 0.007$	$-0.117 \pm 0.056 \pm 0.005$
6	$-0.574 \pm 0.043 \pm 0.014$	$-0.431 \pm 0.110 \pm 0.018$
7	$0.072 \pm 0.045 \pm 0.014$	$-0.810 \pm 0.102 \pm 0.018$
8	$0.522 \pm 0.030 \pm 0.011$	$-0.363 \pm 0.080 \pm 0.010$

Fit strategy. The minimisation of the χ^2 function is performed using the MINUIT package [116]. The free parameters of the fit are the real and imaginary parts of z, the eight hadronic parameters r_b, and, in the simultaneous $\mathrm{D}^0 + \overline{\mathrm{D}}^0$ fit, the real and imaginary parts of Δz. In fits to a single flavour, Δz is fixed to its nominal value. The fit quality is assessed using the minimum χ^2, the number of degrees of freedom, and the convergence and covariance diagnostics provided by the minimiser. The results are shown in Figures 6.1–6.2.

The strong-phase parameters c_b and s_b are treated as free parameters in the fit and constrained through the external Gaussian term included in the χ^2 function.

Extraction of the mixing parameters x and y. Within the bin-flip formalism, the physical mixing parameters x and y are obtained directly from the fitted complex

Table 6.2: Statistical correlation coefficients (in %) between the c_b and s_b parameters.

	c_2	c_3	c_4	c_5	c_6	c_7	c_8	s_1	s_2	s_3	s_4	s_5	s_6	s_7	s_8
c_1	-11	-1	0	0	0	0	0	0	0	0	0	0	0	0	0
c_2		-7	0	0	0	-2	-1	0	-1	0	-1	0	0	0	0
c_3			-6	0	0	-1	0	-1	0	-1	0	0	1	2	0
c_4				-10	0	0	0	0	0	0	1	0	0	0	0
c_5					-9	0	0	0	0	0	-2	-5	0	5	1
c_6						-13	0	-1	0	0	0	-7	-1	0	0
c_7							-4	0	0	0	1	0	-5	0	1
c_8								0	1	2	5	1	0	-1	0
s_1									8	11	-6	-7	0	-4	-1
s_2										2	-6	0	-1	-10	1
s_3											-13	-7	0	0	0
s_4												0	-3	-8	-2
s_5													-1	0	-5
s_6														-7	0
s_7															-13

Table 6.3: Systematic correlation coefficients (in %) between the c_b and s_b parameters.

	c_2	c_3	c_4	c_5	c_6	c_7	c_8	s_1	s_2	s_3	s_4	s_5	s_6	s_7	s_8
c_1	72	64	59	55	42	32	26	49	30	29	25	14	18	-18	-28
c_2		32	31	53	89	62	26	30	29	20	11	14	-22	-22	-14
c_3			18	3	53	77	27	13	20	0	17	42	27	8	2
c_4				31	54	43	11	0	20	-21	-30	-22	36	34	0
c_5					55	20	14	-8	18	27	33	-39	27	27	10
c_6						32	1	-27	-8	-19	27	-4	12	12	-2
c_7							-13	-13	-11	-19	16	-4	15	-17	-8
c_8								11	13	12	18	7	-11	-9	-14
s_1									24	22	19	17	-9	-6	6
s_2										17	19	28	-11	-1	2
s_3											9	22	-16	-28	-19
s_4												22	-19	-16	6
s_5													-9	-15	2
s_6														-9	-11
s_7															-14

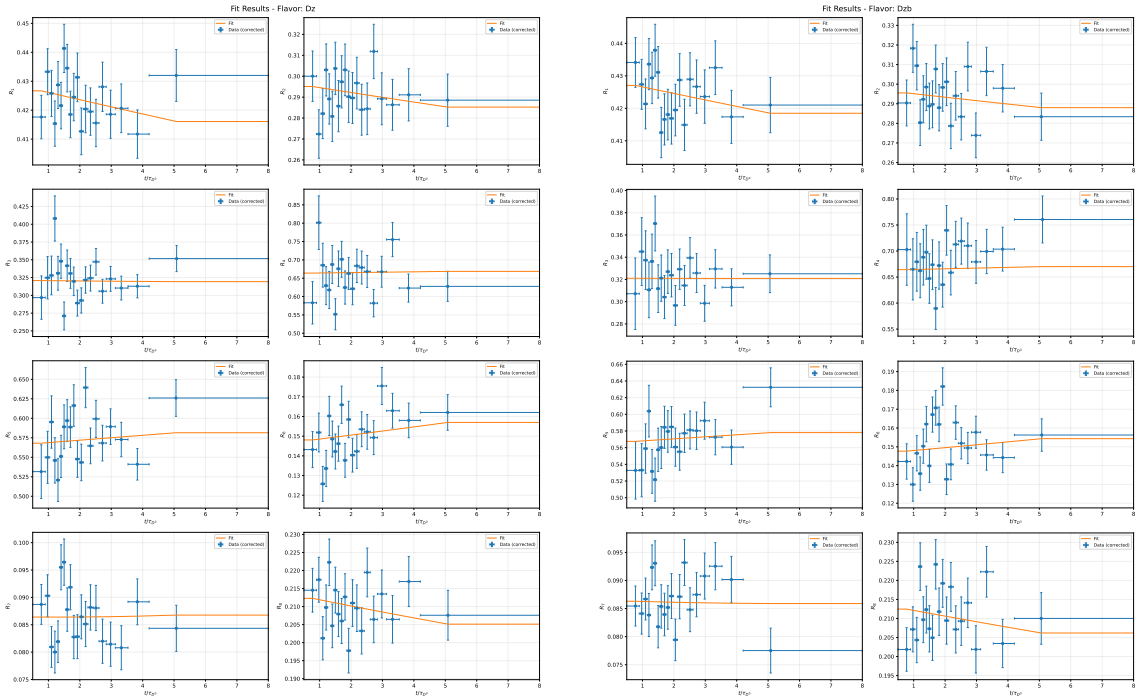

Figure 6.1: Results of the simultaneous fit for the block 8 `TwoTracks` LL sample. The ratios $R_1, \ldots, R_8$ are shown as a function of the reduced decay time for both (left) D^0 and (right) $\overline{\mathrm{D}}^0$ flavours. The blue points are the data after the correction procedure, and the orange line is the fit projection.

parameter z according to

$$x_{CP} = -\mathcal{I}m(z), \qquad y_{CP} = -\mathcal{R}e(z). \tag{6.6}$$

The uncertainties on x_{CP} and y_{CP} are taken directly from the covariance matrix of the fitted parameters $(\mathcal{R}e(z), \mathcal{I}m(z))$, as provided by the minimisation procedure. This approach avoids the need for additional transformations or external inputs and preserves the full correlation structure of the fit.

Extraction of Δx and Δy. In the simultaneous fit to the D^0 and $\overline{\mathrm{D}}^0$ samples, *CP*-violating effects in mixing are parameterised through the complex quantity Δz. The corresponding observables Δx and Δy are obtained directly from the fitted parameters as

$$\Delta x = -\mathcal{I}m(\Delta z), \quad \Delta y = -\mathcal{R}e(\Delta z). \tag{6.7}$$

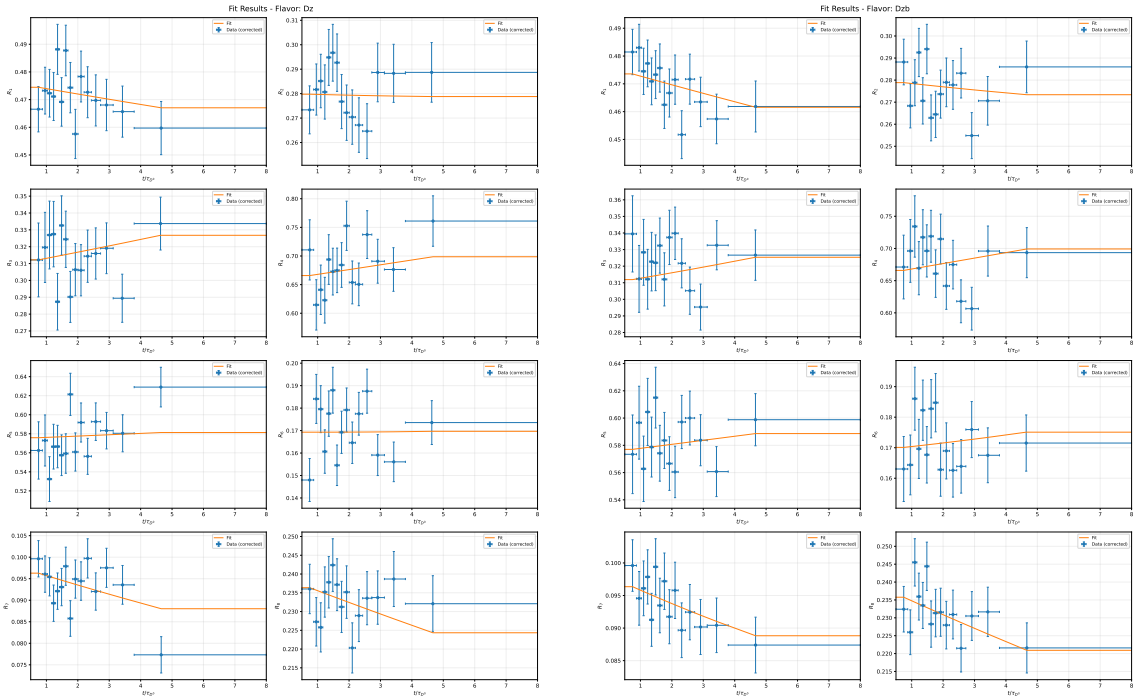

Figure 6.2: Results of the simultaneous fit for the block 8 `TwoTracks` DD sample. The ratios $R_1, \ldots, R_8$ are shown as a function of the reduced decay time for both (left) D^0 and (right) $\overline{\mathrm{D}}^0$ flavours. The blue points are the data after the correction procedure, the orange ones are the raw data before correction, and the green line is the fit.

Their statistical uncertainties are extracted from the covariance matrix of $(\mathcal{R}e(\Delta z), \mathcal{I}m(\Delta z))$, including correlations with the other fit parameters.

Blinding procedure. The estimates of x_{CP}, y_{CP}, Δx and Δy are kept blind until the full analysis procedure is finalised and approved. The blinding is implemented by applying an orthogonal rotation in the (x, y) and $(\Delta x, \Delta y)$ planes, followed by a constant offset. This transformation preserves the statistical uncertainties, correlations, and goodness-of-fit metrics. The fit itself is performed entirely on unblinded internal parameters, and the blinding is applied only at the level of the derived physical observables.

6.2 Final Results

In this section, the final results of the analysis are presented. Table 6.4 summarises the quantitative outcomes of the measurements, while the corresponding distributions are shown in Figures 6.3–6.4.

The figures are provided as consistency cross-checks of the individual trigger-line results. However, they are not used to perform compatibility tests across trigger lines. This choice is motivated by the intrinsic overlap among trigger selections: a single event can satisfy the requirements of multiple trigger lines. As a consequence, the samples associated with different trigger lines are not statistically independent, preventing a meaningful merging of the results or the execution of global compatibility checks based on these figures alone.

Compatibility checks are instead performed across the different data-taking blocks, where statistical independence is ensured. These checks are carried out separately for each trigger line and are quantified using χ^2 tests. The results of these tests are reported in Table 6.5, demonstrating the consistency of the measurements across blocks within each trigger category. The stability of the fit results across data-taking blocks is further illustrated in Figures 6.5 and 6.6, which show the per-block measurements and the corresponding pull distributions for all fitted parameters in the `TwoTracks` LL and DD samples, respectively.

For the DD category, the trigger lines `KS` and `D2KShh` are not included in the comparison. These trigger lines contribute only in blocks 7 and 8 of the dataset and therefore represent a limited fraction of the total DD sample. Their inclusion would not provide sufficient statistical power to improve the robustness of the measurement.

For the LL category, including the remaining trigger lines is expected to increase the effective LL statistics by approximately 20%. This motivates further consideration of alternative strategies to incorporate these events while preserving statistical independence and a coherent acceptance definition across samples. Possible approaches include defining mutually exclusive subsamples based on simplified and well-controlled selections (e.g. using `D2KShh` and `TwoTracks&D2KShh`), or assigning events that satisfy multiple trigger selections randomly to one of the eligible samples. The latter approach would preserve the phase-space coverage but would require a full reprocessing of the dataset to ensure a consistent treatment throughout the analysis.

These strategies represent viable options for enhancing the statistical power of future measurements and will be considered in potential extensions of this work.

Table 6.4: Blind fit results for LL and DD samples. Parameters are expressed in units of 10^{-3}.

(a) LL Sample

Trigger Category	$x[10^{-3}]$	$y[10^{-3}]$	$\Delta x[10^{-3}]$	$\Delta y[10^{-3}]$
TwoTracks	0.62 ± 0.50	10.44 ± 0.78	0.80 ± 0.21	-0.91 ± 0.33
OneTrack	1.30 ± 0.86	10.62 ± 1.42	1.42 ± 0.38	-0.31 ± 0.61
D2Kshh	0.72 ± 0.78	8.67 ± 1.39	0.91 ± 0.37	-1.09 ± 0.66
KS	-0.12 ± 1.04	6.97 ± 1.82	0.62 ± 0.51	-2.00 ± 0.91
TIS	-0.75 ± 1.23	9.01 ± 2.01	0.51 ± 0.61	-0.85 ± 1.00

(b) DD Sample

Trigger Category	$x[10^{-3}]$	$y[10^{-3}]$	$\Delta x[10^{-3}]$	$\Delta y[10^{-3}]$
TwoTracks	2.33 ± 0.60	9.01 ± 0.98	0.93 ± 0.26	-1.21 ± 0.43
OneTrack	3.44 ± 0.91	8.25 ± 1.46	1.48 ± 0.40	-0.62 ± 0.64
TIS	5.34 ± 1.43	10.89 ± 2.39	1.54 ± 0.69	-1.67 ± 1.16

Table 6.5: Goodness of fit results $\chi^2/ndof$ and p-value (in parentheses) for LL and DD samples.

(a) LL Sample

Trigger	x	y	Δx	Δy
TwoTracks	8.51/7 (0.290)	5.93/7 (0.548)	10.16/7 (0.180)	6.44/7 (0.490)
OneTrack	5.06/7 (0.653)	6.54/7 (0.478)	15.00/7 (0.036)	4.12/7 (0.765)
D2Kshh	4.62/7 (0.706)	2.34/7 (0.939)	3.27/7 (0.859)	12.17/7 (0.095)
KS	7.98/7 (0.334)	8.28/7 (0.309)	7.68/7 (0.362)	4.91/7 (0.671)
TIS	8.71/7 (0.274)	6.19/7 (0.518)	7.78/7 (0.353)	3.59/7 (0.826)

(b) DD Sample

Trigger	x	y	Δx	Δy
TwoTracks	7.45/7 (0.384)	4.13/7 (0.765)	17.40/7 (0.015)	8.07/7 (0.327)
OneTrack	4.77/7 (0.688)	5.15/7 (0.641)	17.77/7 (0.013)	5.23/7 (0.632)
TIS	1.95/7 (0.963)	6.20/7 (0.517)	5.06/7 (0.653)	8.16/7 (0.319)

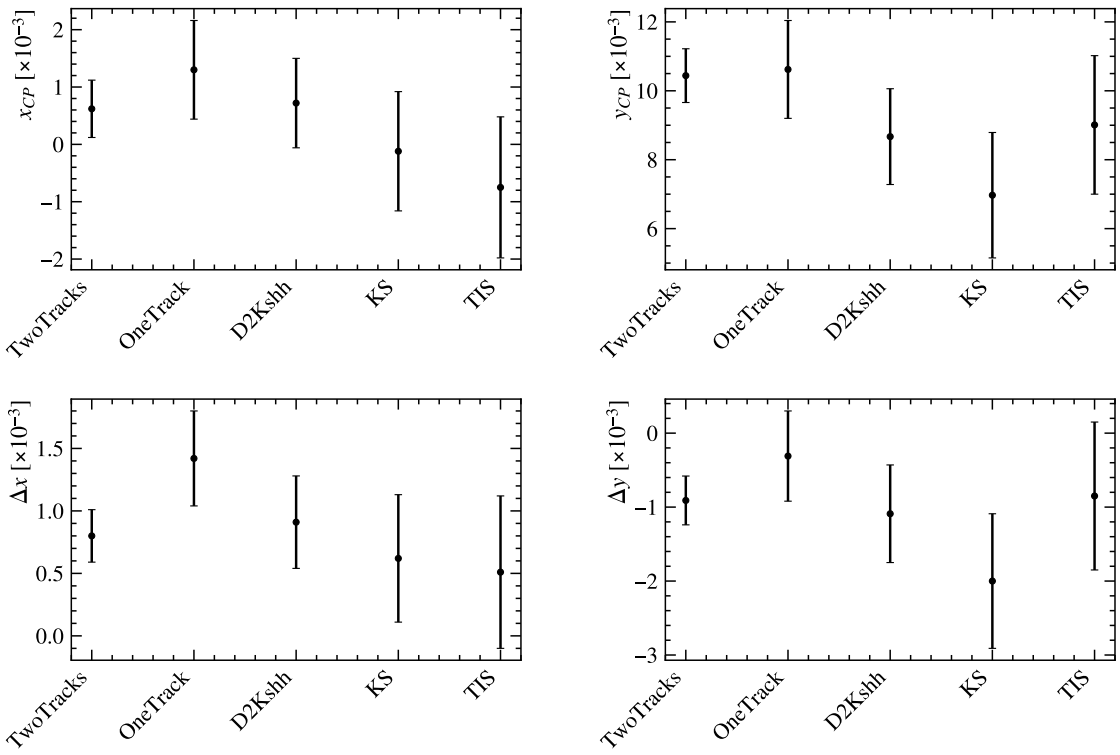

Figure 6.3: Overview of the fit results for (top left) x, (top right) y, (bottom left) Δx and (bottom right) Δy parameters across different trigger categories for LL. The plots show consistency between the trigger samples.

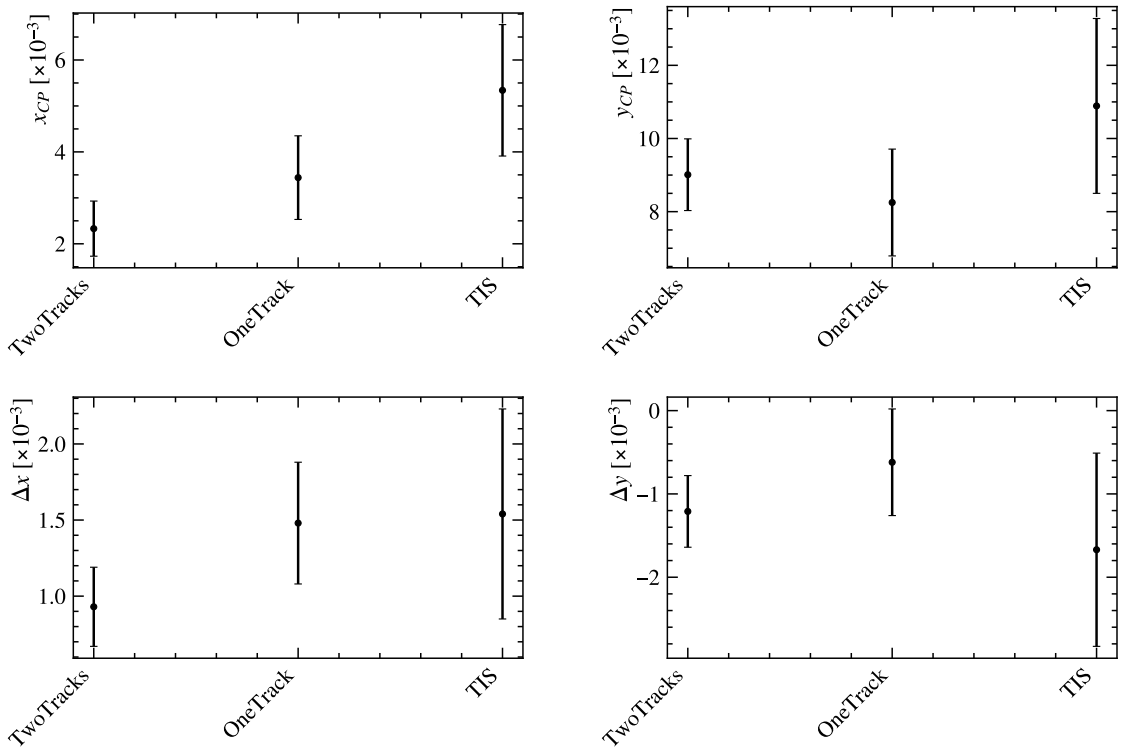

Figure 6.4: Overview of the fit results for (top left) x, (top right) y, (bottom left) Δx and (bottom right) Δy parameters across different trigger categories for DD. The plots show consistency between the trigger samples.

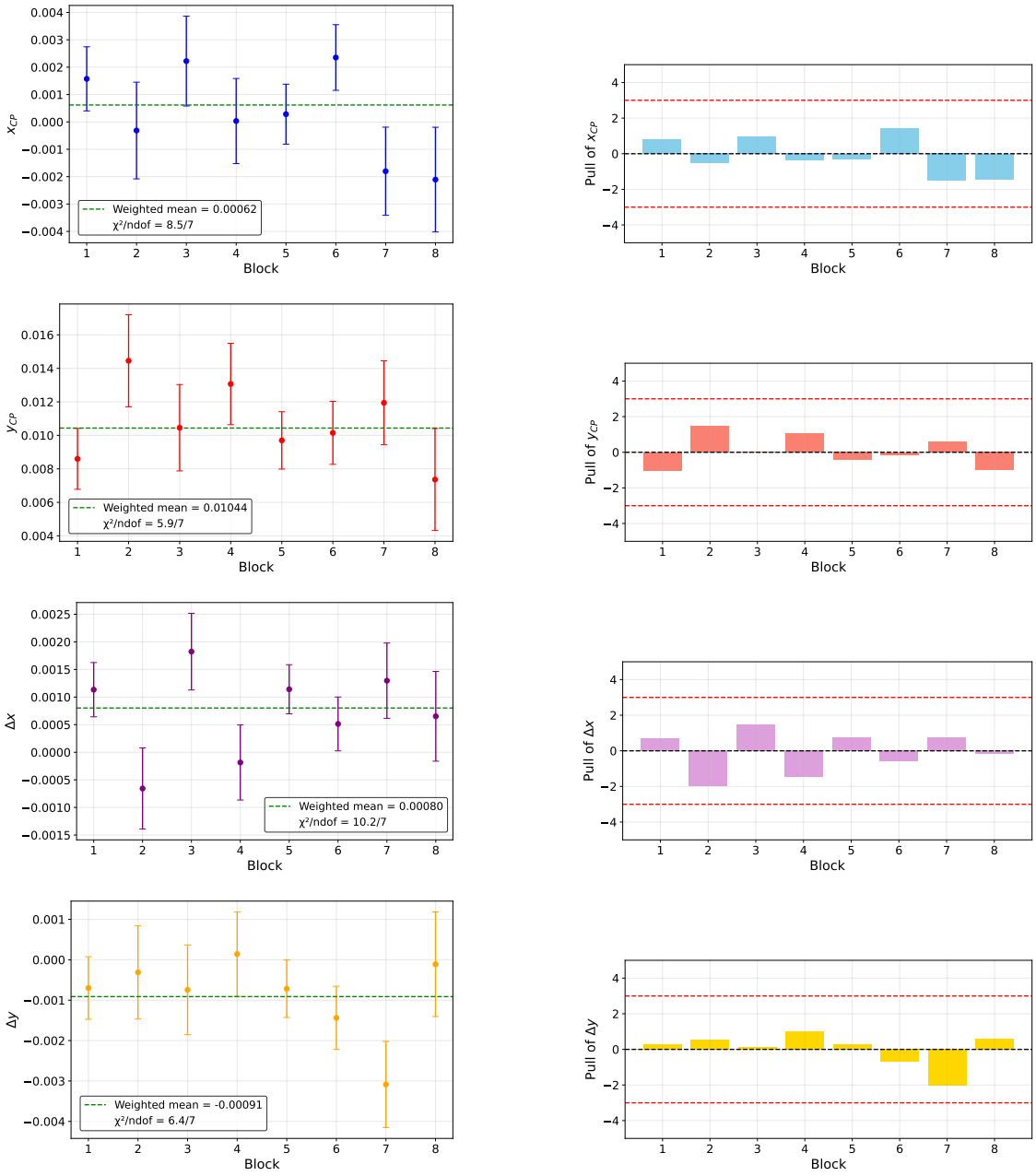

Figure 6.5: Summary of (left column) fit results and (right column) corresponding pulls for the parameters: (first row) x_{CP}, (second row) y_{CP}, (third row) Δx, and (fourth row) Δy. The red dashed lines in the pull plots denote the $\pm 3\sigma$ region. All values are evaluated across data blocks for the `TwoTracks` LL sample.

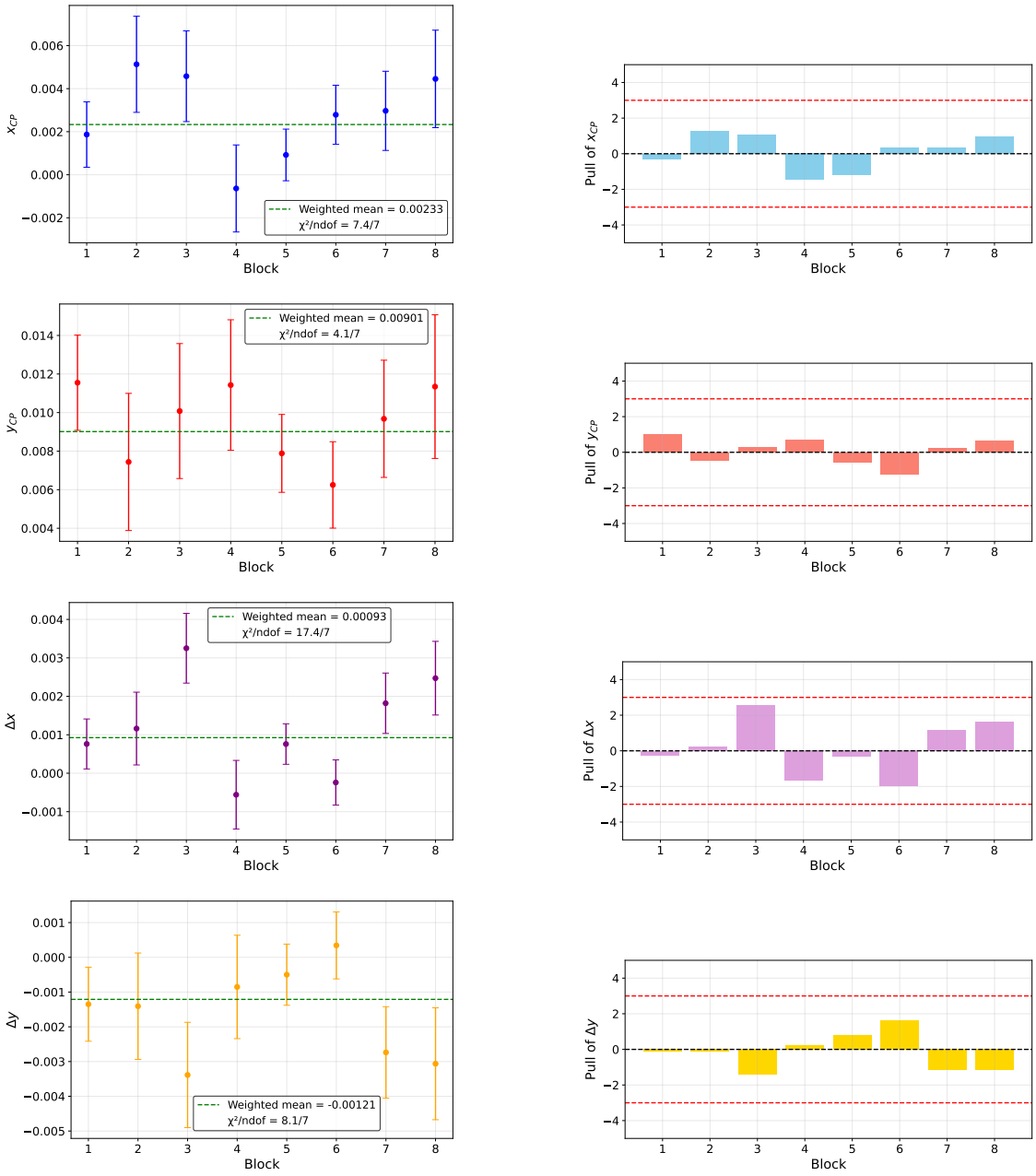

Figure 6.6: Summary of (left column) fit results and (right column) corresponding pulls for the parameters: (first row) x_{CP}, (second row) y_{CP}, (third row) Δx, and (fourth row) Δy. The red dashed lines in the pull plots denote the $\pm 3\sigma$ region. All values are evaluated across data blocks for the `TwoTracks` DD sample.

Chapter 7

Summary

In this thesis, a measurement of charm mixing and CP-violation observables has been presented using 2024 Run 3 data collected by the LHCb experiment. The analysis exploits the increased integrated luminosity and the improved performance of the upgraded detector to achieve a sensitivity that exceeds that obtained during Run 2.

The stability of the measurement has been thoroughly investigated as a function of the data-taking blocks. As discussed in the previous chapter, no strong dependence of the observables on the block structure is observed. This behaviour indicates a stable performance of the detector and reconstruction throughout the data-taking period, and supports the robustness of the analysis strategy.

A quantitative assessment of the compatibility among blocks has been performed using χ^2 tests and corresponding p-values. For most observables, both in the LL and DD samples, good agreement is observed across blocks.

Weighted averages are computed separately for the LL and DD samples; global results are subsequently derived by combining them only for those trigger categories available in both samples. The combination of the two samples takes advantage of their complementary statistical power and leads to a significant reduction in the overall statistical uncertainty.

Focusing on a quantitative assessment of the achieved sensitivity, the discussion in the following is restricted to the `TwoTracks` category, which represents the dominant contribution to the Run 3 dataset. The subdivision of this sample into LL and DD components, together with their mutual compatibility, has been discussed in detail in the previous chapter.

The final combined results obtained from the `TwoTracks` LL and DD samples are

$$
\begin{aligned}
{x_{CP}}^{2024,\texttt{TwoTracks}} &= (1.32 \pm 0.38) \times 10^{-3}, \\
{y_{CP}}^{2024,\texttt{TwoTracks}} &= (9.89 \pm 0.61) \times 10^{-3}, \\
\Delta x^{2024,\texttt{TwoTracks}} &= (0.85 \pm 0.16) \times 10^{-3}, \\
\Delta y^{2024,\texttt{TwoTracks}} &= (-1.02 \pm 0.26) \times 10^{-3}.
\end{aligned}
$$

where the quoted uncertainties are statistical only. The compatibility between the LL and DD measurements is found to be good for most observables, with χ^2/ndof values consistent with statistical fluctuations. A mild tension is observed for x_{CP}, corresponding to a p-value of 2.7%, while no significant discrepancies are found for the remaining parameters 7.1.

Table 7.1: Statistical compatibility between LL and DD for `TwoTracks` sample.

Parameter	$\chi^2/ndof$	p-value
x	4.88 / 1	0.027
y	1.29 / 1	0.257
Δx	0.14 / 1	0.708
Δy	0.31 / 1	0.579

The improvement in statistical precision with respect to Run 2 is most clearly illustrated by the uncertainties on x_{CP} and y_{CP}. Assuming a statistical uncertainty scaling as $1/\sqrt{\mathcal{L}}$, the increase in integrated luminosity from Run 2 to Run 3 corresponds to an expected sensitivity ratio

$$
r = \frac{\sigma_{2024}}{\sigma_{\text{Run2}}} = \sqrt{\frac{\mathcal{L}_{\text{Run2}}}{\mathcal{L}_{2024}}} \approx 0.89,
$$

implying an expected improvement of approximately 11% in statistical precision.

For Run 2, where the dataset included both `OneTrack` and `TwoTracks` selections, the measurements yielded

$$
\begin{aligned}
{x_{CP}}^{\text{Run2}} &= (3.97 \pm 0.46_{\text{stat}} \pm 0.29_{\text{syst}}) \times 10^{-3}, \\
{y_{CP}}^{\text{Run2}} &= (4.59 \pm 1.20_{\text{stat}} \pm 0.85_{\text{syst}}) \times 10^{-3}, \\
\Delta x^{\text{Run2}} &= (-0.27 \pm 0.18_{\text{stat}} \pm 0.01_{\text{syst}}) \times 10^{-3}, \\
\Delta y^{\text{Run2}} &= (\ 0.20 \pm 0.36_{\text{stat}} \pm 0.11_{\text{syst}}) \times 10^{-3}.
\end{aligned}
$$

In comparison, the statistical uncertainties achieved in the Run 3 blind analysis,

$$\sigma_x^{2024,\texttt{TwoTracks}} \simeq 0.38 \times 10^{-3},$$
$$\sigma_y^{2024,\texttt{TwoTracks}} \simeq 0.61 \times 10^{-3},$$
$$\sigma_{\Delta x}^{2024,\texttt{TwoTracks}} \simeq 0.16 \times 10^{-3},$$
$$\sigma_{\Delta y}^{2024,\texttt{TwoTracks}} \simeq 0.26 \times 10^{-3}$$

are consistent with, and in the case of y_{CP} and Δy exceed, the expectations based solely on luminosity scaling.

This additional improvement reflects not only the larger Run 3 dataset, but also the enhanced performance of the upgraded LHCb detector and the benefit of the combined analysis of the LL and DD categories within the `TwoTracks` selection.

Only the `TwoTracks` category is considered for this comparison, as it provides the dominant contribution to the Run 3 dataset (as shown in Figures 3.7-3.8). The subdivision into different trigger-line subsamples is avoided because these samples are not statistically independent: a single event can satisfy multiple trigger requirements. Consequently, these subsamples cannot be merged into a single measurement without introducing complex correlations.

The development of an appropriate strategy to handle overlapping trigger selections, ensuring statistical independence while preserving a coherent acceptance definition, is ongoing and will be addressed in the context of the future publication of these results.

Performances of RICH detectors with Run 3 data

The start of Run 3 at the LHC represents a major milestone for the LHCb experiment. Following the Upgrade I programme, LHCb has been transformed into a fully new detector, designed to operate at higher instantaneous luminosity and to perform a complete software-based event reconstruction and selection. In this new experimental scenario, a detailed assessment of the detector performance using Run 3 data is of fundamental importance in order to validate the design choices, understand the behaviour of the upgraded subsystems, and ensure that the physics goals of the experiment can be successfully achieved.

The Ring Imaging Cherenkov (RICH) detectors play a crucial role by providing charged particle identification over a wide momentum range. As part of the Upgrade I, the RICH system underwent substantial modifications, including new photon detectors, upgraded readout electronics, and a redesigned data acquisition scheme compatible with the fully software-based trigger operation of Run 3. These changes result in significantly different operating conditions with respect to previous runs, making a thorough evaluation of the RICH performance with data.

Several studies have been carried out to characterise the performance of the upgraded RICH detectors during Run 3. This chapter focuses on a selection of these studies, aimed at understanding the detector response and its evolution under different reconstruction and timing conditions. In particular, the analyses presented here investigate the behaviour of the detected photon hit distributions and the impact of timing selections on the overall detector performance, as well as the evolution of background contributions affecting the single photon resolution.

The first part of this chapter is dedicated to the study of the hitmaps' evolution as a function of different time windows. Different timing selections are applied to the detected photon signals to study their impact on background rejection and on the optimisation of the signal-to-noise ratio. By analysing hit distributions for varying time-window configurations, insights are gained into the detector occupancy, the spatial uniformity of the response, and the effectiveness of timing selections in

suppressing uncorrelated background contributions.

The second part of the chapter addresses the evolution of backgrounds in the single-photon resolution. The single photon resolution is a critical parameter for the RICH performance, as it impacts the particle identification capability. A detailed understanding of the sources of background and their dependence on operating conditions is therefore essential. The studies presented here examine how background contributions affect the single photon resolution in Run 3 data and how these effects evolve with different reconstruction settings.

Overall, the results discussed in this chapter provide an important validation of the upgraded RICH detectors in the Run 3 environment as they demonstrate the detector performance under real data-taking conditions.

Chapter 8

Hitmaps evolution with different time windows

This chapter investigates the evolution of RICH detector hitmaps as a function of the photon time window used in the reconstruction. The study exploits Run 3 data and Monte Carlo simulations to assess the impact of time gating on detector occupancy and background rejection under different data-taking conditions.

8.1 Introduction and time-gating strategy

The emission of Cherenkov radiation is intrinsically prompt with respect to the passage of the charged particle through the radiator. In the upgraded LHCb RICH detectors, this feature, combined with the focusing optics and precise photon timing, enables the use of fine time gating to suppress out-of-time background contributions efficiently.

The detected hit time spectrum is characterised by a clear Cherenkov signal peak, accompanied by several background components (Figure 8.1).

These include hits from charged particles travelling directly to the photon detection plane, delayed photons arising from multiple reflections within the optical system, and incoherent background contributions from instrumental noise or scintillation photons produced in the radiators. By selecting an appropriate time window around the Cherenkov signal peak, it is possible to optimise the trade-off between photon detection efficiency and background rejection (Figure 8.2).

Based on extensive commissioning studies, a time-gating window of 6.25 ns was identified as providing the best compromise between signal efficiency and background suppression, and has been adopted as the nominal configuration since the end of 2022. In this chapter, the evolution of detector hitmaps is studied for several time window

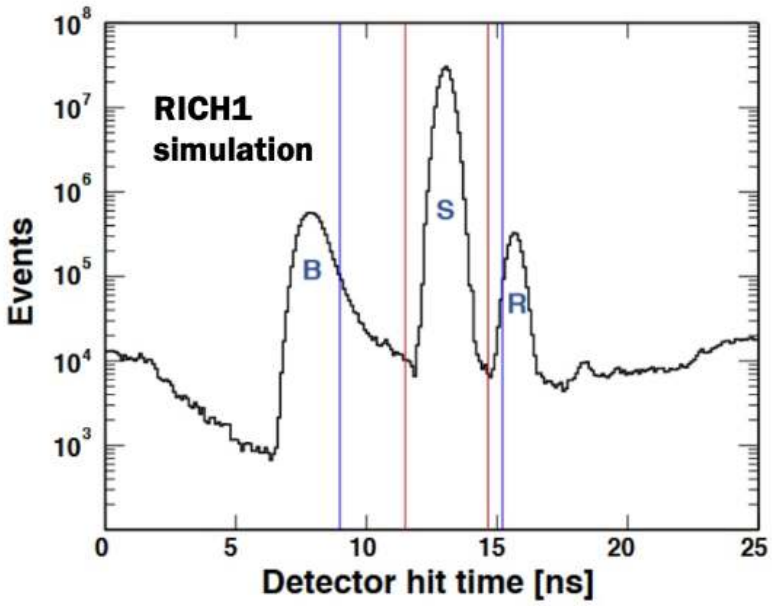

Figure 8.1: RICH1 hit time distribution with simulated data. The "S" area corresponds to the Cherenkov signal, the "B" to background due to particles travelling directly to the photon detection plane and "R" to background due to multiple reflections of Cherenkov photons in the optical system. Furthermore, there is also an incoherent background due to instrumental internal noise or scintillation photons in the radiators.

configurations and compared to the 6.25 ns reference setting.

In LHCb, each subdetector can operate in either *local* or *global* mode during data acquisition. When a subdetector operates in local mode, it runs in a standalone configuration, disconnected from the main data acquisition chain, and its information is not included in the overall LHCb dataset. Conversely, when a subdetector operates in global mode, it is integrated into the complete acquisition chain and contributes its information to the event reconstruction. Physics analyses are performed exclusively on runs where *all* subdetectors operate in global mode, ensuring access to the complete detector information. Local runs serve as diagnostic tools for individual subdetector groups to conduct performance studies, commissioning activities, and to monitor the operational status of their respective systems.

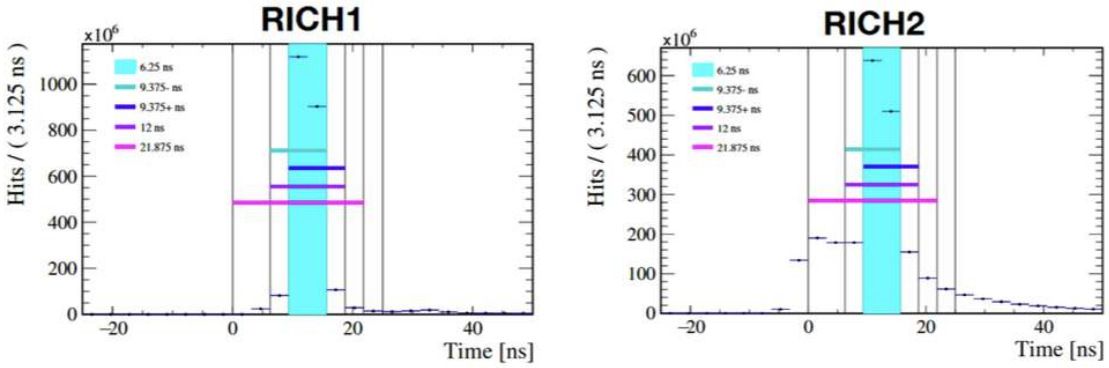

Figure 8.2: Time gating windows for (left) RICH1 and (right) RICH2.

8.2 Local runs

Local runs offer a clean and controlled environment to study the intrinsic response of the RICH detectors. In this configuration, unbiased data samples are selected by requiring colliding bunch–bunch events, using random triggers. The residual micro-bias introduced by this selection is negligible.

For the local run analysis, only *Lumi*-type histograms are considered, since in local only unbiased events are taken.

The data correspond to fills with eight colliding bunches in LHCb, characterised by $\mu = 3.3$, that is, the average number of visible pp interactions per bunch crossing.

The local runs used for these studies are listed in the Table 8.1.

Table 8.1: Time window configurations for different Time IDs.

Time ID	Run Number	Time Window (ns)
1	288969	6.25
2	288970	9.375–
3	288971	9.375+
4	288973	12.5
5	288975	21.875

The peak and average occupancies are studied as a function of the photon time window for both RICH1 and RICH2 (Figures 8.3–8.4). As expected, increasing the time window leads to a higher occupancy due to the accumulation of additional background hits. The observed trends are smooth and reproducible across different runs, indicating stable detector behaviour.

To investigate spatial effects, hitmaps obtained with different time windows are

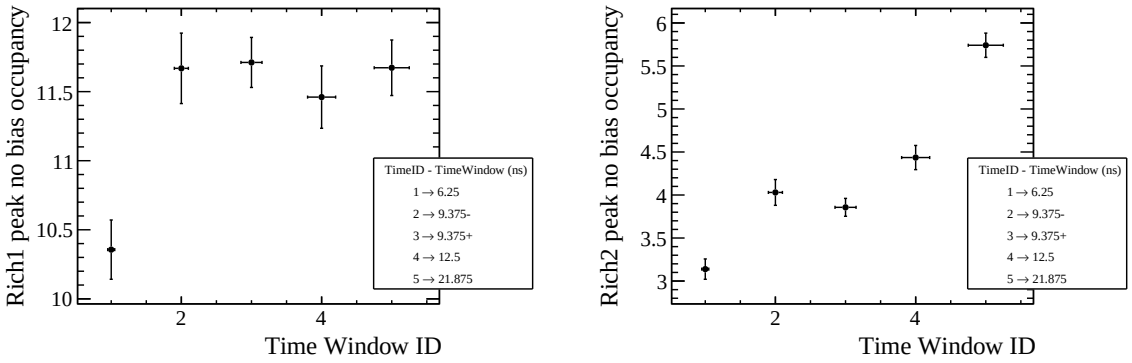

Figure 8.3: Peak occupancy (in %) with *Lumi* (no bias) sample for (left) RICH1 and (right) RICH2.

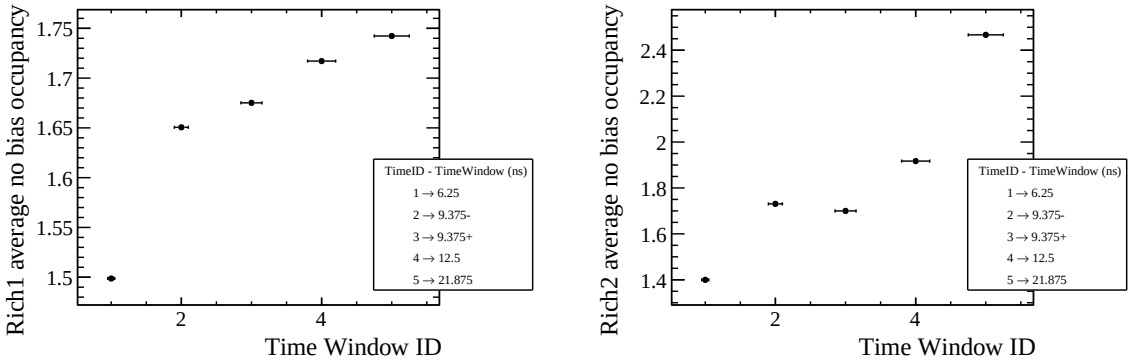

Figure 8.4: Average occupancy (in %) with *Lumi* (no bias) sample for (left) RICH1 and (right) RICH2.

compared by computing the ratio with respect to the nominal 6.25 ns configuration (Figure 8.5). In Figure 8.6, the ratios of the occupancy maps obtained with time windows of 9.375 ns and 21.875 ns, with respect to the nominal one, are shown. An overall increase in the ratio values is observed when enlarging the time window, as expected, and is particularly evident in RICH2.

8.3 Global runs

Global runs correspond to standard LHCb physics data-taking conditions and include the full trigger and reconstruction chain. In this case, two distinct classes of histograms are available: *Lumi* histograms, which remain unbiased, and *Phys*

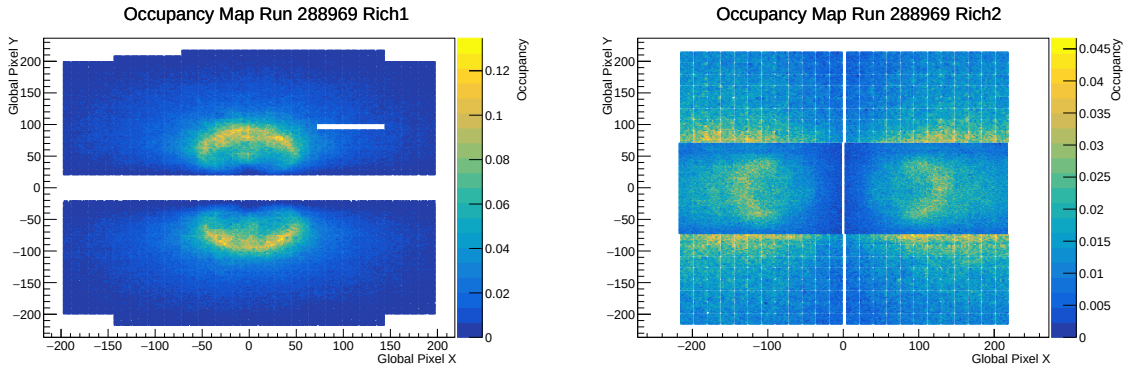

Figure 8.5: Occupancy Maps using the reference 6.25 ns time window with *Local* runs for (left) RICH1 and (right) RICH2.

histograms, which are affected by the HLT1 trigger selection.

The *Lumi* samples are conceptually similar to those used in local runs, while the *Phys* samples contain only events corresponding to colliding bunch–bunch crossings that satisfy the HLT trigger requirements. These events are inelastic proton–proton interactions and are therefore of direct interest for physics analyses. As a consequence, they exhibit a higher detector occupancy. The *Phys* trigger is only available in global runs, as no HLT is present in the local data-taking configuration.

The global run data used in this study correspond to μ = 5.3. The global runs used are listed in the Table 8.2.

Table 8.2: Run numbers corresponding to different Time IDs.

Time ID	Run Numbers
1	[307976]
2	[307982 - 307984 - 307985]
3	[307986 - 307987]
4	[307977 - 307978 - 307979 - 307980]
5	[307967 - 307969 - 307970]

Peak and average occupancies are analysed as a function of the photon time window separately for *Lumi* and *Phys* samples (Figures 8.7–8.9). While the overall trends are consistent with those observed in local runs, higher absolute occupancies are measured, reflecting the increased pile-up and, for the *Phys* case, the trigger-induced bias.

Ratio hitmaps with respect to the nominal time window are computed for both trigger categories (Figure 8.10). The *Lumi* data show a behaviour compatible with

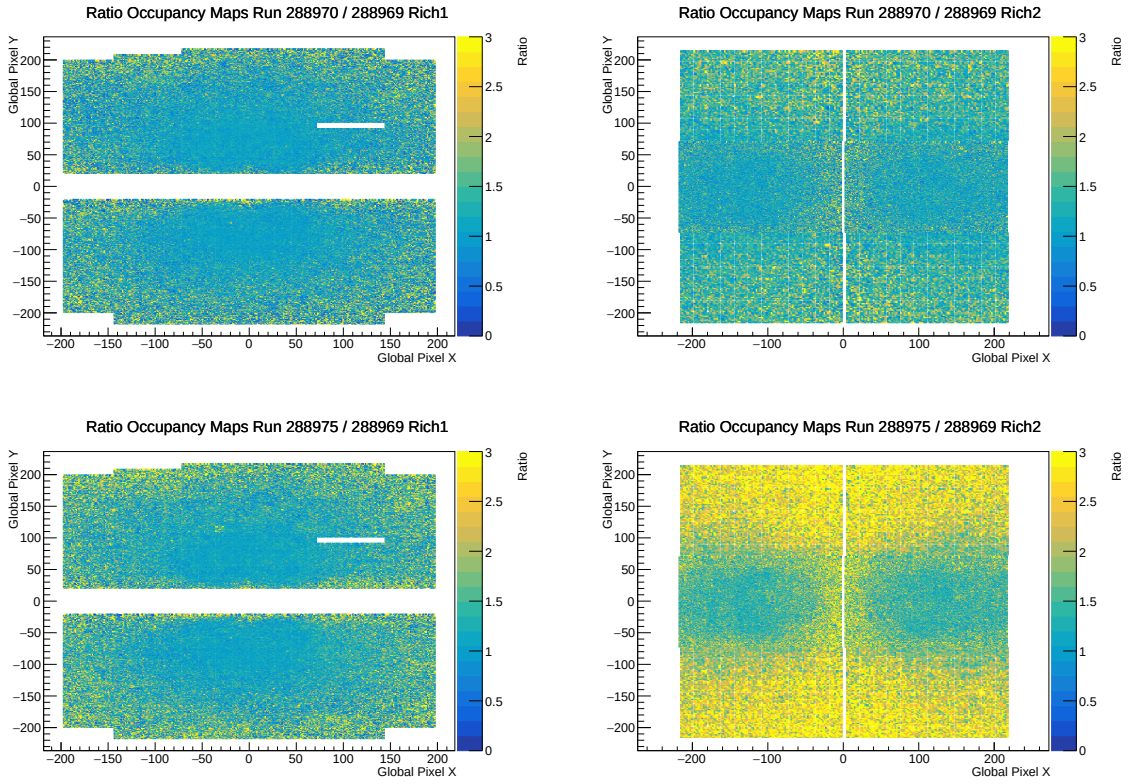

Figure 8.6: Ratio of the Occupancy Maps with respect to the reference one using *Local* runs for (left) RICH1 and (right) RICH2. (Top) Results for the 9.375 ns time window (Run 288970) and (bottom) for the 21.875 ns time window (Run 288975).

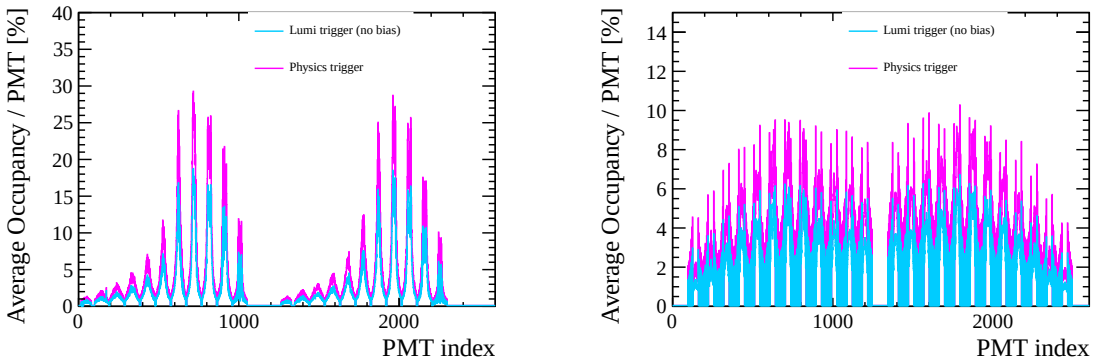

Figure 8.7: Average occupancy/PMT[%] occupancy for the reference 6.25 ns Time Window with *Lumi* (no bias) and *Phys* samples for (left) RICH1 and (right) RICH2.

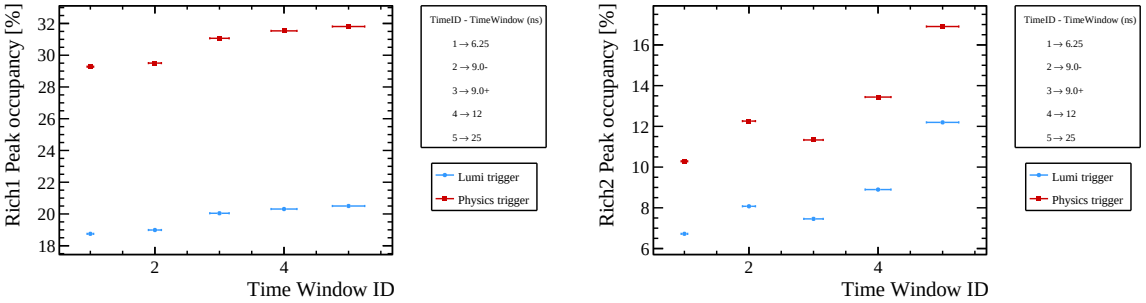

Figure 8.8: Peak occupancy with *Lumi* (no bias) and *Phys* samples for (left) RICH1 and (right) RICH2.

the local run results, confirming the consistency between the two configurations. In contrast, the *Phys* data exhibit enhanced structures, particularly in the outer detector regions, highlighting the combined effect of higher occupancy and trigger bias.

8.4 MC runs

Monte Carlo simulations are used to provide an unbiased reference for the interpretation of the data. The simulated samples employed in this study correspond to minimum-bias events generated with a photon time window of 25 ns and nominal Run 3 luminosity conditions, which corresponds to 2.0×10^{33} cm^{-2}s^{-1}. The corresponding occupancy maps for the two RICH detectors are shown in Figure 8.13.

The ratio of hitmaps obtained with different time windows in data to the reference

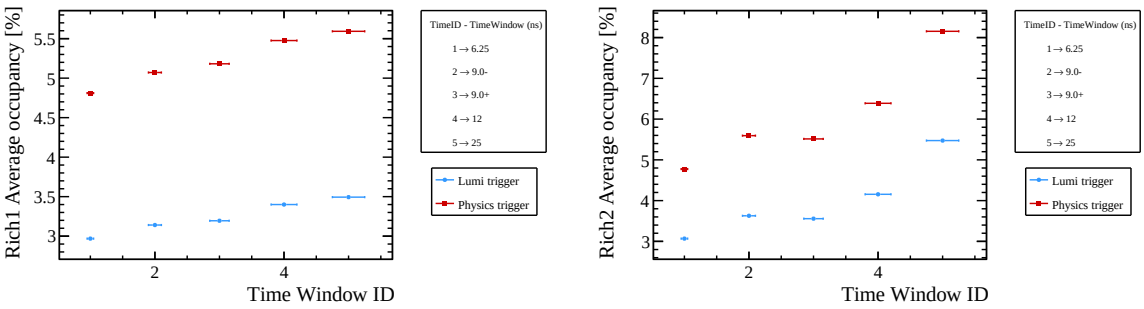

Figure 8.9: Average occupancy with *Lumi* (no bias) and *Phys* samples for (left) RICH1 and (right) RICH2.

Monte Carlo hitmap (generated with a 25 ns time window) is computed (Figure 8.14). This comparison allows the identification of potential discrepancies between data and Monte Carlo, particularly in the modelling of background contributions as a function of the time window.

A good agreement between data and simulation is observed for RICH1, indicating that the dominant background sources are well described. In contrast, RICH2 data show systematically higher background levels than predicted by simulation, especially in the outer regions of the detector. This suggests the presence of additional background contributions not fully accounted for in the current simulation, possibly related to secondary particles produced by interactions with detector materials not completely described in the geometry.

8.5 Summary

The evolution of RICH detector hitmaps with different photon time windows has been studied using local runs, global runs, and Monte Carlo simulations. The analysis confirms that a narrow time gating significantly reduces background contributions while preserving a stable detector response, supporting the choice of a 6.25 ns time window as the nominal configuration.

Consistency is observed between local and global unbiased data, while higher occupancies and additional structures appear in trigger-selected samples. The comparison with simulation shows good agreement for RICH1, whereas RICH2 exhibits excess background in data, motivating further dedicated studies. These results provide essential input for the understanding of background sources and for subsequent investigations of the single photon resolution in Run 3, discussed in Section 9.

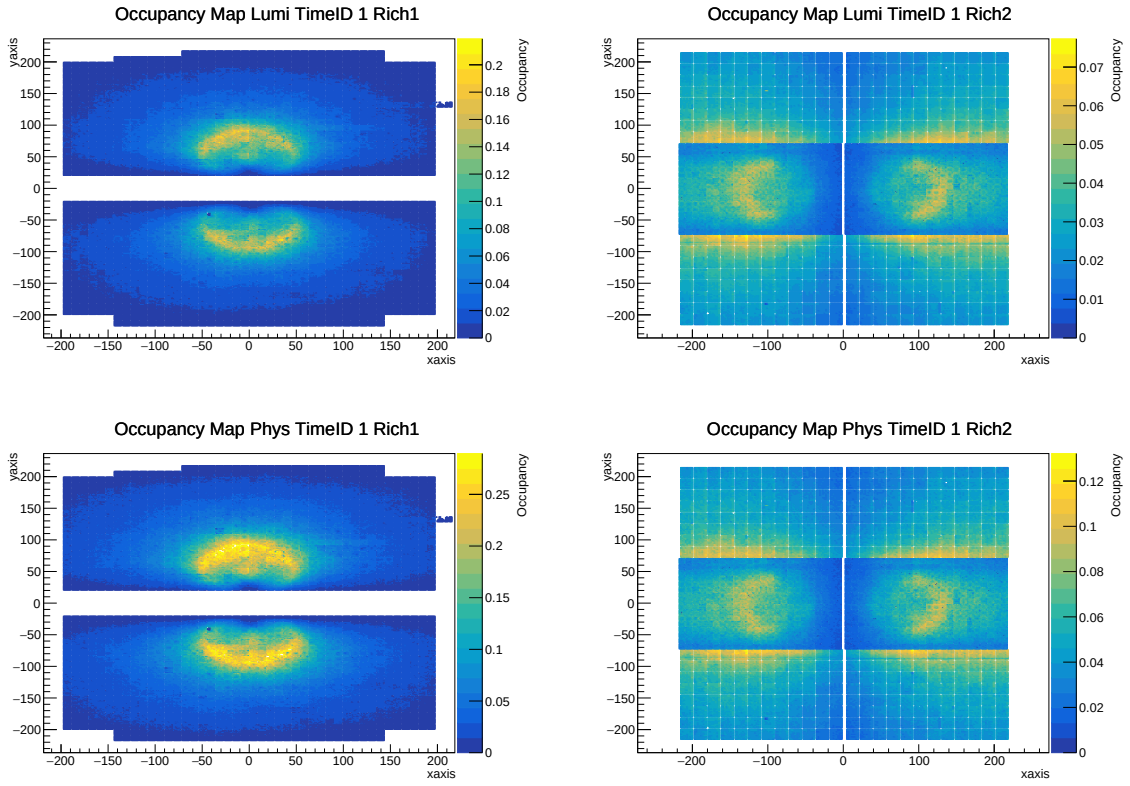

Figure 8.10: Occupancy Maps using a 6.25 ns time window for (left) RICH1 and (right) RICH2. (Top) Results using the *Lumi* (no bias) sample and (bottom) using the *Phys* sample, both from *Global* data.

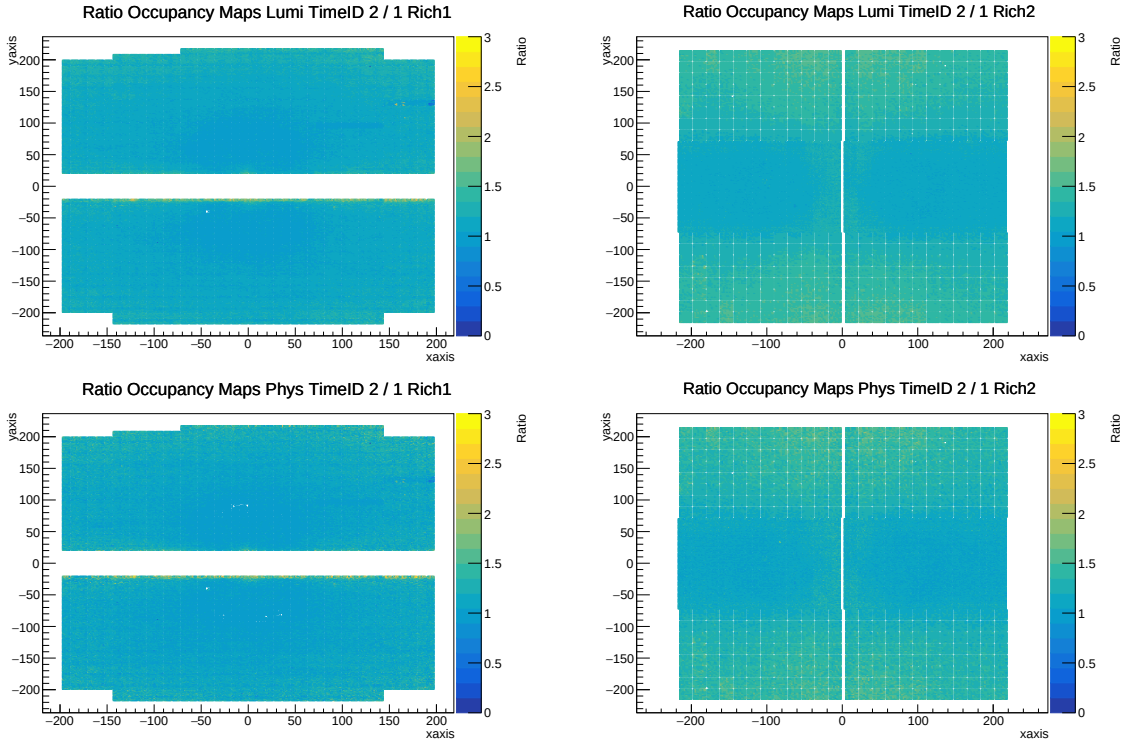

Figure 8.11: Ratio of the Occupancy Maps with respect to the reference one using a 9.0– ns time window for (left) RICH1 and (right) RICH2. (Top) Results using the *Lumi* (no bias) sample and (bottom) using the *Phys* sample, both from *Global* data.

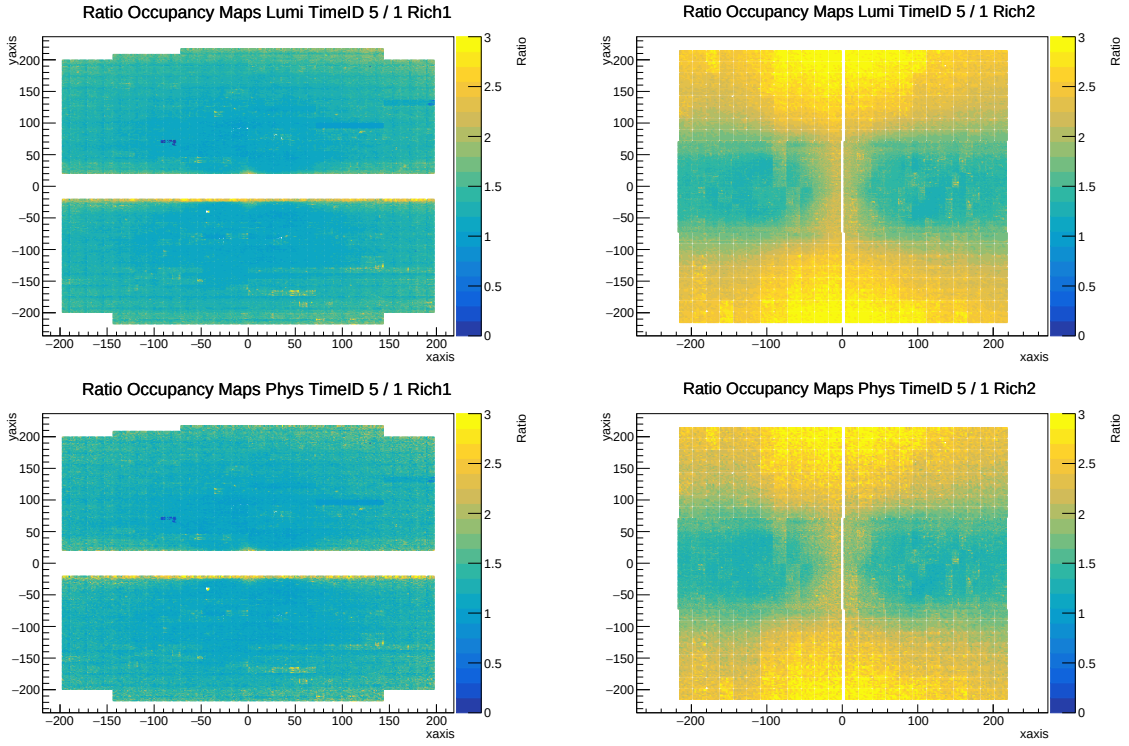

Figure 8.12: Ratio of the Occupancy Maps with respect to the reference one using a 25 ns time window for (left) RICH1 and (right) RICH2. (Top) Results using the *Lumi* (no bias) sample and (bottom) using the *Phys* sample, both from *Global* data.

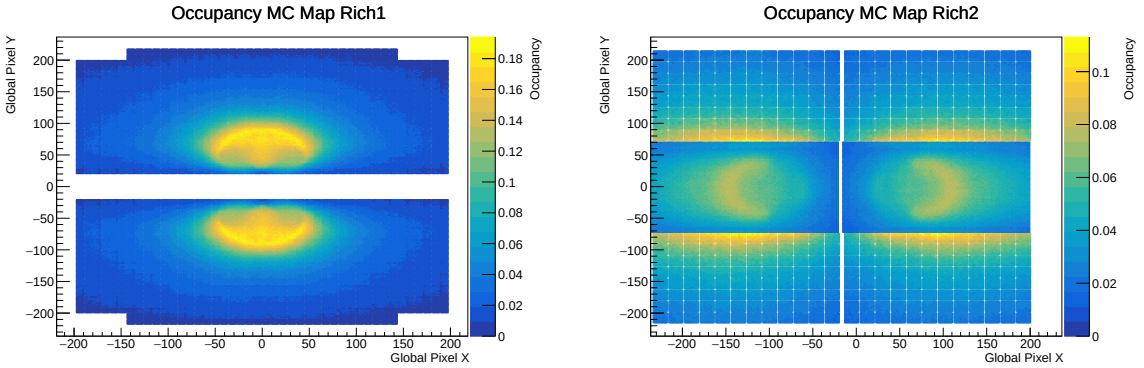

Figure 8.13: Occupancy Maps with the 25 ns Time Window *Monte Carlo* sample for (left) RICH1 and (right) RICH2.

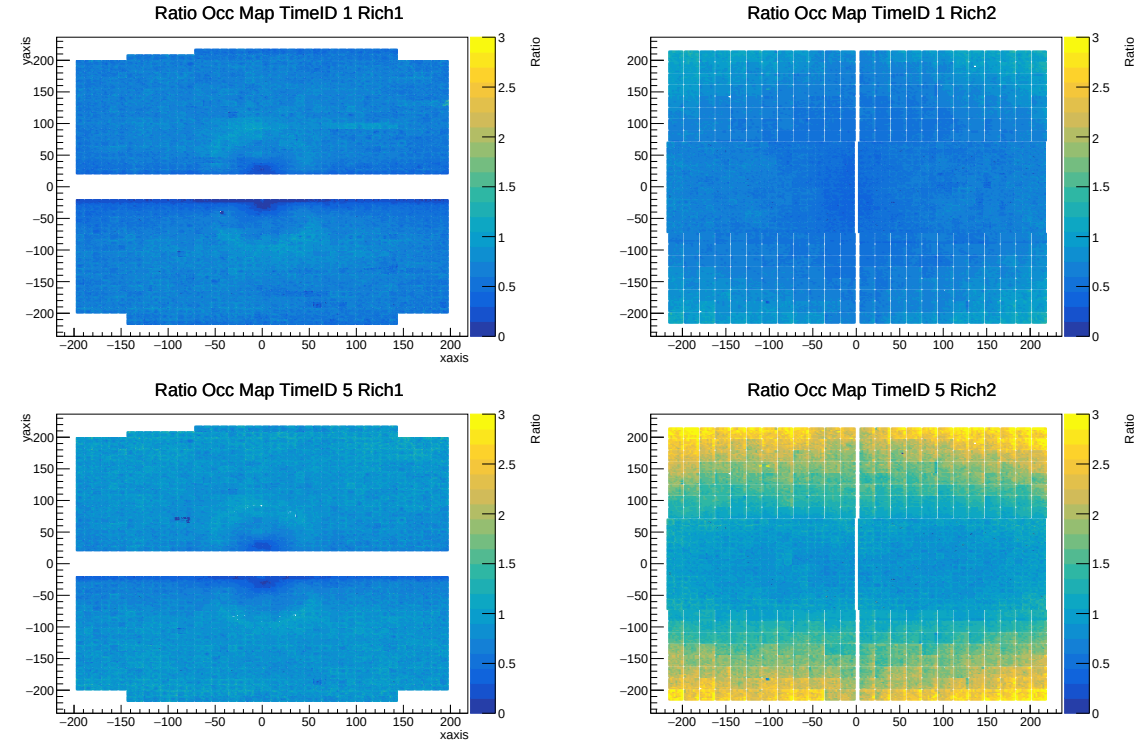

Figure 8.14: Ratio of the Occupancy Maps from *Global* data with respect to the *Monte Carlo* sample for (left) RICH1 and (right) RICH2. (Top) Results using the *Lumi* (no bias) data sample with a 6.25 ns time window and (bottom) with a 25 ns time window.

Chapter 9

Evolution of single photon resolution backgrounds

This chapter presents a detailed study of the evolution of background contributions affecting the single photon resolution in the RICH detectors. The analysis focuses on the photon-level background component and its dependence on the detector geometry and on the applied photon time window, using Run 3 data. These studies provide a validation of the upgraded detector performance and serve as a reference for future optimisation studies in view of Upgrade II.

9.1 Motivation

The single photon resolution is a key performance parameter of the RICH detectors, as it directly determines the Cherenkov angle resolution and, consequently, the particle identification capability. In the Run 3 environment, characterised by higher luminosity and increased detector occupancy, a detailed understanding of the background contributions affecting the single photon resolution is essential.

While previous studies focused on global performance metrics and occupancy-related effects, a more granular investigation is required to disentangle the different sources of background at the photon level. In particular, studying the evolution of the background contribution as a function of the photon time window and of the detector geometry allows one to assess the effectiveness of the time-gating strategy and to identify potential limitations of the current detector modelling.

The goal of this chapter is to study the background component of the single photon resolution for the two RICH detectors, analysing its evolution quadrants by quadrants and for different photon time windows. These studies are performed using Run 3 global data and are intended both as a validation of the upgraded detector

performance and as a reference for future optimisation studies in view of Upgrade II.

9.2 Methodology

The study is based on Run 3 global runs and exploits calibration and monitoring histograms produced within the RICH software framework. The single photon resolution is evaluated using the Cherenkov angle residual distributions, `ckThetaRes`, which represent the difference between the reconstructed and expected Cherenkov angles for individual photons.

The `ckThetaRes` distributions are retrieved from the calibration output files produced by the `RichRefIndexCal` algorithm. The analysed runs correspond to the same set of global runs used in the hitmap studies, ensuring consistency between the different performance investigations.

For each photon time window configuration, the `ckThetaRes` distributions are fitted using the model implemented in the RICH online calibration framework. The fits are performed both on the full detector acceptance and separately for each of the four detector quadrants, allowing the identification of possible spatial non-uniformities in the signal and background contributions. The signal component, corresponding to correctly associated Cherenkov photons, is described by a Gaussian function, while the background component is modelled by a polynomial term (Figure 9.1).

From the fit results, quantities characterising the signal and background contributions are extracted, such as the signal width and the background normalisation (Figure 9.2). In particular, the evolution of the background level, or equivalently, of the signal resolution, is studied as a function of the photon time window. This approach allows one to quantify the impact of time gating on the misassignment of photons to tracks, including contributions from dark counts and other incoherent background sources, and to assess potential quadrant-dependent effects.

In addition to the one-dimensional analysis, a spatial study is performed to investigate the dependence of the background on the detector geometry. Two-dimensional histograms of the track entry position in the photon detection plane, `trackEntryXY`, are analysed separately for each time window (Figure 9.3). For each configuration, the histograms are normalised to the total number of entries and ratio maps are computed with respect to the nominal 6.25 ns time window (Figure 9.4. This approach highlights localised variations of the background contribution across the detector acceptance.

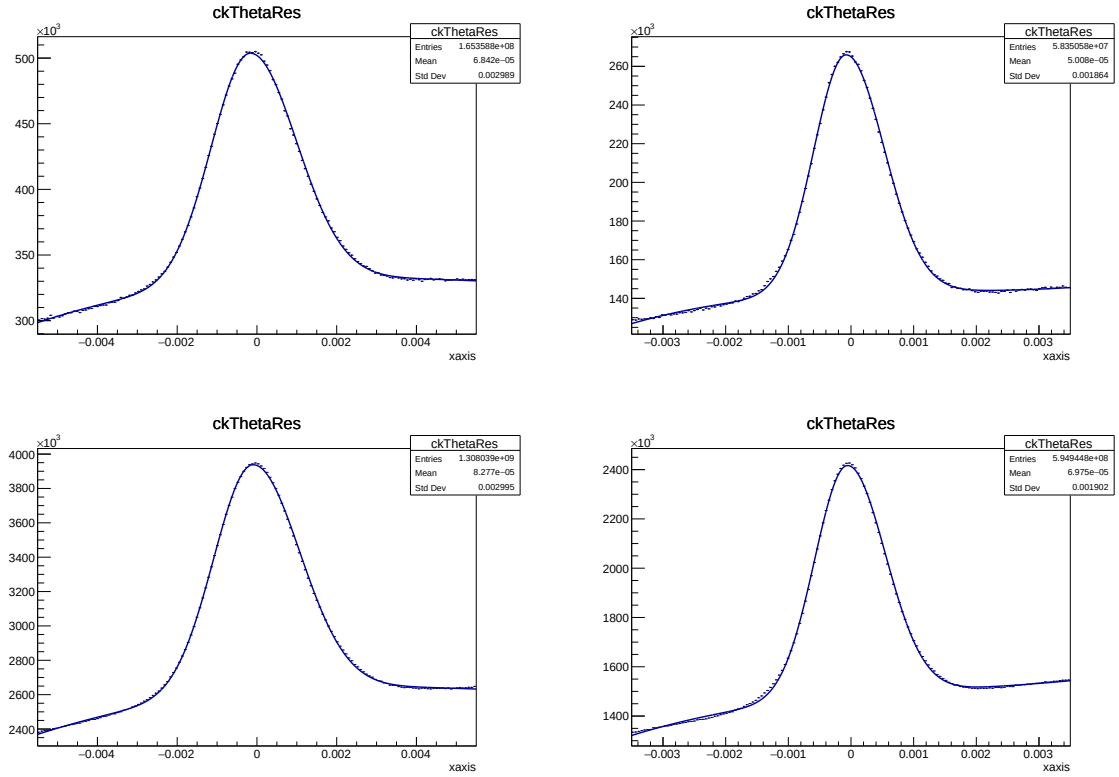

Figure 9.1: Fitted distribution of the Cherenkov angle resolution for RICH1 (left) and RICH2 (right) with (top) 6.25 ns and (bottom) 25 ns time windows. The signal is fitted with a Gaussian, and the background is modelled with a polynomial.

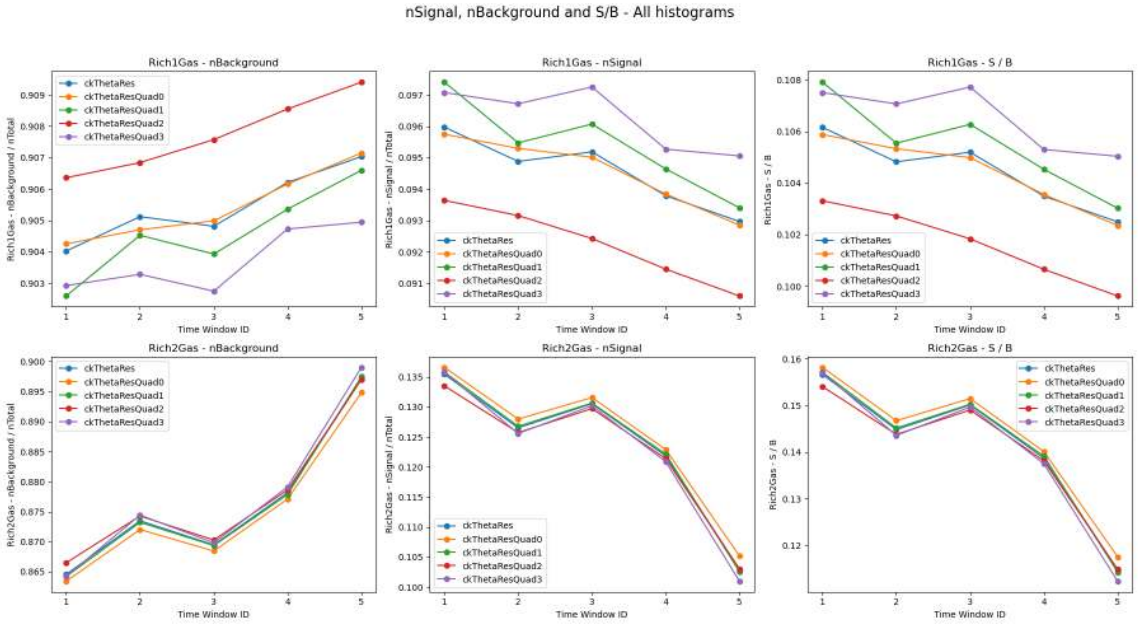

Figure 9.2: Evolution of the signal and background contributions extracted from fits to the `ckThetaRes` distributions as a function of the photon time window. The signal component corresponds to correctly associated Cherenkov photons, while the background component accounts for misassociated photons, including contributions from dark counts and other incoherent sources. The results are shown for Run 3 global data and illustrate the impact of the time-gating selection on the single photon resolution and background level.

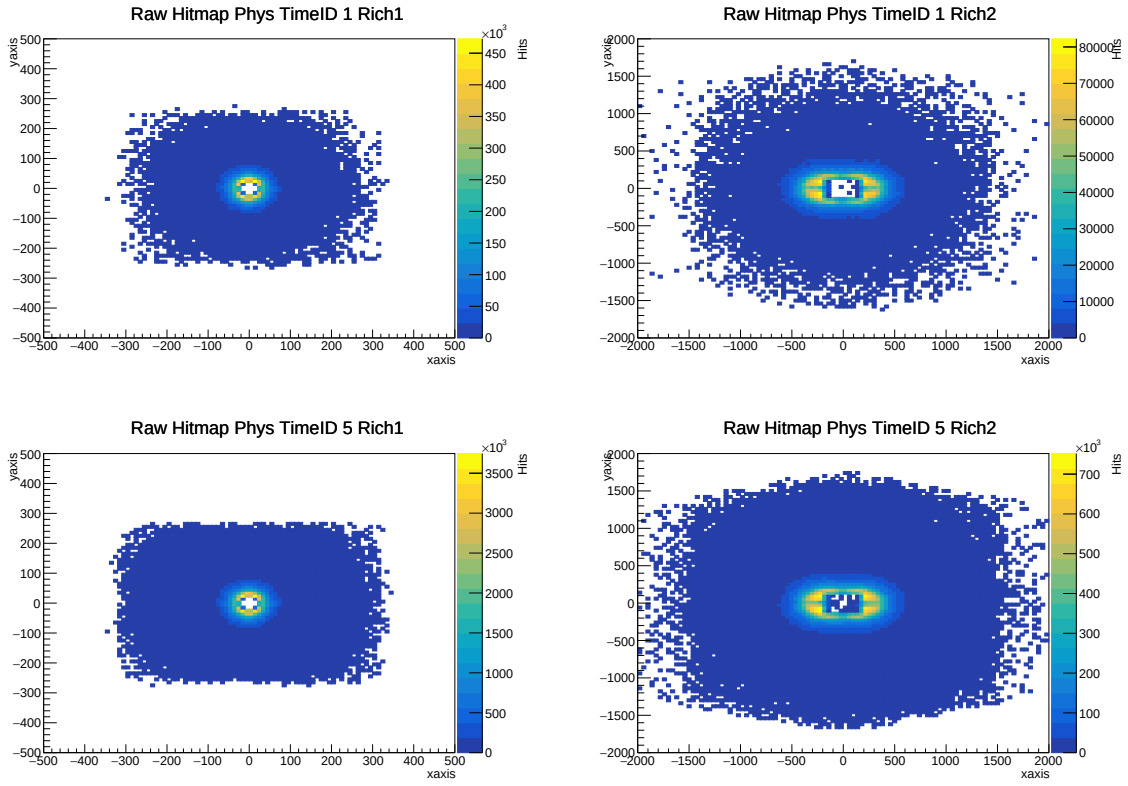

Figure 9.3: Hitmaps using different time windows for (left) RICH1 and (right) RICH2. (Top) Results using the 6.25 ns time window and (bottom) using the 25 ns time window.

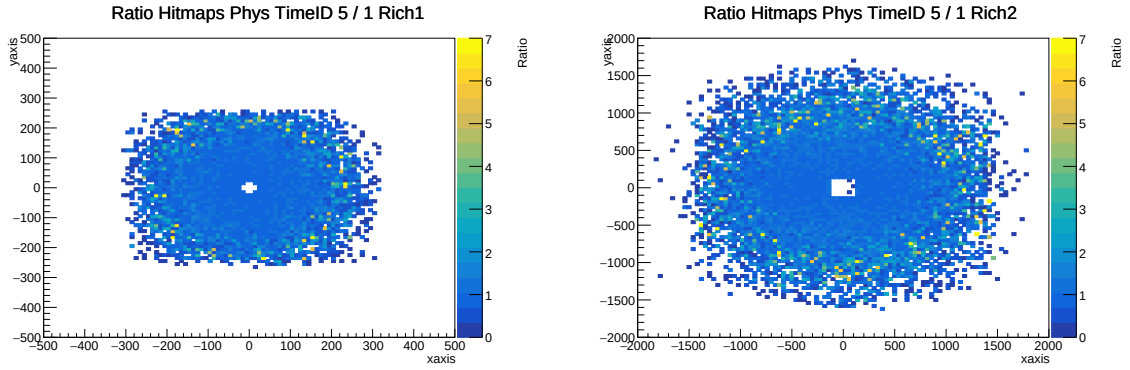

Figure 9.4: Ratio of the Hitmaps with the 25 ns time window sample over the reference 6.25 ns one for (left) RICH1 and (right) RICH2.

9.3 Summary

In this chapter, the evolution of background contributions to the single photon resolution has been investigated using Run 3 data. The analysis focuses on the dependence of the background level on the photon time window and on the detector geometry, providing a detailed characterisation of the performance of the upgraded RICH system.

These studies represent an important validation of the Run 3 detector performance and provide valuable input for the understanding of photon misassignment mechanisms. Moreover, the quadrant-by-quadrant and time-window-dependent analysis establishes a solid basis for future optimisation studies and for the development of improved background mitigation strategies in view of the Upgrade II programme.

Performances of RICH detectors for Upgrade II of LHCb

The identification of charged hadrons, in particular the separation of pions, kaons, and protons, represents one of the strengths of the LHCb experiment. Many of the most precise measurements in flavour physics rely on the ability to correctly assign the species of each reconstructed particle, thereby suppressing backgrounds and enhancing the sensitivity to rare processes. Central to this capability is the Ring Imaging Cherenkov (RICH) system, which provides excellent particle identification (PID) performance across a wide momentum range, extending from a few GeV to well above 100 GeV.

As the Large Hadron Collider enters its high-luminosity era, LHCb is preparing for a major transformation. The Upgrade II programme foresees operation at instantaneous luminosities up to $1.0\text{–}1.5 \times 10^{34}, \mathrm{cm}^{-2}\mathrm{s}^{-1}$ during Run 5 and beyond, enabling the collection of a dataset of the order of $300\,\mathrm{fb}^{-1}$. Operating under such demanding beam conditions introduces unprecedented challenges for detector systems, especially those dedicated to PID, which will be exposed to significantly increased particle flux and detector occupancy.

To sustain performance in this new regime, the RICH detectors must be completely redesigned. A combination of high-granularity photon sensors, improved timing capabilities, and optimised optical configurations is required to allow efficient photon-track association and preserve the resolution on the Cherenkov angle. Meeting these targets necessitates the evaluation of different technological solutions, balancing operational feasibility, cost, and physics performance.

This chapter presents a systematic study of possible RICH configurations for the Upgrade II, focusing on the choice and spatial distribution of photon detectors on the existing detection planes. By assessing the expected PID capabilities in the high-luminosity environment, the aim is to identify the most effective configuration for the future of the experiment. In particular, the analysis compares scenarios with different granularity, timing performance, and detector coverage, providing insight into the trade-offs associated with each option.

Chapter 10

LHCb Upgrade II

This chapter presents performance studies of the upgraded RICH system, evaluating different detector configurations to ensure robust particle identification capabilities under High-Luminosity LHC conditions.

10.1 Upgrade II

The LHCb Upgrade II (U2) represents the next major enhancement of the experiment and is conceived to fully benefit from the operating conditions of the High-Luminosity LHC (HL-LHC).

After the success of Upgrade I, which enabled stable data-taking (Run 3) at values of luminosity about five times higher ($2 \times 10^{33}\,\mathrm{cm^{-2}s^{-1}}$) than the value originally foreseen for LHCb during Runs 1–2 ($4 \times 10^{32}\,\mathrm{cm^{-2}s^{-1}}$), Upgrade II is designed to further increase the detector performance and data throughput.

The upgraded system will sustain data rates one order of magnitude larger than today, allowing for unprecedented precision in flavour-physics measurements and in searches for effects beyond the Standard Model (SM).

Reaching these goals requires significant advances in several key aspects of the detector, including radiation hardness, readout electronics, and real-time data processing. This document summarises performance studies of the RICH system carried out under various proposed machine-operation scenarios.

10.1.1 Luminosity Values

Upgrade II is planned to operate at instantaneous luminosities in the range $[1.0, 1.5] \times 10^{34}\ \mathrm{cm^{-2}s^{-1}}$, up to a factor of ten higher than those expected during Run 3. At these collision rates, an average of about 40 proton–proton interactions per bunch crossing is anticipated, compared to approximately 5 in Upgrade I. Over

the full HL-LHC programme, this corresponds to an integrated luminosity of roughly $300\,\text{fb}^{-1}$.

To assess technical performance and operational feasibility, three scenarios have been defined:

- *Baseline:* operation at 1.5×10^{34} $\text{cm}^{-2}\text{s}^{-1}$ with the complete suite of detector upgrades, maximising physics potential;
- *Middle:* reduced-luminosity running at 1.0×10^{34} $\text{cm}^{-2}\text{s}^{-1}$ with a moderately simplified detector layout;
- *Low:* an even more cost-effective scenario at the same reduced luminosity, with additional compromises on performance.

Further details on these configurations and their projected physics reach can be found in the Scoping Document [117]. Nonetheless, even the most conservative scenario permits LHCb to maintain a leading role worldwide in heavy-flavour physics thanks to the unprecedented statistical precision achievable at HL-LHC.

10.1.2 New Features

Since the HL-LHC baseline design [118] is compatible with LHCb running at the Upgrade I luminosity of $2 \times 10^{33}\,\text{cm}^{-2}\text{s}^{-1}$ (Run 3), during Run 4, LHCb will operate at a similar luminosity thanks to controlled beam defocusing. Operating above this nominal luminosity would require further detector modifications, and the Upgrade II project, targeting Run 5, introduces major innovations to ensure reliable operation and high-precision measurements under these more demanding conditions.

A key element is the implementation of precision timing. New detector components with time resolutions of a few tens of picoseconds will allow the experiment to disentangle multiple proton-proton interactions within a single bunch crossing. This timing capability is crucial for maintaining the excellent vertexing and track reconstruction performance in high pile-up environments.

Another major improvement lies in the use of radiation-hard technologies. Detector regions close to the beam pipe will receive significantly higher radiation doses than in previous LHC runs. To ensure sustained performance over time, new materials and electronics have been developed with enhanced radiation tolerance, particularly for tracking detectors such as the vertex locator (VELO).

Detector granularity and coverage will also be significantly enhanced. Finer segmentation of the tracking systems will help manage the increased occupancy. The electromagnetic calorimeter (ECAL) will be upgraded by replacing its innermost modules with a radiation-hard SpaCal (spaghetti calorimeter) design. In addition, the front-end electronics of the calorimeter and the RICH detectors will be redesigned

to include timing capabilities. The RICH system will benefit from the development of FastRICH ASICs, which combine excellent photon timing resolution with compactness and radiation tolerance, enabling time-based particle identification.

On the data acquisition side, a modern and scalable infrastructure will be adopted. A new generic readout board, the PCIe400, will allow high-speed data transmission and precise synchronisation across the entire detector. Dedicated FPGA-based modules will perform on-the-fly processing and reconstruction of detector signals, including a prototype of a downstream tracker with real-time clustering and decoding capabilities. The trigger system will operate entirely in software, maintaining high efficiency while processing the full 40 MHz collision rate.

Beyond improvements in detector performance, Upgrade II will enhance the LHCb physics programme by enabling more precise measurements, thereby extending the physics reach of LHCb in a way that is expected to remain competitive up to the FCC-hh era. The experiment will continue to lead in flavour physics, enabling unprecedented precision in measurements of *CP*-violating observables and rare decays of beauty and charm hadrons. This includes both tree-level and loop-induced processes, allowing stringent tests of the SM and sensitive probes for virtual contributions from new particles at scales well beyond the direct reach of the LHC. The increased data sample and enhanced detector capabilities will also allow searches for lepton flavour universality violation and new sources of *CP* violation, both of which could help explain the observed matter-antimatter asymmetry of the Universe.

Rare processes will be studied with unparalleled precision, with potential to clarify the origin of current anomalies observed in flavour-changing neutral-current (FCNC) b-hadron decays, such as deviations in branching fractions and angular observables in $b \to s\ell^+\ell^-$ transitions (the so-called "B anomalies") [119–123], and to test the chiral structure of weak interactions.

In the charm sector, the upgrade will enable measurements of time-dependent *CP* asymmetries at the 10^{-5} sensitivity level, probing possible beyond the Standard Model dynamics in up-type quark transitions. Moreover, LHCb will greatly expand its hadron spectroscopy programme, with improved sensitivity to both conventional and exotic states, including doubly heavy baryons and tetraquarks, offering new insights into the strong interaction and hadronic structure.

In addition to flavour physics, Upgrade II will extend LHCb's contribution to heavy-ion studies, including high-multiplicity central Pb–Pb and p–Pb collisions, providing a complementary view on QCD matter under extreme conditions. The fixed-target programme will also continue, offering unique access to the high-x regime of nucleon structure and the study of cold nuclear matter effects. Together, these developments ensure that LHCb remains at the forefront of precision tests of the Standard Model and searches for New Physics across a wide range of observables and energy scales.

Altogether, these new features define LHCb Upgrade II as a highly ambitious and forward-looking project, well-aligned with the scientific priorities of the HL-LHC era. Its advanced technologies and broad physics reach will ensure that LHCb remains a world-leading experiment in flavour physics and beyond.

Table 10.1: Summary of RICH detector scenarios.

Parameter	**Baseline**	**Middle**	**Low**
Luminosity [$\mathrm{cm^{-2}s^{-1}}$]	1.5×10^{34}	1.0×10^{34}	1.0×10^{34}
Inner : Total Area	1 : 3	1 : 4	1 : 4
Inner sensor type	1.4 mm SiPM	2.0 mm SiPM	2.0 mm SiPM
Outer sensor type	2.8 mm SiPM	2.8 mm SiPM	2.8 mm MaPMT
Optics configuration	New	New	New (RICH1 only)
Inner timing resolution	150–300 ps	150–300 ps	150–300 ps
Outer timing resolution	150–300 ps	150–300 ps	600 ps
Readout channels	750,000	469,000	445,000

10.1.3 Proposal of RICH system upgrade

The substantial increase in particle flux expected under the Upgrade II luminosity conditions will strongly affect the particle identification (PID) detectors of the LHCb experiment. In particular, the regions located closest to the beam pipe will experience the highest occupancies, potentially reaching values close to 100% for some subsystems. For the RICH detectors, however, hit occupancy cannot be reliably interpreted above approximately 30–35%. Beyond this level, the probability that multiple photons strike the same channel becomes significant, causing hit merging and saturation effects. Consequently, the effective occupancy must be kept well below this limit to retain a meaningful detector response.

To ensure robust PID performance, the occupancy within each RICH subdetector must therefore remain compatible with the constraints imposed by the readout electronics and the reconstruction algorithms. A key strategy consists of deploying highly granular and radiation-tolerant photon sensors in the regions most exposed to high particle densities. Granularity alone, however, is not sufficient to mitigate the effects of high pile-up. Precise timing information, at the level of a few tens of picoseconds per detected photon, is essential to correctly associate the recorded Cherenkov photons with the originating track.

Achieving such timing precision across a large number of readout channels introduces additional cost and technological complexity. Nevertheless, the use of lower

peak luminosities would naturally reduce occupancy, allowing for more cost-effective configurations with less stringent timing requirements.

The present RICH system delivers efficient separation of charged hadrons over a momentum interval between 3 and 100 GeV, where RICH1 covers the full LHCb acceptance and RICH2 is dedicated to the more forward region populated by high-momentum tracks. Measurements performed with Run 3 data, for an average of $\langle N_{\mathrm{PV}} \rangle \sim 5$, confirm a kaon identification efficiency close to 95% with a pion misidentification probability of only 2–3% (see Figure 10.1). Such performance strongly relies on the resolution of the Cherenkov angle per single photon, σ_{θ_C}, driven mainly by the pixel size, chromatic dispersion, the uncertainty on the emission point of the photon along the track, and the precision of the tracking system. Since the dominant contributions are of comparable magnitude, simultaneous optimisation of all of them is required.

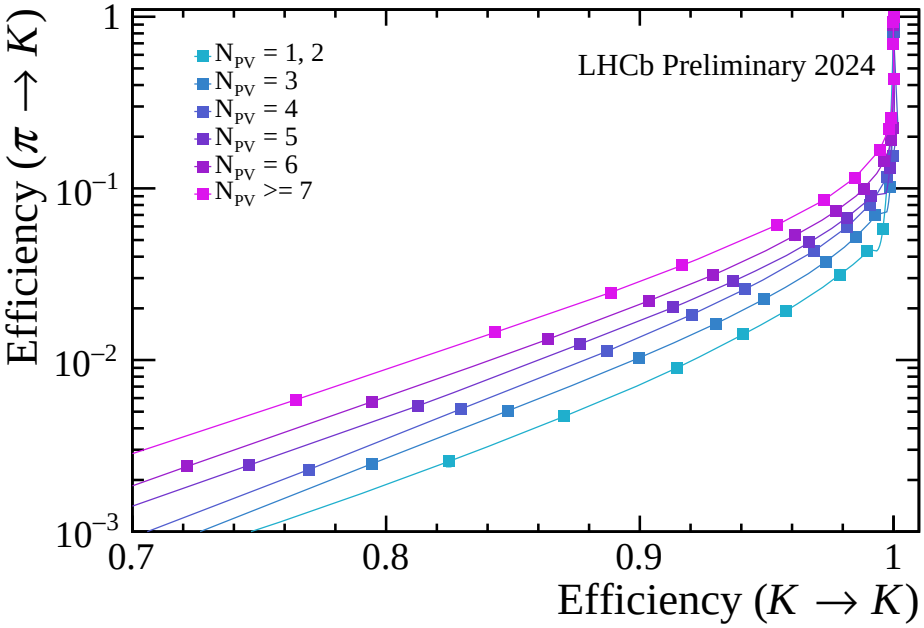

Figure 10.1: Kaon identification efficiency against pion misidentification probability for fill 9986, in different bins of number of primary vertices. The average number of primary vertices is 4.7. The average momenta of the kaons and pions are both 35 GeV [124]

The design for Upgrade II preserves the current placement of RICH1 and RICH2, which has proven to be close to optimal. The target performance for the upgraded system foresees occupancies below 30% and a single-photon Cherenkov angle resolu-

tion better than 0.5 mrad.

To meet these goals, multiple upgrade strategies are evaluated and summarised in Table 10.1. In the *Baseline* scenario, the size of the photodetector pixels is reduced by a factor of four in the innermost, high-occupancy regions (about one-third of the total surface), by replacing the current MaPMTs with faster and more granular devices, either SiPMs or MCP-PMTs. The outer regions remain equipped with sensors of larger pixel size, optimising both performance and cost.

Both candidate sensor technologies must ensure high photon detection efficiency in the green region of the spectrum, where chromatic dispersion is smaller, and provide timing resolutions of the order of tens of picoseconds. SiPMs enable excellent timing performance but require cryogenic cooling to suppress dark noise, increasing infrastructure complexity. MCP-PMTs avoid cooling constraints but require dedicated R&D to guarantee radiation hardness and rate capability in the harsh Upgrade II environment. A key element of the upgrade is the FastRICH front-end ASIC, currently under development, capable of providing ~ 25 ps timing per hit and planned for deployment starting from Run 4 [125]. In addition to new sensors, optical system improvements may be required to minimise aberrations and preserve the targeted angular resolution.

Two additional configurations are considered. The *Middle* scenario reduces the instrumented high-granularity area to roughly one-quarter of the detector plane and permits larger pixels, reflecting the lower occupancy expected. The *Low* scenario further relaxes timing requirements in the outer region, where standard MaPMTs may still be used. Another relevant difference in this *Low* scenario is the absence of the TORCH detector[1], which significantly simplifies the mechanics and optics of RICH2, although at the cost of degraded angular and timing resolution in the least occupied sectors.

All relevant features of the proposed configurations are summarised in Table 10.2. Overall, the RICH upgrade for Upgrade II is designed to preserve outstanding PID capabilities in the high-luminosity environment of the future LHC, while offering flexibility to tailor cost and system complexity to the final luminosity conditions of the experiment.

[1]TORCH (Time Of internally Reflected CHerenkov) is a proposed subdetector for LHCb Upgrade II, designed to provide precise time-of-flight measurements (~ 15 ps) for charged particles over a ~ 10 m flight distance. This enables pion/kaon and kaon/proton separation in the momentum ranges $2-15$ GeV/c and $2-20$ GeV/c, respectively, and allows identification of kaons and protons below the Cherenkov threshold in RICH1. The detector consists of 18 quartz plates, which internally reflect Cherenkov photons that are focused onto fast photodetectors, providing high-precision timing information [23].

Table 10.2: Summary of the *Baseline*, *Middle* and *Low* scenarios for the RICH system. The high occupancy area is referred to as "Inner area", while the low occupancy as "Outer". In all cases SiPMs or MCPs are implied, except for the low occupancy region in the *Low* scenario, where MaPMTs are assumed. For all scenarios, the pixel size of the outer area is $2.8 \times 2.8\,\mathrm{mm}^2$.

Scenario	**Inner area**	**Inner area size (mm)**	**Pixel size inner area**	**New optical layout**
Baseline	1/3	RICH1: x=336, y=364 RICH2: y=300	$1.4 \times 1.4\,\mathrm{mm}^2$	RICH1 RICH2
Middle	1/4	RICH1: x=280, y=336 RICH2: y=244	$2.0 \times 2.0\,\mathrm{mm}^2$	RICH1 RICH2
Low	1/4	RICH1: x=280, y=336 RICH2: y=244	$2.0 \times 2.0\,\mathrm{mm}^2$	RICH1

10.2 Emulation

The performance projections for the Upgrade II detector rely extensively on fast and versatile simulation frameworks. In this context, the emulation of the RICH system is a key element, enabling realistic estimates of the Particle Identification (PID) capabilities anticipated under the different upgrade scenarios. In contrast to full detector simulations, which require substantial computational resources, the emulation approach provides an efficient environment to explore various design options, incorporating parametrised models of the detector response that are informed by current simulation studies.

This chapter describes the methodology employed to emulate the RICH performance for Upgrade II, including the assumptions and parameterisations introduced to model the expected evolution of key detector characteristics. In particular, the treatment of the single-photon Cherenkov angle resolution, photon yields, sensor pixelisation, and timing information is detailed. The strategy is mainly based on scaling the current Run 3 configuration to incorporate the changes foreseen in terms of geometry, optical layout, and readout structure.

The emulation relies on samples of simulated pp collisions containing at least one $b\bar{b}$ pair, generated both for Run 3 and for the Upgrade II luminosity conditions. For these datasets, the detector geometry corresponds to the Run 3 implementation: a single pixelisation scheme in RICH1 with $2.87 \times 2.87\,\mathrm{mm}^2$ channels, and two regions in RICH2, featuring an inner high-granularity area with the same pixel size and an

outer region instrumented with larger $5.6 \times 5.6\,\mathrm{mm}^2$ pixels. Although the underlying geometry corresponds to the current detector, the improved resolution and response expected for Upgrade II are modelled through parametric scaling of key detector characteristics, such as the single-photon Cherenkov angle resolution, photon yields, and pixelisation effects. This approach allows the emulation to reproduce the anticipated performance of the upgraded system without requiring full re-simulation of the modified geometry. A detailed discussion of the methods and parameterisations used to model the expected improvements in detector response is provided in Section 10.2.1.

10.2.1 Resolution function and photon yield input

A key ingredient of the Upgrade II emulation is the description of the single-photon Cherenkov angle resolution, σ_{θ_C}, which directly impacts the separation power between different hadron species. Within the emulation framework, this quantity is obtained by applying configuration-dependent scaling factors to parameterisations extracted from Run 3 simulation studies, thus ensuring consistency with the currently measured detector performance.

The reference parameterisations describe the dependence of the mean single-photon resolution on the track momentum according to the empirical form:

$$\sigma_{\theta_C}(p) = a + b \cdot \left(\tanh\left(-\frac{p}{c} \right) + 1 \right), \tag{10.1}$$

where p denotes the particle momentum in MeV/c, and the coefficients a, b, and c are tuned to reproduce the behaviour observed in a detailed simulation. The functional shape has no particular physical motivation, but it provides an accurate and smooth interpolation across the relevant momentum region. The numerical values of the parameters adopted in this study are summarised in Table 10.3.

Table 10.3: Coefficient a, b, c for RICH1 and RICH2.

	a	b	c [MeV/c]
RICH1	0.00078	0.0012	5000
RICH2	0.00065	0.0011	5000

The baseline resolution functions are subsequently modified through multiplicative scaling factors, specific to each Upgrade II scenario. At first order, this multiplicative approximation is justified, as the single-photon Cherenkov angle resolution, σ_{θ_C}, is determined by independent contributions, such as pixel granularity, optical aberrations, and chromatic dispersion:

$$\sigma^2_{\theta_C} = \sigma^2_{\mathrm{pixel}} + \sigma^2_{\mathrm{optics}} + \sigma^2_{\mathrm{chrom}}, \tag{10.2}$$

and these scaling factors account for the expected impact of changes in the detector parameters. Distinct scale values are applied for the inner and outer regions of both RICH1 and RICH2, reflecting their differing occupancy and geometric constraints. For small modifications of the detector parameters mentioned above, the resulting change in each contribution leads to an approximately proportional change in the total resolution. Consequently, the overall effect of small structural changes can be modelled using a multiplicative scaling of the empirical function, with higher-order non-linear effects being negligible. The numerical inputs used in this study are listed in Table 10.4.

For each correctly associated Cherenkov photon, the reconstructed value of the Cherenkov angle is regenerated by taking the expected angle for the particle under consideration and smearing it according to the corresponding momentum-dependent resolution function. In this way, the key observable for PID,

$$\theta_{\text{rec}} - \theta_{\text{exp}}, \tag{10.3}$$

is explicitly controlled in the emulation. Photons that do not originate from the track under study are left unchanged, as their θ_C distribution is already much broader than the intrinsic detector resolution. This procedure offers a computationally lightweight yet realistic approximation of the separation power across the entire momentum spectrum, while preserving consistency with the underlying reconstruction behaviour.

The momentum dependence of the reference resolution functions for Run 3 is shown in Figure 10.2, together with the pion and kaon Cherenkov thresholds, serving as a performance baseline for the Upgrade II emulation. The full input curves used in the study are displayed for both RICH1 and RICH2 in Figure 10.3. It is worth noting that the precise modelling of the low-momentum region has only a limited effect on the expected PID performance, as in this regime the differences in Cherenkov angles between particles significantly exceed the detector resolution, rendering the particle separation largely insensitive to small variations in σ_{θ_C}.

In addition to the angular resolution, the mean number of detected photons per track is also incorporated in the emulation. These photon yields, extracted from Run 3 simulations and presented in Figure 10.4, are rescaled to reflect variations in optical throughput and sensor technology across the different upgrade scenarios.

The scale factors applied to both θ_C resolution and photon yields are derived from full simulations of the current (Run 3) system equipped with MaPMTs and of the upgraded optical configuration described in the Framework Technical Design Report (FTDR) [126], instrumented with SiPMs. In these simulations, a wavelength cut at $\lambda > 300\,\text{nm}$ is assumed, slightly lower than the $\lambda > 400\,\text{nm}$ value adopted in the FTDR, and nominal photon detection efficiencies are considered (see Figure 10.5). The simulations were performed using SiPMs with a pixel pitch of 1 mm; the resolution impact of larger pixels is included by scaling the corresponding contribution

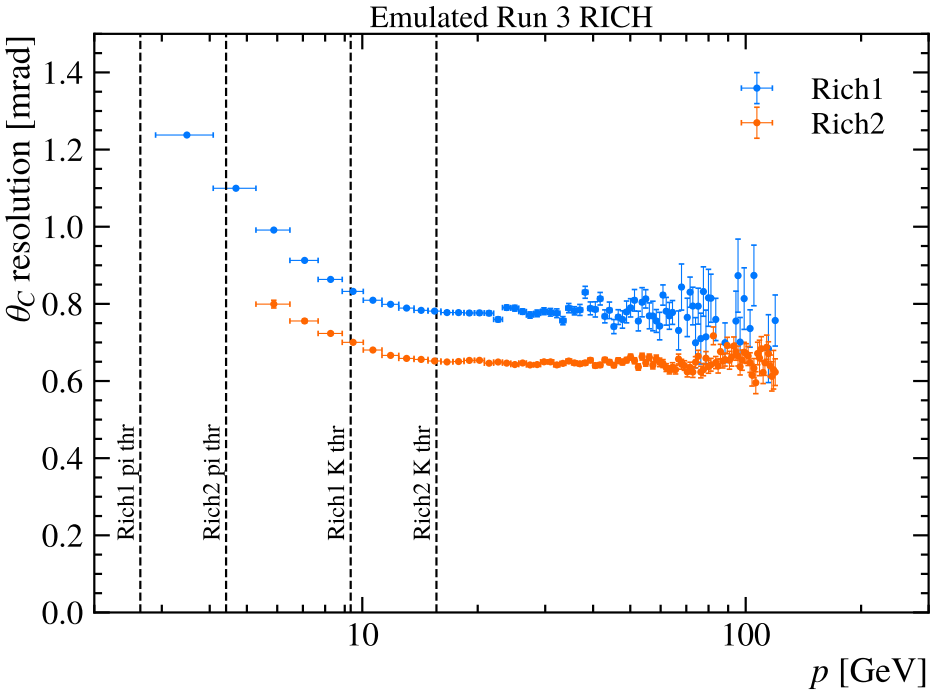

Figure 10.2: Single-photon Cherenkov angle resolution σ_{θ_C} as a function of momentum, shown separately for pions and kaons in RICH1 and RICH2 under Run 3 conditions. These resolution curves serve as the baseline input for the Upgrade II emulation framework, and are scaled depending on the detector scenario.

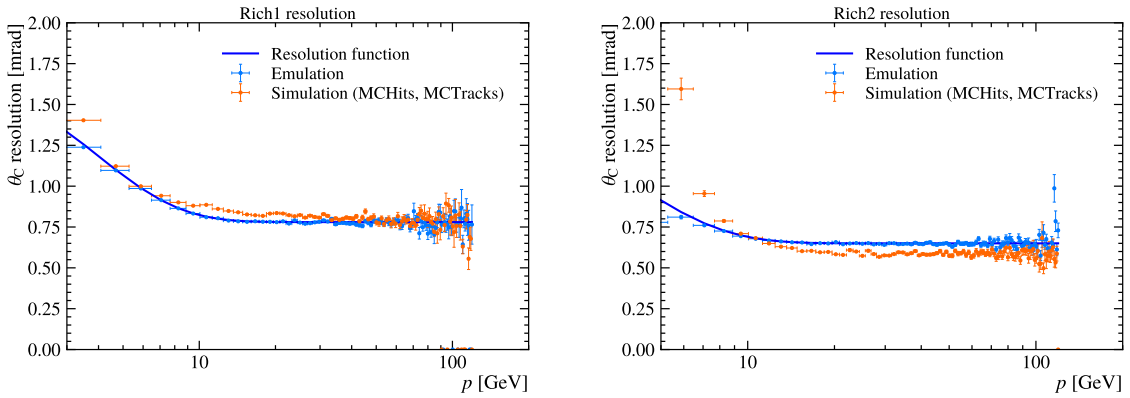

Figure 10.3: Single-photon Cherenkov angle resolution σ_{θ_C} as a function of momentum for the (left) RICH1 and (right) RICH2 detectors. In both cases, the resolution function is compared with the emulation and the full simulation (MCHits, MCTracks).

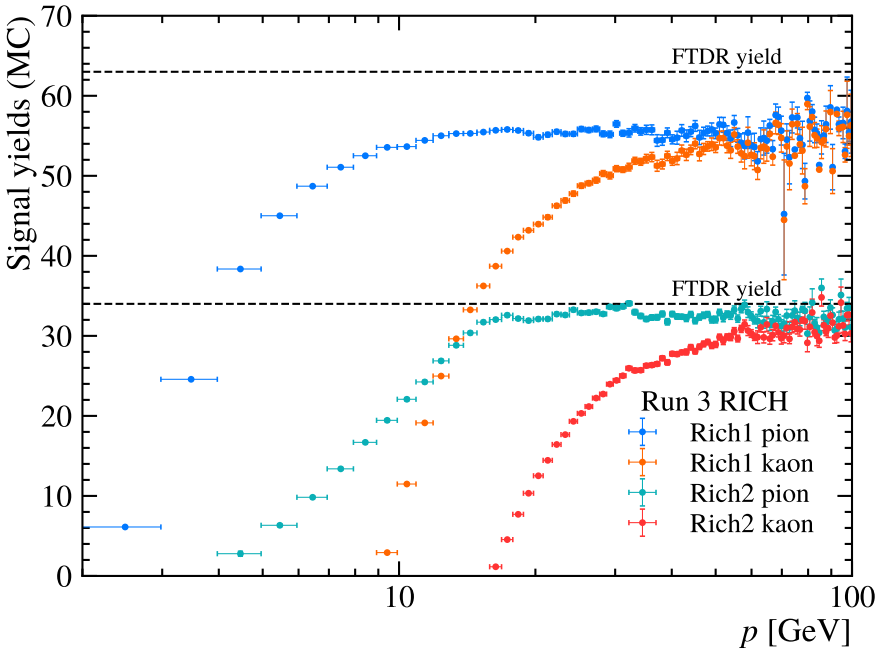

Figure 10.4: Average number of detected Cherenkov photons per track as a function of momentum, separately for pions and kaons in RICH1 and RICH2. These yields are used as default inputs to the Upgrade II emulation and may be rescaled to reflect improvements in quantum efficiency or optics.

linearly with pixel size.

The resulting scale factors for the Cherenkov angle resolution are summarised in Table 10.5, while the photon-yield scale factors are listed in Table 10.4. A single resolution scale is applied independently of momentum, effectively preserving the Run 3 relative contribution of tracking uncertainties to the total θ_C resolution.

All input values used in this study are taken from Ref. [127]. Occupancy estimates are obtained by rescaling the Run 3 simulation to Upgrade II conditions, accounting for the changes in detector area and photon-yield expectations. Additional effects connected to dead-time losses are not evaluated at this stage.

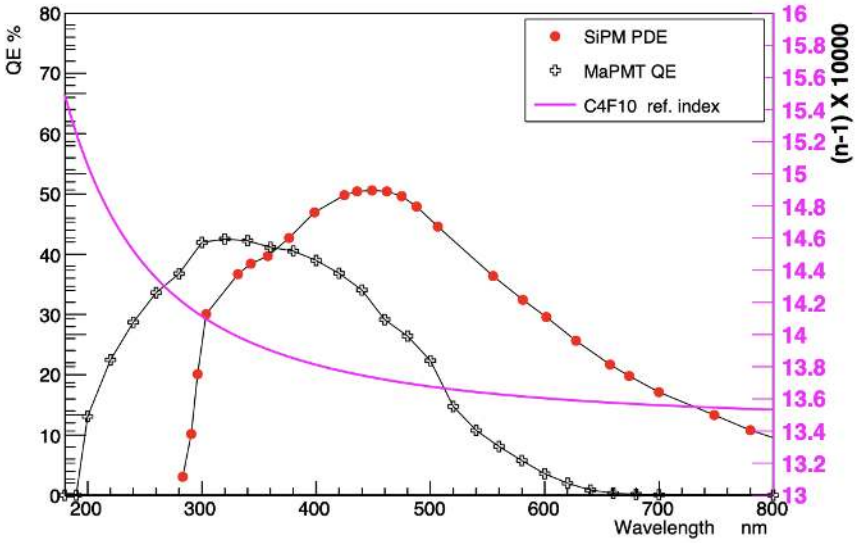

Figure 10.5: Typical SiPM PDE, MaPMT QE and refractive index of RICH1 gas radiator.

To reflect the strong occupancy gradients across the detector acceptance, the RICH volumes are partitioned into two regions: a high-occupancy inner zone and a lower-occupancy outer zone. In the *Baseline* configuration, the inner region covers one third of the total photodetector surface for both RICH1 and RICH2, leaving the remaining two thirds as the outer region. Alternative upgrade scenarios adopt a different split, where the inner region corresponds to one quarter of the area (Table 10.2). This segmentation enables a differentiated modelling of photon yields and angular resolution according to the detector occupancy.

Because a fully operational high-luminosity reconstruction chain was not yet available during the development of these studies, tracking was emulated rather than obtained from the standard digitisation and reconstruction workflow. The *Boole*

Table 10.4: Values of the scaling factors (SF) used in the code to rescale with respect to the Run 3 simulation the photon yield (Yield SF). *Baseline* and *Middle* correspond to SiPM nominal PDE with $\lambda > 300\,\text{nm}$, while *Low* uses MaPMT in the outer region. The Run 3 values, used to obtain the SF, are 63 for RICH1 and 34 for RICH2.

Type	**Inner**		**Outer**	
	Yield	**Yield SF**	**Yield**	**Yield SF**
RICH1 input values				
Baseline	52	0.825	52	0.825
Middle	52	0.825	52	0.825
Low	52	0.825	46	0.730
RICH2 input values				
Baseline	25	0.735	25	0.735
Middle	25	0.735	25	0.735
Low	33	0.970	34	1.000

Table 10.5: Cherenkov angle resolution contributions. The Run 3 values, used as denominators to obtain the scale factors, are 0.806 for RICH1 and 0.516 for RICH2.

Type	**Inner**					**Outer**				
	Chrom.	**Emiss.**	**Pixel**	**Overall**	**SF**	**Chrom.**	**Emiss.**	**Pixel**	**Overall**	**SF**
RICH1 input values										
Baseline	0.28	0.13	0.22	0.379	0.47	0.28	0.13	0.45	0.545	0.676
Middle	0.28	0.13	0.32	0.444	0.55	0.28	0.13	0.45	0.545	0.676
Low	0.28	0.13	0.32	0.444	0.55	0.52	0.13	0.45	0.699	0.867
RICH2 input values										
Baseline	0.19	0.05	0.10	0.220	0.426	0.19	0.05	0.20	0.280	0.542
Middle	0.19	0.05	0.14	0.241	0.467	0.19	0.05	0.20	0.280	0.542
Low	0.19	0.36	0.14	0.430	0.833	0.34	0.36	0.20	0.534	1.034

digitisation step was therefore omitted, and Monte Carlo truth information was used to define the track segments entering the RICH acceptance. The tracking contribution to the Cherenkov angle resolution is embedded in the overall resolution parameterisations. While this is not a complete substitute for a full reconstruction, it reproduces the momentum dependence of the performance with adequate fidelity for comparative detector studies.

A further key ingredient of the emulation is the inclusion of 4D reconstruction, where the timing of photon hits is used alongside their position. The expected photon arrival time is computed from the track production time at the PV, its propagation through the detector, and the photon time of flight to the photodetector plane. Timing windows of 150, 300, or 600 ps (the latter applicable only to MaPMTs) are applied during both photon association and likelihood evaluation to suppress out-of-time background contributions. This assumes that the PV timestamp is provided externally with negligible uncertainty.

To emulate the charged particle passage through the RICH detectors, a dedicated module constructs track-segment objects directly from the truth-level trajectory information produced by Gauss. This includes detailed geometry information for particles traversing the radiators and truth labels for all generated Cherenkov photons. Notably, the use of extended MC information allows below-threshold tracks to be included, improving the realism of the PID evaluation and supporting investigations of hybrid PID approaches involving subdetectors such as TORCH.

The emulated tracks are subsequently required to satisfy basic reconstructibility criteria for "Long" tracks and simple fiducial cuts (e.g. $p_T > 0.2\,\text{GeV}$ and $p > 1\,\text{GeV}$), consistent with the behaviour of standard reconstruction. They are then converted into the same RICH segment data format used by the real PID sequence, ensuring full compatibility with the rest of the pipeline.

Although the tracking description in the emulation is simplified, the resulting Run 3 PID performance is consistent with the one obtained from a full simulation and reconstruction chain. The primary goal of this framework is not to reproduce absolute performance estimates, but rather to enable a robust and efficient comparison of the relative behaviour across different optical configurations and sensor technologies.

10.2.2 Performance studies

The likelihoods for the different particle hypotheses are computed using the standard RICH reconstruction algorithm described in Ref. [128]. Since a full simulation and reconstruction framework for the new detector geometries was not yet available, the PID performance of three Upgrade II configurations was evaluated using the emulation framework. This approach enables rapid and consistent comparisons of detector parameters such as pixel granularity, quantum efficiency, and timing resolution.

The emulation assumes that at most one photon may be detected per pixel per bunch crossing, and average photon yields can be adjusted to reproduce the expected changes in the optical system. Timing information is also incorporated: only photons whose arrival time lies within a configurable window around the expected value are associated to the track. To maintain an efficiency above 95% for signal photons, the timing window is chosen to cover at least $\pm 2\sigma$ of the detector time resolution. Tighter timing cuts combined with improved time resolution enhance the rejection of accidental and background hits.

At the current stage, the emulation does not account for changes in the spatial or spectral photon distributions; reductions in detected light are implemented through global scale factors rather than applied on a per-track basis. Moreover, the response of the front-end electronics is only approximated by rejecting photons that arrive simultaneously on the same pixel. Other effects, such as saturation, spillover, or deadtime, are not yet included.

Performance results are shown for timing windows of 150 and 300 ps. To match these windows, the combined single-photon timing resolution of the photodetector and front-end system is set to 38 and 75 ps, respectively.

Figures 10.6–10.10 summarise the PID performance for the Run 3 detector and the selected Upgrade II scenarios at different time resolutions and luminosity conditions.

Figure 10.6 reports the kaon identification efficiency as a function of momentum for a fixed pion misidentification rate of 1%, while Figure 10.7 shows the same quantity with a relaxed 5% misidentification rate. All upgrade configurations demonstrate adequate performance in the corresponding high-luminosity environments. Below 10 GeV/c, a mild degradation relative to Run 3 is observed, particularly for a 300 ps resolution. Conversely, above 20 GeV/c, the upgraded configurations deliver a clear improvement: the *Baseline* and *Middle* scenarios maintain efficiencies above 80% up to 100 GeV/c, whereas the Run 3 performance rapidly deteriorates beyond 40 GeV/c. Relaxing the misidentification rate to 5% increases the efficiency in all cases while preserving the same performance hierarchy.

Figure 10.8 displays the kaon efficiency as a function of pseudorapidity for a 1% pion misidentification probability. The *Baseline* and *Middle* configurations clearly outperform Run 3 in the forward region ($\eta > 4$), where the efficiency drop is most pronounced in the current detector, while all scenarios show similar results at lower pseudorapidities.

The upgraded designs maintain good efficiency up to 100 GeV/c at 150 ps, while Run 3 begins to lose performance beyond 30 GeV/c. At 300 ps, the p/K and p/π separation capabilities are noticeably reduced at low momentum ($p < 30$ GeV/c) for all upgrade options.

Overall, the *Baseline* scenario delivers the most robust performance at the luminosity for which it is designed. At its operating luminosity, the *Middle* configuration achieves similar performance, particularly at 150 ps, and consistently outperforms the *Low* scenario under all tested conditions.

10.2.3 Occupancy studies

Occupancy in the photon detectors is a crucial parameter, as it directly affects both the reconstruction efficiency and the performance of the trigger system. To ensure reliable pattern recognition and to prevent signal saturation, the design target is to keep pixel occupancy below 30% in all RICH detectors.

To manage the high hit density, all layouts implement smaller pixel sizes in the inner RICH regions. In the *Baseline* scenario, one-third of the photon detector area is equipped with fine-granularity pixels, while the remaining two-thirds employ larger pixels ($\sim 2.8\,\text{mm}^2$). In the *Middle* and *Low* scenarios, the high-granularity region is reduced to one-fourth of the total area.

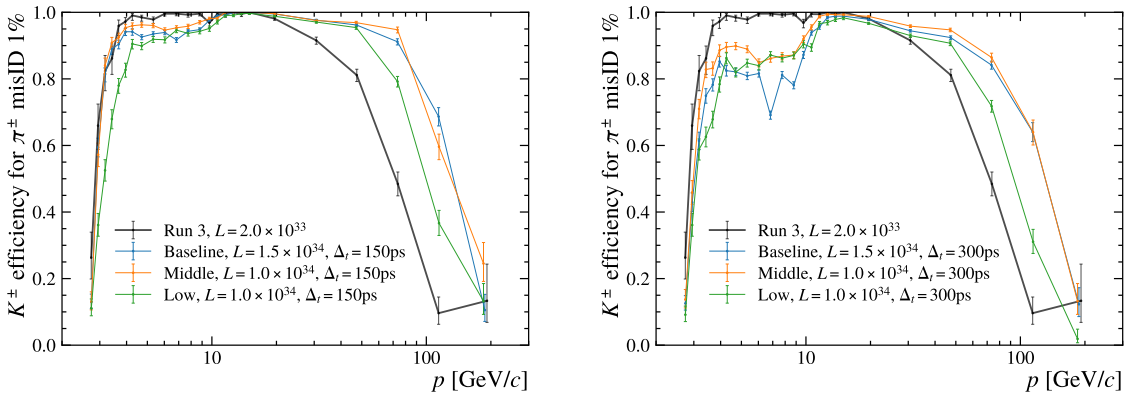

Figure 10.6: Kaon efficiency for 1% pion misidentification versus momentum, for the Run 3 and the three RICH Upgrade II options at different luminosities, for (left) 150 ps and (right) 300 ps time windows, assuming the same average photoelectron yields.

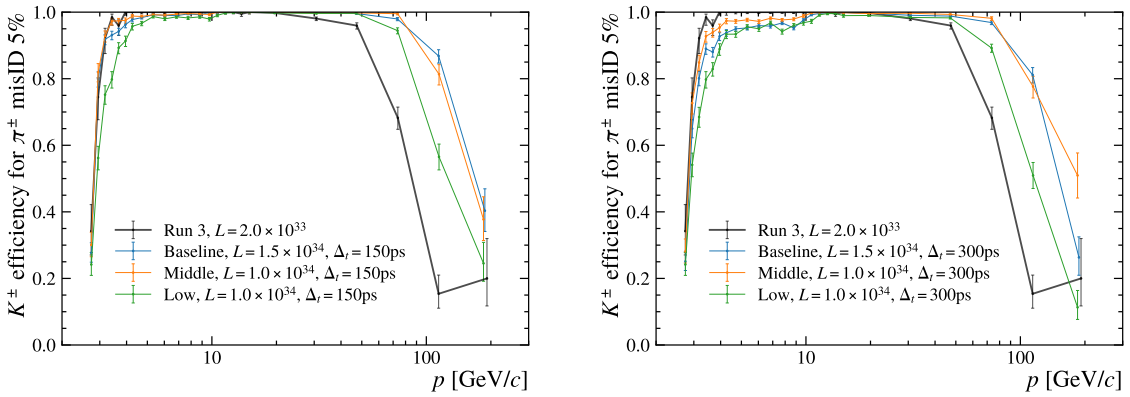

Figure 10.7: Kaon efficiency for 5% pion misidentification versus momentum, for the Run 3 and the three RICH Upgrade II options at different luminosities, for (left) 150 ps and (right) 300 ps time windows, assuming the same average photoelectron yields.

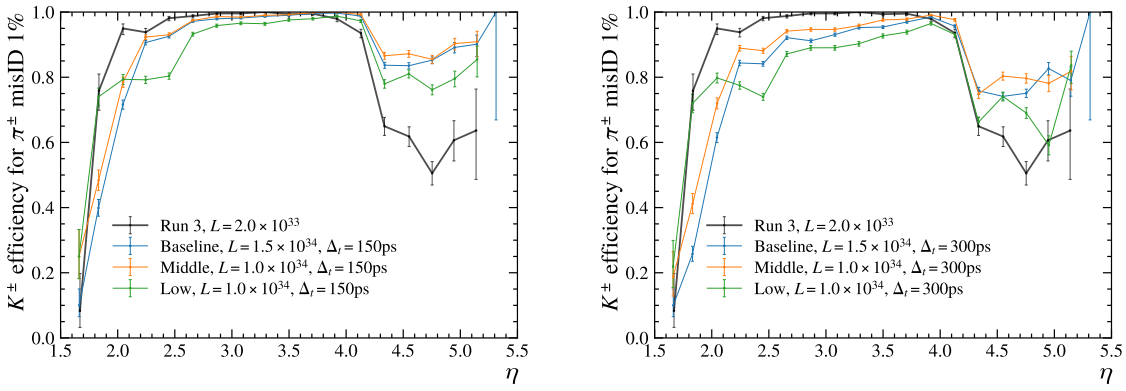

Figure 10.8: Kaon efficiency for 1% pion misidentification versus pseudo-rapidity η, for the Run 3 and the three RICH Upgrade II options at different luminosities, for (left) 150 ps and (right) 300 ps time windows, assuming the same average photoelectron yields.

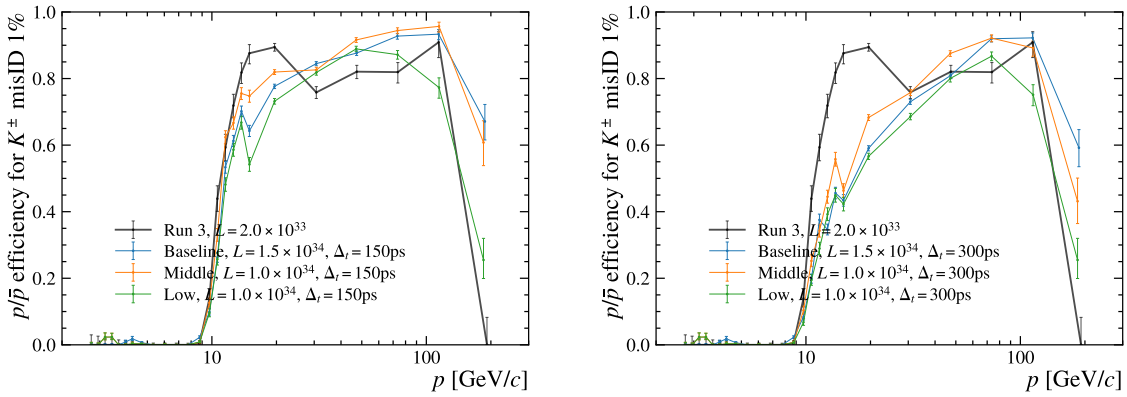

Figure 10.9: proton/anti-proton efficiency for 1% kaon misidentification versus momentum, for the Run 3 and the three RICH Upgrade II options at different luminosities, for (left) 150 ps and (right) 300 ps time windows, assuming the same average photoelectron yields.

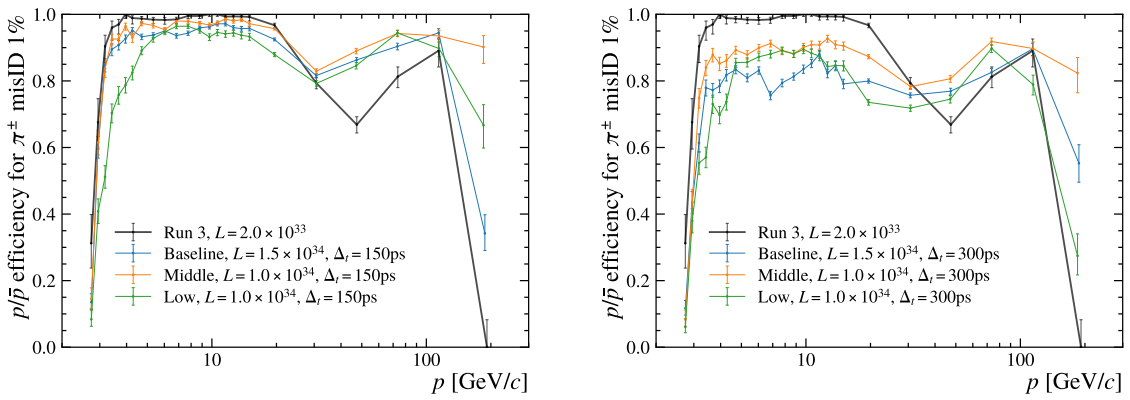

Figure 10.10: proton/anti-proton efficiency for 1% pion misidentification versus momentum, for the Run 3 and the three RICH Upgrade II options at different luminosities, for (left) 150 ps and (right) 300 ps time windows, assuming the same average photoelectron yields.

Run 5 simulations indicate that in the *Middle* scenario (Figure 10.12), occupancy in the inner RICH1 region with $2 \times 2\,\text{mm}^2$ pixels slightly exceeds the 30% limit, suggesting that smaller pixels or additional mitigation strategies might be necessary. In contrast, the *Baseline* layout (Figure 10.12) maintains occupancy below the threshold across all regions.

High time resolution plays a significant role in disentangling overlapping events, effectively lowering the time-integrated occupancy. This is particularly important for fast sensors, such as SiPMs or MCP-PMTs, capable of sub-nanosecond photon timing.

Overall, occupancy considerations motivate the use of high-granularity photon detectors combined with precise timing, especially in RICH1. Among the scenarios, the *Baseline* configuration offers the optimal compromise between performance and occupancy, though it entails higher system complexity and resource demands. The choice of photosensors is also a key factor: while MaPMTs, employed in the *Low* scenario, provide a well-established technology and reduce risk, their timing resolution is insufficient to fully mitigate event complexity, potentially leading to some performance degradation.

Beyond global occupancy maps, a channel-by-channel analysis was performed to study localised hit rates in more detail. The resulting occupancy distributions for RICH1 inner, RICH1 outer, RICH2 inner, and RICH2 outer channels are displayed in Figure 10.11. This granular view is essential for identifying regions with elevated occupancy, assessing detector efficiency, and anticipating possible issues such

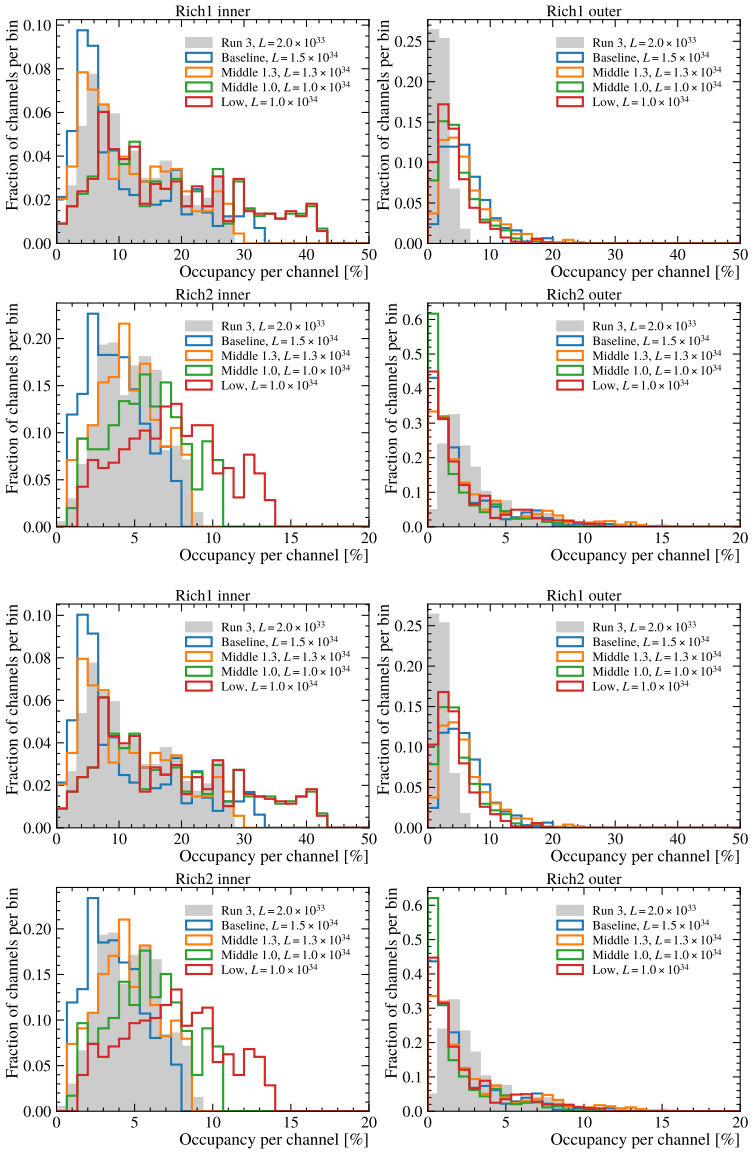

Figure 10.11: Channel occupancy distributions for the RICH detectors under various luminosity conditions. The top plot shows results for a temporal resolution of 300 ps, while the bottom plot displays results for 150 ps. The distinct lines represent different luminosity scenarios, including Run 3 ($L = 2.0 \times 10^{33}$), Baseline ($L = 1.5 \times 10^{34}$), Middle 1.3 ($L = 1.3 \times 10^{34}$), Middle 1.0 ($L = 1.0 \times 10^{34}$), and Low ($L = 1.0 \times 10^{34}$). As expected, the occupancy distributions are largely independent of the temporal resolution, with similar shapes observed in both 300 ps and 150 ps plots.

as channel saturation or pile-up under high-luminosity conditions. Moreover, these histograms show how occupancy varies across different luminosity scenarios, providing a comprehensive picture of the detector's behaviour under diverse operational conditions.

10.3 Dark Counts

Dark counts (DCs) are spurious signals produced by photodetectors even in the absence of incoming photons. These signals mainly originate from thermal excitations or other intrinsic noise processes within the sensor. In the context of RICH detectors, dark counts can generate false hits, potentially interfering with the reconstruction of Cherenkov rings and reducing the overall particle identification performance. Quantifying the impact of a given dark count rate is therefore essential for optimising the readout electronics, refining event reconstruction algorithms, and preserving detector efficiency under high-luminosity operating conditions.

It should be emphasised that, in the current DC rate studies, the absence of the `Boole` simulation step may influence the quantitative interpretation of the results. In particular, the reduced detection efficiency effects associated with dark count modelling cannot be fully accounted for without including `Boole`. Nevertheless, the study provides valuable qualitative insights, though potential systematic effects from this limitation should be considered when interpreting the results quantitatively.

10.3.1 Emulation of Dark Counts

Dark counts have been emulated in the framework by generating hits uniformly in both time and across the photodetector plane, using the same pixel count and layout as in the Run 3 configuration. The total number of dark counts per event in each detector region is calculated as:

$$N_{\mathrm{DC},i} = R \times S_i \times T$$

where R represents the dark count rate in Hz/mm^2, S_i is the effective sensitive area of the relevant RICH region (e.g., RICH1, RICH2-inner, RICH2-outer), and T is the integration time window (typically 25 ns). The effective areas are obtained by multiplying the pixel area by the number of pixels in each region:

- RICH1: $S_1 = 8.266\ \mathrm{mm}^2 \times 124,000 = 1.02 \times 10^6\ \mathrm{mm}^2$
- RICH2-inner: $S_{2,\mathrm{in}} = 8.266\ \mathrm{mm}^2 \times 49,000 = 0.406 \times 10^6\ \mathrm{mm}^2$
- RICH2-outer: $S_{2,\mathrm{out}} = 36\ \mathrm{mm}^2 \times 24,600 = 0.885 \times 10^6\ \mathrm{mm}^2$

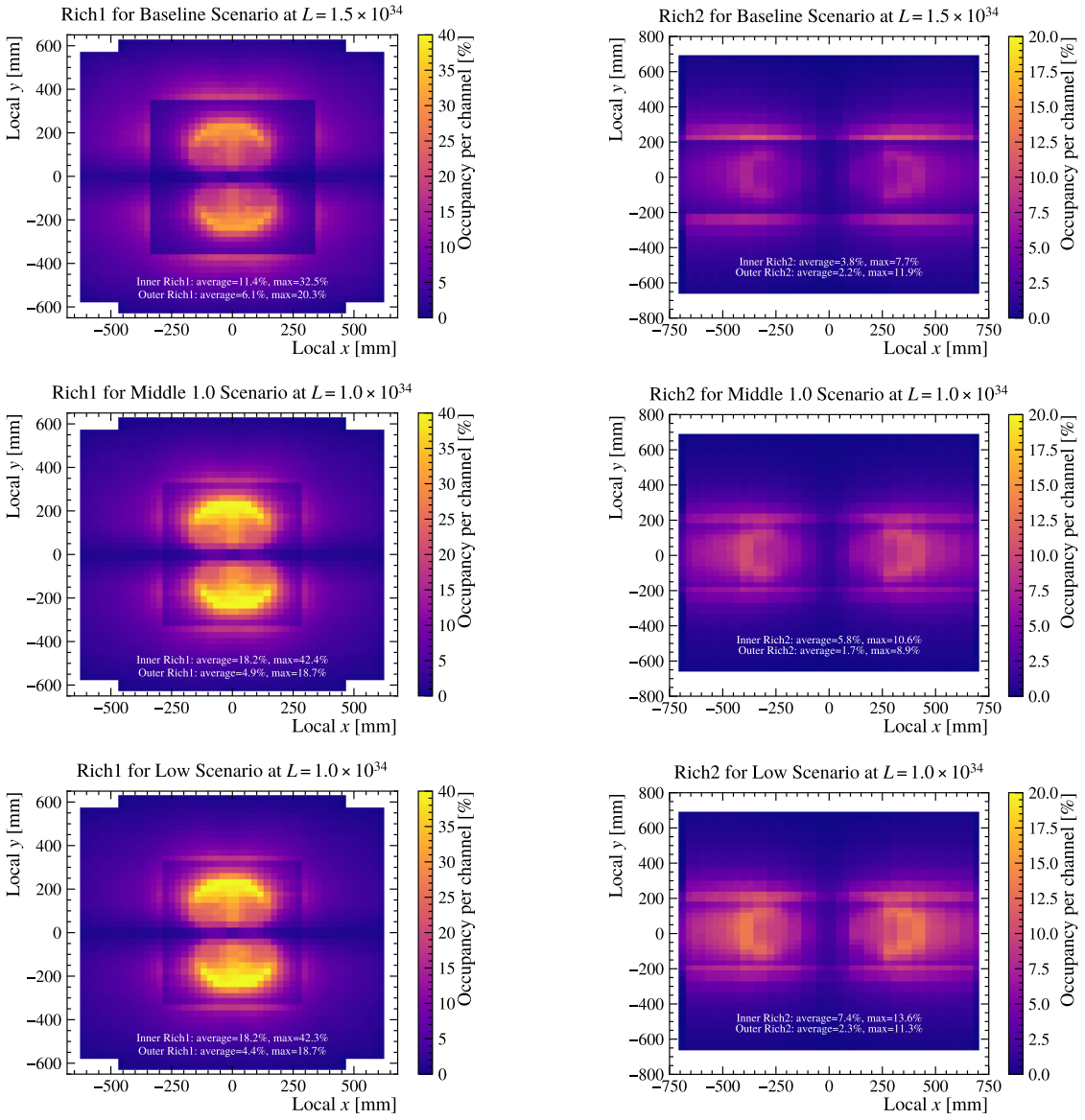

Figure 10.12: Simulated occupancy on the (left) RICH1 and (right) RICH2 detector planes for the (top) *Baseline*, (center) *Middle*, and (bottom) *Low* scenarios. In the *Baseline* case, the central high-occupancy area covers 1/3 of the total with a pixel size of $1.4 \times 1.4\,\mathrm{mm}^2$. For the *Middle* and *Low* scenarios, this area is 1/4 of the total with $2 \times 2\,\mathrm{mm}^2$ pixels. Peak occupancy reaches $\sim 30\%$ in the inner regions of RICH1 for the *Baseline* and *Middle* configurations, while MaPMTs are employed in the outer regions for the *Low* scenario.

The dark count rate (R_{DC}) has been varied across different scenarios. For a reference signal rate of $10\,\mathrm{MHz}/\,\mathrm{mm}^2$, the dark count rates were emulated at specific fractions of this rate. For instance, a DC rate of $10^5\,\mathrm{Hz}/\,\mathrm{mm}^2$ (i.e., $100\,\mathrm{kHz}/\,\mathrm{mm}^2$) corresponds to approximately $2,500$ dark counts in RICH1. With $124,000$ pixels in RICH1 (Run 3), this amounts to roughly 0.02 hits per pixel in a 25 ns window. Higher rates were also considered: $10^6\,\mathrm{Hz}/\,\mathrm{mm}^2$ gives 0.2 hits per pixel, $5 \times 10^6\,\mathrm{Hz}/\,\mathrm{mm}^2$ gives 1 hit per pixel, and $10^7\,\mathrm{Hz}/\,\mathrm{mm}^2$ corresponds to 2 hits per pixel, all within the 25 ns window.

The same efficiency factors applied to signal photons were also used for dark counts, including the scale factors from Table 10.4 and the global readout efficiency of 95%. For the *Middle* scenario, the effective dark count numbers are scaled as:

$$N_{\mathrm{DC,R1}} = 0.78 \times R_{\mathrm{DC}}$$
$$N_{\mathrm{DC,R2}} = 0.70 \times R_{\mathrm{DC}}$$

Thus, a nominal $10^5\,\mathrm{Hz}/\,\mathrm{mm}^2$ in the legend effectively corresponds to 0.78 and 0.70×10^5 $\mathrm{Hz}/\,\mathrm{mm}^2$ in RICH1 and RICH2, respectively.

Once generated, the dark count hits are added to the simulated hit map and processed through the full reconstruction chain. If two hits occur on the same pixel, only the first is retained. Consequently, if a dark count precedes a signal photon in the same pixel, the time of the dark count is used, emulating a dead time up to 12.5 ns. If the signal photon arrives first, the subsequent dark count is discarded.

It should be noted that no after-pulsing or cross-talk effects are included in this emulation.

10.3.2 Performance studies

To evaluate the impact of dark counts on the RICH detector performance, the studies described in Section 10.2.2 were repeated, this time including the effects of dark count contributions.

From Figure 10.13, which shows the kaon identification efficiency ($K^{\pm}$) at a fixed 1% pion misidentification rate as a function of momentum for 150 and 300 ps time windows, it is evident that the efficiency decreases as the dark count rate, R_{DC}, increases. This effect is particularly pronounced at low momentum and becomes more severe for the highest dark count rates, demonstrating that elevated background levels can significantly degrade kaon identification while maintaining a low pion mis-ID. Rates above $10^6\,\mathrm{Hz}/\,\mathrm{mm}^2$ show the most substantial impact.

Comparing the two panels highlights that increasing the photon time window from 150 ps to 300 ps leads to a further reduction in $K^{\pm}$ efficiency under high dark count conditions. Although a wider time window allows the collection of more signal photons, it also admits more uncorrelated dark counts, increasing background and

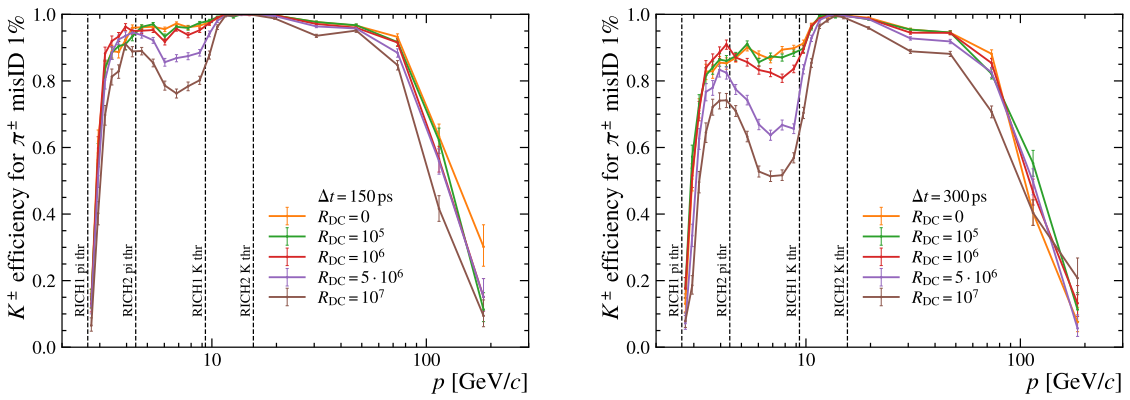

Figure 10.13: Kaon ($K^\pm$) identification efficiency at a fixed pion misidentification rate of 1% as a function of momentum, for time windows of (left) 150 ps and (right) 300 ps. The vertical dashed lines indicate the momentum thresholds where RICH1 and RICH2 contribute to particle identification, contextualising the relevant regions of each detector.

lowering the signal-to-noise ratio, which in turn reduces kaon identification performance for a given misidentification tolerance.

A similar behaviour is observed when examining the efficiency as a function of pseudo-rapidity η, shown in Figure 10.14. In both panels, kaon efficiency decreases with increasing dark count rate. The degradation is most pronounced at the highest rates (5×10^6 and $10^7\,\mathrm{Hz/mm^2}$), with efficiency curves falling well below those for lower background levels. The efficiency typically peaks in the central η region ($\eta \approx 3.0$–4.0) and gradually declines toward the detector edges. The forward region ($\eta > 4.5$) is especially sensitive, showing a significant loss in performance under high dark count conditions.

Overall, for both momentum and pseudo-rapidity distributions, the 300 ps time window consistently results in lower efficiencies compared to the 150 ps window when dark counts are present.

10.3.3 Occupancy studies

To evaluate the effect of dark counts (DC) on signal detection, occupancy hitmaps have been generated for different detector configurations and varying dark count rates. For each configuration, the pixel-level ratio $S/(S + DC)$, where S represents the signal and DC the dark counts, has been computed and displayed for both RICH1 and RICH2.

This ratio provides a quantitative indication of the system's ability to distinguish

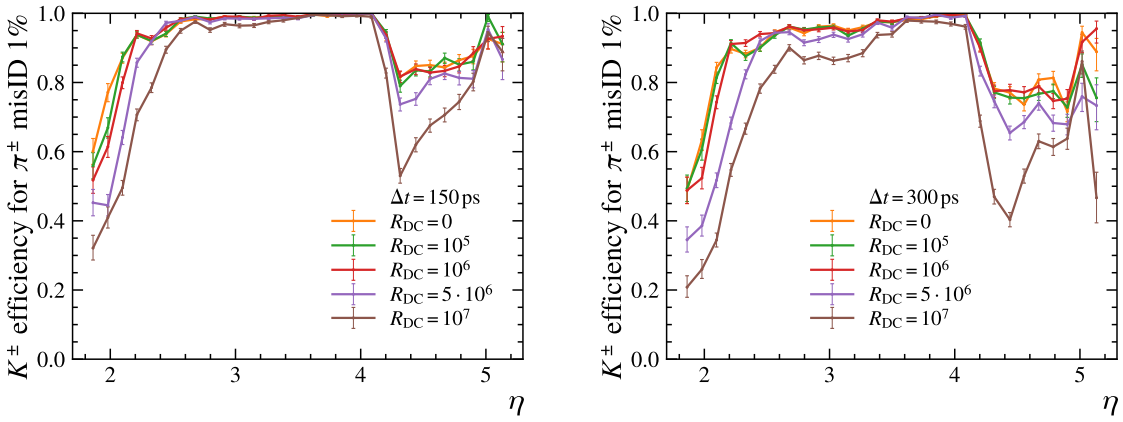

Figure 10.14: Kaon ($K^\pm$) identification efficiency at a fixed pion misidentification rate of 1% as a function of pseudo-rapidity, for time windows of (left) 150 ps and (right) 300 ps.

true signal hits from background noise. Values of $S/(S + DC)$ close to 1 indicate regions where the signal clearly dominates over dark counts, corresponding to well-defined Cherenkov ring patterns. Ratios near 0.5 or lower indicate that the signal is comparable to or weaker than the background, making reliable detection more challenging.

The hitmaps are particularly effective at revealing spatial regions where the signal contribution is significant relative to the background. This is especially relevant when dark counts are uniformly distributed, whereas the signal forms localised, structured patterns in areas of high track density.

In addition, these maps allow for direct comparisons between different detector configurations, optical layouts, and dark count rates, offering valuable insights into how hardware parameters—such as pixel size or timing window—impact the system's sensitivity to the signal.

Figure 10.15 displays the pixel-by-pixel $S/(S + DC)$ ratio maps for RICH1 and RICH2 at progressively increasing dark count rates of 10^5, 10^6, and $10^7\,\text{Hz}/\,\text{mm}^2$. As the dark count rate rises, the contrast between regions with a strong signal and the uniform background becomes increasingly blurred. Note that the z-axis scales are adjusted individually for each plot in Figure 10.15 to provide a clearer view of the occupancy distribution for each rate.

At the lowest dark count rate ($10^5\,\text{Hz}/\,\text{mm}^2$), both detectors show ratios near unity in high track-density regions, indicating that the signal clearly dominates over background. For intermediate rates ($10^6\,\text{Hz}/\,\text{mm}^2$), the ratios decrease across the

detector planes, reflecting the growing influence of dark counts. At the highest rate ($10^7\,\mathrm{Hz/\,mm^2}$), the signal-to-background contrast is heavily diminished, particularly in RICH2, where the signal is almost indistinguishable from the background. These visualisations underscore the importance of minimising dark counts and optimising both pixel size and timing resolution to preserve the fidelity of the Cherenkov signal under high-luminosity conditions.

10.4 Conclusions

The studies presented in this chapter evaluate the performance of several design options for the RICH detectors within the LHCb Upgrade II, expected to operate at luminosities up to $1.5 \times 10^{34}\,\mathrm{cm^{-2}s^{-1}}$. The primary objective is to maintain excellent particle identification, particularly K/π separation, under conditions of high occupancy and increased background due to dark counts.

Three Upgrade II configurations were considered: *Baseline*, *Middle*, and *Low*, each representing different trade-offs between performance, complexity, and cost.

The *Baseline* scenario uses a highly granular SiPM layout with $1.4 \times 1.4\,\mathrm{mm^2}$ pixels in the inner regions, aiming for a time resolution of 150–300 ps. At 150 ps, it delivers the best overall performance across all studied channels, achieving high kaon identification efficiencies up to $100\,\mathrm{GeV}/c$ for a 1% pion misidentification rate, while maintaining proton separation comparable to Run 3. At 300, ps performance remains competitive at high momentum, but both p/K and p/π separations degrade at low momentum, falling below Run 3 benchmarks. Maximum occupancy stays below 30% at the target luminosity, confirming the feasibility of this configuration.

The *Middle* scenario features slightly larger $2.0{\times}2.0\,\mathrm{mm^2}$ pixels in the inner region, with the high-granularity area reduced to roughly 25% of the total. This configuration provides a good compromise between cost and performance, closely tracking the *Baseline* efficiency at lower luminosity.

The *Low* scenario is a cost-optimised option, using SiPMs only in the central area and MaPMTs in the outer region, with timing performance of 150–300 ps in the inner region and around 600 ps elsewhere. Its PID performance above $30\,\mathrm{GeV}/c$ largely reproduces Run 3 behaviour.

Simulations including dark counts show that performance remains robust up to rates of 10^5–$10^6\,\mathrm{Hz/\,mm^2}$, while higher rates lead to significant degradation, especially in the very-forward region ($\eta > 4.5$). As expected, shorter time windows (150 ps) mitigate the impact of dark counts compared to 300 ps.

Occupancy studies highlight the critical role of pixel granularity. RICH2 generally operates within safe occupancy levels (max ~ 13%), whereas RICH1's inner region requires careful consideration due to localised hotspots. The *Baseline* scenario pro-

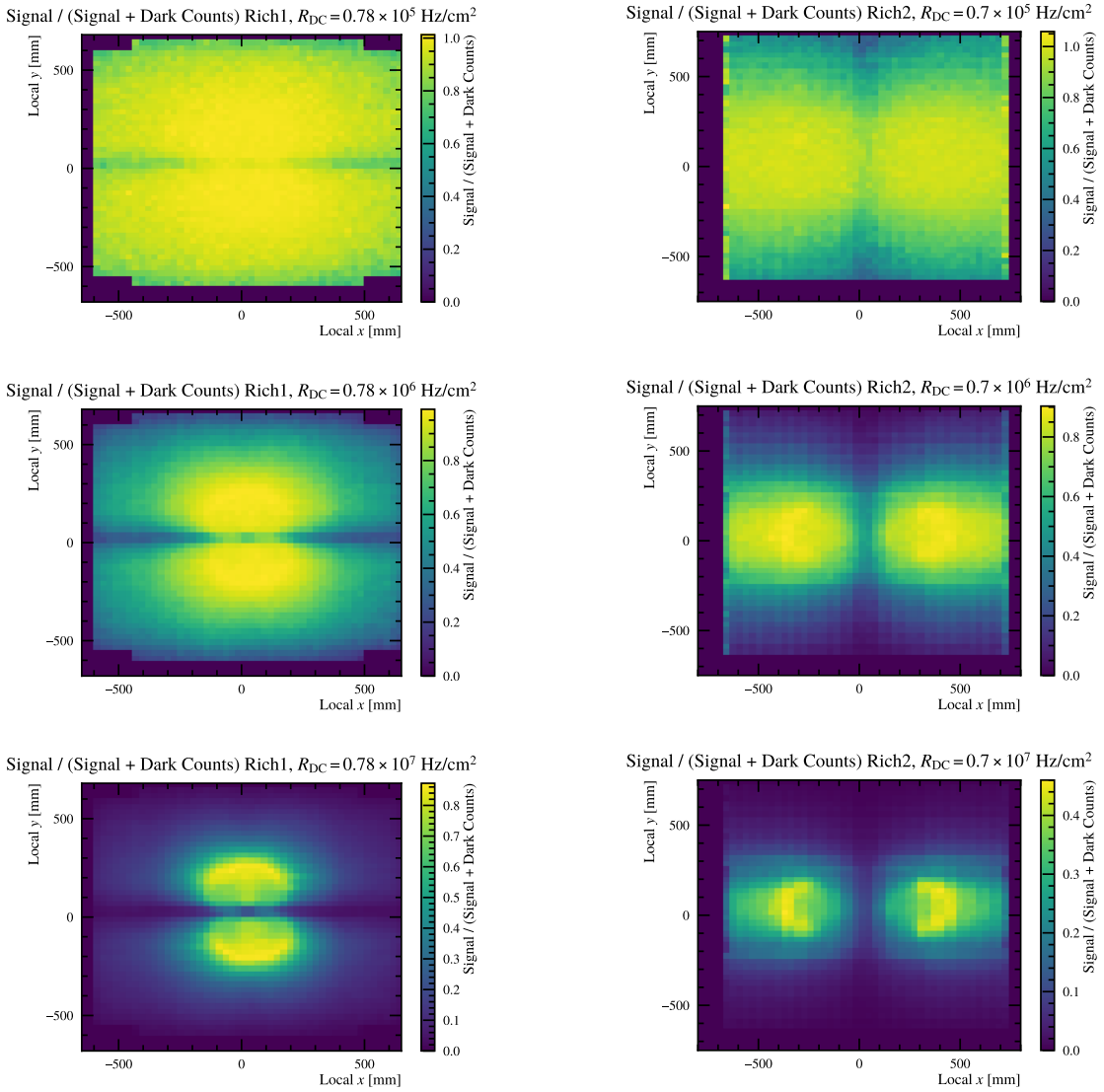

Figure 10.15: Pixel-wise $S/(S + DC)$ ratio maps for (left) RICH1 ($R_{DC} = 0.78 \times 10^5\,\mathrm{Hz/mm^2}$) and (right) RICH2 ($R_{DC} = 0.70 \times 10^5\,\mathrm{Hz/mm^2}$) at different dark count rates: (top) $10^5\,\mathrm{Hz/mm^2}$ where the ratio remains close to unity; (middle) $10^6\,\mathrm{Hz/mm^2}$ where the ratio begins to decrease and (bottom) $10^7\,\mathrm{Hz/mm^2}$ where the signal becomes strongly suppressed relative to the dark background.

vides the most robust solution under high-luminosity, high-background conditions, though with higher technical and financial demands. The *Middle* scenario achieves a good balance, managing occupancy effectively under intermediate conditions and avoiding the most critical hotspots present in the *Low* scenario.

In summary, the *Baseline* scenario emerges as the most performant and resilient choice, fulfilling the stringent PID requirements of Upgrade II with advanced timing and spatial resolution, albeit requiring careful integration of new sensors and associated systems. The *Middle* scenario offers a solid compromise, delivering reliable performance for intermediate luminosities, while the *Low* scenario may serve as a fallback under resource constraints, with some trade-offs in physics reach.

Conclusions and Outlook

This thesis presents a coherent set of studies carried out within the LHCb experiment, combining a precision measurement in charm physics with detailed investigations of detector performance for both the current Run 3 operation and the future Upgrade II programme. Together, these results highlight the close interplay between advanced analysis techniques and an in-depth understanding of detector behaviour, which is essential for the success of precision flavour physics measurements.

The first part of this thesis is dedicated to a measurement of charm mixing and *CP*-violation observables using Run 3 data collected by the LHCb experiment in the decay channel $D^0 \to K^0_S\pi^+\pi^-$. The analysis is based on the data recorded during the 2024 data-taking period, corresponding to a subset of the full Run 3 dataset. Although this sample already exceeds the integrated luminosity collected during Run 2, it does not yet correspond to the full Run 3 dataset and therefore represents an intermediate stage towards the ultimate sensitivity achievable with Run 3.

The analysis exploits the bin-flip method, a model-independent approach that avoids reliance on amplitude modelling and mitigates systematic effects related to efficiency variations across the Dalitz plane. Benefiting from the improved performance of the upgraded detector and the increased available statistics, a sensitivity is achieved that is slightly improved with respect to that obtained during Run 2.

A detailed study of the stability of the measurement as a function of the data-taking blocks shows no strong dependence of the extracted observables on the block structure, indicating stable detector and reconstruction performance throughout the analysed period. Quantitative compatibility tests performed across data-taking blocks demonstrate good overall agreement for most observables in both the LL and DD samples, corresponding to K^0_S candidates reconstructed with long tracks in the vertex detector and downstream tracks reconstructed only in the tracking stations downstream of the magnet.

The results obtained in the dominant `TwoTracks` selection category are found to be statistically consistent between the LL and DD samples for most observables. A mild tension is observed in the determination of x_{CP}, corresponding to a p-value of 2.7%, while no significant discrepancies are found for the remaining parameters.

Given the current statistical precision, this behaviour is compatible with statistical fluctuations.

The combined Run 3 results follow the expected improvement in statistical precision driven by the increased integrated luminosity with respect to Run 2. In particular, the uncertainties achieved on x_{CP}, y_{CP}, Δx and Δy are consistent with, and in the case of y_{CP} and Δy, exceed the expectations based on simple luminosity scaling. This reflects not only the larger dataset but also the improved detector performance, including the enhanced trigger efficiency achieved in Run 3, particularly for the LL category.

The subdivision of the dataset into different trigger-line subsamples has not been used to derive a single combined result, as these samples are not statistically independent: individual events can satisfy the requirements of multiple trigger selections. The development of an appropriate strategy to handle overlapping trigger selections, ensuring statistical independence while preserving a coherent acceptance definition, is ongoing and will be addressed in the context of the future publication of these results.

Looking forward, the inclusion of the full Run 3 dataset, together with further improvements in calibration, alignment, and systematic uncertainty control, is expected to significantly enhance the precision of the measurement and to fully exploit the potential of the upgraded LHCb detector.

The second part of the thesis focuses on the performance of the upgraded RICH detectors using Run 3 data collected in 2024. In the new operational conditions introduced by the fully software-based trigger and higher instantaneous luminosity, a detailed characterisation of detector behaviour is essential. The studies presented here investigate the evolution of background contributions to the single photon resolution as a function of photon time windows and detector geometry. The results demonstrate that timing information plays a key role in suppressing uncorrelated background and confirm that the performance of the upgraded RICH system is well understood under Run 3 conditions. These analyses provide an important validation of the detector and establish a solid basis for future optimisation efforts.

The final part of the thesis addresses the challenges posed by the forthcoming Upgrade II of the LHCb experiment. Several design scenarios for the future RICH detectors are evaluated using simulation, exploring different trade-offs between performance, complexity, and cost. The studies indicate that high granularity and precise timing are critical to maintaining excellent particle identification performance in the high-luminosity environment expected during Run 5 and beyond. Among the configurations considered, the *Baseline* scenario provides the most robust and performant solution under extreme occupancy and background conditions, while the *Middle* scenario emerges as a well-balanced alternative. The *Low* scenario, although more cost-effective, entails some compromises in physics reach.

Overall, the results presented in this thesis demonstrate that precision measurements in the charm sector can fully benefit from the upgraded LHCb detector, provided that detector performance is carefully validated and optimised. The bin-flip method is confirmed as a powerful tool for model-independent charm analyses, particularly well suited for the large datasets collected in Run 3 and beyond.

Looking forward, the full Run 3 dataset will enable a significant improvement in the precision of charm mixing and CP-violation measurements, strengthening constraints on the Standard Model and enhancing sensitivity to potential new physics effects. At the same time, the detector studies presented here contribute directly to the preparation of Upgrade II, ensuring that the excellent particle identification capabilities of LHCb can be preserved in the high-luminosity era of the LHC. Together, these developments place the experiment in a strong position to pursue an ambitious and competitive flavour physics programme in the years to come.

Appendix A

Background studies for K^0_S mass

The K^0_S invariant mass distributions for the different track categories and trigger selections are shown in Figure A.1. A longitudinal separation requirement of $\Delta z > 10\,\mathrm{mm}$ is applied to the LL sample, while $\Delta z > 220\,\mathrm{mm}$ is required for DD candidates. The corresponding retention rates are:

- 56% for the LL sample,
- 86.5% for the LL Low Bias sample,
- 95.6% for the LL No Bias sample,
- 43.9% for the DD sample,
- 52.9% for the DD Low Bias sample.

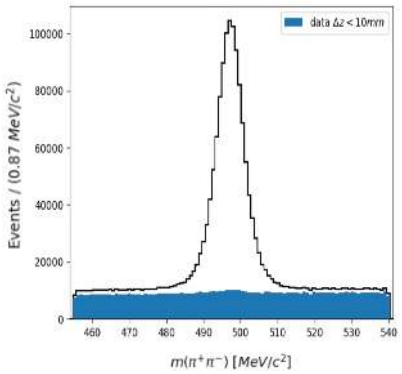

(a) LL sample.

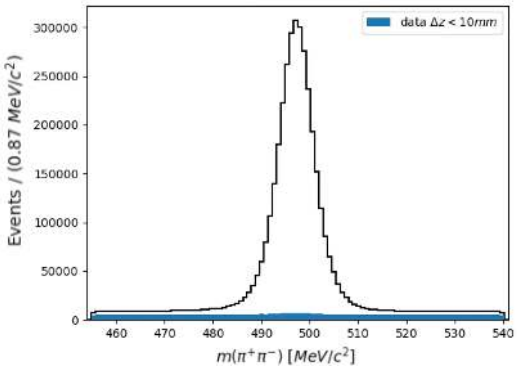

(b) LL Low Bias sample.

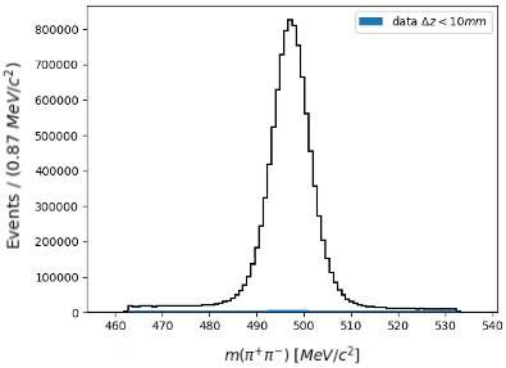

(c) LL No Bias sample.

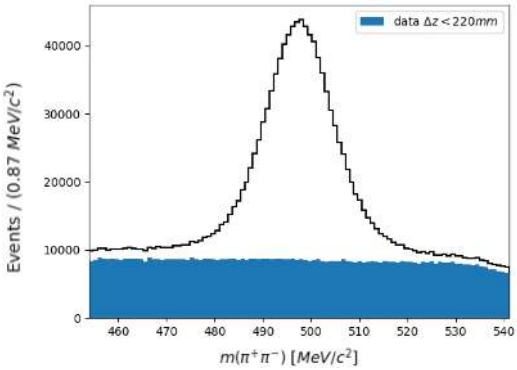

(d) DD sample.

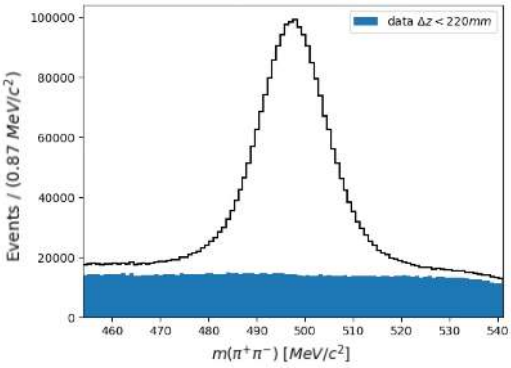

(e) DD Low Bias sample.

Figure A.1: $m(K^0_S)$ distribution for the different sample.

Appendix B

RICH Upgrade II Framework

B.1 Emulation Setup and Execution

To perform the emulation procedure, the first step is to compile the required software stack. This can be done by executing the `curl` command with:
`https://gitlab.cern.ch/rmatev/lb-stack-setup/raw/master/setup.py | python3 - stack` which sets up the environment.
Once the stack is configured, the correct platform must be loaded by pointing to the `utils/config.py` file and specifying the appropriate `binaryTag`, which in our case is `x86_64_v2-el9-gcc13+detdesc-opt`. After setting up the platform, the `Rec` package must be compiled. The actual emulation of the different scenarios is handled through the `RichFuture.py` script, located in `Rec/Rich/RichFutureRecSys/`. This script allows customisation of several parameters relevant to the emulation.

To use Monte Carlo information for hits and tracks, the variables `"USEMCHITS"` and `"USEMCTRACKS"` must be set to `true`.

Time window values for the photon detection in the RICH detectors can be configured through the variables `"R1INNERPHOTWIN"`, `"R1OUTERPHOTWIN"`, `"R2INNERPHOTWIN"`, and `"R2OUTERPHOTWIN"`.

The values are expressed in nanoseconds within the emulation framework, so values such as 0.075, 0.15, and 0.3 correspond to 150 ps, 300 ps, and 600 ps windows, respectively. These values are chosen to ensure signal capture within a $\pm 2\sigma$ interval. Performance results indicate that the combined photodetector and electronics single-photon timing resolutions are 38 ps and 75 ps (1σ) for the 150 ps and 300 ps time windows, respectively, justifying the use of 0.075 ns and 0.15 ns in the configuration to fully cover the $\pm 2\sigma$ detection range. The spatial dimensions of the inner and outer regions can be set using `"R1INNERXPIX"`, `"R1INNERYPIX"`, `"R2INNERXPIX"`, and `"R2INNERYPIX"`.

To override the default detector geometry and apply scenario-specific configu-

rations, it is necessary to enable `"OVERRIDEDETREGIONS"`. Pixel sizes for the different regions can then be adjusted via `"R1INNERPIXQUANT"`, `"R1OUTERPIXQUANT"`, `"R2INNERPIXQUANT"`, and `"R2OUTERPIXQUANT"`. For full 4D reconstruction capabilities, the variables `"ENABLE4D"`, `"USEPIXELMCINFO"`, and `"USEPHOTONMCINFO"` should also be set to `true`.

Photon yields can be configured through `"R1INNERPIXEFF"`, `"R1OUTERPIXEFF"`, `"R2INNERPIXEFF"`, and `"R2OUTERPIXEFF"`, while resolution scale factors are specified using `"INNERR1RESSCALEF"`, `"INNERR2RESSCALEF"`, `"OUTERR1RESSCALEF"`, and `"OUTERR2RESSCALEF"`.

Finally, to set the luminosity corresponding to the scenario of interest, the variable `"LUMI"` should be assigned to a valid string value, such as `"2.0e32"`, `"2.0e33"`, `"3.0e33"`, `"1.0e34"`, `"1.3e34"`, or `"1.5e34"`. For instance, to fix the luminosity for Run 3, corresponding to 2.0×10^{33} cm^{-2}s^{-1}, one should use `"LUMI" = "2.0e33"`. These settings allow for precise emulation of different detector configurations under various operational conditions.

B.2 Algorithms of the RICH Emulation Framework

The RICH emulation framework developed for Upgrade II builds upon Monte Carlo truth information to simulate the detector response and perform fast reconstruction of PID-related quantities. The reconstruction sequence is implemented within the `RichFutureRecSys` package and is organised in a modular way to facilitate testing of alternative geometries, reconstruction strategies, and detector configurations.

The reconstruction is initiated by reading simulated RICH photon hits. These are stored in a specific event location from which they are unpacked using a dedicated tool, the `MCRichHitUnpacker`. This tool accesses the packed hit information produced by the simulation step, extracts relevant quantities such as hit position, time-of-flight, energy, and sensor ID, and stores them in a format suitable for further processing. The decoding step is performed using the algorithm `DecodedDataFromMCRichHits`, which converts the unpacked data into a structure interpretable by downstream clustering and reconstruction algorithms.

Once the hit data is decoded, the reconstruction proceeds through a series of algorithmic subsequences. The first is the so-called `RichPixels` sequence. This stage performs clustering of photon hits using the `SmartIDClustering` algorithm. Although some intermediate modules related to local and global cluster coordinates are present in the codebase, they are not explicitly invoked within the main reconstruction sequence and may instead be handled implicitly by the Gaudi framework. The output of this clustering stage is a summary of pixel information optimised for vectorised processing, implemented through a SIMD-friendly structure.

The second major component of the reconstruction is the `RichMCReco` sequence, which handles the emulation of track propagation and photon emission within the RICH detectors. In this part of the reconstruction, truth-matched MC tracks are used to avoid the need for full tracking. These tracks are segmented by the `SegmentCreator`, which uses MC particle information to create idealised RICH track segments. Each segment is then propagated to the photodetector plane, and its projection is computed in both local and global coordinates. From these track segments, several quantities are derived, including the number of expected emitted photons and the Cherenkov angle for each mass hypothesis. These computations are handled by a suite of algorithms, including those estimating emitted photon yields, building ray-traced Cherenkov cones, computing geometrical efficiencies, and parameterising the expected angular resolutions. Segments are also filtered to retain only those that contribute significantly to the RICH response, based on geometry and acceptance.

Following track-based computations, the `RichPhotonsMC` subsequence focuses on reconstructing photon candidates.
This is accomplished using the `SIMDQuarticPhotonReco` algorithm, which solves the geometrical constraints defining Cherenkov emission using quartic equation solvers. Each photon candidate is assigned an expected pixel signal, computed by matching the track direction and emission angle to the photodetector geometry. These predictions are refined by comparing the expected signal to the actual hit pattern observed in the clustering stage.

The final reconstruction stage is concerned with particle identification and is handled by the `RichPIDMC` sequence. This part of the framework begins by initialising the PID information for each reconstructed track and proceeds by estimating the background contributions to the photon signal for each mass hypothesis. This is crucial for the likelihood calculation that follows, where a global likelihood minimisation is performed to determine the most probable particle type associated with each track. The minimisation algorithm iteratively evaluates the likelihoods associated with each hypothesis and refines the track-PID assignment based on the observed photon yield and angular distribution. At the end of the sequence, the reconstructed RICH PID information is written out and stored for further analysis.

Overall, the framework follows a highly structured but adaptable logic. Each component is designed to be independently tunable, which allows for rapid iteration over different sensor technologies, optics layouts, and time resolution assumptions. The use of truth-matched MC tracks and truth-level photon hits ensures fast processing times while maintaining sufficient realism for relative performance comparisons. This structure is especially valuable in the early stages of Upgrade II design, where full simulation and reconstruction pipelines are not yet finalised.

Bibliography

[1] SNO Collaboration. "Measurement of the Rate of $\nu_e + d \rightarrow p + p + e^-$ Interactions Produced by ^8B Solar Neutrinos at the Sudbury Neutrino Observatory". In: *Phys. Rev. Lett.* **87** (2001). URL: https://link.aps.org/doi/10.1103/PhysRevLett.87.071301.

[2] Super-Kamiokande Collaboration. "Evidence for Oscillation of Atmospheric Neutrinos". In: *Phys. Rev. Lett.* **81** (1998). URL: https://link.aps.org/doi/10.1103/PhysRevLett.81.1562.

[3] S. Mertens. "Direct Neutrino Mass Experiments". In: *Journal of Physics: Conference Series* **718**.2 (2016). URL: https://dx.doi.org/10.1088/1742-6596/718/2/022013.

[4] A. D. Sakharov. "Violation of CP invariance, C asymmetry, and baryon asymmetry of the universe". In: *Soviet Physics Uspekhi* **34**.5 (1991). URL: https://dx.doi.org/10.1070/PU1991v034n05ABEH002497.

[5] M. Kobayashi and T. Maskawa. "CP-Violation in the Renormalizable Theory of Weak Interaction". In: *Progress of Theoretical Physics* **49**.2 (1973). ISSN: 0033-068X. URL: https://doi.org/10.1143/PTP.49.652.

[6] N. Cabibbo. "Unitary Symmetry and Leptonic Decays". In: *Phys. Rev. Lett.* **10** (12 1963). URL: https://link.aps.org/doi/10.1103/PhysRevLett.10.531.

[7] J. H. Christenson et al. "Evidence for the 2π Decay of the K_2^0 Meson". In: *Phys. Rev. Lett.* **13** (4 1964). URL: https://link.aps.org/doi/10.1103/PhysRevLett.13.138.

[8] KTeV Collaboration. "Observation of Direct CP Violation in $K_{S,L} \rightarrow \pi\pi$ Decays". In: *Phys. Rev. Lett.* **83** (1 1999). URL: https://link.aps.org/doi/10.1103/PhysRevLett.83.22.

[9] NA48 Collaboration. "A precise measurement of the direct CP violation parameter $\Re(\epsilon'/\epsilon)$". In: *Eur. Phys. J. C* **22** (2001). URL: https://cds.cern.ch/record/522234.

[10] BABAR Collaboration. "Observation of CP Violation in the B^0 Meson System". In: *Phys. Rev. Lett.* **87** (9 2001). URL: https://link.aps.org/doi/10.1103/PhysRevLett.87.091801.

[11] Belle Collaboration. "Observation of Large CP Violation in the Neutral B Meson System". In: *Phys. Rev. Lett.* **87** (9 2001). URL: https://link.aps.org/doi/10.1103/PhysRevLett.87.091802.

[12] BABAR Collaboration. "Direct CP Violating Asymmetry in $B^0 \to K^+\pi^-$ Decays". In: *Phys. Rev. Lett.* **93** (13 2004). URL: https://link.aps.org/doi/10.1103/PhysRevLett.93.131801.

[13] Belle Collaboration. "Evidence for Direct CP Violation in the $B^0 \to K^+\pi^-$ Decays". In: *Phys. Rev. Lett.* **93** (19 2004). URL: https://link.aps.org/doi/10.1103/PhysRevLett.93.191802.

[14] LHCb Collaboration. "Observation of CP violation in B±→DK± decays". In: *Physics Letters B* **712**.3 (2012). ISSN: 0370-2693. URL: https://www.sciencedirect.com/science/article/pii/S0370269312004893.

[15] LHCb Collaboration. "First Observation of CP Violation in the Decays of B_s^0 Mesons". In: *Phys. Rev. Lett.* **110** (22 2013). URL: https://link.aps.org/doi/10.1103/PhysRevLett.110.221601.

[16] S. L. Glashow, J. Iliopoulos, and L. Maiani. "Weak Interactions with Lepton-Hadron Symmetry". In: *Phys. Rev. D* **2** (7 1970). URL: https://link.aps.org/doi/10.1103/PhysRevD.2.1285.

[17] BABAR Collaboration. "Search for CP violation in the decays $D^0 \to K^-K^+$ and $D^0 \to \pi^-\pi^+$". In: *Phys. Rev. Lett.* **100** (2008), p. 061803. DOI: 10.1103/PhysRevLett.100.061803. arXiv: 0709.2715 [hep-ex].

[18] Belle Collaboration. "CP violation in charm decays at Belle". In: *PoS* **EPS-HEP2013** (2013), p. 354. DOI: 10.22323/1.180.0354. arXiv: 1310.3891 [hep-ex].

[19] CDF Collaboration. "Measurement of the difference of CP–violating asymmetries in $D^0 \to K^+K^-$ and $D^0 \to \pi^+\pi^-$ decays at CDF". In: *Phys. Rev. Lett.* **109** (2012), p. 111801. DOI: 10.1103/PhysRevLett.109.111801. arXiv: 1207.2158 [hep-ex].

[20] LHCb Collaboration. "Observation of D^0–$\overline{D}^0$ Oscillations". In: *Phys. Rev. Lett.* **110** (10 2013). URL: https://link.aps.org/doi/10.1103/PhysRevLett.110.101802.

[21] LHCb Collaboration. "Observation of CP Violation in Charm Decays". In: *Phys. Rev. Lett.* **122** (21 2019). URL: https://link.aps.org/doi/10.1103/PhysRevLett.122.211803.

[22] A. Di Canto et al. "Novel method for measuring charm-mixing parameters using multibody decays". In: *Phys. Rev. D* **99** (1 2019), p. 012007. URL: https://link.aps.org/doi/10.1103/PhysRevD.99.012007.

[23] LHCb collaboration. "LHCb Upgrade II Scoping Document". Tech. rep. Geneva: CERN, 2024. URL: https://cds.cern.ch/record/2903094.

[24] H. Fritzsch, M. Gell-Mann, and H. Leutwyler. "Advantages of the color octet gluon picture". In: *Physics Letters B* **47**.4 (1973). URL: https://doi.org/10.1016/0370-2693(73)90625-4.

[25] David J. Gross and Frank Wilczek. "Asymptotically Free Gauge Theories. I". In: *Phys. Rev. D* **8** (10 1973). URL: https://link.aps.org/doi/10.1103/PhysRevD.8.3633.

[26] D. J. Gross and F. Wilczek. "Ultraviolet Behavior of Non-Abelian Gauge Theories". In: *Phys. Rev. Lett.* **30** (26 1973). URL: https://link.aps.org/doi/10.1103/PhysRevLett.30.1343.

[27] H. David Politzer. "Reliable Perturbative Results for Strong Interactions?" In: *Phys. Rev. Lett.* **30** (26 1973). URL: https://link.aps.org/doi/10.1103/PhysRevLett.30.1346.

[28] Steven Weinberg. "Non-Abelian Gauge Theories of the Strong Interactions". In: *Phys. Rev. Lett.* **31** (7 1973). URL: https://link.aps.org/doi/10.1103/PhysRevLett.31.494.

[29] S. Weinberg. "A Model of Leptons". In: *Phys. Rev. Lett.* **19** (21 1967). URL: https://link.aps.org/doi/10.1103/PhysRevLett.19.1264.

[30] A. Salam. "Weak and Electromagnetic Interactions". In: *Conf. Proc. C* **680519** (1968). DOI: 10.1142/9789812795915_0034.

[31] A. Salam and J.C. Ward. "Electromagnetic and weak interactions". In: *Physics Letters* **13**.2 (1964). URL: https://www.sciencedirect.com/science/article/pii/0031916364907115.

[32] S. L. Glashow. "Partial-symmetries of weak interactions". In: *Nuclear Physics* **22**.4 (1961). URL: https://www.sciencedirect.com/science/article/pii/0029558261904692.

[33] S. Navas et al. "Review of particle physics". In: *Phys. Rev. D* **110**.3 (2024). URL: https://link.aps.org/doi/10.1103/PhysRevD.110.030001.

[34] F. Englert and R. Brout. "Broken Symmetry and the Mass of Gauge Vector Mesons". In: *Phys. Rev. Lett.* **13** (9 1964). URL: https://link.aps.org/doi/10.1103/PhysRevLett.13.321.

[35] P.W. Higgs. "Broken symmetries, massless particles and gauge fields". In: *Physics Letters* **12**.2 (1964). URL: https://link.aps.org/doi/10.1103/PhysRevLett.13.508.

[36] P. W. Higgs. "Broken Symmetries and the Masses of Gauge Bosons". In: *Phys. Rev. Lett.* **13** (16 1964). URL: https://link.aps.org/doi/10.1103/PhysRevLett.13.508.

[37] T. W. B. Kibble. "Symmetry Breaking in Non-Abelian Gauge Theories". In: *Phys. Rev.* **155** (5 1967). URL: https://link.aps.org/doi/10.1103/PhysRev.155.1554.

[38] C. Burgard. "Standard model of physics programmed in TikZ". URL: https://texample.net/tikz/examples/model-physics/.

[39] R. P. Feynman and M. Gell-Mann. "Theory of the Fermi Interaction". In: *Phys. Rev.* **109** (1 1958). URL: https://link.aps.org/doi/10.1103/PhysRev.109.193.

[40] T. D. Lee and C. N. Yang. "Question of Parity Conservation in Weak Interactions". In: *Phys. Rev.* **104** (1 1956). URL: https://link.aps.org/doi/10.1103/PhysRev.104.254.

[41] C. S. Wu et al. "Experimental Test of Parity Conservation in Beta Decay". In: *Phys. Rev.* **105** (4 1957). URL: https://link.aps.org/doi/10.1103/PhysRev.105.1413.

[42] G. W. S. Hou. "Source of CP violation for the baryon asymmetry of the Universe". In: *International Journal of Modern Physics D* **20**.08 (2011). URL: https://doi.org/10.1142/S0218271811019694.

[43] N. Cabibbo. "Unitary Symmetry and Leptonic Decays". In: *Phys. Rev. Lett.* **10** (12 1963). URL: https://link.aps.org/doi/10.1103/PhysRevLett.10.531.

[44] J. J. Aubert et al. "Experimental Observation of a Heavy Particle J". In: *Phys. Rev. Lett.* **33** (23 1974). URL: https://link.aps.org/doi/10.1103/PhysRevLett.33.1404.

[45] J. -E. Augustin et al. "Discovery of a Narrow Resonance in e^+e^- Annihilation". In: *Phys. Rev. Lett.* **33** (23 1974). URL: https://link.aps.org/doi/10.1103/PhysRevLett.33.1406.

[46] L. Wolfenstein. "Parametrization of the Kobayashi-Maskawa Matrix". In: *Phys. Rev. Lett.* **51** (21 1983). URL: https://link.aps.org/doi/10.1103/PhysRevLett.51.1945.

[47] C. Jarlskog. "Commutator of the Quark Mass Matrices in the Standard Electroweak Model and a Measure of Maximal CP Nonconservation". In: *Phys. Rev. Lett.* **55** (10 1985). URL: https://link.aps.org/doi/10.1103/PhysRevLett.55.1039.

[48] Y. Grossman, Y. Nir, and G. Perez. "Testing New Indirect CP Violation". In: *Phys. Rev. Lett.* **103** (7 2009). URL: https://link.aps.org/doi/10.1103/PhysRevLett.103.071602.

[49] A. L. Kagan and M. D. Sokoloff. "Indirect CP violation and implications for $D^0 - \overline{D}^0$ and $B_s - \overline{B}_s$ mixing". In: *Phys. Rev. D* **80** (7 2009). URL: https://link.aps.org/doi/10.1103/PhysRevD.80.076008.

[50] Particle Data Group et al. "Review of Particle Physics". In: *Progress of Theoretical and Experimental Physics* **2022**.8 (2022). URL: https://doi.org/10.1093/ptep/ptac097.

[51] Sw. Banerjee et al. "Averages of b-hadron, c-hadron, and τ-lepton properties as of 2023". In: (2024). arXiv: 2411.18639 [hep-ex]. URL: https://arxiv.org/abs/2411.18639.

[52] CDF Collaboration. "Observation of B_s^0–$\overline{B}_s^0$ Oscillations". In: *Phys. Rev. Lett.* **97** (24 2006). URL: https://link.aps.org/doi/10.1103/PhysRevLett.97.242003.

[53] BABAR Collaboration. "Evidence for D^0–$\overline{D}^0$ Mixing". In: *Phys. Rev. Lett.* **98** (21 2007). URL: https://link.aps.org/doi/10.1103/PhysRevLett.98.211802.

[54] Belle Collaboration. "Evidence for D^0–$\overline{D}^0$ Mixing". In: *Phys. Rev. Lett.* **98** (21 2007). URL: https://link.aps.org/doi/10.1103/PhysRevLett.98.211803.

[55] A. Dery and Y. Nir. "Implications of the LHCb discovery of CP violation in charm decays". In: *JHEP* **1912** (2019). URL: https://cds.cern.ch/record/2705802.

[56] A. L. Kagan and L. Silvestrini. "Dispersive and absorptive CP violation in $D^0 - \overline{D}^0$ mixing". In: *Phys. Rev. D* **103** (2021). URL: https://link.aps.org/doi/10.1103/PhysRevD.103.053008.

[57] R. Aaij et al. "Erratum to: Measurements of prompt charm production cross-sections in pp collisions at $\sqrt{s} = 13$ TeV". In: *Journal of High Energy Physics* **2016** (2016). DOI: 10.1007/JHEP09(2016)013.

[58] LHCb Collaboration. "Measurement of the Time-Integrated CP Asymmetry in $D^0 \to K^-K^+$ Decays". In: *Phys. Rev. Lett.* **131** (9 2023). URL: https://link.aps.org/doi/10.1103/PhysRevLett.131.091802.

[59] LHCb Collaboration. "Measurement of CP asymmetry in $D^0 \to K^0_S K^0_S$ decays". In: *Phys. Rev. D* **104** (3 2021). URL: https://link.aps.org/doi/10.1103/PhysRevD.104.L031102.

[60] LHCb Collaboration. "Search for time-dependent CP violation in $D^0 \to K^+K^-$ and $D^0 \to \pi^+\pi^-$ decays". In: *Phys. Rev. D* **104** (7 2021). URL: https://link.aps.org/doi/10.1103/PhysRevD.104.072010.

[61] LHCb Collaboration. "Search for charge-parity violation in semileptonically tagged $D^0 \to K^+\pi^-$ decays". In: *Journal of High Energy Physics* **2025**.3 (2025). URL: http://dx.doi.org/10.1007/JHEP03(2025)149.

[62] LHCb Collaboration. "Measurement of $D^0 - \overline{D}^0$ mixing and search for CP violation with $D^0 \to K^+\pi^-$ decays". In: *Phys. Rev. D* **111** (1 2025). URL: https://link.aps.org/doi/10.1103/PhysRevD.111.012001.

[63] LHCb Collaboration. "Model-independent measurement of charm mixing parameters in $\overline{B} \to D^0(\to K^0_S\pi^+\pi^-)\mu^-\overline{\nu}_\mu X$ decays". In: *Phys. Rev. D* **108** (5 2023). URL: https://link.aps.org/doi/10.1103/PhysRevD.108.052005.

[64] "Simultaneous determination of the CKM angle γ and parameters related to mixing and CP violation in the charm sector". Tech. rep. Geneva: CERN, 2025. DOI: 10.17181/CERN.GFHE.LM6W. URL: https://cds.cern.ch/record/2948394.

[65] LHCb Collaboration. "Observation of the Mass Difference between Neutral Charm-Meson Eigenstates". In: *Phys. Rev. Lett.* **127** (11 2021). URL: https://link.aps.org/doi/10.1103/PhysRevLett.127.111801.

[66] LHCb Collaboration. "Measurement of the charm mixing parameter $y_{CP} - y^{K\pi}_{CP}$ using two-body D^0 meson decays". In: *Phys. Rev. D* **105** (9 2022). URL: https://link.aps.org/doi/10.1103/PhysRevD.105.092013.

[67] T. Pajero and M. J. Morello. "Mixing and CP violation in $D^0 \to K^-\pi^+$ decays". In: *Journal of High Energy Physics* **2022**.3 (2022). URL: http://dx.doi.org/10.1007/JHEP03(2022)162.

[68] BESIII Collaboration. "Improved measurement of the strong-phase difference $\delta^{K\pi}_D$ in quantum-correlated $D\bar{D}$ decays". In: *Eur. Phys. J. C* **82**.11 (2022). URL: https://doi.org/10.1140/epjc/s10052-022-10872-2.

[69] CLEO Collaboration. "Model-independent determination of the strong-phase difference between D^0 and $\overline{D}^0 \to K^0_{S,L}h^+h^-$ ($h = \pi$, K) and its impact on the measurement of the CKM angle γ/ϕ_3". In: *Phys. Rev. D* **82** (11 2010). URL: https://link.aps.org/doi/10.1103/PhysRevD.82.112006.

[70] BABAR Collaboration. "Improved measurement of the CKM angle γ in $B^{\mp} \to D^{(*)}K^{(*)\mp}$ decays with a Dalitz plot analysis of D decays to $K^0_S\pi^+\pi^-$ and $K^0_S K^+K^-$". In: *Phys. Rev. D* **78** (3 2008). URL: https://link.aps.org/doi/10.1103/PhysRevD.78.034023.

[71] BESIII Collaboration. "Updated model-independent measurement of the strong-phase differences between D^0 and $\bar{D}^0 \to K^0_{S/L}\pi^+\pi^-$ decays". In: (Mar. 2025). arXiv: 2503.22126 [hep-ex].

[72] Belle and Belle II Collaborations. "Model-independent measurement of D^0–$\overline{D}^0$ mixing parameters in $D^0 \to K^0_S\pi^+\pi^-$ decays at Belle and Belle II". In: *Phys. Rev. D* **111** (11 2025). URL: https://link.aps.org/doi/10.1103/7p5s-f9qp.

[73] Babar Collaboration. "Measurement of D0-antiD0 mixing parameters using D0 —> K(S)0 pi+ pi- and D0 —> K(S)0 K+ K- decays". In: *Phys. Rev. Lett.* **105** (2010), p. 081803. DOI: 10.1103/PhysRevLett.105.081803. arXiv: 1004.5053 [hep-ex].

[74] Belle Collaboration. "Measurement of $D^0 - \bar{D}^0$ mixing and search for indirect CP violation using $D^0 \to K^0_S\pi^+\pi^-$ decays". In: *Phys. Rev. D* **89**.9 (2014), p. 091103. DOI: 10.1103/PhysRevD.89.091103. arXiv: 1404.2412 [hep-ex].

[75] E. Lopienska. "The CERN accelerator complex, layout in 2022". General Photo. 2022. URL: https://cds.cern.ch/record/2800984.

[76] CERN. "LHC". URL: https://home.cern/science/accelerators/.

[77] ATLAS Collaboration. "The ATLAS Experiment at the CERN Large Hadron Collider". In: *Journal of Instrumentation* **3**.08 (2008). URL: https://dx.doi.org/10.1088/1748-0221/3/08/S08003.

[78] CMS Collaboration. "The CMS experiment at the CERN LHC". 2008. URL: https://dx.doi.org/10.1088/1748-0221/3/08/S08004.

[79] ALICE Collaboration. "The ALICE experiment at the CERN LHC". In: *Journal of Instrumentation* **3**.08 (2008). URL: https://dx.doi.org/10.1088/1748-0221/3/08/S08002.

[80] LHCb Collaboration. "The LHCb Detector at the LHC". In: *Journal of Instrumentation* **3**.08 (2008). URL: https://dx.doi.org/10.1088/1748-0221/3/08/S08005.

[81] CERN. "The LHC lead-ion collision run starts, CERN news". URL: https://home.cern/news/news/experiments/lhc-lead-ion-collision-run-starts.

[82] C. Hasse. "Simple sketch of the LHC". URL: https://github.com/hassec/LHC_Sketch.

[83] LHCb Collaboration. "The LHCb Upgrade I". In: *JINST* **19**.05 (2024). URL: https://inspirehep.net/literature/2660905.

[84] C. Elsasser. "$\bar{b}b$ production angle plots". URL: https://lhcb.web.cern.ch/lhcb/speakersbureau/html/bb_ProductionAngles.html.

[85] LHCb Collaboration. "LHCb VELO Upgrade Technical Design Report". Tech. rep. 2013. URL: https://cds.cern.ch/record/1624070.

[86] LHCb Collaboration. "LHCb Tracker Upgrade Technical Design Report". Tech. rep. 2014. URL: https://cds.cern.ch/record/1647400.

[87] S. Amato et al. "LHCb magnet". Technical design report. LHCb. Geneva: CERN, 2000. URL: https://cds.cern.ch/record/424338.

[88] O. Callot and S. Hansmann-Menzemer. "The Forward Tracking". Tech. rep. Geneva: CERN, 2007. URL: https://cds.cern.ch/record/1033584.

[89] M. Needham. "Performance of the Track Matching". Tech. rep. Geneva: CERN, 2007. URL: https://cds.cern.ch/record/1060807.

[90] R. E. Kalman. "A New Approach to Linear Filtering and Prediction Problems". In: *Transactions of the ASME–Journal of Basic Engineering* **82**.Series D (1960), pp. 35–45. URL: https://www.cs.unc.edu/~welch/kalman/media/pdf/Kalman1960.pdf.

[91] E. Rodrigues. "Dealing with clones in the tracking". Tech. rep. Geneva: CERN, 2006. URL: https://cds.cern.ch/record/1000723.

[92] M. De Cian et al. "Fast neural-net based fake track rejection in the LHCb reconstruction". Tech. rep. Geneva: CERN, 2017. URL: https://cds.cern.ch/record/2255039.

[93] LHCb Collaboration. "LHCb PID Upgrade Technical Design Report". Tech. rep. 2013. URL: https://cds.cern.ch/record/1624074.

[94] M. Adinolfi et al. "Performance of the LHCb RICH detector at the LHC". In: *Eur. Phys. J. C* **73** (2013). URL: https://cds.cern.ch/record/1495721.

[95] R. Calabrese et al. "Performance of the LHCb RICH detectors during LHC Run 2". In: *Journal of Instrumentation* **17**.07 (2022). URL: https://dx.doi.org/10.1088/1748-0221/17/07/P07013.

[96] C. D'Ambrosio. "The future of RICH detectors through the light of the LHCb RICH". In: *Nuclear Instruments and Methods in Physics Research Section A: Accelerators, Spectrometers, Detectors and Associated Equipment* **876** (2017). The 9th international workshop on Ring Imaging Cherenkov Detectors (RICH2016). URL: https://www.sciencedirect.com/science/article/pii/S0168900217302760.

[97] M. Andreotti et al. "Characterisation of signal-induced noise in Hamamatsu R11265 Multianode Photomultiplier Tubes". In: *Journal of Instrumentation* **16**.11 (2021). URL: https://dx.doi.org/10.1088/1748-0221/16/11/P11030.

[98] C. Gotti. "An ASIC for fast single photon counting in the LHCb RICH upgrade". In: *Journal of Instrumentation* **12**.03 (2017). URL: https://dx.doi.org/10.1088/1748-0221/12/03/C03016.

[99] M. Baszczyk et al. "CLARO: an ASIC for high rate single photon counting with multi-anode photomultipliers". In: *Journal of Instrumentation* **12**.08 (2017). URL: https://dx.doi.org/10.1088/1748-0221/12/08/P08019.

[100] M.K. Baszczyk et al. "Test of the photon detection system for the LHCb RICH Upgrade in a charged particle beam". In: *Journal of Instrumentation* **12**.01 (2017). URL: https://dx.doi.org/10.1088/1748-0221/12/01/P01012.

[101] A. Papanestis, F. Keizer, and S.A. Wotton. "The upgrade of the LHCb RICH system for the LHC Run 3". In: *Journal of Instrumentation* **15**.09 (2020). URL: https://dx.doi.org/10.1088/1748-0221/15/09/C09022.

[102] C. Abellán Beteta et al. "Calibration and performance of the LHCb calorimeters in Run 1 and 2 at the LHC". 2020. URL: https://arxiv.org/abs/2008.11556.

[103] P.R Barbosa-Marinho et al. "LHCb muon system". Technical design report. LHCb. 2001. URL: https://cds.cern.ch/record/504326.

[104] LHCb Collaboration. "Computing Model of the Upgrade LHCb experiment". Tech. rep. 2018. URL: https://cds.cern.ch/record/2319756.

[105] LHCb Collaboration. "RTA and DPA dataflow diagrams for Run 1, Run 2, and the upgraded LHCb detector". 2020. URL: https://cds.cern.ch/record/2730181.

[106] R. Aaij et al. "Allen: A High-Level Trigger on GPUs for LHCb". In: *Computing and Software for Big Science* **4**.1 (2020). URL: http://dx.doi.org/10.1007/s41781-020-00039-7.

[107] A. Scarabotto. "Tracking on GPU at LHCb's fully software trigger". 2022. URL: https://cds.cern.ch/record/2823783.

[108] LHCb Collaboration. "Moore documentation". URL: https://lhcbdoc.web.cern.ch/lhcbdoc/moore/master/index.html.

[109] A. Abdelmotteleb et al. "The LHCb Sprucing and Analysis Productions". In: *Computing and Software for Big Science* **9**.1 (2025). URL: http://dx.doi.org/10.1007/s41781-025-00144-5.

[110] LHCb Collaboration. "LHCb Analysis Productions documentation". URL: https://lhcb-ap.docs.cern.ch.

[111] LHCb Collaboration. "DaVinci Documentation". 2025. URL: https://lhcb-davinci.docs.cern.ch/.

[112] LHCb Collaboration. "Observation of the Mass Difference between Neutral Charm-Meson Eigenstates". In: *Phys. Rev. Lett.* **127** (11 Sept. 2021), p. 111801. DOI: 10.1103/PhysRevLett.127.111801. URL: https://link.aps.org/doi/10.1103/PhysRevLett.127.111801.

[113] Muriel Pivk and Francois R. Le Diberder. "SPlot: A Statistical tool to unfold data distributions". In: *Nucl. Instrum. Meth. A* **555** (2005), pp. 356–369. DOI: 10.1016/j.nima.2005.08.106. arXiv: physics/0402083.

[114] I. Adachi et al. "Measurement of $\cos 2\beta$ in $B^0 \to D^{(*)}h^0$ with $D \to K^0_S\pi^+\pi^-$ decays by a combined time-dependent Dalitz plot analysis of BaBar and Belle data". In: *Phys. Rev. D* **98**.11 (2018), p. 112012. DOI: 10.1103/PhysRevD.98.112012. arXiv: 1804.06153 [hep-ex].

[115] LHCb Collaboration. "Search for CP violation in $D_s^+ \to K^0_S\pi^+$, $D^+ \to K^0_S K^+$ and $D^+ \to \phi\pi^+$ decays". In: *Phys. Rev. Lett.* **122** (2019), p. 191803. DOI: 10.1103/PhysRevLett.122.191803. arXiv: 1903.01150. URL: https://cds.cern.ch/record/2665515.

[116] F. James. "MINUIT: Function Minimization and Error Analysis Reference Manual". In: (1998). CERN Program Library Long Writeups. URL: https://cds.cern.ch/record/2296388.

[117] LHCb. "LHCb Upgrade II Scoping Document". Tech. rep. CERN-LHCC-2024-010, LHCB-TDR-026. Geneva: CERN, 2024. URL: https://cds.cern.ch/record/2903094.

[118] Apollinari G. et al. "High-Luminosity Large Hadron Collider (HL-LHC)". CERN Yellow Reports: Monographs. Geneva: CERN, 2017. DOI: 10.23731/CYRM-2017-004. URL: https://cds.cern.ch/record/2284929.

[119] LHCb Collaboration. "Determination of short- and long-distance contributions in $B^0 \to K^{*0}\mu^+\mu^-$ decays". In: *Phys. Rev. D* **109** (5 Mar. 2024), p. 052009. DOI: 10.1103/PhysRevD.109.052009. URL: https://link.aps.org/doi/10.1103/PhysRevD.109.052009.

[120] LHCb Collaboration. "Amplitude Analysis of the $B^0 \to K^{*0}\mu^+\mu^-$ Decay". In: *Phys. Rev. Lett.* **132** (13 Mar. 2024), p. 131801. DOI: 10.1103/PhysRevLett.132.131801. URL: https://link.aps.org/doi/10.1103/PhysRevLett.132.131801.

[121] LHCb Collaboration. "Erratum to: Comprehensive analysis of local and non-local amplitudes in the $B^0 \to K^{*0}\mu^+\mu^-$ decay". In: *JHEP* **05** (May 2025). Erratum to JHEP 09 (2024) 026, p. 208. DOI: 10.1007/JHEP05(2025)208.

[122] LHCb Collaboration. "Measurement of lepton universality parameters in the $B^+ \to K^+\ell^+\ell^-$ and $B^0 \to K^{*0}\ell^+\ell^-$ decays". In: *Phys. Rev. D* **108** (3 Aug. 2023), p. 032002. DOI: 10.1103/PhysRevD.108.032002. URL: https://link.aps.org/doi/10.1103/PhysRevD.108.032002.

[123] LHCb Collaboration. "Test of Lepton Universality in $b \to s\ell^+\ell^-$ Decays". In: *Phys. Rev. Lett.* **131** (5 Aug. 2023), p. 051803. DOI: 10.1103/PhysRevLett.131.051803. URL: https://link.aps.org/doi/10.1103/PhysRevLett.131.051803.

[124] LHCb. "Hadron PID Performance in 2024". LHCb-FIGURE-2024-031. URL: https://cds.cern.ch/record/2913359.

[125] Rolf Lindner. "LHCb Particle Identification Enhancement Technical Design Report". Tech. rep. Geneva: CERN, 2023. DOI: 10.17181/CERN.LAZM.F5OH. URL: https://cds.cern.ch/record/2866493.

[126] LHCb. "Framework TDR for the LHCb Upgrade II". Tech. rep. CERN-LHCC-2021-012, LHCB-TDR-023. Geneva: CERN, 2021. URL: https://cds.cern.ch/record/2776420.

[127] S. Easo. "RICH and TORCH: Design status". Presentation at the Upgrade II Workshop, Heidelberg. Available at https://indico.cern.ch/event/1491351/contributions/6377158/attachments/3039774/5369122/RICH-TORCH-design-Status-Upgrade2-Heidelberg-2025.pdf. Mar. 27, 2025.

[128] R W Forty and O Schneider. "RICH pattern recognition". Tech. rep. LHCb-98-040. Geneva: CERN, 1998. URL: https://cds.cern.ch/record/684714.